Statistical and Numerical Investigations of Fluid Turbulence

Michael Wilczek

November 2010

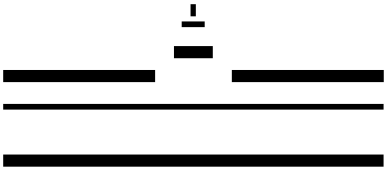

Westfälische
Wilhelms-Universität
Münster

Theoretische Physik

Statistical and Numerical Investigations of Fluid Turbulence

Inauguraldissertation
zur Erlangung des Doktorgrades
der Naturwissenschaften im Fachbereich Physik
der Mathematisch-Naturwissenschaftlichen Fakultät
der Westfälischen Wilhelms-Universität Münster

vorgelegt von
Michael Wilczek
aus Salzkotten

– 2010 –

revised online version: 03.02.2011

Dekan:	Prof. Dr. Johannes P. Wessels
Erster Gutachter:	Prof. Dr. Rudolf Friedrich
Zweiter Gutachter:	Prof. Dr. Frank Jenko
Tag der mündlichen Prüfung:	28.01.2011
Tag der Promotion:	28.01.2011

Abstract

The statistical description of fully developed turbulence up to today remains a central open issue of classical physics. Apart from the fact that turbulence plays a key role in many natural and engineering environments, the solution of the problem is also of interest on a conceptual level. Hydrodynamical turbulence may be regarded as a paradigmatic example for a strongly interacting system with a high number of degrees of freedom out of equilibrium, for which a comprehensive statistical mechanics is yet to be formulated.

The statistical formulation of turbulent flows can either be approached from a phenomenological side or by deriving statistical relations right from the basic equations of motion. While phenomenological theories often lead to a good description of a variety of statistical quantities, the amount of physical insights to be possibly gained depends heavily on the validity of the assumptions made. On the contrary, statistical theories based on first principles have to face the famous closure problem of turbulence, which prevents a straightforward solution of the statistical problem.

The present thesis aims at the investigation of a statistical theory of turbulence in terms of probability density functions (PDFs) based on first principles. To this end we make use of the statistical framework of the Lundgren-Monin-Novikov hierarchy, which allows to derive evolution equations for probability density functions right from the equations of fluid motion. The arising unclosed terms are estimated from highly resolved direct numerical simulations of fully developed turbulence, which allows to make a connection between basic dynamical features of turbulence and the observed statistics.

As a technical prerequisite, a parallel pseudospectral code for the direct numerical simulation (DNS) of fully developed turbulence has been developed and tested within this thesis. A number of standard statistical evaluations are presented with the purpose both to benchmark the numerical results as well as to characterize the statistical features of turbulence.

Studying the PDF equations, a comprehensive treatment of the single-point velocity and vorticity statistics is achieved within the current work. By making use of statistical symmetries present in the case of homogeneous isotropic turbulence, exact expressions for, e.g., the stationary PDF are derived in terms of correlations between the turbulent field and various quantities determining the dynamics of the field. The joint numerical and analytical investigations eventually lead to an explanation of the slightly sub-Gaussian tails for the velocity statistics and the highly non-Gaussian vorticity statistics with pronounced tails. To contribute to the characterization of the multi-point statistics of turbulence, the two-point enstrophy statistics is investigated. The results quantify

the interaction of different spatial scales and give insights into the spatial structure of the vorticity field. Along the lines of preceding works in this context the local conditional structure of the vorticity field and its relation to the multi-point statistics of the vorticity field is discussed and applied to the two-point enstrophy statistics. Finally, the closure problem of turbulence is treated on a more conceptual level by pursuing the question how to establish a model for the two-point PDF which is consistent with the single-point evolution equation and a number of statistical constraints to be imposed on probability density functions. A simple analytical model for the joint PDF is developed and improvements in the context of maximum entropy methods are discussed. Both models are compared to results from DNS.

Altogether, the results of the current thesis help to establish a connection between the flow topology, dynamical quantities that determine the temporal evolution of the turbulent fields and the resulting statistics. Beyond the characterization and explanation of these statistical quantities this provides new insights for future modeling and closure strategies.

Kurzfassung

Die statistische Beschreibung voll entwickelter Turbulenz bleibt bis heute ein zentrales ungelöstes Problem der klassischen Physik. Neben der Tatsache, dass Turbulenz eine zentrale Rolle in vielen natürlichen und ingenieurstechnischen Umgebungen spielt, ist die Lösung des Problems auch auf einer konzeptionellen Ebene von Interesse. So kann hydrodynamische Turbulenz als ein paradigmatisches Beispiel für ein stark wechselwirkendes System mit vielen Freiheitsgraden jenseits des thermodynamischen Gleichgewichts angesehen werden, für das eine umfassende statistische Beschreibung noch fehlt.

Die statistische Beschreibung turbulenter Strömungen kann einerseits im Rahmen phänomenologischer Theorien oder durch Ableiten statistischer Relationen direkt aus den Bewegungsgleichungen für das Fluid erfolgen. Während phänomenologische Theorien oftmals eine adäquate Beschreibung vieler statistischer Größen zulassen, hängt die Möglichkeit physikalische Einsichten aus ihnen zu gewinnen stark von der Gültigkeit der zugrundeliegenden phänomenologischen Annahmen ab. Im Gegensatz dazu stehen Theorien, die direkt aus den Grundgleichungen abgeleitet werden, dem bekannten Schließungsproblem der Turbulenz gegenüber, welches eine einfache Lösung des statistischen Problems verhindert.

Gegenstand der vorliegenden Arbeit ist die Untersuchung einer statistischen Theorie der Turbulenz, die in Form von Wahrscheinlichkeitsdichtefunktionen (PDFs) formuliert wird und auf den Grundgleichungen der Hydrodynamik basiert. Dies geschieht im Rahmen der statistischen Gleichungen der Lundgren-Monin-Novikov Hierarchie, welche es erlauben, Entwicklungsgleichungen für Wahrscheinlichkeitsdichtefunktionen direkt aus den Bewegungsgleichungen für ein Fluid abzuleiten. Die dabei auftretenden ungeschlossenen Terme werden mit Hilfe von hochauflösenden direkten numerischen Simulationen voll entwickelter Turbulenz bestimmt, wodurch eine direkte Verbindung zwischen grundlegenden dynamischen Eigenschaften turbulenter Strömungen und der beobachteten Statistik hergestellt werden kann.

Um die technischen Voraussetzungen für die Durchführung dieser Arbeit zu schaffen, ist ein paralleler Pseudospektralcode für die direkte numerische Simulation voll entwickelter Turbulenz entwickelt und getestet worden. In diesem Zusammenhang wird eine Auswahl gängiger statistischer Größen präsentiert, um sowohl die Simulationsergebnisse zu validieren, als auch um einen Einblick in die statistischen Eigenschaften voll entwickelter Turbulenz zu gewähren.

Durch die Untersuchung der PDF-Gleichungen wird im Rahmen der vorliegenden Arbeit eine umfassende Behandlung der Einpunktstatistik von Geschwindigkeit und Wirbelstärke erreicht. Die Ausnutzung statistischer Symmetrien, wie sie bei homogen isotroper Turbulenz vorzufinden sind, erlaubt es, exakte Ausdrücke für beispielsweise die

stationäre Verteilungsfunktion des jeweils betrachteten turbulenten Feldes herzuleiten. Dabei wird die Verteilungsfunktion durch verschiedene Korrelationen zwischen dem turbulenten Feld und Größen, welche die Dynamik dieses Feldes bestimmen, ausgedrückt. Die Verknüpfung numerischer und analytischer Untersuchungen führt schließlich zu einer Erklärung für die leicht sub-Gauß'schen Flügel der Geschwindigkeitsverteilung und der stark nicht-Gauß'schen Wirbelstärkenverteilung mit ausgeprägten Flügeln. Weiterhin wird die Zweipunktstatistik der Enstrophie untersucht, um zu einer Charakterisierung der Mehrpunktstatistik turbulenter Strömungen beizutragen. Die Ergebnisse verdeutlichen die Interaktion verschiedener räumlicher Skalen und ermöglichen Einblicke in die räumliche Struktur des Wirbelfeldes. Aufbauend auf frühere Arbeiten wird in diesem Zusammenhang die lokale bedingte Struktur des Wirbelfeldes und ihre Verbindung zur Mehrpunkverteilung des Wirbelfeldes diskutiert und schließlich auf die Zweipunkt-Enstrophiestatistik angewendet. Zu guter Letzt wird das Schließungsproblem auf konzeptioneller Ebene behandelt, indem der Frage nachgegangen wird, wie ein Modell für die Zweipunktverteilung formuliert werden kann, das sowohl in Einklang mit der Entwicklungsgleichung für die Einpunktverteilung steht, als auch weitere statistische Randbedingungen für Wahrscheinlichkeitsdichteverteilungen erfüllt. Es wird ein einfaches analytisches Modell für die Verbundwahrscheinlichkeit entworfen, und Verbesserungen im Rahmen von Maximum-Entropie-Methoden werden diskutiert. Beide Modelle werden mit Ergebnissen direkter numerischer Simulationen verglichen.

Insgesamt helfen die Ergebnisse der vorliegenden Arbeit, eine Verbindung zwischen der Topologie der Strömung, dynamischen Größen, welche die zeitliche Entwicklung der turbulenten Felder bestimmen, und der resultierenden Statistik herzustellen. Über die Charakterisierung und Erklärung dieser Statistik hinaus vermittelten die Ergebnisse neue Einsichten für zukünftige Modellierungs- und Schließungsansätze.

Contents

Introduction

When writing a thesis on the topic of turbulence, it is nearly impossible to formulate some introductory remarks without repeating the views and ideas that have come up frequently in the literature over the last decades or even centuries. One of the reasons for this is that the dynamics of flowing fluids is a topic not only accessible to experts, it is rather a phenomenon which belongs to fundamental everyday experiences of every human being, such that contemplating about the topic almost inevitably brings up the common examples. For instance, everybody can recall a vivid picture of a flowing river or the spreading of a droplet of ink in a glass of water. It is also accessible on this intuitive level that a fluid driven strongly enough reaches a state of spatial and temporal disorder known as turbulence. If one tries to describe the properties of, for example, the rising smoke of a fire or the motion of rapidly moving fluid behind an obstacle in a few simple words, it is immediately clear that the observed phenomenon shows signatures of complexity both in space and time.

Although turbulence is something known to everyone, its concise physical description remains a challenge of classical physics up to today. This is even more astonishing as the properties of turbulence are not only of academic interest, the turbulent state of fluid flow is rather found in many natural and engineering environments. The complex dynamics of the atmosphere, the oceans or different chemical species in a combustion reaction may serve as the most prominent examples. Beyond its ubiquitous appearance in nature, turbulence can be seen as a paradigmatic physical system with a number of interesting features. On this level one can distinguish between features that are more specific to "real world systems", which include the influence of specific boundary conditions or forcing schemes like buoyancy or Coriolis forces on the flow, and the idealized situation of a fully developed turbulent flow far away from the boundaries. This "pure" turbulence is especially suited to expose the nonlocal and nonlinear nature of the governing equations of motion and is characterized by highly fluctuating spatio-temporal patterns without regular structure and no distinct direction.

It is mainly the latter situation which motivates a description of turbulence with statistical methods. While the methods of statistical mechanics yield a comprehensive description of systems in thermodynamic equilibrium and also give insights into the statistics of weakly interacting systems driven slightly out of equilibrium, these methods fail in the case of turbulent flows for a number of reasons. First of all, fully developed turbulence is a system driven far out of equilibrium; in the case of three-dimensional turbulence the flow is usually generated by a large-scale external forcing. Energy then is transferred by nonlinear interactions to ever smaller scales until dissipated on the smallest scales. For the case of stationary turbulence a constant flux of energy is established,

which maintains the statistical properties of the turbulent system. Second, and closely related to the nonlinear and nonlocal character of the equations of motion, the emergence of coherent structures in the flow is a typical feature. These structures are especially noticeable when considering the vorticity field. It turns out that this field is characterized by a global entangled net of small filamentary vortex structures, which interact in a nonlinear manner and are advected due to their collectively produced velocity field. Hence turbulent fields display signatures of order, yet being a rather complicated and fluctuating one. In this sense turbulence may be regarded as too unstructured to be described with methods appropriate for systems displaying a pronounced order, but still is too structured to be described in terms of simple stochastic methods only. All of these features are the signatures of a strongly interacting nonlinear system, which basically constitute the challenge in developing a statistical theory of turbulence.

First attempts to derive a comprehensive statistical theory from first principles go back to the middle of the twentieth century when measurements of even the most simple fluctuating quantities were a grand challenge and the insights to be gained from computer simulations were technically out of reach. Still the pioneering works of Kolmogorov, Batchelor, Hopf, Lundgren, Monin, Yaglom and Novikov (to name only but a few) paved the way for the whole branch of statistical fluid mechanics. This was achieved by deriving statistical equations right from the Navier-Stokes equations in a couple of different approaches. Maybe the most comprehensive one in this respect is to formulate a statistical equation for the whole velocity field. While this approach pursued by Hopf indeed allows for a concise formulation of the problem, the resulting equations for the characteristic functional up to today remain mathematically too complicated to obtain useful results. Also motivated by experimental measurement techniques, it is interesting to study the statistics of turbulence not on this comprehensive level, it rather often suffices to characterize the statistics at a single point or few points in space and time. When deriving statistical equations for this condensed type of information, one has to face the central problem of statistical turbulence research, the closure problem. For example, when deriving evolution equations for statistical averages, so-called moments, these equations couple to higher-order moments. If one now proceeds to derive the corresponding evolution equations for these moments, even higher-order moments show up. Something similar is observed when formulating the problem in terms of probability density functions. In this case the closure problem becomes manifest by the fact that for each evolution equation information involving more points in space than currently taken into account is needed. In both cases one ends up with an infinite hierarchy of equations. It up to today remains one of the central issues to solve these equations either exactly or in an approximate manner to obtain physically reasonable results.

The current thesis takes some of these classical theoretical foundations as a starting point to investigate the statistics of fully developed turbulence in terms of probability density functions. Apart from a purely analytical treatment of the problem, direct numerical simulations of fully developed turbulence are used to provide information on the statistical properties and establish a connection between the basic dynamical aspects, the flow topology and the resulting statistics. The thesis is subdivided into

three distinct parts.

The first part is devoted to give an introduction into the basic equations of motion as well as to provide a first glimpse at the phenomena observed in a fully developed turbulent flow. Then the conceptual foundations for the statistical description of turbulence are introduced and exemplified with some classic results. We then turn to a detailed description of the implementation of the algorithm with which all of the numerical results in this thesis have been generated.

The second part starts with a detailed presentation of statistical properties of turbulence, where the aim is both to characterize turbulence as well as to benchmark the numerical results. Additionally, some comparisons to experimentally obtained data are presented to highlight strengths and shortcomings of numerical simulations. In view of the fact that the full Navier-Stokes equations are analytically hard to investigate, we turn to a simplified nonlinear system to study some deterministic aspects. By studying the velocity gradients of the Burgers equations, some mechanisms also found in incompressible flows are investigated.

The third and central part then deals with a joint analytical and numerical investigation of the statistics of fully developed turbulence in terms of probability density functions. After a short introduction including some historical remarks and a review of the basic techniques necessary to derive the equations, we turn to an investigation of the single-point statistics of velocity and vorticity. To mention only a single result of this part, we derive relations that connect the shape and evolution of the single-point probability density function to the correlations of different dynamical quantities, which then can be interpreted and discussed on the basis of physical intuition. Furthermore, the results obtained from DNS can be used to test and validate these relations demonstrating the consistency of the theoretical framework. Especially the origin of the differing statistics of the velocity and vorticity field is discussed here. After this rather comprehensive treatment of the single-point statistics, the remaining two chapters deal with different aspects of the two-point statistics of vorticity. Starting with an investigation of the two-point statistics of enstrophy characterizing the spatial structure of the vorticity field, then the questions is pursued how the closure problem of turbulence is related to the local conditional structure of the vorticity field. In the last chapter this question then is extended to the proper modeling of two-point PDFs, which are consistent with the statistical equations and further statistical constraints. Finally, the conclusions are drawn and some perspectives on future research are given.

Part I.

Fundamentals

1. Fundamental Features of Turbulent Flows

This chapter shall give a brief overview of the governing equations of motion and the observed phenomena in fully developed turbulence. To this end we will discuss the Navier-Stokes and related equations, before we present some visualizations from numerical simulations. To get a better impression of the fine-scale structure of the field, then some properties of vortex solutions are discussed.

1.1. Basic Equations of Motion

The temporal evolution of the velocity field $\boldsymbol{u}(\boldsymbol{x},t)$ of an incompressible fluid in three dimensions with unit density is given by the Navier-Stokes equation

$$\frac{\partial}{\partial t}\boldsymbol{u}(\boldsymbol{x},t) + \boldsymbol{u}(\boldsymbol{x},t)\cdot\nabla\boldsymbol{u}(\boldsymbol{x},t) = -\nabla p(\boldsymbol{x},t) + \nu\Delta\boldsymbol{u}(\boldsymbol{x},t) + \boldsymbol{F}(\boldsymbol{x},t) \quad , \tag{1.1}$$

where p denotes the pressure field, ν is the kinematic viscosity, and $\boldsymbol{F}$ denotes an external forcing which drives the fluid. Incompressibility is ensured by the additional equation

$$\nabla\cdot\boldsymbol{u}(\boldsymbol{x},t) = 0 \quad , \tag{1.2}$$

which is nothing else than the continuity equation for a fluid with constant density. These equations have been formulated by Claude-Luis Navier (in 1822) and George Gabriel Stokes (in 1845), several decades after the inviscid Euler equations have been introduced. The equation displays two major mathematical difficulties. The nonlinearity of the advective term on the left-hand side and additionally the nonlocality of the pressure term. This nonlocality can be seen by taking the divergence of the equation, which yields an inhomogeneous Poisson equation for the pressure

$$\Delta p(\boldsymbol{x},t) = -\nabla\cdot[\boldsymbol{u}(\boldsymbol{x},t)\cdot\nabla\boldsymbol{u}(\boldsymbol{x},t)] \quad , \tag{1.3}$$

which can be solved yielding

$$p(\boldsymbol{x},t) = \frac{1}{4\pi}\int \mathrm{d}\boldsymbol{x}'\,\frac{\nabla_{\boldsymbol{x}'}\cdot[\boldsymbol{u}(\boldsymbol{x}',t)\cdot\nabla_{\boldsymbol{x}'}\boldsymbol{u}(\boldsymbol{x}',t)]}{|\boldsymbol{x}-\boldsymbol{x}'|} \quad . \tag{1.4}$$

Here, we have assumed an infinitely extended fluid and a solenoidal external forcing. This relation indicates that the pressure at a given point in space is determined by the

instantaneous velocity at all other points in the domain, weighted by an algebraically slow decaying integral kernel. This instantaneous dependence comes from the assumption of incompressibility, which implies an infinite speed of sound. The assumption of incompressibility is fulfilled in many real-world situations as it holds whenever the velocity of the fluid is small compared to the speed of sound in the medium. Dropping the pressure term from equation (1.1) yields the so-called (three-dimensional) Burgers equation, which will be discussed in chapter 5. By dropping the pressure term, the fluid becomes perfectly compressible and the solutions of this equation will be very different from those of the incompressible Navier-Stokes equation as features of highly compressible flows like shocks will develop.

The velocity field may be decomposed into a scalar and a vector potential according to

$$\boldsymbol{u}(\boldsymbol{x},t) = \nabla\phi(\boldsymbol{x},t) + \nabla \times \boldsymbol{A}(\boldsymbol{x},t) \quad , \tag{1.5}$$

from which the two Poisson equations

$$\Delta\phi(\boldsymbol{x},t) = \nabla \cdot \boldsymbol{u}(\boldsymbol{x},t) \tag{1.6a}$$

$$\Delta\boldsymbol{A}(\boldsymbol{x},t) = -\nabla \times \boldsymbol{u}(\boldsymbol{x},t) \tag{1.6b}$$

are readily obtained (where we chose $\nabla \cdot \boldsymbol{A}(\boldsymbol{x},t) = 0$ due to gauge freedom). It is clear that ϕ is related to the sinks and sources and hence compressible components of the velocity field, whereas $\boldsymbol{A}$ is determined by the rotational part of the fluid. In a general compressible situation (as, for example, the Burgers equation for non-potential initial conditions) both potentials will play a role, whereas the incompressible case is determined by the rotational component only. In fact the vorticity, defined as

$$\boldsymbol{\omega}(\boldsymbol{x},t) = \nabla \times \boldsymbol{u}(\boldsymbol{x},t) \quad , \tag{1.7}$$

will play a key role in the following. As the curl of the velocity field it indicates locally swirling regions of the flow. Loosely speaking, a vortex can be regarded as a localized region of strong vorticity. It turns out that three-dimensional turbulence shows a complicated structure consisting of thin, elongated vortex tubes, which will be demonstrated in section 1.2. The incompressible Navier-Stokes equation can be expressed in terms of the vorticity by taking the curl of equation (1.1). The resulting so-called vorticity equation reads

$$\begin{aligned}\frac{\partial}{\partial t}\boldsymbol{\omega}(\boldsymbol{x},t) + \boldsymbol{u}(\boldsymbol{x},t) \cdot \nabla\boldsymbol{\omega}(\boldsymbol{x},t) &= \boldsymbol{\omega}(\boldsymbol{x},t) \cdot \nabla\boldsymbol{u}(\boldsymbol{x},t) + \nu\Delta\boldsymbol{\omega}(\boldsymbol{x},t) + \nabla \times \boldsymbol{F}(\boldsymbol{x},t) \\ &= \mathrm{S}(\boldsymbol{x},t)\boldsymbol{\omega}(\boldsymbol{x},t) + \nu\Delta\boldsymbol{\omega}(\boldsymbol{x},t) + \nabla \times \boldsymbol{F}(\boldsymbol{x},t) \quad , \end{aligned} \tag{1.8}$$

where the last equality makes use of the fact that the vorticity "feels" only the symmetric part $\mathrm{S}(\boldsymbol{x},t) = \frac{1}{2}(\mathrm{A} + \mathrm{A}^T)$ of the velocity gradient tensor $\mathrm{A}(\boldsymbol{x},t) = \nabla\boldsymbol{u}(\boldsymbol{x},t)$. This formulation makes the interpretation of the vortex-stretching term $\mathrm{S}(\boldsymbol{x},t)\boldsymbol{\omega}(\boldsymbol{x},t)$ particularly intuitive. As S is a symmetric second-order tensor, it has three real eigenvalues, from which only two are independent due to solenoidality of the velocity field. Now when

this term is considered in the eigenframe in which S is diagonal, it is obvious that the vorticity will be stretched or damped due to this tensor. It turns out that stretching is predominant on the mean, which motivates the nomenclature. By taking the curl of the Navier-Stokes equation, the pressure gradient has dropped out. The nonlocality is now transferred to the velocity field, which again is related to the vorticity due to the Poisson equation

$$\Delta \boldsymbol{u}(\boldsymbol{x},t) = -\nabla \times \boldsymbol{\omega}(\boldsymbol{x},t) \quad , \tag{1.9}$$

which is solved by Biot-Savart's law

$$\boldsymbol{u}(\boldsymbol{x},t) = -\frac{1}{4\pi}\int \mathrm{d}\boldsymbol{x}' \, \frac{\boldsymbol{x}-\boldsymbol{x}'}{|\boldsymbol{x}-\boldsymbol{x}'|^3} \times \boldsymbol{\omega}(\boldsymbol{x}',t) \quad . \tag{1.10}$$

In order to characterize the fine-scale motion of turbulent flows further, sometimes the evolution equation for the velocity gradient tensor is considered, which takes the form

$$\frac{\partial}{\partial t}A_{ij} + u_k \frac{\partial}{\partial x_k}A_{ij} = -A_{ik}A_{kj} - \frac{\partial^2}{\partial x_i \partial x_j}p + \nu \frac{\partial^2}{\partial x_k^2}A_{ij} \quad , \tag{1.11}$$

where we have dropped the dependence on space and time. This equation is obtained from the Navier-Stokes equation by taking derivatives with respect to a spatial coordinate. Apart from the nonlinear advective term, the quadratic self-amplification term and the nonlocal pressure Hessian on the right-hand side constitute the main mathematical difficulties of this equation. When the velocity gradient tensor is decomposed into its symmetric and antisymmetric parts

$$\mathrm{S} = \frac{1}{2}(\mathrm{A} + \mathrm{A}^T) \quad \text{and} \quad \mathrm{W} = \frac{1}{2}(\mathrm{A} - \mathrm{A}^T) \quad , \tag{1.12}$$

two separate equations of motion can be obtained, of which the second is just the vorticity equation, as the antisymmetric part of the tensor is connected to the vorticity according to $\omega_i = -\epsilon_{ijk}\mathrm{W}_{jk}$.

1.2. A Panopticon of Turbulent Fields

Most of the results presented in this thesis will be of statistical nature. To better understand some of the statistical features investigated later on, it is useful to have a look at the spatial structure of the turbulent fields under consideration. The following visualizations are the result of direct numerical simulations of fully developed turbulence, the numerical technique will explained in chapter 3. All volume renderings within this thesis are produced with `VAPOR` [CR05, CMNR07], a free visualization tool especially suited for flow visualization. Before presenting the visualizations, a word of caution is in order. The features highlighted in a volume rendering depend strongly on the transfer function used. In that sense, the visualizations are to a certain degree subjective interpretations of the data. The aim of the presentation is to highlight typical features

of the flow, which necessarily means to fade out others. Consequently, this presentation should be understood as a qualitative panopticon to give a first impression of the structure of turbulent fields.

The top left picture in figure 1.1 shows events of strong vorticity in a direct numerical simulation at a Taylor-based Reynolds number (defined in chapter 3) of $R_\lambda = 112$ (`sim_512`). The region shown is the full simulation in height and width and half of the domain in depths. The vorticity field is organized into small, filamentary vortex tubes spread all over the domain. However, they do not seem to be distributed homogeneously, one can rather observe the tendency to form clusters. Within these clusters, the vortices form an entangled local structure indicating a complicated vorticity dynamics.

Right of this picture the velocity field produced by these vortices is shown. At first glance, it varies on much larger scales and does not contain clearly identifiable coherent structures like the vorticity field. The comparably large-scale character of the field comes due to the fact that the Biot-Savart law (1.10) may be regarded as a kind of smoothing filter. Although there are regions in which high velocities coincide with strong vorticity, a clear correlation is absent. This fact will play an important role whenever the joint statistics of large-scale and small-scale quantities is of interest. And although showing large-scale correlations, the velocity field exhibits pronounced gradients, which are related to regions of strong shear or rotation.

The bottom left picture shows the acceleration field. The acceleration field varies on scales comparable or slightly larger than the vorticity and a strong correlation between the vorticity and the acceleration is evident. A closer look, however, reveals that the acceleration takes its highest values *near* the vortex tubes, but not at the exactly same place. This will become clear in the following section, when a single vortex tube is considered.

The bottom right picture shows the field of the rate of energy dissipation highlighting regions of strong shear. Again strong correlations with the spatial structure of the vorticity are apparent. This is quite intuitive as the region between two strong vortices is a region of strong shear. While it is a well-known fact that the spatial average of squared vorticity (times viscosity) equals the average the rate of energy dissipation, it is apparent from this figure that these quantities do not coincide locally.

To clarify the Reynolds number dependence of these findings, figure 1.2 shows the vorticity and velocity field for two additional simulations at $R_\lambda = 76, 225$. A striking feature is that the tendency to form clusters is absent in the case of low Reynolds number and increases for higher Reynolds numbers. Especially for the high Reynolds number case it is evident that turbulence cannot be regarded as an ensemble of a small number of vortices. The velocity field maintains its large-scale correlations with the Reynolds number, however, an increasing separation between the smallest and the largest scales in the field is apparent, the field is becoming increasingly rough on the small scales. This indicates that the gradients of the velocity are becoming steeper with the Reynolds number, which will play a role when it comes to characterize the small-scale statistical features of the flow.

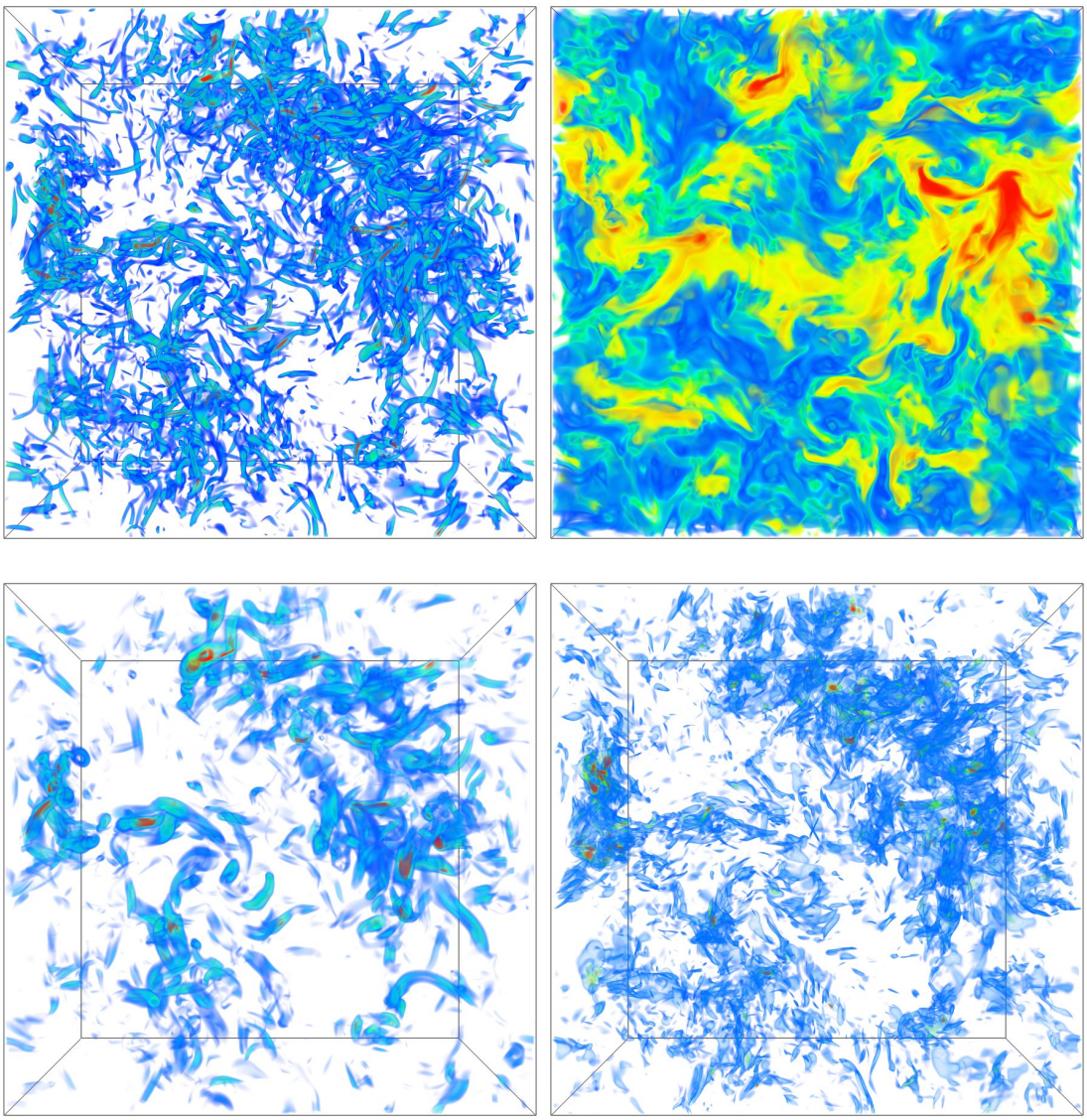

Figure 1.1.: Volume rendering of the vorticity (magnitude), velocity (magnitude), acceleration (magnitude) and dissipation fields (from top left to bottom right) from a direct numerical simulation at $R_\lambda = 112$. Half of the simulation domain is shown (`sim_512`).

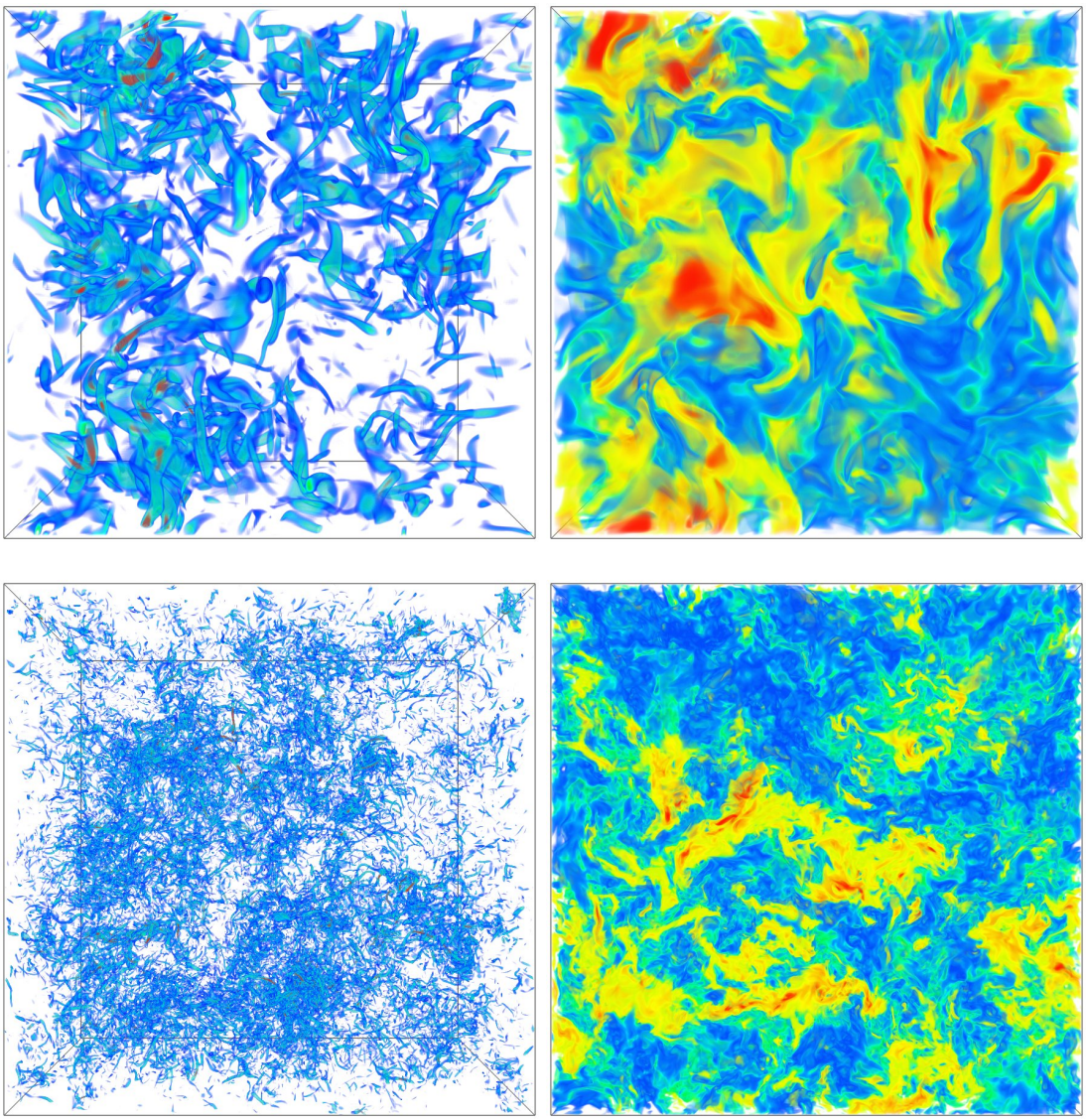

Figure 1.2.: Volume rendering of the magnitude of the vorticity and velocity at different Reynolds numbers ($R_\lambda = 76$ for the upper panel, $R_\lambda = 225$ for the lower panel) (`sim_256`, `sim_1024`).

1.3. Coherent Structures and Vortex Solutions

As we have seen in the preceding paragraph, the vorticity tends to organize into thin, slender vortex tubes in a fully developed turbulent flow. Compared to the velocity field, the vorticity field in this sense turns out to be more localized, something which could already been guessed from the fact that vorticity is related to the velocity gradients. This fact, which has been studied extensively numerically and experimentally (see, e.g., [SJO90, JWSR93, JW98, MHK03, MHK04]), has motivated a whole branch of turbulence research for a number of reasons. One of them is that the appearance of structures indicates that turbulence is not purely random and that conclusions on statistical properties of the flow might be drawn from the understanding of isolated structures. And while early direct numerical simulations at low resolution suggested that turbulence may be described in terms of a few localized structures, results from higher Reynolds number flows revealed that a low-dimensional description of turbulence is not feasible [YIU$^+$02] as the number of structures rapidly increases with the Reynolds number.

Nevertheless, many physical properties of the fine-scale structure of turbulence may be studied from simple vortex solutions of the Navier-Stokes equation (see, e.g., [Tow51] for an early account), and various modeling attempts take an ensemble of vortices as a starting point [HK97, Lun93, WJF08] making use of the fact that some vortex solutions are analytically known.

To find vortex solutions, one usually starts with considering a two-dimensional flow with an axisymmetric vorticity field. In this case the vorticity equation takes the form of the (linear) heat equation and has the famous Lamb-Oseen vortex as a solution [Saf92], a Gaussian vorticity profile, which produces an azimuthal velocity field. If this two-dimensional flow now is embedded in three dimensions and subject to a potential strain field, a three-dimensional solution can be found called the Burgers vortex [Bur48], a strained vortex solution of the Navier-Stokes equation. This vortex solution shares some features with the coherent structures observed in fully developed turbulence, but still is analytically fully accessible; hence we will discuss some of the properties in the following section. One has to keep in mind, though, that while a single Burgers vortex is a solution of the Navier-Stokes equation, a random ensemble generally is not, such that no dynamical information can be deduced from such considerations. Additionally, due to its axisymmetry, the Burgers vortex does not capture all the details of a vortex observed in turbulent flow. A more realistic vortex with an inner spiral structure has been introduced by Lundgren [Lun82], which, however, is beyond the scope of this short presentation.

1.3.1. Anatomy of a Vortex Tube

We now take a closer look at the Burgers vortex [Bur48], which can be obtained from the Navier-Stokes equation considering a velocity field which is decomposed into a

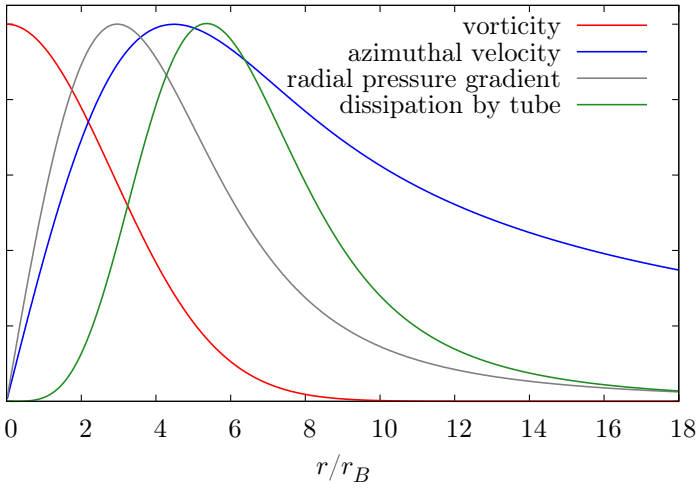

Figure 1.3.: Anatomy of a Burgers vortex with $\Gamma = 1$, $\nu = 1$ and $a = 1$. The vorticity field is localized and decays exponentially fast, whereas the remaining quantities show an algebraic decay for large distances. It is also noticeable that the maxima of the different quantities do not coincide. Amplitudes have been adjusted for a better comparison.

two-dimensional rotational and three-dimensional potential velocity

$$\boldsymbol{u}(\boldsymbol{x},t) = \boldsymbol{u}^{2d}(\boldsymbol{x},t) + \boldsymbol{u}^{3d}(\boldsymbol{x},t) \quad \text{with} \quad \boldsymbol{u}^{2d} = (u_x, u_y, 0) \quad \boldsymbol{u}^{3d} = \left(-\frac{a}{2}x, -\frac{a}{2}y, az\right) \quad . \tag{1.13}$$

As the rotational part is purely two-dimensional, the vorticity is a scalar quantity pointing into z-direction, $\boldsymbol{\omega} = \omega \boldsymbol{e}_z$. By introducing cylindrical coordinates it is possible to express the velocity field as $\boldsymbol{u}(\boldsymbol{x},t) = u_r\,\boldsymbol{e}_r + u_\varphi\,\boldsymbol{e}_\varphi + u_z\,\boldsymbol{e}_z$ with

$$u_r = -\frac{a}{2}r + v_r(r,\varphi,t) \tag{1.14a}$$

$$u_\varphi = v_\varphi(r,\varphi,t) \tag{1.14b}$$

$$u_z = az \quad , \tag{1.14c}$$

where v_r and v_φ are induced by the rotational part of the velocity field only, the remaining terms stem from the potential field. This simplifies equation (1.8) to

$$\frac{\partial\omega}{\partial t} + \left(-\frac{a}{2} + v_r\right)\frac{\partial\omega}{\partial r} + \frac{v_\varphi}{r}\frac{\partial\omega}{\partial\varphi} = a\omega + \nu\Delta\omega \quad . \tag{1.15}$$

If one now seeks for axisymmetric, time-independent solutions, i.e. $\omega(r,\varphi,t) = \omega(r)$, one can, due to Biot-Savart's law, conclude $v_r = 0$. Altogether the vorticity equation simplifies further to

$$-\frac{a}{2}\frac{\partial\omega}{\partial r} = a\omega + \nu\frac{1}{r}\frac{\partial}{\partial r}r\frac{\partial}{\partial r}\omega \quad . \tag{1.16}$$

The solution of this equation is the famous Burgers vortex with a vorticity field according to

$$\omega(r) = \frac{\Gamma a}{4\pi\nu}\,\mathrm{e}^{-\frac{ar^2}{4\nu}} \quad . \tag{1.17}$$

The vorticity displays a stationary Gaussian profile, where the radius $r_B = \left(\frac{4\nu}{a}\right)^{\frac{1}{2}}$ is determined by the ratio of the kinematic viscosity and the strain parameter of the potential velocity field. The amplitude of the vortex is additionally determined by the circulation Γ. With this exponential dependence, the vorticity of the Burgers vortex is strongly localized in space. The azimuthal velocity field, induced by the vortex tube only, is readily calculated with Biot-Savart's law yielding

$$u_\varphi = \frac{\Gamma}{2\pi r}\left(1 - \mathrm{e}^{-\frac{ar^2}{4\nu}}\right) \quad . \tag{1.18}$$

For large r we have an algebraic decay $\sim \frac{1}{r}$, indicating the long-range character of the velocity, which is consistent with the preceding observations.

Another interesting quantity is the acceleration induced by the vortex tube, which consists of the pressure gradient and the viscous term. These vectors are written in cylindrical coordinates according to

$$-\nabla p = (-\nabla p)_r\,\boldsymbol{e}_r + (-\nabla p)_\varphi\,\boldsymbol{e}_\varphi + (-\nabla p)_z\,\boldsymbol{e}_z \tag{1.19a}$$

$$\nu\Delta\boldsymbol{u} = (\nu\Delta\boldsymbol{u})_r\,\boldsymbol{e}_r + (\nu\Delta\boldsymbol{u})_\varphi\,\boldsymbol{e}_\varphi + (\nu\Delta\boldsymbol{u})_z\,\boldsymbol{e}_z \quad . \tag{1.19b}$$

The calculation of these terms is straightforward, but somewhat lengthy. For the pressure gradient one obtains

$$(-\nabla p)_r = \frac{a^2}{4}r - \frac{\Gamma^2}{4\pi^2 r^3}\left(1 - \mathrm{e}^{-\frac{ar^2}{4\nu}}\right)^2 \tag{1.20a}$$

$$(-\nabla p)_\varphi = 0 \tag{1.20b}$$

$$(-\nabla p)_z = a^2 z \quad . \tag{1.20c}$$

The terms $\sim a^2$ originate from the potential flow, whereas the second term of the negative radial pressure gradient is induced by the vortex tube. With an algebraic decay $\sim r^{-3}$ the pressure forces induced by the tube are of also of long-range type, however, with a faster decay than the velocity field. The viscous terms take the form

$$(\nu\Delta\boldsymbol{u})_r = 0 \tag{1.21a}$$

$$(\nu\Delta\boldsymbol{u})_\varphi = -\frac{\Gamma a^2 r}{8\pi\nu}\,\mathrm{e}^{-\frac{ar^2}{4\nu}} \tag{1.21b}$$

$$(\nu\Delta\boldsymbol{u})_z = 0 \quad , \tag{1.21c}$$

from which it is clear that only azimuthal contributions are induced by the vortex tube, which decay exponentially. As there is no radial contribution by the diffusive forces, the

radial acceleration induced by the tube comes from the pressure gradient only. It is also interesting to calculate the energy dissipation field $\varepsilon = 2\nu \mathrm{Tr}(\mathrm{S}^2)$. Due to the different contributions to the velocity field also the rate-of-strain tensor may be decomposed into a potential part and a part coming from the vortex tube. Calculating the energy dissipation field, it turns out that the cross terms vanish, such that we end up with

$$\begin{aligned} \varepsilon &= \varepsilon_{\mathrm{pot}} + \varepsilon_{\mathrm{tube}} \\ \varepsilon_{\mathrm{pot}} &= 3\nu a^2 \\ \varepsilon_{\mathrm{tube}} &= \frac{\Gamma^2}{16\pi^2 \nu r^4} \mathrm{e}^{-\frac{ar^2}{2\nu}} \left[ar^2 + 4\nu \left(1 - \mathrm{e}^{\frac{ar^2}{4\nu}} \right) \right]^2 \quad . \end{aligned} \tag{1.22}$$

Figure 1.3 shows the vorticity field, the azimuthal velocity field as well as the (negative) radial acceleration and the energy dissipation field induced by a Burgers vortex. As discussed before, the vorticity field is strongly localized, whereas the velocity field decays slowly. Additionally the velocity field vanishes inside the vortex core and peaks at about $5r_B$ (for the presented choice of parameters). Also the acceleration is peaked outside the vortex core, such that high accelerations may be expected in the vicinity of a vortex tube, but not inside the vortex. And although we have the equality $\langle \varepsilon \rangle = \langle \nu \omega^2 \rangle$ for homogeneous turbulence, the two quantities do not coincide locally; while the vorticity is concentrated inside the vortex tube, the induced dissipation field is not.

To illustrate that this behavior can qualitatively be found in fully developed turbulence, figure 1.4 shows the close-up of a vortex tube from a direct numerical simulation with 256^3 grid points (`sim_256`). Here, we see a volume rendering of the absolute values of vorticity, velocity, acceleration (i.e. the sum of pressure gradient and viscous terms) and the kinetic energy dissipation. In agreement with the above calculations we find that the vortex tube is strongly localized and is also inducing a strong velocity field locally. However, the velocity field contains contributions from distant vorticity as well, such that it displays a more large-scale structure. The acceleration field is also localized near the vortex core, and one in fact gets the impression that the acceleration does not peak in the core of the vortex. The kinetic energy dissipation field is also localized near the core, but also other regions of strong shear, which are not induced by the tube, are visible. One can conclude that the qualitative structure of these fields is consistent with the above calculations for an isolated vortex tube. More pronounced differences, however, become apparent when considering the inner structure of the vortex tube by inspecting the field lines of the vorticity field. The field lines of the same vortex tube are shown in figure 1.5 from two different perspectives. They indicate a twisted inner structure of the vortex tube, which is not taken into account by the simple Burgers vortex.

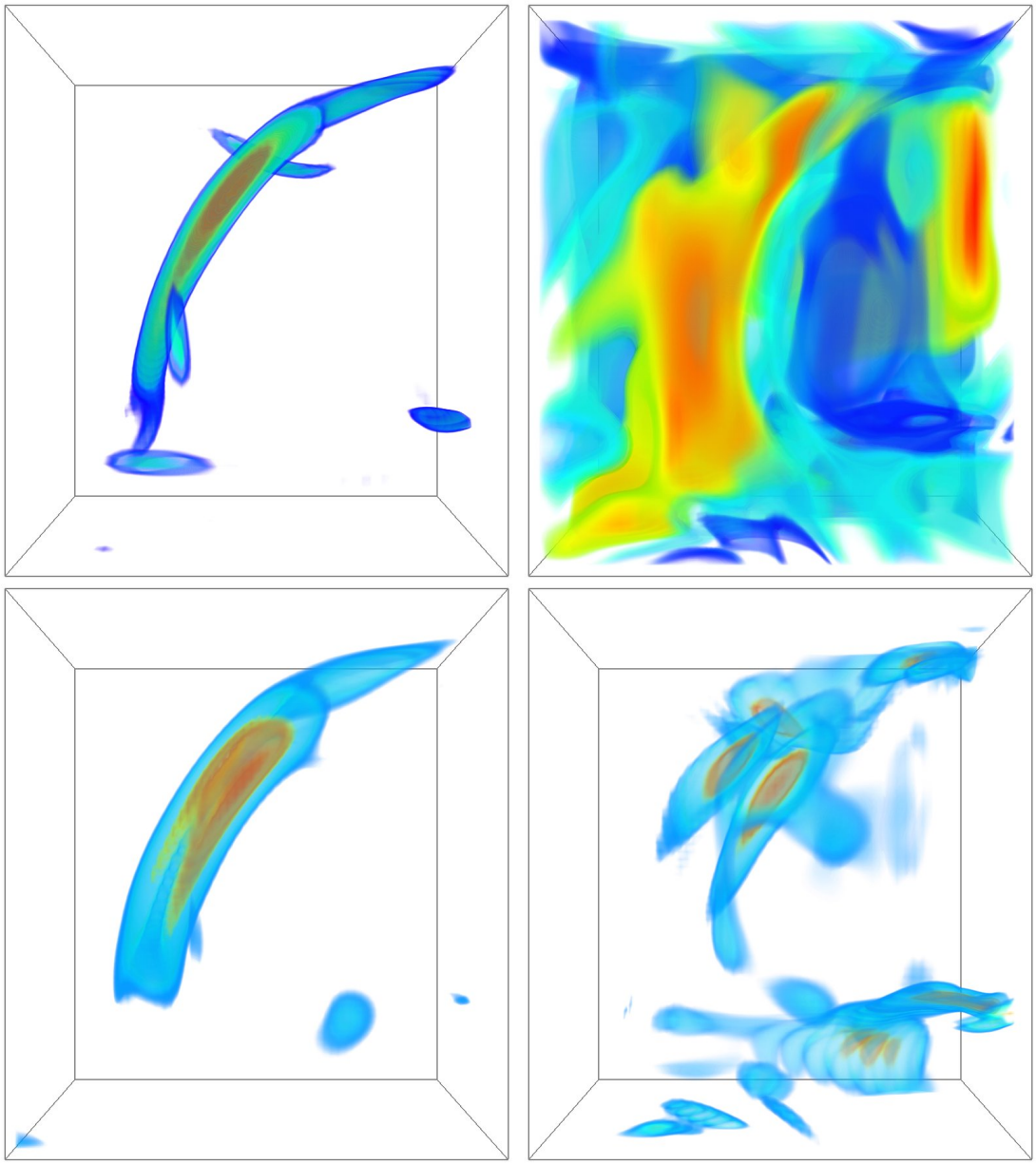

Figure 1.4.: Close-up of a vortex tube in a direct numerical simulation (`sim_256`). From upper left to lower right: volume rendering of the absolute values of vorticity, velocity, acceleration and dissipation. While the vorticity field is strongly localized, the velocity field appears to contain contributions from distant vorticity. The acceleration is localized near the vortex tube as well as the dissipation.

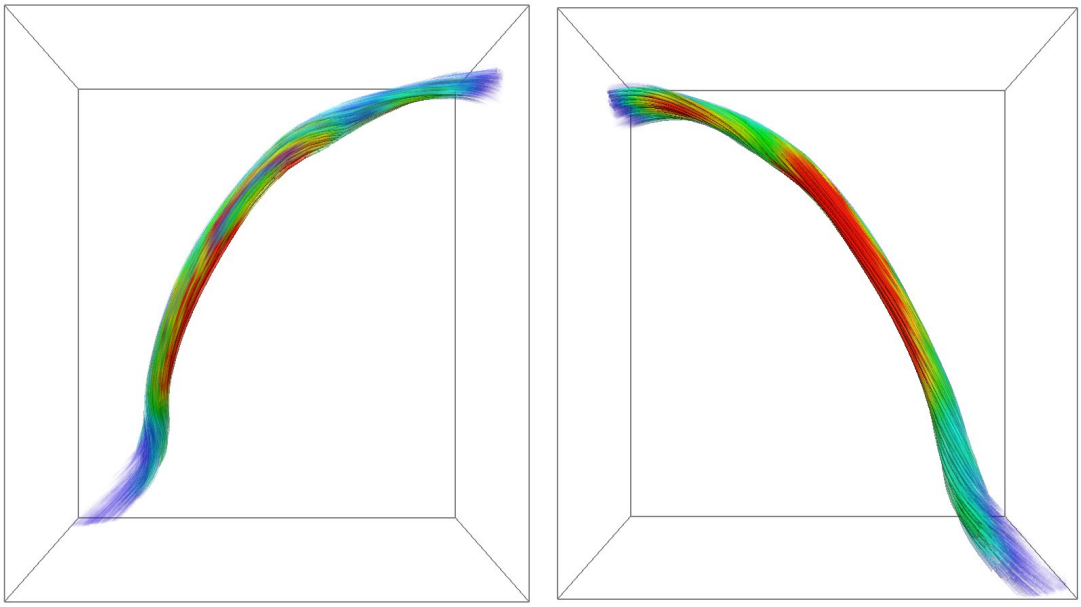

Figure 1.5.: Field lines of the same vortex tube as in figure 1.4 from two different perspectives. The field lines indicate an inner, non-axisymmetric structure of the vortex tube.

2. Statistical Hydrodynamics in a Nutshell

2.1. The Need For a Statistical Description

We have seen in chapter 1 that fluid flows are described by the Navier-Stokes equations. Unless a probabilistic external forcing is applied, these equations are completely deterministic, i.e., the temporal evolution is fully fixed by the initial condition. From a naïve point of view, there is no need for a statistical description on this level. Taking a glimpse at a turbulent time series, however, immediately reveals the stochastic nature of the problem. The strong fluctuations suggest a certain degree of randomness. How does this randomness enter the phenomenon of turbulence?

The reason for this is that the Navier-Stokes equations represent a set of nonlinear, nonlocal partial differential equations with solutions exhibiting spatio-temporal complexity as we have seen in chapter 1. The spatial component of this complexity is evident from the visualizations presented there, which illustrate the (probably) most fundamental part of the problem; the system is too unstructured to be described by a small number of degrees of freedom, which makes it intractable to methods from pattern formation. At the same time the turbulent fields do not appear as purely random, the coherent structures indicate a certain degree of spatial organization, yet being a rather complicated one. As a consequence a simple stochastic modeling will be inappropriate. Together with the chaotic behavior in time the whole system displays a sensitive dependence on the initial conditions: Small changes in the experimental (or numerical) environment will eventually cause a completely different time evolution of the system. We can take data from a parallel simulation of the Navier-Stokes equations as a peculiar example. Figure 2.1 shows the average rate of kinetic energy dissipation from a 256^3 run of fully developed turbulence. The run was repeated with identical initial conditions, but because of rounding errors inherent to the parallel implementation the temporal evolution deviates over time.[1] Remarkably, even the average over the whole field is a fluctuating quantity.

These considerations show that the nature of turbulence is intrinsically stochastic and therefore requires a statistical description. This, on the one hand, lets hope fade away that the problem of turbulence may be understood by a careful analysis of the basic

[1] Though being also subject to numerical rounding errors, a numerical solution of this problem on a single core is completely deterministic. The fluctuations enter due to the fact that `MPI` does not define in which order, e.g., global averages are computed over all cores. Thus two different simulations will produce different rounding errors, which add up yielding a differing temporal evolution.

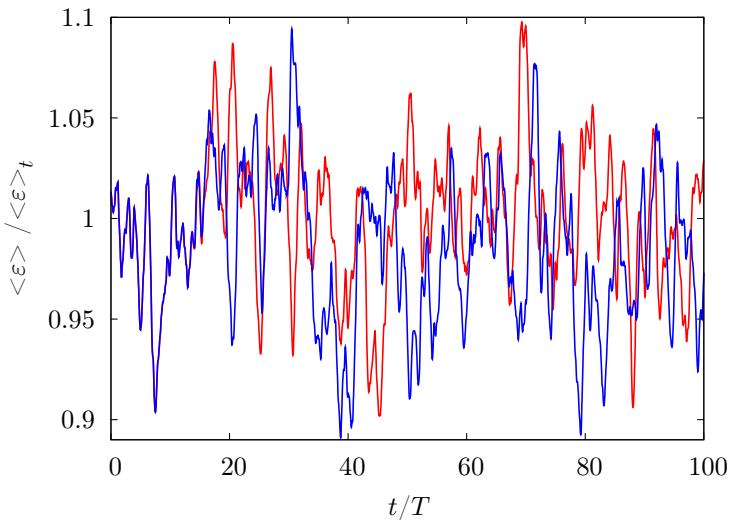

Figure 2.1.: Average rate of energy dissipation as a function of time for two DNS runs with identical initial conditions. The runs deviate from $t \approx 20T$ on, exemplifying the sensitivity on small external fluctuations.

equations of motion only. On the other hand, it may be regarded as a relief: Maybe we do not have to understand all details to solve the problem. From a practical point of view, lets say from an engineer, this is quite clear; the precise flow configuration over an airfoil is rather irrelevant, drag and lift (i.e. mean values) matter.

The remaining part of the chapter is structured as follows. We first will introduce some basic mathematical prerequisites for a statistical description. Then some comments on the concept of homogeneous isotropic turbulence are in order, before we will make a first contact with the closure problem of turbulence. We then turn to a short overview over phenomenological theories of turbulence, which contrast the efforts to find a theory from first principle.

2.2. Averages, PDFs etc.

We cannot give a comprehensive introduction into the mathematical formulation of statistical problems at this point. However, we would like to introduce some of the quantities that will be of major interest within this thesis. We refer the reader to [MY71, MY75] for a complete introduction to this subject.

Consider a typical experimental situation, in which a component of velocity $u(t)$ of a turbulent jet is measured at a single point in space. Assuming that the experimental conditions maintain a stationary situation, it is possible to estimate the probability density function (PDF) of velocity by taking the temporal average over the measurement

interval T_m,

$$f(v) = \frac{1}{T_m} \int_0^{T_m} \mathrm{d}t \, \delta(u(t) - v) = \langle \, \delta(u(t) - v) \, \rangle_t \quad . \tag{2.1}$$

Here v denotes the sample space variable, whereas $u(t)$ denotes the actual realization of this fluctuating quantity. This formula defines a procedure how the histogram $f(v)$ is generated; consider a fixed (infinitesimal) bin with the value v. The delta function then increments this bin each time $v = u(t)$ is found. If the measured time series is "representative" for the system, the estimated PDF will converge to the "true" PDF as $T_m \to \infty$. Unfortunately, at this stage it is by no means clear, what "representative" and "true" means. By assuming that there is a "true" PDF we actually take the existence of a well-defined probability measure of turbulence for granted. Although this has not been rigorously proven, the consistent outcome of many experimental and numerical experiments suggests this to be a reasonable assumption. By "representative" we mean the assumption that the velocity will take on all possible values representatively often during a long enough measurement period, which is closely related to the ergodicity assumption for this system. Both of these points being unproven (but reasonable) hypotheses, may be regarded as the axiomatic foundations of the statistical description of turbulence. We refer the reader to [MY71, Tsi09] for more details on this issue.

In the same manner as the velocity PDF may be estimated from the numerical data, it is possible to obtain averages according to

$$\langle u(t)^n \rangle_t = \frac{1}{T_m} \int_0^{T_m} \mathrm{d}t \, u(t)^n \quad . \tag{2.2}$$

Under the given circumstances these averages will coincide with the moments of the PDF

$$\langle v^n \rangle_v = \int \mathrm{d}v \, v^n \, f(v) \quad . \tag{2.3}$$

In most literature on probability theory only the last notation is used. This comes due to the fact that there the discrimination between sample space variable and realization does not have to be made. With these considerations the situation for an experimentalist is quite clear, once the above axiomatic assumptions are accepted. If the system is prepared to yield "representative" results, it is evident how to extract mean values from the gathered data.

For theoretical purposes it is useful to introduce the concept of ensemble averaging. Again assuming the existence of a probability measure, $\langle \cdot \rangle$ from now on means "average over all possible realizations of the system". In this sense, the PDF of the velocity field can be defined as the ensemble average of a fine-grained PDF $\hat{f}$

$$f(\boldsymbol{v}; \boldsymbol{x}, t) = \langle \, \delta(\boldsymbol{u}(\boldsymbol{x}, t) - \boldsymbol{v}) \, \rangle =: \langle \, \hat{f}(\boldsymbol{v}; \boldsymbol{x}, t) \, \rangle \quad . \tag{2.4}$$

Here $\boldsymbol{u}(\boldsymbol{x}, t)$ again denotes a realization of the velocity field, whereas $\boldsymbol{v}$ denotes the corresponding sample space variable. The notation indicates that $f(\boldsymbol{v}; \boldsymbol{x}, t)$ is a density

with respect to $\boldsymbol{v}$ and a function with respect to $\boldsymbol{x}$ and t. The interpretation of the fine-grained PDF is intuitive: unless we choose $\boldsymbol{v}$ exactly identical to the value of the realization $\boldsymbol{u}$ at point $\boldsymbol{x}$ and time t, we will have a vanishing probability density. In this sense the fine-grained PDF represents a sharply peaked PDF. Mean values can formally be obtained via

$$\begin{aligned} \langle\, u_i^n(\boldsymbol{x},t)\,\rangle &= \left\langle\, u_i^n(\boldsymbol{x},t) \int \mathrm{d}\boldsymbol{v}\, \delta(\boldsymbol{u}(\boldsymbol{x},t)-\boldsymbol{v}) \,\right\rangle = \left\langle \int \mathrm{d}\boldsymbol{v}\, v_i^n\, \delta(\boldsymbol{u}(\boldsymbol{x},t)-\boldsymbol{v}) \,\right\rangle \\ &= \int \mathrm{d}\boldsymbol{v}\, v_i^n\, f(\boldsymbol{v};\boldsymbol{x},t) = \langle\, v_i^n\,\rangle_v \quad , \end{aligned} \tag{2.5}$$

where we make use of the identity $\int \mathrm{d}\boldsymbol{v}\, \delta(\boldsymbol{u}(\boldsymbol{x},t)-\boldsymbol{v}) = 1$ and the sifting property of the delta function. We especially see that mean values coincide with the moments of the PDF within this ensemble concept. More mathematical properties of the delta function are summarized in appendix A.1. As we have seen that within a properly established ensemble $\langle \ldots \rangle_v = \langle \ldots \rangle$, we will omit the subscript from now on. Of course, this whole concept may be generalized to multiple points in space. For example, the PDF for N points in space may be defined as

$$f_N(\boldsymbol{v}_1,\ldots,\boldsymbol{v}_N;\boldsymbol{x}_1,\ldots,\boldsymbol{x}_N,t) = \langle\, \delta(\boldsymbol{u}_1(\boldsymbol{x},t)-\boldsymbol{v}_1)\ldots\delta(\boldsymbol{u}_N(\boldsymbol{x},t)-\boldsymbol{v}_N)\,\rangle \quad , \tag{2.6}$$

i.e., as the ensemble average of the product of fine-grained PDFs. PDFs defined in this manner will play a central role of the statistical theory treated in the later chapters of this thesis. A more detailed presentation of the properties of these functions will be addressed in chapter 6 and following. More details on these probabilistic concepts are found in [MY71, Fri95, Pop00].

2.3. The Concept of Stationary Homogeneous Isotropic Turbulence

When considering the complexity of fully developed turbulent flows, the first thing apparent is that a statistical description is inevitable. Taking a closer look then reveals (as, for example, can be guessed from the visualizations in section 1.2) that there is apparently no distinguished direction in the flow. And although a single field is clearly not homogeneous, there is no reason why, e.g., a cluster of vortices should form only in a certain region of an experimental volume when the experiment is repeated often. This has led to the concept of homogeneous isotropic turbulence, which is inseparably connected to the history of theoretical turbulence research. The list of textbooks on homogeneous isotropic turbulence is nearly endless, but one maybe should mention [Bat53] as one of the most classic ones.

Homogeneity, isotropy and stationarity represent statistical symmetries. *Statistical* symmetry means that a single realization in general will not display the assumed symmetries, but the statistical, ensemble averaged quantities will. Let us exemplify the

situation with the single-point velocity PDF $f(\boldsymbol{v};\boldsymbol{x},t)$. If the statistics is assumed to be stationary, this PDF should not depend on time. Due to homogeneity, it should not depend on the spatial position $\boldsymbol{x}$. And finally, due to isotropy, it should be a function of the absolute value of velocity v only, as any dependence on a vector would distinguish a spatial direction. And indeed, as can be seen by a simple calculation, the PDF of the velocity vector is fully determined by the PDF of the absolute value:

$$\begin{aligned}\tilde{f}(v) &= \int \mathrm{d}\boldsymbol{v}\, \delta(v-|\boldsymbol{v}|)\, f(\boldsymbol{v}) \\ &= \int \mathrm{d}v\, \mathrm{d}\varphi\, \mathrm{d}\vartheta\, v^2 \sin\vartheta\, \delta(v-|\boldsymbol{v}|)\, f(\boldsymbol{v}) \\ &= 4\pi v^2 f(\boldsymbol{v}) \\ \Rightarrow f(\boldsymbol{v}) &= \frac{1}{4\pi v^2}\tilde{f}(v) \quad . \end{aligned} \tag{2.7}$$

The calculation is only possible knowing that $f(\boldsymbol{v})$ depends on v only. The concept is readily generalized to more complicated situations. For the two-point PDF $f_2(\boldsymbol{v}_1,\boldsymbol{v}_2;\boldsymbol{x}_1,\boldsymbol{x}_2,t)$ homogeneity, for example, means that this function may only depend on the distance vector $\boldsymbol{r}=\boldsymbol{x}_2-\boldsymbol{x}_1$, as the difference vector does not change when the whole configuration is shifted in space. Stationarity for a two-time quantity accordingly means that it can only depend on the temporal distance $\tau = t_2 - t_1$.

This already gives a hint on how general expressions under these statistical symmetries can be obtained; one considers the action of mathematical transformations related to the symmetry on the statistical quantity and requires invariance under this transformation. Consider some statistical quantity depending on the points $\boldsymbol{x}_1 \ldots \boldsymbol{x}_N$ in space and times $t_1 \ldots t_M$ in time. Stationarity simply means that the statistical quantity under investigation will be invariant under a shifting of all time dependencies

$$t_i \mapsto t_i + \tau \quad . \tag{2.8}$$

In consequence, it will only depend on time differences

$$\begin{aligned} t_1 &= t_2 - t_1 \\ &\vdots \\ t_{N-1} &= t_N - t_{N-1} \quad . \end{aligned} \tag{2.9}$$

For homogeneity we consider a shifting in space

$$\boldsymbol{x}_i \mapsto \boldsymbol{x}_i + \tilde{\boldsymbol{x}} \quad . \tag{2.10}$$

As a consequence, this quantity can only depend on a (not uniquely defined) set of difference vectors, for example,

$$\begin{aligned} \boldsymbol{r}_1 &= \boldsymbol{x}_2 - \boldsymbol{x}_1 \\ &\vdots \\ \boldsymbol{r}_{N-1} &= \boldsymbol{x}_N - \boldsymbol{x}_{N-1} \quad . \end{aligned} \tag{2.11}$$

The examples show that these two statistical symmetries in general reduce the number of independent variables by one. Isotropy yields even more possibilities for simplification. In general isotropy is defined as the invariance of the statistical quantity under rotations and reflections, i.e. under the action of transformations $\mathrm{R} \in \mathrm{O}(3)$. To explain this, let us start with a scalar function, say a simple one-point PDF (where we have already taken into account homogeneity and stationarity). Isotropy implies

$$f(\boldsymbol{v}) = f(\mathrm{R}\boldsymbol{v}) \quad \forall \mathrm{R} \in \mathrm{O}(3) \quad . \tag{2.12}$$

That means, the scalar function can only depend on invariants (with respect to these transformations) of $\boldsymbol{v}$. The only invariant of a vector is its absolute value, such that we find the above-mentioned result that this PDF can depend on v only. The notion of invariants comes from tensor calculus and (probably) was introduced into hydrodynamics in the works of Robertson and Chandrasekhar [Rob40, Cha51]. We again refer the reader to [Bat53] for more detailed information. Let us take another example, the two-point PDF f_2, which has to fulfill

$$f_2(\boldsymbol{v}_1, \boldsymbol{v}_2; \boldsymbol{r}) = f_2(\mathrm{R}\boldsymbol{v}_1, \mathrm{R}\boldsymbol{v}_2; \mathrm{R}\boldsymbol{r}) \quad \forall \mathrm{R} \in \mathrm{O}(3) \quad . \tag{2.13}$$

f_2 is a density with respect to six variables and a function with respect to additional three variables. A complete set of invariants, for example, reads

$$v_1,\, v_2,\, r,\, \boldsymbol{r} \cdot \boldsymbol{v}_1,\, \boldsymbol{r} \cdot \boldsymbol{v}_2,\, \boldsymbol{v}_1 \cdot \boldsymbol{v}_2 \tag{2.14}$$

as the specification of these quantities suffices to unambiguously determine the full vectorial configuration of $\boldsymbol{v}_1$, $\boldsymbol{v}_2$ and $\boldsymbol{r}$. This shows that the number of independent variables reduces from nine to six, which is still a tremendous amount of information. When the joint PDF of two components is considered, further information can be extracted from the relation (2.13). By choosing the proper rotation from O(3), we for instance directly obtain

$$f_2(v_{1,x}, v_{2,x}) = f_2(v_{1,y}, v_{2,y}) \quad . \tag{2.15}$$

Of course, this concept can be generalized to an arbitrary number of points, for the N-point PDF isotropy it implies

$$f_N(\boldsymbol{v}_1, \ldots, \boldsymbol{v}_N; \boldsymbol{r}_1, \ldots \boldsymbol{r}_{N-1}) = f_N(\mathrm{R}\boldsymbol{v}_1, \ldots, \mathrm{R}\boldsymbol{v}_N; \mathrm{R}\boldsymbol{r}_1, \ldots \mathrm{R}\boldsymbol{r}_{N-1}) \quad \forall \mathrm{R} \in \mathrm{O}(3)\,. \tag{2.16}$$

So the next task in reducing the complexity of this object would be to find a list of a possible set of all invariants, which we will not exemplify at this point.

Not only scalar quantities, but also higher-order tensors play an important role in the statistical description of turbulence.[2] We now examine a statistical vectorial quantity $\boldsymbol{a}(\boldsymbol{r})$ depending on the spatial distance $\boldsymbol{r}$. Isotropy now implies that $\boldsymbol{a}$ transforms in the same manner as $\boldsymbol{r}$,

$$\mathrm{R}\boldsymbol{a}(\boldsymbol{r}) = \boldsymbol{a}(\mathrm{R}\boldsymbol{r}) \quad \forall \mathrm{R} \in \mathrm{O}(3) \quad . \tag{2.17}$$

[2] We refer the reader to [Dai09] for some more mathematical details.

This can only be the case if $\boldsymbol{a}$ points into the direction of $\boldsymbol{r}$. Additionally there is a scalar function determining the amplitude of the vector, which, just like in the case of the above scalar functions, may only depend on the invariant r. Thus we have

$$\boldsymbol{a}(\boldsymbol{r}) = g(r)\,\hat{\boldsymbol{r}} \quad . \tag{2.18}$$

This scalar function is obtained by projecting this expression onto $\hat{\boldsymbol{r}}$ yielding

$$g(r) = \hat{\boldsymbol{r}} \cdot \boldsymbol{a}(\boldsymbol{r}) \quad . \tag{2.19}$$

The transformation properties of a matrix in the case of isotropic statistics is

$$\mathrm{B}(\mathrm{R}\boldsymbol{r}) = \mathrm{R}\mathrm{B}(\boldsymbol{r})\mathrm{R}^T \quad \forall \mathrm{R} \in \mathrm{O}(3) \quad . \tag{2.20}$$

As $B(\boldsymbol{r})\hat{\boldsymbol{r}}$ is a vectorial function, it has to take the form (2.18),

$$\mathrm{B}(\boldsymbol{r})\hat{\boldsymbol{r}} = \lambda(r)\hat{\boldsymbol{r}} \quad , \tag{2.21}$$

obviously demonstrating that $\hat{\boldsymbol{r}}$ is an eigenvector of B. The corresponding eigenvalue $\lambda(r)$ is readily obtained by projection,

$$\lambda(r) = \hat{\boldsymbol{r}} \cdot \mathrm{B}(\boldsymbol{r})\hat{\boldsymbol{r}} \quad . \tag{2.22}$$

We now want to consider the special case of symmetric matrices. We then know by the spectral theorem that the two additional eigenvectors $\hat{\boldsymbol{s}}_1$ and $\hat{\boldsymbol{s}}_2$ of B will be perpendicular to $\hat{\boldsymbol{r}}$ and will constitute an orthonormal basis of $\mathbb{R}^3$. By considering the rotation $\mathrm{R}_{\boldsymbol{r}}^T$ with rotation axis $\hat{\boldsymbol{r}}$, which transforms $\hat{\boldsymbol{s}}_1$ into $\hat{\boldsymbol{s}}_2$, it is easily shown that the corresponding eigenvalues $\mu_1(r)$ and $\mu_2(r)$ coincide,

$$\mu_1 = \hat{\boldsymbol{s}}_1 \cdot \mathrm{B}\hat{\boldsymbol{s}}_1 \overset{\text{isotropy}}{=} \left(\mathrm{R}_{\boldsymbol{r}}^T \hat{\boldsymbol{s}}_1\right) \cdot \mathrm{B}\left(\mathrm{R}_{\boldsymbol{r}}^T \hat{\boldsymbol{s}}_1\right) = \hat{\boldsymbol{s}}_2 \cdot \mathrm{B}\hat{\boldsymbol{s}}_2 = \mu_2 \quad . \tag{2.23}$$

Thus the general form of a symmetric matrix depending on $\boldsymbol{r}$ under isotropic statistics is [Bat53, Dai09]

$$B_{ij}(\boldsymbol{r}) = \mu(r)\,\delta_{ij} + [\lambda(r) - \mu(r)]\,\hat{r}_i\,\hat{r}_j \quad . \tag{2.24}$$

By this we have reached a stunning reduction of complexity; instead of considering nine independent scalar functions, only two have to be considered in this case. Of course, these results also hold when quantities depending on, e.g., sample space variables are considered. When the statistical quantities depend on more variables, generalizations of these expressions have to be found. We will make extensive use of statistical symmetries throughout this thesis. It will turn out that some statistical evaluations of numerical data only become possible due to these simplifications.

To proceed one step further, we can establish kinematic relations. As an example we consider the correlation tensor of velocity at two points in space (which coincides with

the covariance tensor up to the constant factor of one third the mean squared velocity), which due to homogeneity will depend on the distance vector $\boldsymbol{r}$ only,

$$C_{ij}(\boldsymbol{r}) = \frac{3}{\langle \boldsymbol{u}^2 \rangle} \big\langle u_i(\boldsymbol{x}_1)\, u_j(\boldsymbol{x}_2) \big\rangle \overset{(2.24)}{=} g(r)\, \delta_{ij} + [f(r) - g(r)]\, \hat{r}_i\, \hat{r}_j \quad . \tag{2.25}$$

By explicitly choosing $\boldsymbol{r} = r\, \boldsymbol{e}_1$ we obtain

$$C_{11}(\boldsymbol{r}) = \frac{3}{\langle \boldsymbol{u}^2 \rangle} \big\langle u_1(\boldsymbol{x}_1)\, u_1(\boldsymbol{x}_2) \big\rangle = f(r) \tag{2.26a}$$

$$C_{22}(\boldsymbol{r}) = \frac{3}{\langle \boldsymbol{u}^2 \rangle} \big\langle u_2(\boldsymbol{x}_1)\, u_2(\boldsymbol{x}_2) \big\rangle = g(r) \tag{2.26b}$$

showing that f and g are the longitudinal and transversal correlation functions, respectively. One now can make use of incompressibility $\nabla \cdot \boldsymbol{u}(\boldsymbol{x}, t) = 0$ and the fact that derivatives commute with averaging which implies

$$\begin{aligned} \frac{\partial}{\partial x_{2,j}} C_{ij}(\boldsymbol{r}) = \frac{\partial}{\partial r_j} C_{ij}(\boldsymbol{r}) = f'(r)\, \hat{r}_i + 2\, \frac{f - g}{r}\, \hat{r}_i = 0 \\ \Rightarrow \quad g = f + \frac{1}{2} r f' \quad . \end{aligned} \tag{2.27}$$

That means, the transversal correlation function is fully determined by the longitudinal correlation function. This kinematic relation finally reduces the number of independent scalar functions for the correlation tensor to one. This simple example shows how powerful the concept of homogeneous isotropic turbulence is. We will establish more kinematic relations for the vorticity covariance tensor as well as for the fourth-order velocity gradient covariance tensor in section 4.2 and check them with the help of numerical results.

From a theoretical point of view, the concept of stationary homogeneous isotropic turbulence yields beautiful simplifications, but its validity is based on empirical facts. It turns out to be an idealized situation, which is hardly achievable in experiments. Boundaries and mean flow will usually have their influence, such that there are anisotropies in the measured signals and also in numerical simulations. We will discuss this issue in section 3.4. To what extent anisotropies are expected to occur also depends on the quantity under consideration. Small-scale quantities like vorticity and velocity gradients are expected to reach isotropy easier than large-scale quantities like the velocity. How the length scales of these quantities are related will be discussed in section 4.2 and numerical examples are also given in section 3.4.

2.4. The Closure Problem of Turbulence

The previous section has shown how statistical symmetries and kinematic relations may drastically simplify the mathematical structure of statistical quantities. The remaining task would be to determine these quantities right from the basic equations of motion.

While the steps in the mathematical formulation of turbulence up to this point raised hope that this actually is possible, this task until today remains the great unsolved problem of the subject. In this sense we now approach the heart of the problem. We will continue discussing it at the example of the covariance tensor of the velocity field. Our aim is to derive an evolution equation for the covariance tensor $\langle u_i(\boldsymbol{x}_1,t)u_j(\boldsymbol{x}_2,t)\rangle =: \langle u_i u'_j\rangle$ considering unforced turbulence. The procedure is quite straightforward: Take the temporal derivative of the velocity product, use the Navier-Stokes equation and finally take the ensemble average. The result is readily obtained and reads

$$\frac{\partial}{\partial t}\langle u_i u'_j\rangle + \frac{\partial}{\partial x_k}\langle u_i u_k u'_j\rangle + \frac{\partial}{\partial x_{k'}}\langle u_i u'_j u'_k\rangle = -\frac{\partial}{\partial x_i}\langle u'_j p\rangle - \frac{\partial}{\partial x_{j'}}\langle u_i p'\rangle + \nu\frac{\partial^2}{\partial x_k^2}\langle u_i u'_j\rangle + \nu\frac{\partial^2}{\partial x_{k'}^2}\langle u_i u'_j\rangle \quad . \tag{2.28}$$

We now have an obvious problem, because new unknown functions enter. Due to the nonlinear term, the third-order tensor $\langle u_i u_k u'_j\rangle$ is introduced as well as the velocity-pressure covariance $\langle u_i p'\rangle$ due to the nonlocal term in the Navier-Stokes equation. Taking into account homogeneity allows to express the spatial derivatives according to

$$\frac{\partial}{\partial x_k} = -\frac{\partial}{\partial r_k}\,, \quad \frac{\partial}{\partial x_{k'}} = \frac{\partial}{\partial r_k} \quad . \tag{2.29}$$

By additionally considering isotropic turbulence, it is quite easy to show that the pressure contributions vanish in this equation. To this end we note that in this case the velocity-pressure covariance takes the form

$$\langle u_i p'\rangle = a(r)\,\hat{r}_i \quad . \tag{2.30}$$

Solenoidality yields an equation for $a(r)$,

$$a' + \frac{2}{r}a = 0 \quad . \tag{2.31}$$

This equation has the obvious two solutions $a(r) = 0$ or $a(r) = r^2$, of which the latter can be ruled out, as the correlation should vanish for $r \to \infty$. Thus the evolution equation simplifies to

$$\frac{\partial}{\partial t}\langle u_i u'_j\rangle + \frac{\partial}{\partial r_k}\left(\langle u_i u'_j u'_k\rangle - \langle u_i u_k u'_j\rangle\right) = 2\nu\frac{\partial^2}{\partial r_k^2}\langle u_i u'_j\rangle \quad . \tag{2.32}$$

Although the equation has taken a pretty compact form now, nothing can be done about the fact that third-order moments appear in this equation. Of course, one now can derive the evolution equations for these third-order moments as well, however, they will couple to higher-order moments in the same manner. Additionally, the pressure contributions in general do not vanish for the higher-order equations. This is exactly the closure problem of turbulence. Whenever evolution equations for statistical quantities

are derived, unknown functions enter the equations. When trying to derive evolution equations for these functions even more unknown functions will appear. We will encounter the closure problem repeatedly throughout this work and in a sense it is the central problem in this thesis (like in so many others on turbulence theory). For example, it will play a key role when evolution equations for probability density functions are considered in chapter 6.

2.4.1. The Kármán-Howarth Equation

Though it seems that we now have encountered an unsolvable problem, equation (2.32) is not useless. It actually is the starting point for the derivation of the famous Kármán-Howarth equation, which may be used to derive the celebrated $4/5$-law by Kolmogorov. The derivation of these relations involves rather lengthy calculations, which exceed the scope of this presentation. However, we think it is useful to outline the main steps, as they show how valuable insights can be gained in this difficult situation.

We first will motivate that equation (2.32) may eventually be simplified to a relation of two scalar functions in view of the symmetries present. To this end a closer inspection of the tensor $B_{ij,k} = \langle u_i u_j u'_k \rangle$ is necessary. Proceeding in the same manner as above, it can be made clear that this tensor is determined by different two-point correlations involving the different longitudinal and transversal vectorial configurations of the two velocities at point $\boldsymbol{x}_1$ and one velocity at point $\boldsymbol{x}_2$. However, it turns out that for a solenoidal field, this tensor is determined by a single scalar function only, which may be chosen as the longitudinal triple correlation, i.e., for $\boldsymbol{r} = r\,\boldsymbol{e}_1$ it is determined by $B_{11,1} := \sigma^3\, T(r)$ with the abbreviation $\sigma = \sqrt{\frac{1}{3}\langle \boldsymbol{u}^2 \rangle}$. This is arrived at by an analogous, but slightly more complicated computation like the one leading to the relation (2.27) when $\frac{\partial}{\partial r_k} B_{ij,k} = 0$ is considered. We refer the reader to, e.g., [MY75] for further details. With these simplifications $B_{ij,k}$ may be expressed as

$$B_{ij,k} = \sigma^3 \left(\frac{1}{2}\big(T - rT'\big)\, \hat{r}_i \hat{r}_j \hat{r}_k + \frac{1}{4}\big(2T + rT'\big)\, \big(\hat{r}_i \delta_{jk} + \hat{r}_j \delta_{ik}\big) - \frac{1}{2} T\, \delta_{ij} \hat{r}_k \right) \quad . \tag{2.33}$$

Now this result can be inserted into equation (2.32), where additionally $B_{i,jk}(\boldsymbol{r}) = B_{jk,i}(-\boldsymbol{r})$ is used. As f and g are not independent functions, it suffices to collect the terms proportional to δ_{ij}. After a lengthy calculation and making use of equation (2.27), one eventually arrives at the equation [MY75]

$$\left(1 + \frac{r}{2}\frac{\partial}{\partial r}\right) \frac{\partial}{\partial t} f = \left(1 + \frac{r}{2}\frac{\partial}{\partial r}\right) \left[\left(\frac{\partial}{\partial r} + \frac{4}{r} \right) \sigma T + 2\nu \left(\frac{\partial^2}{\partial r^2} + \frac{4}{r}\frac{\partial}{\partial r} \right) f \right] \quad . \tag{2.34}$$

Now demanding regularity in $r = 0$, this equation is integrated yielding

$$\begin{aligned} \frac{\partial}{\partial t} f &= \left(\frac{\partial}{\partial r} + \frac{4}{r} \right) \left[\sigma T + 2\nu \frac{\partial}{\partial r} f \right] \\ &= \frac{\sigma}{r^4} \frac{\partial}{\partial r} r^4 T + \frac{2\nu}{r^4} \frac{\partial}{\partial r} r^4 \frac{\partial}{\partial r} f \quad . \end{aligned} \tag{2.35}$$

This is the famous Kármán-Howarth equation, which connects the longitudinal velocity correlation function to the corresponding third-order correlation.

2.4.2. The 4/5-Law

The Kármán-Howarth equation eventually leads to the famous 4/5-law, derived by Kolmogorov in his seminal paper [Kol41a, Kol91a], where the K41 phenomenology is introduced, which we will discuss in the next section. To proceed, we introduce the longitudinal structure functions

$$S_n(r,t) = \langle\, [(\boldsymbol{u}(\boldsymbol{x}+\boldsymbol{r},t) - \boldsymbol{u}(\boldsymbol{x},t)) \cdot \hat{\boldsymbol{r}}]^n \,\rangle \quad . \tag{2.36}$$

When considered in Fourier space, one may see that S_2 is related to the energy distribution across scales, whereas S_3 is related to the flux of energy across scales. Furthermore, it may be noted that the relations

$$\sigma^2 f = \sigma^2 - \frac{1}{2} S_2 \tag{2.37a}$$

$$\sigma^3 T = \frac{1}{6} S_3 \tag{2.37b}$$

hold [Pop00], such that equation (2.35) may be expressed as

$$3r^4 \frac{\partial}{\partial t} S_2 + \frac{\partial}{\partial r} r^4 S_3 = 6\nu \frac{\partial}{\partial r} r^4 \frac{\partial}{\partial r} S_2 - 4\langle\varepsilon\rangle r^4 \quad , \tag{2.38}$$

which may be integrated yielding

$$\frac{3}{r^4} \int_0^r s^4 \frac{\partial}{\partial t} S_2(s,t)\, \mathrm{d}s + S_3 = 6\nu \frac{\partial}{\partial r} S_2 - \frac{4}{5} \langle\varepsilon\rangle r \quad . \tag{2.39}$$

It was now reasoned by Kolmogorov that for locally isotropic turbulence (a notion we will come to in the next section), the time-dependent term is negligible and the viscous term should be unimportant within the inertial range. This finally leads to the simple result

$$S_3(r) = -\frac{4}{5} \langle\varepsilon\rangle r \tag{2.40}$$

within the inertial range of scales, which is known as the 4/5-law. As S_3 is related to the energy transfer across the scales, this result basically tells us that there is a flux of energy from large to small scales, something which is known as the direct energy cascade.

In this sense, the 4/5-law demonstrates how quantitative information can be deduced right from the basic equations of motion, although the closure problem hinders a comprehensive solution of the statistical problem.

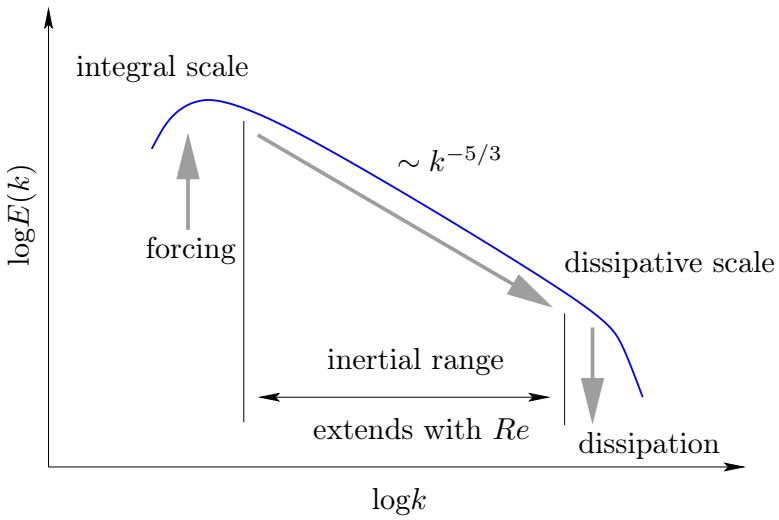

Figure 2.2.: Schematic of the energy cascade in three-dimensional turbulence: Energy is injected at the integral length scale of the flow and is successively transferred to smaller scales, where it finally is dissipated.

2.4.3. Phenomenological Theories of Turbulence

K41 phenomenology

Of course, it would be desirable to deduce more relations like (2.40) from the Navier-Stokes equations. However, due to the closure problem the 4/5-law up to today remains one of the sparse analytical results deduced from first principles. To overcome this problem, Kolmogorov introduced some phenomenological assumptions to derive further relations. However, being based on assumptions, the results cannot be taken as laws. Indeed, it turns out that most of them actually do not hold exactly. However, they play an important role up to today, and much contemporary research is based on Kolmogorov's phenomenology. Hence a short outline of the phenomenological theories seems useful at this point.

The basic setting invokes the picture of the energy cascade, meaning that when energy is injected at the large scales of the system, it is successively transferred to smaller scales, where it finally is dissipated. This is schematically shown in figure 2.2. The large scale is basically of the order of the correlation length of forcing and is usually denoted as the integral length scale L. The range in which the energy cascades without being dissipated is called the inertial range. This inertial range can be shown to extend with the Reynolds number, such that theoreticians often consider the limit of infinite Reynolds number to study inertial range physics. Eventually, at smaller scales, viscous dissipation sets in and kinetic energy is dissipated into heat. This range is called the dissipative range.

The Kolmogorov phenomenology now makes assumptions about the quantities that

determine the statistics in the inertial and dissipative range. In this context an important conceptual notion in Kolmogorov's work is the so-called locally isotropic turbulence. To this end he considers the PDFs of velocity differences between N points in a certain space-time region of limited extents. He now calls this PDF locally isotropic if it is homogeneous and in addition to that invariant with respect to rotations and reflections. In some formulations additionally temporal stationarity is added to these assumptions. In this sense local isotropy assumes the maximum symmetry of the PDF for a sufficiently small space-time region. Although the following hypotheses underlying the Kolmogorov phenomenology can be made more precisely, a rather loose formulation will suffice to introduce the basic notion at this point. We refer the reader to [Kol41b, Kol41a, Kol91b, Pop00, Fri95] for a concise description. The assumptions may be termed in the following way:

Hypothesis of local isotropy In any turbulent flow with a sufficiently large Reynolds number, the turbulence is approximately locally isotropic if the considered space-time region is sufficiently small.

First similarity hypothesis For locally isotropic turbulence, the N-point PDF is uniquely determined by the viscosity ν and the mean rate of energy dissipation $\langle\varepsilon\rangle$.

Second similarity hypothesis In case that the distances between the different points in space all lie within the inertial range, the dependence of the velocity PDF reduces to the mean rate of energy dissipation $\langle\varepsilon\rangle$.

By these hypotheses a powerful tool for analyzing statistical quantities is at hand: dimensional analysis. For example, it is possible to define time, velocity and length scales in terms of ν and $\langle\varepsilon\rangle$

$$\eta = \left(\frac{\nu^3}{\langle\varepsilon\rangle}\right)^{\frac{1}{4}} \qquad u_\eta = (\nu\langle\varepsilon\rangle)^{\frac{1}{4}} \qquad \tau_\eta = \left(\frac{\nu}{\langle\varepsilon\rangle}\right)^{\frac{1}{2}} \tag{2.41}$$

which characterize the small scales of the flow, where viscous dissipation is important. More importantly, dimensional analysis can be used to derive the functional form of a variety of statistical properties. The derivations are covered in detail in almost all textbooks on turbulence theory (see, e.g., [MY75, Fri95, Dav04]), such that we only mention some of the main results. As already indicated in figure 2.2, the energy spectrum takes the form

$$E(k) \sim \langle\varepsilon\rangle^{\frac{2}{3}} k^{-\frac{5}{3}} \tag{2.42}$$

in the inertial range, something which has been found to be true in good approximation in many experiments and numerical simulations. Also the scaling properties of the longitudinal structure functions may be dimensionally analyzed yielding the result

$$S_n(r) \sim \left(\langle\varepsilon\rangle r\right)^{\frac{n}{3}} \quad , \tag{2.43}$$

which is in perfect agreement with the 4/5-law and the shape of the energy spectrum. And while the 4/5-law has been derived by first principles (and neglecting viscous effects), the prediction for the remaining orders are strongly based on the hypotheses. When formulated in terms of the PDFs of the longitudinal velocity increments, the prediction is a self-similar scaling in the inertial range, a beautiful, but false prediction. It turns out by experimental and numerical investigation that the PDFs do not scale self-similarly in the inertial range and deviations from the relation (2.43) are found for increasing orders. This fact is commonly referred to as intermittency and is often related to the spatial structure of the fields. We will present numerical results on this in section 4.1.

K62 phenomenology

To overcome the shortcomings of the K41 phenomenology, Kolmogorov reconsidered the basis of his dimensional argument. It showed that the assumption that the mean rate of energy dissipation determines the shape of the PDFs is by far too strong. Instead, by introducing the conditional statistics of velocity differences and energy dissipation averaged over the corresponding interval in space, he reformulated his theory in terms of a spatially fluctuating quantity [Kol62], an assumption which nowadays is well documented by experimental and numerical results. It turns out that this generalization maintains the shape of the Kolmogorov spectrum and the 4/5-law, but allows for deviations at higher orders of structure functions according to

$$S_n(r) \sim \big(\langle\varepsilon\rangle r\big)^{\zeta_n} \quad \text{with} \quad \zeta_n = \frac{1}{3}n[1 - \frac{1}{6}\mu(n-3)] \quad , \tag{2.44}$$

where μ is called the intermittency parameter. Indeed, in the absence of intermittency (i.e. for $\mu = 0$) K41-scaling is recovered. While the refined predictions match the data much better, they turn out to yield unphysical results for very high orders of n, as the ζ_n eventually become negative.

Beyond Kolmogorov Phenomenlogy

Since the sixties of the twentieth century a variety of other models dealing with the velocity increment statistics have been developed. The ideas of K62 have been developed further within the multifractal model, which assumes a fractal structure of turbulence (see [Fri95] for a detailed account), to name only a single one. All of these models have in common that they make strong assumptions on the properties of turbulent flows to derive predictions. Whether these assumptions are fulfilled then determines the validity of the predictions made.

Recently, a different phenomenological approach was presented in [FP97], where the velocity increment statistics was regarded as a stochastic process, for which the Markov property has been validated experimentally. The strength of this approach is that the underlying assumptions can be checked experimentally and that predictions of joint PDFs for different scales can be made.

Again, the purpose of this short excursion on phenomenological approaches is to contrast this work. In this thesis, we will follow an entirely different approach: Based on works by Lundgren, Monin and Novikov, we will formulate a statistical theory starting from the basic equations of motion and will then apply numerical results to investigate the unclosed terms. In this sense it will not be possible to make predictive statements like the scaling of structure functions, however, we will find useful insights into the statistical structure of turbulence. This theory will be outlined in chapter 6 and then be applied to the statistics of velocity and vorticity in the following chapters. Once the local structure of turbulence is examined in this way, models for more complicated statistical properties can be deduced. This will be discussed in detail in chapters 9 and 10.

3. Direct Numerical Simulation of Turbulent Flows

> The entire experience with the subject indicates that the purely analytical approach is beset with difficulties, which at this moment are still prohibitive... Under these conditions there might be some hope to 'break the deadlock' by extensive, but well-planned, computational efforts...
>
> *(John von Neumann, 1949)*

The Direct Numerical Simulation (DNS) of turbulent flows has a long tradition in turbulence research. Ever since the pioneering works of Orszag and Patterson and Rogallo [PO71, OP72, Rog77, Rog81] it has become an indispensable tool for the field. While numerical simulations allow engineers to consider complex situations, which are analytically intractable, the purpose of DNS is (at least) two-fold for theoretical physicists. On the one hand, it may serve as a benchmarking tool for theoretical ideas, and the history of turbulence research is full of examples, where theoretical ideas had to fall because of experimental or numerical evidence. On the other hand, numerical input often has given rise to new ideas. For example, the existence of coherent structures has first been extensively studied with the help of DNS data [Sig81, SJO90, JWSR93, JW98].

For theoreticians the idealized case of fully developed stationary homogeneous isotropic turbulence is a scenario to develop and test new ideas. Luckily, the algorithms to generate this situation numerically are quite performant and comparably easy to implement. Consequently, the rough code design is well-established for a couple of decades and each new generation of supercomputers is used to give insights into turbulence at even higher Reynolds number. (It has to be mentioned, though, that the highest Reynolds numbers reached in experimental or real-world situations are way out of reach.)

For the work presented in this thesis DNS plays a major role and much effort has been spent to write a parallel code for simulating fully developed turbulence. Hence the present chapter shall give an overview of the most important numerical tool of this work. Its structure is as follows. First, we will outline the basic algorithmic details, i.e. the time stepping scheme and the pseudospectral method for the spatial discretization. Stability criteria, the different forcing schemes and the interpolation of Lagrangian particle paths will also be discussed here. In the following sections the code design as well as parallelization strategies will be presented. Also the scaling performance of the code will be presented there.

These sections will be followed by an overview of the simulations that have been conducted for the scientific results of this thesis. The chapter will be closed by a discussion to what extent numerical simulations are capable of producing the idealized situation of stationary homogeneous isotropic turbulence.

3.1. Algorithm

3.1.1. Some Words on Pseudospectral Methods

Pseudospectral methods have proven to be useful for hydrodynamical problems on periodic domains. Their main advantages are efficiency, accuracy and ease of implementation. The method makes use of Fourier transforms, which for a 2π-periodic scalar field may be defined as

$$\tilde{f}_{\boldsymbol{k}} = \frac{1}{(2\pi)^{\frac{3}{2}}} \int \mathrm{d}\boldsymbol{x}\, f(\boldsymbol{x})\, \exp(-\mathrm{i}\boldsymbol{k}\cdot\boldsymbol{x}) \qquad \boldsymbol{k} \in \mathbb{Z} \tag{3.1a}$$

$$f(\boldsymbol{x}) = \frac{1}{(2\pi)^{\frac{3}{2}}} \sum_{\boldsymbol{k}\in\mathbb{Z}} \tilde{f}_{\boldsymbol{k}}\, \exp(\mathrm{i}\boldsymbol{k}\cdot\boldsymbol{x}) \qquad \boldsymbol{x} \in [0, 2\pi]^3 \quad . \tag{3.1b}$$

For the numerical implementation the considered fields have, of course, to be discretized on a grid with N^3 grid points

$$\boldsymbol{x} \in \left\{ (i,j,k)\frac{2\pi}{N} \middle| 1 \le i,j,k \le N \right\} \quad , \tag{3.2}$$

which effectively determines the minimal scale of structures resolved by the grid. Due to the imposed periodic boundary conditions the possible wave vectors form a discrete set in Fourier space, and this set becomes finite because of the spatial discretization,

$$\boldsymbol{k} \in \left\{ (i,j,k)\frac{2\pi}{N} \middle| -\frac{N}{2} + 1 \le i,j,k \le \frac{N}{2} \right\} \quad . \tag{3.3}$$

As a consequence, we have a finite number of Fourier coefficients in the numerical implementation.

The basic concept now is to evaluate differential operators in Fourier space, where they take an especially simple form. Consider, for example, the differentiation of a scalar field,

$$\frac{\partial}{\partial x} f(\boldsymbol{x}) \xrightarrow{\mathcal{F}} \mathrm{i}\, k_x\, \tilde{f}_{\boldsymbol{k}} \quad , \tag{3.4}$$

i.e., differentiation reduces to a multiplication with the imaginary unit and the corresponding wave vector component in Fourier space. Once the partial differential equation is given in Fourier space, all linear terms involving differentiation can be treated in this way. Besides the ease of this method, one should pronounce that the obtained results are also very accurate as this kind of differentiation is exact within the numerical accuracy of the Fourier transform and the floating point precision.

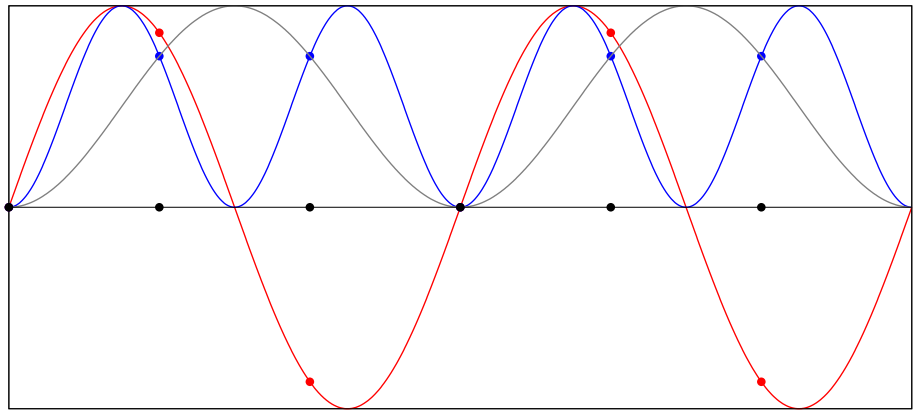

Figure 3.1.: On aliasing. The red curve is hardly resolved with six points. The squared signal (blue curve) is obviously under-resolved and may be misinterpreted with a signal with half frequency (gray curve).

When treating nonlinear terms, however, one is faced with the problem that multiplications in real space become convolutions in Fourier space, for example,

$$f(\boldsymbol{x})^2 \xrightarrow{\mathcal{F}} \mathcal{F}[\tilde{f}_{\boldsymbol{k}}] * \mathcal{F}[\tilde{f}_{\boldsymbol{k}}] \quad . \tag{3.5}$$

Evaluating such an expression on a discretized grid involves $\mathcal{O}(N^{2\cdot 3})$ operations. Thanks to the fast Fourier transform algorithm, a numerical Fourier transform is possible with $\mathcal{O}(N^3 \log N^3)$ operations, so that nonlinear terms are multiplied in real space and then transformed back to Fourier space for further computations, e.g., differentiation.

Nonlinear terms give rise to another problem known as aliasing. Consider, e.g., a sinusoidal signal $\sin(kx)$ on a line. If this signal is squared, we find $\sin(x)^2 = \frac{1}{2}\left[1 - \cos(2x)\right]$, the spatial frequency has doubled. Now if the original signal was resolved hardly by the grid, the squared signal will be under-resolved. This under-resolution results in a misinterpretation (aliasing) of the squared signal, which is demonstrated in figure 3.1. To circumvent this problem, the signals entering the nonlinearity may only contain spatial frequencies, that are resolved after the nonlinearity has been evaluated. For phenomena like turbulence, where a broad wave number band is excited, dealising techniques are used to reduce aliasing errors.

The time stepping can be done either in real space for the discretized field or for the Fourier coefficients in wave number space. For a complete account on pseudospectral methods we refer the reader to [CHQZ87] and [Boy01].

3.1.2. Eulerian Fields

We now come to the details of the numerical implementation of the simulation code. The code solves the Navier-Stokes equation in the vorticity formulation, which may be

formulated as

$$\frac{\partial}{\partial t}\boldsymbol{\omega}(\boldsymbol{x},t) = \nabla \times [\boldsymbol{u}(\boldsymbol{x},t) \times \boldsymbol{\omega}(\boldsymbol{x},t)] + \nu\Delta\boldsymbol{\omega}(\boldsymbol{x},t) + \boldsymbol{F}(\boldsymbol{x},t) \quad . \tag{3.6}$$

Writing the vorticity equation this way proves to be especially efficient for the numerical implementation.[1] The boundary conditions are triply periodic on a simulation domain of box length 2π. The whole equation is solved in Fourier space, where the equation takes the form

$$\begin{aligned}\frac{\partial}{\partial t}\tilde{\boldsymbol{\omega}}_{\boldsymbol{k}}(t) &= \mathrm{i}\,\boldsymbol{k} \times \mathcal{F}_{\boldsymbol{k}}\left[\boldsymbol{u}(\boldsymbol{x},t) \times \boldsymbol{\omega}(\boldsymbol{x},t)\right] - \nu k^2 \tilde{\boldsymbol{\omega}}_{\boldsymbol{k}}(t) + \tilde{\boldsymbol{F}}_{\boldsymbol{k}}(t) \\ &= \tilde{\boldsymbol{N}}_{\boldsymbol{k}}[\tilde{\boldsymbol{\omega}}] - \nu k^2 \tilde{\boldsymbol{\omega}}_{\boldsymbol{k}}(t) \quad .\end{aligned} \tag{3.7}$$

The Laplacian is treated by an integrating factor technique [CHQZ87], allowing for an accurate treatment. By introducing the transformation

$$\widehat{\boldsymbol{\omega}}_{\boldsymbol{k}} = \tilde{\boldsymbol{\omega}}_{\boldsymbol{k}} \exp(\nu k^2 t) \tag{3.8}$$

equation (3.7) turns into

$$\frac{\partial}{\partial t}\widehat{\boldsymbol{\omega}}_{\boldsymbol{k}}(t) = \tilde{\boldsymbol{N}}_{\boldsymbol{k}}[\widehat{\boldsymbol{\omega}} \exp(-\nu k^2 t)] \exp(\nu k^2 t) =: \hat{\boldsymbol{N}}_{\boldsymbol{k}}[\widehat{\boldsymbol{\omega}} \exp(-\nu k^2 t)] \quad . \tag{3.9}$$

The numerical implementation can now be split up into two separate problems, the time integration and the computation of the right-hand side, which is illustrated now.

Time Stepping Scheme

Equation (3.9) is integrated with a memory-saving third-order Runge-Kutta method. The details of this scheme are provided in [SO88]. The temporal discretization takes the form [Hom06]

$$\widehat{\boldsymbol{\omega}}_1 = \widehat{\boldsymbol{\omega}}_0 + \Delta t\, \hat{\boldsymbol{N}}[\widehat{\boldsymbol{\omega}}_0] \tag{3.10a}$$

$$\widehat{\boldsymbol{\omega}}_2 = \frac{3}{4}\widehat{\boldsymbol{\omega}}_0 + \frac{1}{4}\widehat{\boldsymbol{\omega}}_1 + \frac{1}{4}\Delta t\, \hat{\boldsymbol{N}}[\widehat{\boldsymbol{\omega}}_1] \tag{3.10b}$$

$$\widehat{\boldsymbol{\omega}}_3 = \frac{1}{3}\widehat{\boldsymbol{\omega}}_0 + \frac{2}{3}\widehat{\boldsymbol{\omega}}_2 + \frac{2}{3}\Delta t\, \hat{\boldsymbol{N}}[\widehat{\boldsymbol{\omega}}_2] \quad . \tag{3.10c}$$

$\widehat{\boldsymbol{\omega}}_0$ denotes the field at time t, whereas $\widehat{\boldsymbol{\omega}}_3$ denotes the field at time $t + \Delta t$, after the time step has been carried out. Note that the computation of $\widehat{\boldsymbol{\omega}}_3$ does not involve $\widehat{\boldsymbol{\omega}}_1$,

[1] One should note that we have denoted the forcing term here as $\boldsymbol{F}$ instead of $\nabla \times \boldsymbol{F}$ as in the first chapter, where the forcing was introduced on the level of the Navier-Stokes equation. Whenever a direct comparison of the Navier-Stokes and the vorticity equation will be made, we will discriminate these two cases. For the technical implementation described in this chapter the loose notation allows for a clearer presentation.

so that effectively only two additional fields have to be stored. Transforming back to $\tilde{\boldsymbol{\omega}}$ yields [Hom06]

$$\tilde{\boldsymbol{\omega}}_{1,\boldsymbol{k}} = \tilde{\boldsymbol{\omega}}_{0,\boldsymbol{k}}\, \mathrm{e}^{-\nu k^2 \Delta t} + \Delta t\, \tilde{\boldsymbol{N}}_{\boldsymbol{k}}[\tilde{\boldsymbol{\omega}}_0]\, \mathrm{e}^{-\nu k^2 \Delta t} \tag{3.11a}$$

$$\tilde{\boldsymbol{\omega}}_{2,\boldsymbol{k}} = \frac{3}{4}\tilde{\boldsymbol{\omega}}_{0,\boldsymbol{k}}\, \mathrm{e}^{-\nu k^2 \frac{\Delta t}{2}} + \frac{1}{4}\tilde{\boldsymbol{\omega}}_{1,\boldsymbol{k}}\, \mathrm{e}^{\nu k^2 \frac{\Delta t}{2}} + \frac{1}{4}\Delta t\, \tilde{\boldsymbol{N}}_{\boldsymbol{k}}[\tilde{\boldsymbol{\omega}}_1]\, \mathrm{e}^{\nu k^2 \frac{\Delta t}{2}} \tag{3.11b}$$

$$\tilde{\boldsymbol{\omega}}_{3,\boldsymbol{k}} = \frac{1}{3}\tilde{\boldsymbol{\omega}}_{0,\boldsymbol{k}}\, \mathrm{e}^{-\nu k^2 \Delta t} + \frac{2}{3}\tilde{\boldsymbol{\omega}}_{2,\boldsymbol{k}}\, \mathrm{e}^{-\nu k^2 \frac{\Delta t}{2}} + \frac{2}{3}\Delta t\, \tilde{\boldsymbol{N}}_{\boldsymbol{k}}[\tilde{\boldsymbol{\omega}}_2]\, \mathrm{e}^{-\nu k^2 \frac{\Delta t}{2}} \quad . \tag{3.11c}$$

Time Step Control

Controlling the time step size is comparably easy for partial differential equations with advection and diffusion as the Courant-Friedrichs-Lewy criterion is at hand. This criterion basically states that any information (think, e.g., of a passive tracer particle) may not travel more than the distance of the grid spacing per time step in order to maintain a stable simulation. Apart from being very intuitive restriction, it can be proven rigorously for linear partial differential equations, see [Boy01] for further details.

Let $\Delta x = \frac{2\pi}{N}$ denote the grid spacing of the simulation domain with box length 2π. For the advective term we consider the global maximum of the absolute value of the velocity components

$$u_{\max} = \max\{|u_x|, |u_y|, |u_z|\} \quad . \tag{3.12}$$

The maximum distance travelled by a fictive particle per time step is $\Delta x = u_{\max}\Delta t$, which yields the upper bound

$$\Delta t_{\mathrm{adv}} = \frac{\Delta x}{u_{\max}} = \frac{2\pi}{u_{\max} N} \quad . \tag{3.13}$$

The second restriction comes from the diffusive term of the equation. According to the mean square displacement of a diffusion process in three dimensions with the diffusion constant ν we have

$$\Delta x^2 = 6\nu\Delta t \quad , \tag{3.14}$$

which yields the second restriction

$$\Delta t_{\mathrm{diff}} = \frac{\Delta x^2}{6\nu} = \frac{2\pi^2}{3\nu N^2} \quad . \tag{3.15}$$

The overall timestep is then chosen as

$$\Delta t = \lambda \min\{\Delta t_{\mathrm{adv}}, \Delta t_{\mathrm{adv}}\} \quad , \tag{3.16}$$

where $\lambda < 1$ is the Courant number. For the simulations usually $\lambda \approx 0.5$ is chosen. Note that in the case of the employed integrating factor technique the diffusive restriction becomes redundant. In the turbulent regime, however, the advective nonlinearity is dominant over viscous diffusion, however, the advective restriction determines the time step.

Evaluation of the Right-Hand Side

As explained, the diffusive term of the right-hand side of equation (3.7) is treated within the time stepping scheme. The different forcing schemes also act implicitly on the vorticity field and will be explained in the next section. For the evaluation of the right-hand side it remains to explain the treatment of the nonlinear term. The procedure now is to

- compute the velocity field from the vorticity field in Fourier space,
- transform both the vorticity field and the velocity field to real space,
- compute the nonlinearity $\boldsymbol{u}(\boldsymbol{x},t) \times \boldsymbol{\omega}(\boldsymbol{x},t)$,
- transform the nonlinearity back to Fourier space,
- dealias the nonlinearity and
- finally take the curl $\mathrm{i}\boldsymbol{k} \times \mathcal{F}\left[\boldsymbol{u}(\boldsymbol{x},t) \times \boldsymbol{\omega}(\boldsymbol{x},t)\right]$.

To compute the velocity field, one starts with the relation

$$\boldsymbol{\omega}(\boldsymbol{x},t) = \nabla \times \boldsymbol{u}(\boldsymbol{x},t) \quad . \tag{3.17}$$

Taking the curl of this expression yields

$$\nabla \times \boldsymbol{\omega}(\boldsymbol{x},t) = \nabla \times \nabla \times \boldsymbol{u}(\boldsymbol{x},\boldsymbol{t}) = \nabla\big(\underbrace{\nabla \cdot \boldsymbol{u}(\boldsymbol{x},t)}_{=0}\big) - \Delta \boldsymbol{u}(\boldsymbol{x},t) = -\Delta \boldsymbol{u}(\boldsymbol{x},t)\,. \tag{3.18}$$

In Fourier space this expression simply reads

$$\mathrm{i}\boldsymbol{k} \times \tilde{\boldsymbol{\omega}}_{\boldsymbol{k}} = k^2 \tilde{\boldsymbol{u}}_{\boldsymbol{k}} \quad , \tag{3.19}$$

which is easily inverted to

$$\tilde{\boldsymbol{u}}_{\boldsymbol{k}} = \begin{cases} \frac{\mathrm{i}\boldsymbol{k} \times \tilde{\boldsymbol{\omega}}_{\boldsymbol{k}}}{k^2} & \text{if} \quad k^2 \neq 0 \\ \boldsymbol{0} & \text{else} \quad . \end{cases} \tag{3.20}$$

Choosing $\tilde{\boldsymbol{u}}_{\boldsymbol{0}} = \boldsymbol{0}$ corresponds to considering turbulence without mean flow.

Forcing Schemes

Several forcing schemes are implemented within the code. Originally the "frozen mode" scheme was the only implemented forcing scheme. Regarding the isotropy of long-range correlated fields like the velocity, this scheme yielded poor results. Within a diploma thesis by Anton Daitche, several other forcing schemes have been adopted and tested. For the sake of completeness these forcing schemes are presented here. We refer the reader to [Dai09] for further details and tests.

All forcing schemes act implicitly in Fourier space, i.e., we do not have an additive term like indicated in equation (3.7), the vorticity field rather is manipulated after each evaluation of the right-hand side. All of the implemented forcing schemes are deterministic and may be described in the following way. Consider a set of wave vectors B in Fourier space

$$B = \left\{ \boldsymbol{k} \middle| k_{\min} < k < k_{\max} \right\} \quad . \tag{3.21}$$

The forcing schemes act exclusively in this so-called forcing band via the functional $\Phi[\tilde{\boldsymbol{\omega}}_b, \tilde{\boldsymbol{\omega}}_a]$,

$$\tilde{\boldsymbol{\omega}}_{\boldsymbol{k}} \mapsto \begin{cases} \Phi_{\boldsymbol{k}}[\tilde{\boldsymbol{\omega}}_b, \tilde{\boldsymbol{\omega}}_a] & \boldsymbol{k} \in B \\ \tilde{\boldsymbol{\omega}}_{\boldsymbol{k}} & \boldsymbol{k} \notin B \end{cases} \quad . \tag{3.22}$$

Here, $\tilde{\boldsymbol{\omega}}_b$ denotes the field in Fourier space *before* each evaluation of the right-hand side, whereas $\tilde{\boldsymbol{\omega}}_a$ denotes the field *afterwards*. If one wants to express the forcing as an additive term, this term is formally given as

$$\tilde{\boldsymbol{F}}_{\boldsymbol{k}} = \begin{cases} \lim_{\Delta t \to 0} \frac{\Phi_{\boldsymbol{k}}[\tilde{\boldsymbol{\omega}}_b, \tilde{\boldsymbol{\omega}}_a] - \tilde{\boldsymbol{\omega}}_{\boldsymbol{k},a}}{\Delta t} & \boldsymbol{k} \in B \\ \boldsymbol{0} & \boldsymbol{k} \notin B \end{cases} \quad . \tag{3.23}$$

Now the different types of forcing correspond to a differing choice of Φ.

Frozen Mode Forcing The frozen mode forcing is specified by

$$\Phi_{\boldsymbol{k}} = \tilde{\boldsymbol{\omega}}_{\boldsymbol{k},b} \quad , \tag{3.24}$$

i.e., after each evaluation of the right-hand side the Fourier coefficients are set to the old value within the forcing band. As the forcing usually is chosen to act in a low wave number band, the large scale modes of the flow do not evolve in time. It is immediately clear that this type of forcing cannot yield large-scale isotropy if the initial condition displays anisotropies. However, small-scale statistics are unaffected by this problem and the implementation is very easy.

Frozen Amplitude Forcing To allow for large-scale dynamics of the flow field, the frozen mode forcing has been generalized. Now the amplitude of each each Fourier mode

$$\|\tilde{\boldsymbol{\omega}}_{\boldsymbol{k}}\| = \sqrt{\tilde{\boldsymbol{\omega}}_{\boldsymbol{k}}^* \cdot \tilde{\boldsymbol{\omega}}_{\boldsymbol{k}}} \tag{3.25}$$

is kept constant, whereas the phases may evolve freely. The corresponding forcing function is defined as

$$\Phi_{\boldsymbol{k}} = \frac{\|\tilde{\boldsymbol{\omega}}_{\boldsymbol{k},b}\|}{\|\tilde{\boldsymbol{\omega}}_{\boldsymbol{k},a}\|} \, \tilde{\boldsymbol{\omega}}_{\boldsymbol{k},a} \quad . \tag{3.26}$$

The large-scale isotropy is significantly improved by this forcing scheme.

Energy-Conserving Forcing In addition it might be desirable to keep the simulation at a fixed energy. This is why an energy-conserving forcing scheme has been

developed in [Dai09]. The idea is to amplify the amplitudes in the forcing band, such that the kinetic energy dissipated within the whole range of wave numbers is counterbalanced. The kinetic energy is obtained by

$$E_{\text{kin}} = \frac{1}{2}\sum_{\boldsymbol{k}} \|\tilde{\boldsymbol{u}}_{\boldsymbol{k}}\|^2 = \frac{1}{2}\sum_{\boldsymbol{k}} \frac{\|\tilde{\boldsymbol{\omega}}_{\boldsymbol{k}}\|^2}{k^2} =: E^B_{\text{kin}} + E^R_{\text{kin}} \quad , \tag{3.27}$$

i.e., as the sum of the kinetic energy in the forcing band and the kinetic energy contained in the remaining wave numbers. To counterbalance the loss of energy, we have to determine the factor α in

$$E_{\text{kin},a} = \alpha^2 E^B_{\text{kin},a} + E^R_{\text{kin},a} \stackrel{!}{=} E_{\text{kin},b} \quad . \tag{3.28}$$

This equation obviously holds for

$$\alpha^2 = \frac{E_{\text{kin},b} - E^R_{\text{kin},a}}{E^B_{\text{kin},a}} \quad . \tag{3.29}$$

Hereby the forcing functional is defined as

$$\Phi_{\boldsymbol{k}} = \begin{cases} \alpha\, \tilde{\boldsymbol{\omega}}_{\boldsymbol{k},a} & \text{if} \qquad \alpha^2 \geq 0 \\ \tilde{\boldsymbol{\omega}}_{\boldsymbol{k},a} & \text{else} \quad . \end{cases} \tag{3.30}$$

From a physical point of view it is clear that $E_{\text{kin},b} - E^R_{\text{kin},a} > E_{\text{kin},b} - E_{\text{kin},a} > 0$ as the rate of kinetic energy dissipation is strictly positive, such that $\alpha^2 > 0$. The numerical tests in [Dai09] indicate that this type of forcing delivers very satisfying results regarding the obtained statistical symmetries. Large-scale isotropy is obtained on shorter time scales than with the frozen amplitude forcing. A modification of this forcing scheme, which only conserves the energy contained in the forcing band, has also been implemented.

Componentwise Energy-Conserving Forcing To improve the performance regarding statistical symmetries even more, a modification of the energy-conserving forcing scheme has been developed. In this scheme the "energy" contained in each component of the vorticity field is (approximately) held constant and identical for each component. The aim is to reduce anisotropies by driving the system toward a more isotropic state. To this end we define the componentwise "energy"

$$E_{\text{kin},i} = \sum_{\boldsymbol{k}} \frac{|\tilde{\omega}_{\boldsymbol{k},i}|^2}{k^2} \quad . \tag{3.31}$$

Maintaining a constant reference energy E_{kin} now requires

$$E_{\text{kin},a} = \sum_{i=1}^{3} \alpha_i^2 E^B_{\text{kin},i,a} + E^R_{\text{kin},i,a} \stackrel{!}{=} E_{\text{kin}} \quad . \tag{3.32}$$

A possible solution of this equation, for example, reads

$$\alpha_i^2 = \frac{{}^{E_{\text{kin}}}/_3 - E^R_{\text{kin},i,a}}{E^B_{\text{kin},i,a}} \quad . \tag{3.33}$$

By construction this factor introduces more energy to a component which deviates from the isotropic state (for which $E_{\text{kin},i} = \frac{E_{\text{kin}}}{3}$). Thus this type of forcing is expected to yield even better results regarding isotropy. However, if each component is treated individually, the resulting vorticity field cannot be expected to be solenoidal anymore, which requires $\boldsymbol{k}\cdot\tilde{\boldsymbol{\omega}}_{\boldsymbol{k}}$=0. Now let P denote the projection operator

$$P_{ij} = \delta_{ij} - \frac{k_i k_j}{k^2} \tag{3.34}$$

and A the diagonal matrix with α_i as entries. The forcing functional is then defined as

$$\Phi_{\boldsymbol{k}} = \begin{cases} \text{PA}\,\tilde{\boldsymbol{\omega}}_{\boldsymbol{k},a} & \text{if} \qquad \alpha_i^2 \geq 0 \quad \forall i \\ \tilde{\boldsymbol{\omega}}_{\boldsymbol{k},a} & \text{else} \quad . \end{cases} \tag{3.35}$$

Due to the projection operator it is not clear if this forcing scheme actually maintains constant energy. It was tested numerically, however, that this holds. The results in [Dai09] show that this type of forcing performs slightly better than the ordinary energy-conserving forcing. However, the ordinary energy-conserving forcing appears to be less artificial and is numerically easier to implement.

Dealiasing

The aliasing problem discussed in the introductory part may be reduced by dealiasing techniques. For quadratic nonlinearities like encountered in the Navier-Stokes equation several dealiasing techniques have been developed. From a purely mathematical point of view the famous ²/₃-rule can be shown to eliminate aliasing errors from the simulations [Ors71]. The ²/₃-rule simply reads

$$\tilde{\boldsymbol{\omega}}_{\boldsymbol{k}} \mapsto \begin{cases} \tilde{\boldsymbol{\omega}}_{\boldsymbol{k}} & \text{if} \quad k^2 < \left(\frac{2}{3}k_{\max}\right)^2 = \left(\frac{N}{3}\right)^2 \\ \boldsymbol{0} & \text{else} \quad . \end{cases} \tag{3.36}$$

This rule, however, has two major drawbacks. First, as a sharp filter in Fourier space, it has the tendency to produce Gibbs oscillations in the dealiased fields, which introduces numerical errors to the fields on small scales. Second, for three-dimensional simulations only $\left(\frac{2}{3}\right)^3 = \frac{8}{27}$ of the simulated modes are dynamically active, which seems pretty uneconomical. One way to overcome this situation is to allow for aliasing errors. For example, it was suggested in [Hom06] to extend the range of allowed modes and maintain a sharp filter. Recently, a different type of dealiasing filter has been suggested in [HL07], which makes use of a smooth Fourier filter, where the dealiased Fourier modes are given

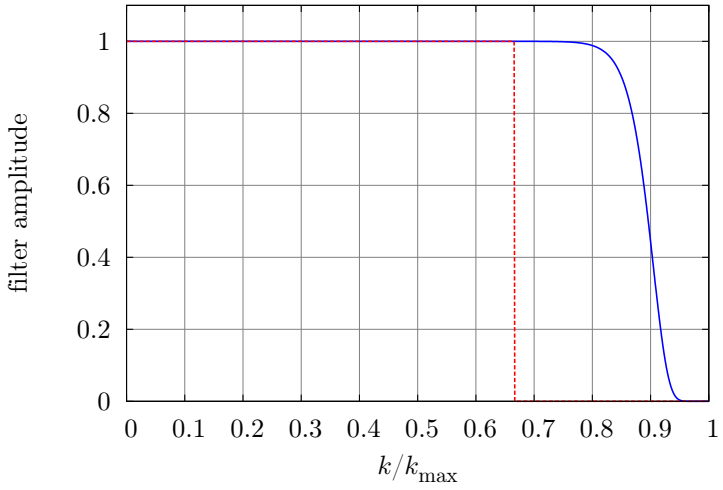

Figure 3.2.: On dealiasing. 2/3-rule (red curve) vs. the smooth Fourier filter suggested in [HL07] (blue curve).

by

$$\tilde{\boldsymbol{\omega}}_{\boldsymbol{k}} \mapsto \tilde{\boldsymbol{\omega}}_{\boldsymbol{k}} \exp\left[-\alpha \left(\frac{k}{k_{\max}}\right)^{\beta}\right] \quad . \tag{3.37}$$

The numerical parameters have been chosen as $\alpha = 36$ and $\beta = 36$. To test the performance, the filter has been used in simulations of the one-dimensional Burgers equation and the results have been shown to converge better to the true solution than the results of a simulation using the 2/3-rule. It then was suggested in [HL07] to use this kind of dealising filter for computing solutions of the Euler equation with pseudospectral methods.

All of the presented dealising filters have been implemented. The smooth Fourier filter then has been used for all production runs.

3.1.3. Lagrangian Particles

The simulation code optionally allows to follow Lagrangian tracer particles. This part of the code has also been developed by Anton Daitche as part of a diploma thesis and is described in [Dai09]. The code design is such that the Lagrangian part is held independent from the Eulerian part; this part can be included at compile time with a compiler flag. Again, for the sake of completeness the algorithmic details are presented here as well.

The position $\boldsymbol{X}(t, \boldsymbol{y})$ of a Lagrangian particle starting from $\boldsymbol{y}$ obeys the differential equation

$$\dot{\boldsymbol{X}}(t, \boldsymbol{y}) = [\boldsymbol{u}(\boldsymbol{x}, t)]_{\boldsymbol{x}=\boldsymbol{X}(t,\boldsymbol{y})} =: \boldsymbol{U}(t, \boldsymbol{y}) \quad . \tag{3.38}$$

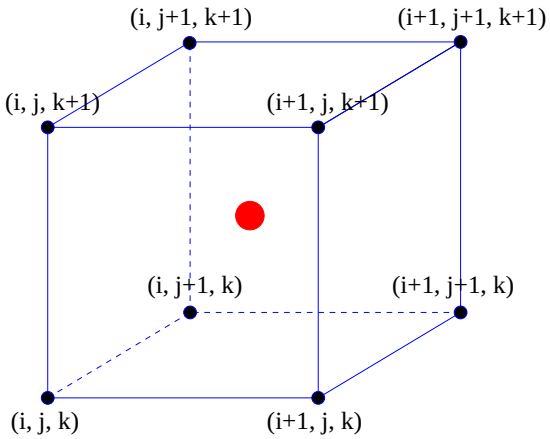

Figure 3.3.: Particle (red) in a grid cell.

The argument $\boldsymbol{y}$ will be omitted when no confusion has to be expected. To solve this equation numerically, it is required to interpolate the velocity field at a given position and to implement a time stepping scheme for the tracer particles. Additionally it is of interest to determine other quantities like, e.g., the vorticity along Lagrangian particle paths, which has also been implemented.

Interpolation of Eulerian Fields

As the tracer particles move between the Eulerian grid points, it is necessary to interpolate the Eulerian field. We have chosen a tricubic interpolation scheme, which yields a good balance between accuracy and performance.

For the following, consider the function f which is known on the Eulerian grid points. The aim is to interpolate this function between these grid points. We introduce the local coordinates

$$t = \frac{x - x_i}{\Delta x} \quad u = \frac{y - y_i}{\Delta x} \quad v = \frac{z - z_i}{\Delta x} \quad , \tag{3.39}$$

which specify the particle position relative to the lower left corner of the cube defined by the surrounding Eulerian grid points. Figure 3.3 exemplifies the situation. In the case of a tricubic scheme we have to specify the coefficients c_{ijk} of the third-order polynomial

$$f\left(t, u, v\right) = \sum_{i=0}^{3} \sum_{j=0}^{3} \sum_{k=0}^{3} c_{ijk}\, t^i u^j v^k \quad . \tag{3.40}$$

To determine the 64 coefficients, eight equations have to be specified on each of the

eight cell corners, which involve the function f and its derivatives,

$$f_{\alpha\beta\gamma} = \sum_{i=0}^{3}\sum_{j=0}^{3}\sum_{k=0}^{3} c_{ijk}\,\alpha^i\beta^j\gamma^k \tag{3.41a}$$

$$f^{(t)}_{\alpha\beta\gamma} = \sum_{i=0}^{3}\sum_{j=0}^{3}\sum_{k=0}^{3} i\,c_{ijk}\,\alpha^{i-1}\beta^j\gamma^k \tag{3.41b}$$

$$f^{(u)}_{\alpha\beta\gamma} = \sum_{i=0}^{3}\sum_{j=0}^{3}\sum_{k=0}^{3} j\,c_{ijk}\,\alpha^i\beta^{j-1}\gamma^k \tag{3.41c}$$

$$f^{(v)}_{\alpha\beta\gamma} = \sum_{i=0}^{3}\sum_{j=0}^{3}\sum_{k=0}^{3} k\,c_{ijk}\,\alpha^i\beta^j\gamma^{k-1} \tag{3.41d}$$

$$f^{(tu)}_{\alpha\beta\gamma} = \sum_{i=0}^{3}\sum_{j=0}^{3}\sum_{k=0}^{3} ij\,c_{ijk}\,\alpha^{i-1}\beta^{j-1}\gamma^k \tag{3.41e}$$

$$f^{(tv)}_{\alpha\beta\gamma} = \sum_{i=0}^{3}\sum_{j=0}^{3}\sum_{k=0}^{3} ik\,c_{ijk}\,\alpha^{i-1}\beta^j\gamma^{k-1} \tag{3.41f}$$

$$f^{(uv)}_{\alpha\beta\gamma} = \sum_{i=0}^{3}\sum_{j=0}^{3}\sum_{k=0}^{3} jk\,c_{ijk}\,\alpha^i\beta^{j-1}\gamma^{k-1} \tag{3.41g}$$

$$f^{(tuv)}_{\alpha\beta\gamma} = \sum_{i=0}^{3}\sum_{j=0}^{3}\sum_{k=0}^{3} ijk\,c_{ijk}\,\alpha^{i-1}\beta^{j-1}\gamma^{k-1} \tag{3.41h}$$

$$\alpha,\beta,\gamma \in \{0,1\} \quad .$$

Here the superscripts indicate differentiation with respect to the different variables, and the subscript denotes the different corners of the cube. Since the function f is known on the Eulerian grid, its derivatives are computed via centered finite differences. To evaluate the derivatives, f has to be known on the 64 grid points

$$\left\{ x_{i+l,j+m,k+n} \middle| l,m,n \in \{-1,0,1,2\} \right\} \quad . \tag{3.42}$$

The derivatives are then given by

$$f^{(t)}_{\alpha\beta\gamma} = \frac{f_{\alpha+1,\beta,\gamma} - f_{\alpha-1,\beta,\gamma}}{2} \tag{3.43a}$$

$$f^{(tu)}_{\alpha\beta\gamma} = \frac{f^{(t)}_{\alpha,\beta+1,\gamma} - f^{(t)}_{\alpha,\beta-1,\gamma}}{2} \tag{3.43b}$$

$$\vdots$$

The whole set of equations specifying the function f and its derivatives on the cell corners is a linear system of equations, which can be seen introducing the notation

$$f^{(\lambda)}_{\alpha\beta\gamma} = \sum_{i=0}^{3}\sum_{j=0}^{3}\sum_{k=0}^{3} A_{[\lambda,\alpha\beta\gamma],[ijk]} c_{ijk} \tag{3.44}$$
$$\alpha,\beta,\gamma \in \{0,1\} \quad \lambda \in \{\emptyset, t, u, v, tu, tv, uv, tuv\}$$

with

$$\mathrm{A}_{[\lambda,\alpha\beta\gamma],[ijk]} = \begin{cases} \alpha^i\beta^j\gamma^k & \lambda = \emptyset \\ i\,\alpha^{i-1}\beta^j\gamma^k & \lambda = t \\ j\,\alpha^i\beta^{j-1}\gamma^k & \lambda = u \\ k\,\alpha^i\beta^j\gamma^{k-1} & \lambda = v \\ ij\,\alpha^{i-1}\beta^{j-1}\gamma^k & \lambda = tu \\ ik\,\alpha^{i-1}\beta^j\gamma^{k-1} & \lambda = tv \\ jk\,\alpha^i\beta^{j-1}\gamma^{k-1} & \lambda = uv \\ ijk\,\alpha^{i-1}\beta^{j-1}\gamma^{k-1} & \lambda = tuv \end{cases} \tag{3.45}$$
$$\alpha,\beta,\gamma \in \{0,1\} \qquad i,j,k \in \{0,1,2,3\} \quad .$$

By a renaming of indices

$$(i,j,k) \to l = 16i + 4j + k \tag{3.46}$$

it is clear that A is a 64×64 matrix, which can be inverted. This determines the interpolation coefficients

$$c_{ijk} = \sum_{\lambda,\alpha,\beta,\gamma} \mathrm{A}^{-1}_{[ijk],[\lambda,\alpha\beta\gamma]} f^{(\lambda)}_{\alpha\beta\gamma} \quad . \tag{3.47}$$

The explicit inversion of A has to be done once as it does not depend on f or its derivatives. This was achieved with the computer algebra system `Maple`, which allows to export the output in `Fortran` form.

Lagrangian Time Stepping Scheme

The parallelization of the Lagrangian part of the code is technically intricate as we will describe later on. It turns out that a time stepping scheme is desirable, which has to be evaluated only once each time step of the Eulerian part of the simulation. That is why a third-order Adams-Bashforth-Moulton predictor-corrector scheme has been chosen. For a detailed description of the algorithmic details we refer the reader to [Gea71, Dai09].

This multistep method can be written down according to

$$\boldsymbol{X}'_{n,0} = \boldsymbol{X}_{n-1} + \frac{\Delta t}{2}\left(3\,\boldsymbol{U}_{n-1} - \boldsymbol{U}_{n-2}\right) \tag{3.48a}$$

$$\boldsymbol{X}'_{n,m} = \boldsymbol{X}_{n-1} + \frac{\Delta t}{12}\left(5\,\boldsymbol{u}\left[\boldsymbol{X}'_{n,m-1}, t_n\right] + 8\,\boldsymbol{U}_{n-1} - \boldsymbol{U}_{n-2}\right) \; m \leq m_{\max} \tag{3.48b}$$

$$\boldsymbol{X}_n = \boldsymbol{X}'_{n,m_{\max}} \quad . \tag{3.48c}$$

This notation requires some explanation. Primed variable indicate that their values are only used within the time stepping scheme and will not be stored. Unprimed variables in equations (3.48a) and (3.48b) correspond to values actually obtained in the past. For example, $\boldsymbol{X}_{n-1}$ and $\boldsymbol{U}_{n-1}$ denote the position and velocity of a Lagrangian particle at time step t_{n-1}, respectively. $\boldsymbol{u}[\boldsymbol{X}'_{n,m-1}, t_n]$ indicates that here an extra interpolation of the velocity field is necessary within the scheme to obtain the value at the positions $\boldsymbol{X}'_{n,m-1}$. The first step (3.48a) is the so-called predictor step, here performed with a second-order Adams-Bashforth scheme. Then $m_{\max}$ corrector steps follow according to equation (3.48b), allowing for an increasingly precise estimate of the actual position of the particle. In the simulation code we choose $m_{\max} = 2$. The result of the last corrector step then is taken as the value of the Lagrangian particle $\boldsymbol{X}_n$, indicated in (3.48c). The introduced error of this method is of $\mathcal{O}(\Delta t^4)$.

This method can additionally be transformed from a multistep method to a multivalue method, in this case the set of equation has been transformed to the so-called Nordsieck form. This transformation basically allows to interpret part of the arising expressions in terms of the coefficients of a Taylor expansion,

$$\boldsymbol{X}(t_n + \Delta t) = \boldsymbol{X}_n + \Delta t\,\boldsymbol{U}_n + \frac{1}{2}\Delta t^2\,\boldsymbol{A}_n + \mathcal{O}(\Delta t^3) \quad , \tag{3.49}$$

where $\boldsymbol{A}_n$ denotes the Lagrangian acceleration. The main advantage is that adaptive step size control is easily achievable within this formulation by adjusting the prefactors of the Taylor expansion. A second (minor) advantage is that the Lagrangian acceleration is automatically computed within this scheme. For starting up the particle integration, not all necessary information for evaluating (3.48b) is available, that is why a second-order Adams-Bashforth scheme (more precisely: the Nordsieck form of the Heun scheme) is used in this situation. In addition to this third-order scheme, the corresponding fourth-order scheme has been implemented. However, delivering satisfactory results, the third-order scheme is used by default.

3.2. Parallelization, Code Design and Performance

3.2.1. The Need For a Parallel Implementation

The numerical simulation of turbulent flows longs for high resolutions for several reasons. When inertial range statistics is studied, a broad inertial range is of interest, i.e., the forcing scale and the dissipative scale of the fluid should be well separated. This

separation increases with the Reynolds number, that is why one seeks for high Reynolds number simulations. For simulations with fixed box length (which basically limits the integral length scale) increasing the inertial range means to decrease dissipative scale, i.e., the size of the smallest structures. This obviously calls for a higher resolution. The concept of the inertial range has already been introduced in section 2.4.3 (see figure 2.2) and some spectra from simulations are shown in figure 3.4. This whole issue can be made more quantitative. The Kolmogorov length scale can be related to the Reynolds number

$$\eta \sim \left(\frac{uL}{\nu}\right)^{-3/4} L = Re^{-3/4} L \quad . \tag{3.50}$$

Here L, u and denote the integral length scale and a typical velocity, respectively. As this scale should be adequately resolved, we demand $\Delta x \sim \eta$. For a box length of 2π this gives an estimate how the number of grid points needed for simulation increases with the Reynolds number

$$N_x = \left(\frac{2\pi}{\Delta x}\right)^3 \sim \left(\frac{2\pi}{L}\right) Re^{9/4} \quad . \tag{3.51}$$

It is clear from the Courant-Friedrichs-Lewy conditions that also the time step has to decrease with increasing grid resolution, which also has to be taken into account when estimating the computational costs. The number of time steps to resolve a large-eddy turnover time T increases according to

$$N_t = \frac{T}{\Delta t} \sim \frac{T}{\Delta x/u} \sim \frac{T}{L/u} Re^{3/4} \quad . \tag{3.52}$$

The overall computational costs roughly increase with the product of both

$$N_x N_t \sim \left(\frac{T}{L/u}\right) \left(\frac{2\pi}{L}\right)^3 Re^3 \quad , \tag{3.53}$$

ending up with a cubic dependence on the Reynolds number. This immediately shows why a parallel implementation is necessary.

3.2.2. Parallelization of the Eulerian Part

The simulation code is written as a `MPI` parallel version for the use on distributed memory architectures. The parallelization scheme of the Eulerian part of the code depends strongly on the type of fast Fourier transform employed. For the current simulation code, the `MPI` parallel version of the `FFTW 2.1.5` (downloadable from [fft], see also [FJ05] for details) is used. This fast Fourier transform makes use of a slab domain decomposition, i.e., the simulation domain is cut into slices, which is shown in figure 3.5. Consequently, each core holds only subarrays of the whole Eulerian fields needed to compute the temporal evolution. As the Fourier transform is a nonlocal operation, information from these subarrays has to be exchanged between all cores. This, however,

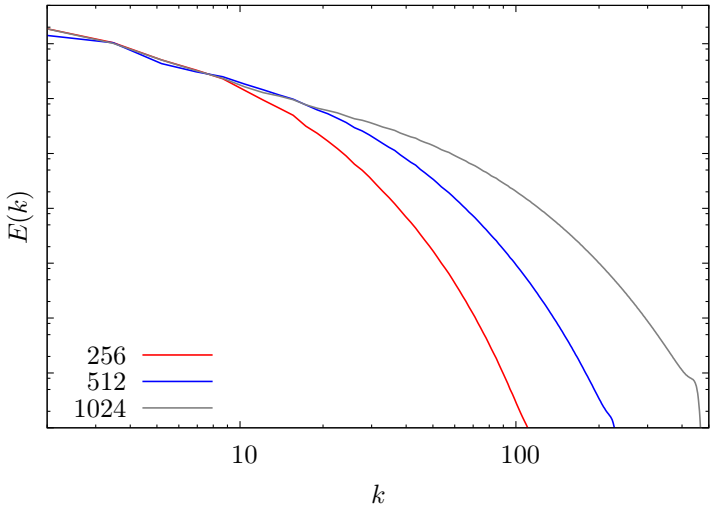

Figure 3.4.: Energy spectra from different numerical simulations in a double logarithmic plot, varying in grid resolution from 256 to 1024 grid points. The Taylor-based Reynolds numbers are $R_\lambda = 76, 112, 225$. An inertial range is hardly detectable, however it is clear to see that the range of wave number with approximate algebraic behavior extends with increasing Reynolds number. The plots have been shifted vertically.

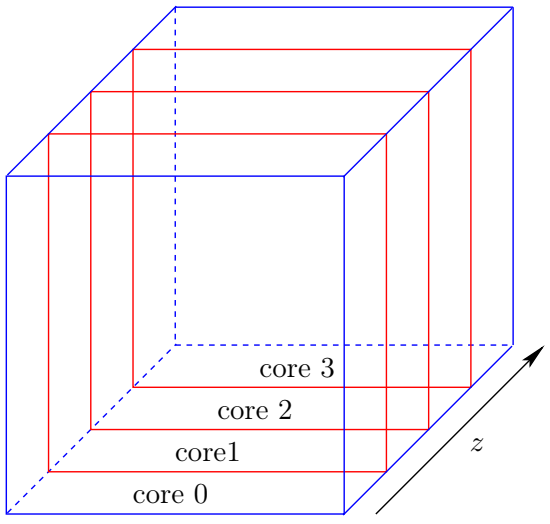

Figure 3.5.: Slab domain decomposition.

is managed by the implementation of the `FFTW` and does not have to be programmed from scratch. While the `FFTW` routines are written in `C`, the rest of the simulation code is written in `Fortran 90`.

One of the intricate tasks is to take into account the correct ordering of the Fourier coefficients. This may be exemplified by the ordering of the corresponding wave vectors. Once this array is specified correctly, all differentiation operations correspond to componentwise multiplications with this array.

To keep the following considerations simple, we consider a $N \times N \times N$ grid with box length 2π. Additionally we assume that N is divisible by the number of cores N_{core}. We adopt `Fortran` notation in the following. For the non-parallelized case the array $\boldsymbol{k}$ is a real $\left(\frac{N}{2}+1\right) \times N \times N$ array (as we are considering real-to-complex transformations), which takes the values

$$\boldsymbol{k}[i,j,k] = [\alpha,\beta,\gamma] \quad \text{with} \quad \{i,j,k\} \in \left[1, \frac{N}{2}+1\right] \times [1,N] \times [1,N] \quad , \tag{3.54}$$

where

$$\alpha = i - 1 \tag{3.55a}$$

$$\beta = \begin{cases} j-1 & \text{if} \quad 1 \leq j \leq \frac{N}{2}+1 \\ j-N-1 & \text{if} \quad \frac{N}{2}+2 \leq j \leq N \end{cases} \tag{3.55b}$$

$$\gamma = \begin{cases} k-1 & \text{if} \quad 1 \leq k \leq \frac{N}{2}+1 \\ k-N-1 & \text{if} \quad \frac{N}{2}+2 \leq k \leq N \end{cases} \quad . \tag{3.55c}$$

In the case of a parallel version running on N_{core} cores, a local subarray $\boldsymbol{k}^m[i,j,k]$ (with $m \in \{0,\ldots,N_{\text{core}}-1\}$) is allocated on each of the cores. With $N_{\text{local}} = \frac{N}{N_{\text{core}}}$ each of these arrays has the size $\left(\frac{N}{2}+1\right) \times N \times N_{\text{local}}$. The corresponding local offset is

$$k^m_{\text{offset}} = m \cdot N_{\text{local}} \quad . \tag{3.56}$$

Consequently, the subarrays take the form

$$\boldsymbol{k}^m[i,j,k] = [\alpha,\beta,\gamma] \quad \text{with} \quad \{i,j,k\} \in \left[1, \frac{N}{2}+1\right] \times [1,N] \times [1,N_{\text{local}}] \quad , \tag{3.57}$$

with

$$\alpha = i - 1 \tag{3.58a}$$

$$\beta = \begin{cases} j-1 & \text{if} \quad 1 \leq j \leq \frac{N}{2}+1 \\ j-N-1 & \text{if} \quad \frac{N}{2}+2 \leq j \leq N \end{cases} \tag{3.58b}$$

$$\gamma = \begin{cases} k+k^m_{\text{offset}}-1 & \text{if} \quad 1 \leq k+k^m_{\text{offset}} \leq \frac{N}{2}+1 \\ k+k^m_{\text{offset}}-N-1 & \text{if} \quad \frac{N}{2}+2 \leq k+k^m_{\text{offset}} \leq N \end{cases} \quad . \tag{3.58c}$$

The internal computation of the fast Fourier transform involves a number of transpositions of the global array. As an operation involving global communication, this is rather time-consuming. The `FFTW` allows to spare the final transposition, leaving the last two dimensions in transposed order. This can be taken into account by exchanging the last two dimensions of the wave vector array,

$$\boldsymbol{k}^m_{\text{transposed}}[i,j,k] = [\alpha,\gamma,\beta] \quad \{i,j,k\} \in \left[1, \frac{N}{2}+1\right] \times [1,N] \times [1,N_{\text{local}}] \quad . \tag{3.59}$$

The performance gain is up to 30% per computed Fourier transform. We refer the reader to the online documentation of `FFTW` for more detailed information.

Apart from the array handling, a number of global communication operations arise throughout the code. For example, the CFL restriction necessitates to determine the maximal velocity component for the whole velocity field. Elsewhere in the code mean values like the kinetic energy or enstrophy are evaluated as averages over the whole field. These quantities are evaluated using global reduction operations implemented in the `MPI` library.

Input and output of the Eulerian field is done with `MPI I/O`, which allows to write the local arrays to a single file, which holds the global arrays. This is especially useful when the checkpointing capabilities of the code are used and a simulation is continued with a differing number of cores.

3.2.3. Parallelization of the Lagrangian Part

Several technical aspects have to be taken into account for the parallelization of this part of the code. First, the particles move freely through the whole simulation domain passing through several slices of the decomposed domain. For the typical scenario of fully developed homogeneous isotropic turbulence the tracer particles may be assumed to be uniformly distributed over the whole simulation domain. To achieve load balancing, each core performs the computations for the Lagrangian particles residing in its slice. As the domain is decomposed in z-direction, the core the tracer particle belongs to is determined by

$$z(t+\Delta t) \mapsto \left\lfloor \frac{\left[\!\left[\frac{z(t+\Delta t)}{\Delta x} \right]\!\right] \mod N}{N/N_{\text{core}}} \right\rfloor \quad . \tag{3.60}$$

In this mapping, the nominator determines the nearest (rounded to the next integer) local grid point, division by the denominator and rounding then maps this value to the actual number of the core. $z(t+\Delta t)$ is approximated by the predictor step of the time stepping scheme. More details on this can be found in [Dai09].

Second, for a Lagrangian tracer particle near the edge of a slice, the interpolation requires data from neighboring grid points. This requires an exchange of Eulerian data each time step. In the numerical implementation halo slices of two grid points width are exchanged each time step for each quantity, that is interpolated. This is especially easy

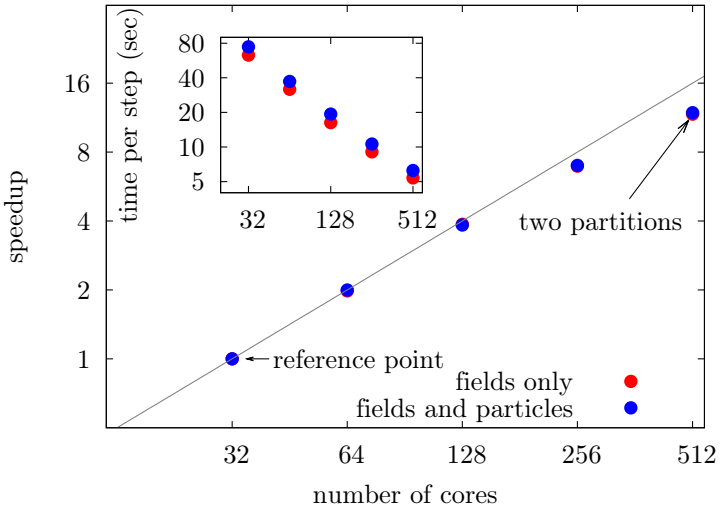

Figure 3.6.: Scaling results of a 1024^3 run with and without ten million tracer particles. The gray line indicates ideal scaling. The inset display the time needed for a single simulation step.

to implement and turned out to be rather performant; this part of the communication consumes about 2%–12% of the time spent for the Lagrangian part of the code [Dai09].

Finally, input and output of Lagrangian data is also implemented using `MPI I/O`. It turns out that disk access is a performance bottleneck, that is why the Lagrangian data is buffered, such that I/O is only necessary every several hundreds of time steps. To achieve the required ordering of the particles, each particle carries an id and is sent to its "home core" prior to output.

3.2.4. Scaling Performance

The production runs presented in this thesis were conducted within the *grand challenge project h0963* at the LRZ Munich. The machine is a `SGI Altix 4700`, a `Linux` based cluster with 9728 cores based on `Intel Itanium2 Montecito Dual Core` processors. For the scaling tests we chose a typical simulation scenario with a grid resolution of 1024^3 and optionally ten millions of Lagrangian tracer particles. The tests were performed on the low density partitions of the `HLRB II`, the results are shown in figure 3.6. Both the simulations with and without particles perform very good. Slight performance penalties arise when using two partitions. As the calculation of the time evolution of the flow fields relies heavily on the use of Fourier transforms, the performance and scalability of this part of the code mirrors the effective implementation of the `FFTW`. But also the parallel performance of the Lagrangian part of the code is quite satisfactory. The code scales just as well as without particles and the overall computational costs increase by 15–20%.

3.3. Overview of Conducted Simulations

3.3.1. Typical Runs

A typical simulation basically consists of two stages. First, a proper initial condition has to be obtained. To this end an artificial large-scale initial condition decays for some large-eddy turnover times. During this time a turbulent flow develops. Then the forcing is applied, and the system approaches statistical stationarity after some large-eddy turnover times. This simulation stage is performed with adaptive time stepping. To save computational costs, the initial conditions for highly resolved simulations can be obtained from lower resolved simulations by up-sampling in Fourier space. The duration of the thermalization stage of the up-sampled field is shorter than for a random large-scale initial condition. It turns out that this thermalization stage of the simulation is rather costly, making up a considerable amount of the computational resources needed.

After the preparation of proper initial conditions the actual simulation is performed. Here, the flow field is advanced in the statistically stationary state. During this period fields (velocity, vorticity, velocity gradients etc.) are stored with a sampling rate sufficient to form a statistical ensemble. The statistical analysis is performed during the postprocessing stage. Optionally tracer particles are advected with the flow and stored frequently. A typical 1024^3 run requires several tens of thousands of cpu hours for the preparation of initial conditions and the actual simulation. An Eulerian field here requires 12 GB of disk space, and the Lagrangian data produced per time step is of the order 100 MB. In total, such a run easily produces a terabyte of data. Within the *grand challenge project* runs with resolutions between 256^3 and 1024^3 grid points with Taylor-based Reynolds numbers ranging from about 75 to 250 have been performed, giving insight into the Reynolds number dependence of the statistical quantities under consideration as well as resolution issues.

3.3.2. Characterizing Quantities

For comparison with other simulations or experiments introducing a number of characterizing quantities is useful. These quantities are determined for each simulation either as an average over the full simulation or as an instantaneous average for a fixed time step. The latter then allows to judge, e.g., the stationarity of the simulation. Some of the quantities have already been introduces earlier in this thesis, for a better overview, however, we repeat them here.

Maybe the most fundamental quantity is the Reynolds number defined as

$$Re = \frac{u_{\mathrm{rms}} L}{\nu} \quad . \tag{3.61}$$

Here $u_{\mathrm{rms}} = \sqrt{\frac{1}{3}\langle \boldsymbol{u}^2 \rangle} = \sqrt{\frac{2}{3} E_{\mathrm{kin}}}$ denotes the root mean square of the velocity of a single

component, ν denotes the kinematic viscosity. The integral length scale, estimated as[2]

$$L \approx \frac{u_{\mathrm{rms}}^3}{\langle \varepsilon \rangle} \quad , \tag{3.62}$$

involves the average rate of energy dissipation

$$\langle \varepsilon \rangle = \frac{\nu}{2} \left\langle \sum_{i,j=1}^{3} \left(\frac{\partial u_i}{\partial x_j} + \frac{\partial u_j}{\partial x_i} \right)^2 \right\rangle \quad . \tag{3.63}$$

Another number quantifying the large scales of the flow is the integral time scale

$$T = \frac{L}{u_{\mathrm{rms}}} \quad . \tag{3.64}$$

The Taylor-based Reynolds number can be estimated from the Reynolds number by [Dav04, Pop00, Fri95]

$$R_\lambda = \sqrt{15 Re} \quad . \tag{3.65}$$

Apart from the rate of energy dissipation, the small scales of the flow are characterized by the Kolmogorov scales, which are defined as

$$\eta = \left(\frac{\nu^3}{\langle \varepsilon \rangle} \right)^{1/4} \tag{3.66a}$$

$$\tau_\eta = \left(\frac{\nu}{\langle \varepsilon \rangle} \right)^{1/2} \tag{3.66b}$$

$$u_\eta = \left(\nu \langle \varepsilon \rangle \right)^{1/4} \quad . \tag{3.66c}$$

The Kolmogorov length scale helps to quantify the spatial resolution of a simulation. As a rule of thumb, a simulation is considered as well-resolved if

$$q_r = \gamma \, k_{\max} \, \eta \gtrsim 1.5 \quad , \tag{3.67}$$

where γ is a factor determined by the dealiasing technique. For the smooth Fourier filter, this factor can be estimated as $\gamma = 0.8$ as the filter is approximately constant for the first 80% of wave numbers, see figure 3.2. As the smallest structure of the fields are of about 10η of size, this rule basically suggests to resolve these structures. Figure 3.7 shows energy spectra for different values of q_r, demonstrating the effect of under-resolution.

The parameters and characterizing quantities for the production runs performed for the statistical evaluations in this thesis are summarized in table 3.3.2.

[2] This estimate usually involves an additional constant of the order one. We here, however, adapt the estimate frequently used in the literature involving experiments or numerical simulations. Note that changes in this estimate directly affect the numerical value of the Reynolds number.

	sim_256	sim_512	sim_1024	sim_1024_ext
N	256	512	1024	1024
Re	389	841	3386	3373
R_λ	76	112	225	225
u_{rms}	0.26	0.54	0.81	0.81
ν	0.001	0.001	0.0004	0.0004
L	1.49	1.55	1.67	1.67
T	5.69	2.86	2.07	2.06
duration (in T)	181.0	78.7	5.8	13.6
η	0.017	0.010	0.004	0.004
τ_η	0.289	0.098	0.0356	0.0355
u_η	0.059	0.101	0.106	0.106
E_{kin}	0.102	0.442	0.98	0.98
$\langle\varepsilon\rangle$	0.012	0.103	0.316	0.317
q_r	1.74	2.03	1.55	1.54
λ	0.5	0.5	< 0.5	< 0.5

Table 3.1.: Parameters and characterizing quantities for the different simulations. `sim_1024_ext` is an extended version of `sim_1024` for a better convergence to isotropic statistics. All runs have been conducted with the energy-conserving forcing scheme

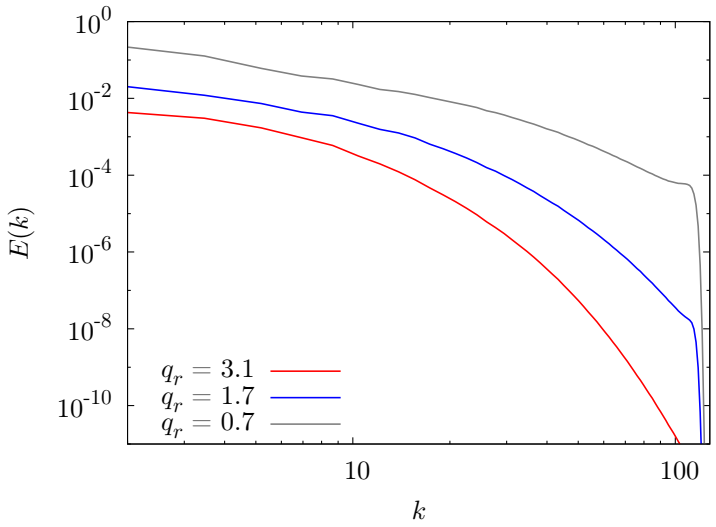

Figure 3.7.: Energy spectra for three different values of q_r from a simulation with 256^3 grid points. The under-resolved simulation displays strong spectral blocking for high wave numbers. The small-scale statistics of this simulation is supposed to be affected by this artifact. Lowering the effective resolution further will eventually cause a numerical instability.

3.4. DNS and Statistical Symmetries

As discussed in chapter 2, statistical hydrodynamics is based on defining suitable averages. Within theoretical considerations the averages are usually ensemble averages over a large number of realizations. For highly resolved numerical simulations, however, this is computationally out of reach. In the case of numerical results the ensemble average is usually replaced by a temporal average in the case of stationary turbulence and a spatial average in the case of homogeneous turbulence. Isotropy additionally allows to treat different spatial direction equivalently and helps to simplify statistical quantities as we have motivated in chapter 2.

Whether it is possible to define a statistical ensemble in this manner can be doubted on different levels. On a very fundamental level, it is not clear if turbulence is ergodic. If not, the above replacement of averages is forbidden. A deeper discussion on this point is presented in [Tsi09]. Based on the results presented there and in the corresponding references, we take the assumption of ergodicity for granted, at least to the extent that averaging over single realizations of the flow is assumed to yield statistically robust results. Even if one accepts these points, however, several technical aspects have to be taken into account.

In order to make up a proper ensemble under temporal averaging, the fields from the numerical simulations should be widely separated in time, such that no temporal correlations exist any more. This obviously necessitates long runs. That is why it might be useful, at least for some statistical analyzes, to go for a rather long simulation instead of choosing a higher grid resolution and consequently Reynolds number.

Comparable problems arise, when spatial averaging is considered. As the Reynolds number increases with the integral length scale L, increasing this quantity is desirable. At the same time, when L becomes comparable to the length of the simulation domain, finite size effects induced by the periodic boundary conditions may play a role. This issue is discussed in [Dav04], where it is estimated that simulations, in which L is twenty times smaller than the box length, should reduce the problem. This, however, results in ridiculously low Reynolds numbers and is therefore usually not practiced.

The issue of isotropy has already been indicated in combination with the forcing schemes. A temporal evolution of the forcing scales has been identified as a necessary condition to obtain isotropic statistics on the large scales.

This brings us to another important point. The capability of a numerical simulation to fulfill these statistical symmetries varies strongly with the type of quantity under consideration. It was shown in the introductory part of this thesis that, e.g., the vorticity appears to be shorter correlated than the velocity. In the same manner one can expect that the vorticity varies on a much shorter time scale, probably comparable to τ_η, whereas the velocity varies on a time scale comparable to T. Thus data from a short numerical simulation may make up a good statistical ensemble when small-scale quantities are considered, while it may yield poor results in terms of long-range correlated quantities. This point shall be made clear with a couple of numerical examples now. Figures 3.8 and 3.9 show PDFs and longitudinal correlation functions of velocity and vorticity for

an increasing number of fields, over which the average is taken. The fields are taken from the simulation `sim_256` and are approximately separated by $1.8T$ in time. Besides the increasing statistical quality, it is clear to see that the quantities converge to an isotropic state with increasing number of field realizations. The velocity takes more field realizations to show approximately isotropic statistics.

Consequently, the statement of this short paragraph is that a single snapshot from a numerical simulation cannot be expected to fulfill statistical homogeneity and isotropy. If, however, a well-suited external forcing allows to perform a stationary simulation over a long duration, the gathered data is able to constitute an ensemble which approximately fulfills the idealized concept of stationary, homogeneous and isotropic turbulence.

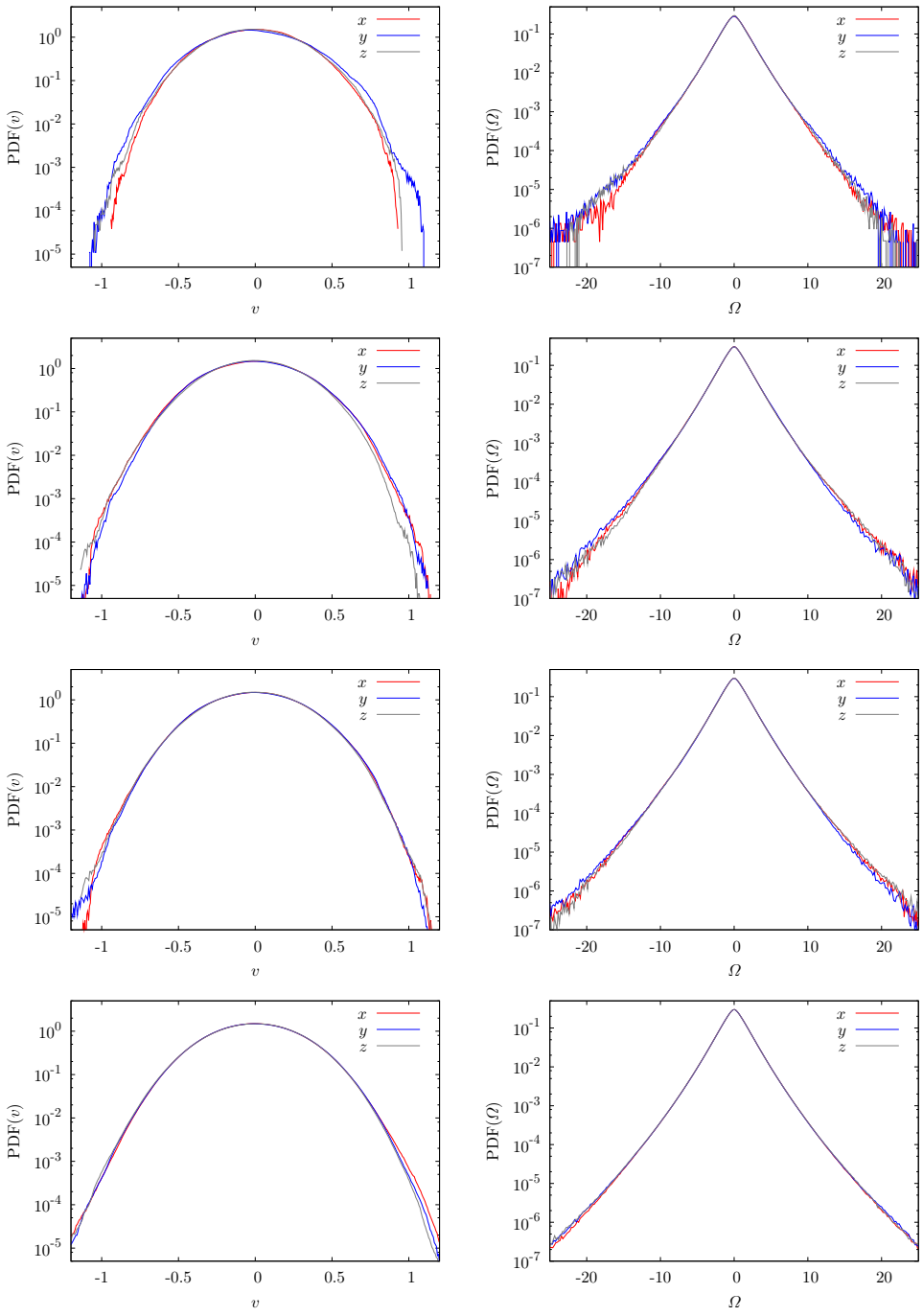

Figure 3.8.: PDFs of the components of velocity (left) and vorticity (right). From upper to lower panel: average taken over $1, 5, 10, 101$ field(s), respectively. Nearly isotropic statistics are obtained with an increasing number of samples. The vorticity PDFs converge earlier to an isotropic state.

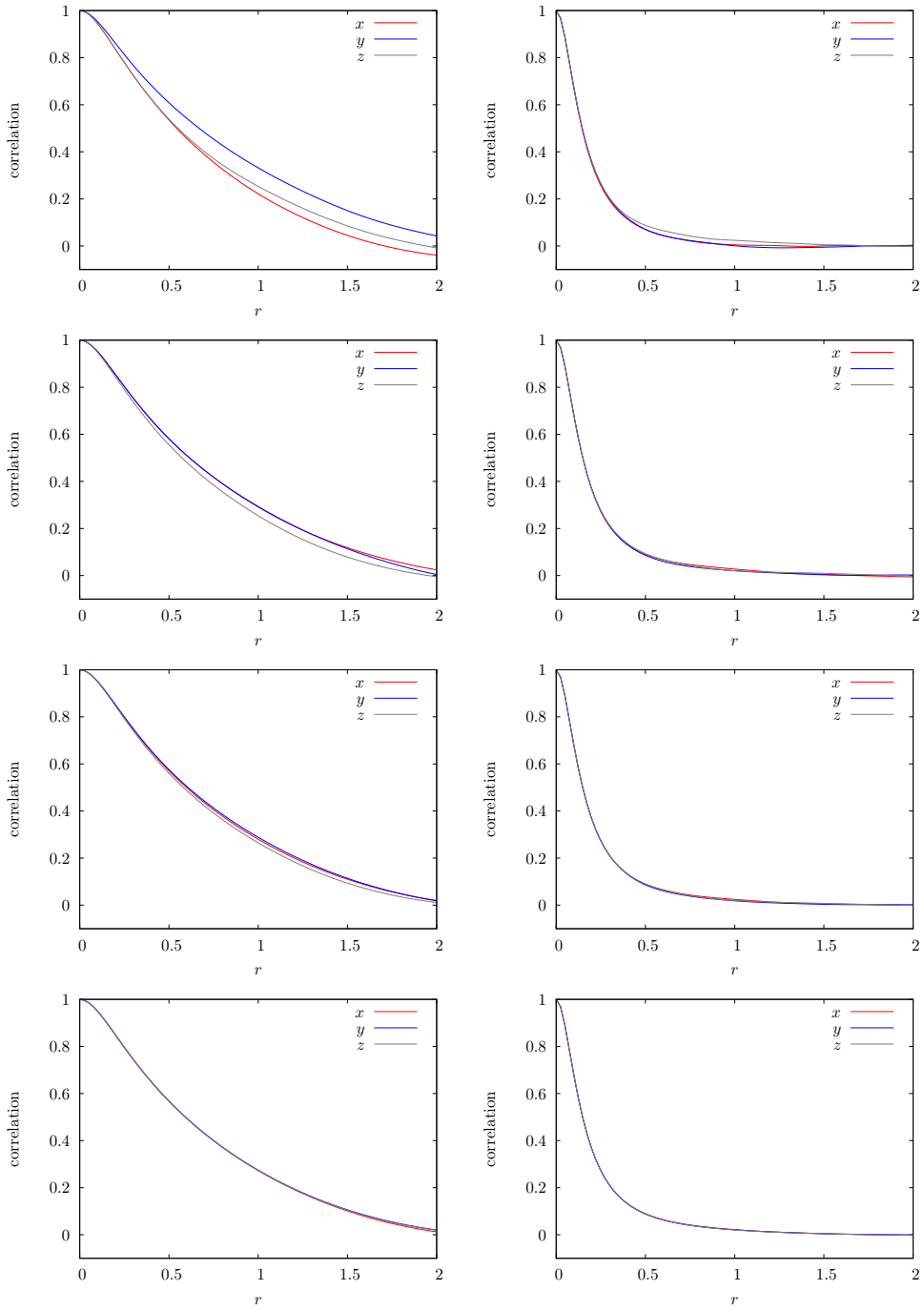

Figure 3.9.: Longitudinal correlation functions of the components of velocity and vorticity. From upper to lower panel: average taken over $1, 5, 10, 101$ field(s), respectively. Nearly isotropic statistics are obtained with an increasing number of samples.

Part II.

Dynamics and Statistics of Three-Dimensional Turbulence

4. Statistical Characterization of Fully Developed Turbulence Obtained by DNS

In this chapter we will present a collection of statistical quantities of fully developed turbulence obtained by the direct numerical simulation code described in the last chapter. Therefore the purpose of this chapter is two-fold. On the one hand, it will further elucidate the statistical nature of fully developed turbulence, on the other hand it serves as a benchmark presentation to characterize the numerical results of the thesis.

This chapter is structured as follows. After presenting PDFs of the velocity, vorticity and velocity gradient tensor to characterize the intermittent nature of the small scales in turbulence, we will turn to two-point statistics characterizing the direct energy cascade. We then establish a number of new theoretical kinematic relations on two-point correlations of different turbulent observables, which then will be checked with our numerical simulations. To give a more detailed characterization of the fine-scale structure of turbulence, we compare the properties of turbulent fields to those of random fields in the following section. The chapter is closed with a comparison of DNS results and experimental data of a free jet and a cylinder wake in order to highlight the advantages and disadvantages of DNS over experiments.

4.1. PDFs and Structure Functions

4.1.1. Single-Point Statistics

We start with a presentation of single-point statistics of the basic dynamical quantities. Figure 4.1 shows the PDF of the velocity components and its magnitude. As can be seen from the PDFs of the components, the statistics is nearly isotropic with some deviations for large values of velocity. The PDFs are nearly Gaussian, but display systematic deviations toward sub-Gaussian tails. This becomes especially clear, when the magnitude of velocity is considered and compared to an angle-integrated Gaussian. This observation is consistent with earlier numerical and experimental investigations [Bat53, VM91, GFN02, NWL$^+$97], but due to the nearly Gaussian behavior remains an often-discussed issue up to today. We will present a theoretical framework explaining the deviations from Gaussianity in chapter 7.

In figure 4.2 the single-point statistics of the vorticity is presented. In contrast to the velocity field, the vorticity exhibits strongly non-Gaussian PDFs with slowly decaying

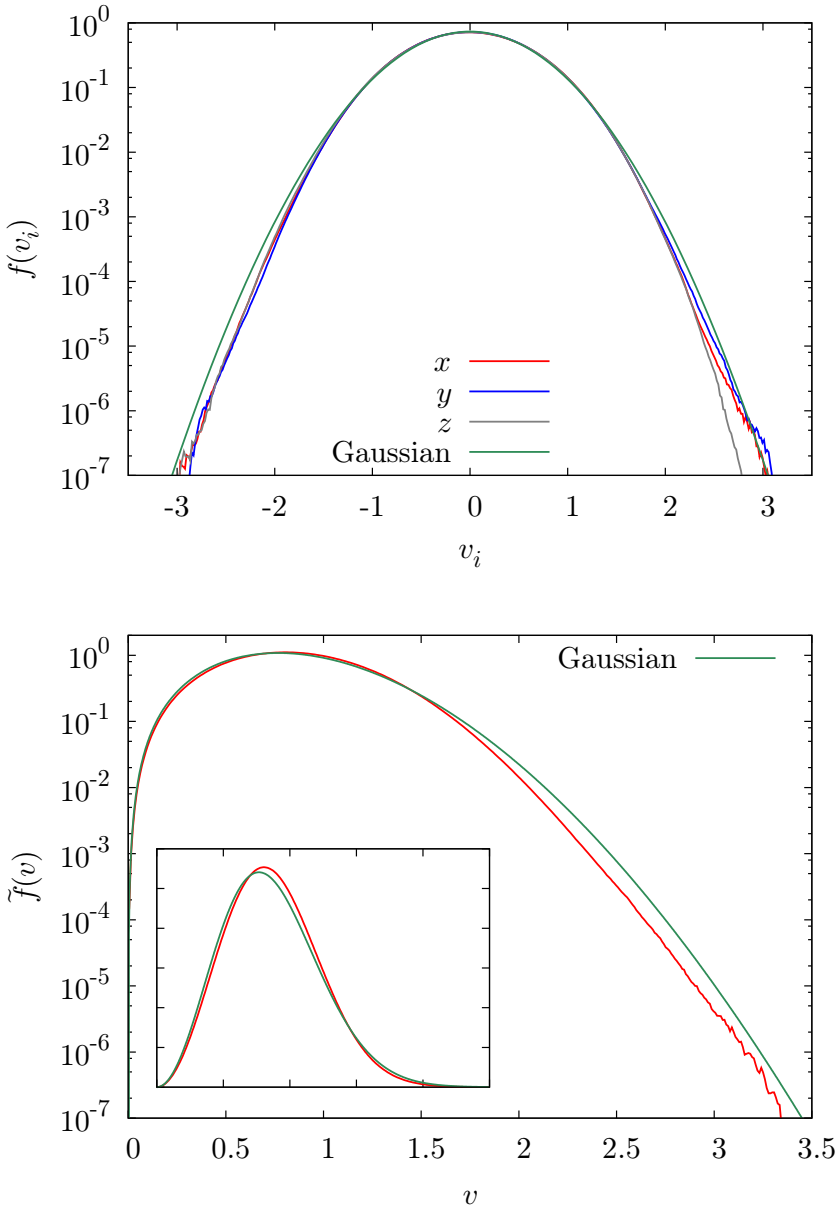

Figure 4.1.: PDFs of the components of the velocity (upper figure) and the magnitude of velocity (lower figure). The PDFs display nearly Gaussian behavior with a tendency to sub-Gaussian tails (`sim_512`).

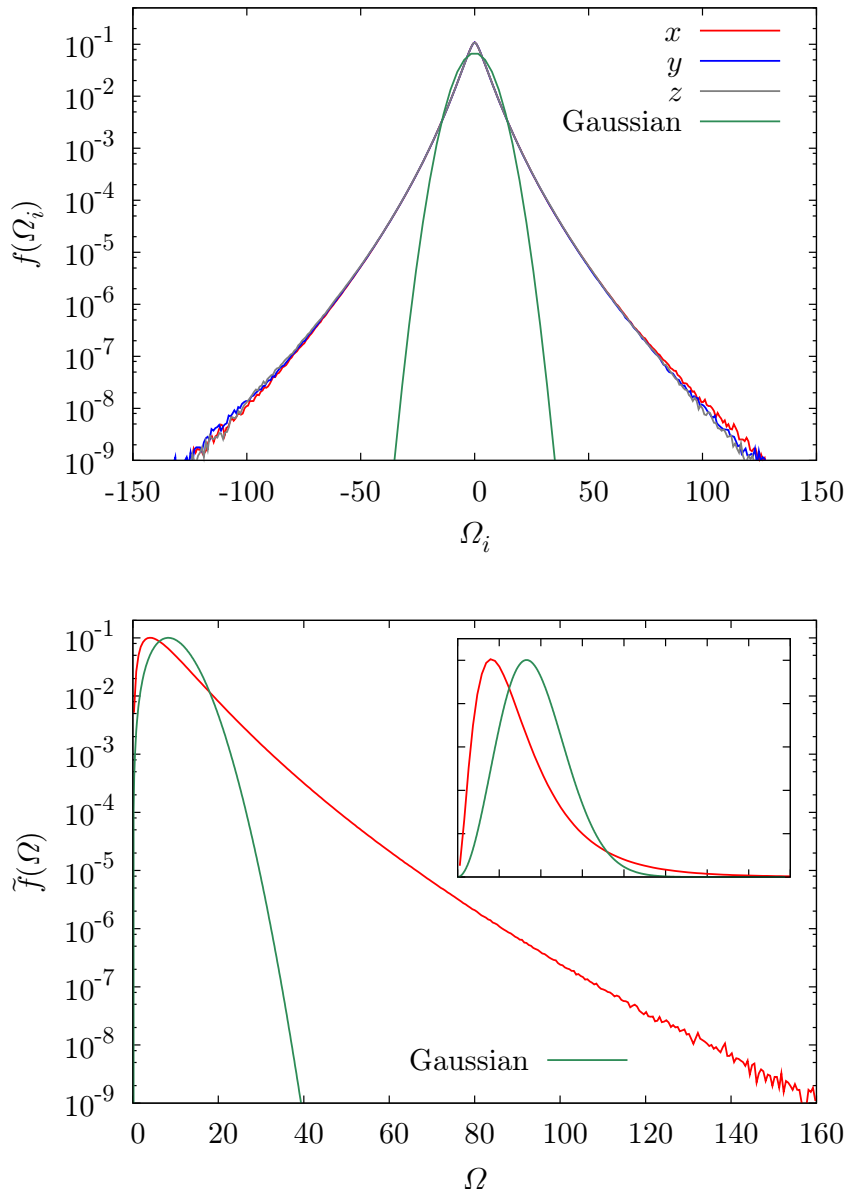

Figure 4.2.: PDFs of the components of the vorticity (upper figure) and the magnitude of vorticity (lower figure). The vorticity PDFs are strongly non-Gaussian exhibiting pronounced tails (`sim_512`).

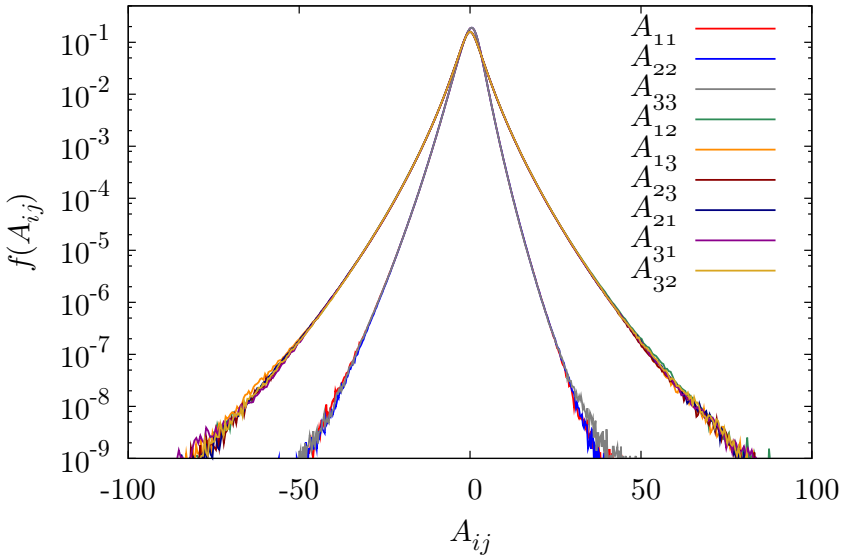

Figure 4.3.: PDFs of the components of the velocity gradient tensor. The PDFs of the diagonal components of the tensor are skewed and heavy-tailed. The the off-diagonal components display even stronger tails, but are non-skewed (`sim_512`).

tails, i.e., the occurrence of strong vorticity events is orders of magnitudes more likely than for a Gaussian field. The collapse of the different components indicates that the vorticity statistics shows less anisotropies, as expected from a quantity fluctuating on small scales. The investigation of the vorticity statistics and its relation to dynamical effects like enstrophy production and dissipation will be at the center of the theoretical results presented in chapter 8.

We finally turn to a related quantity, the velocity gradient tensor. The single-point PDFs of all nine components are shown in figure 4.3. One can observe that the diagonal components show a different statistics than the off-diagonal elements. While the diagonal components are skewed, the off-diagonal components are not. On the other hand, the off-diagonal entries display a greater flatness as will become more clear, when the cumulants of the velocity increments will be considered in one of the following sections. Instead of considering the nine components of the velocity gradient tensor independently, one often focuses of the statistics of the invariants, here defined as the prefactors of the characteristic polynomial of this tensor,

$$\chi_{\mathrm{A}}(X) = X^3 + Q'X + R' \quad . \tag{4.1}$$

Here we have already taken into account solenoidality of the velocity field, which implies

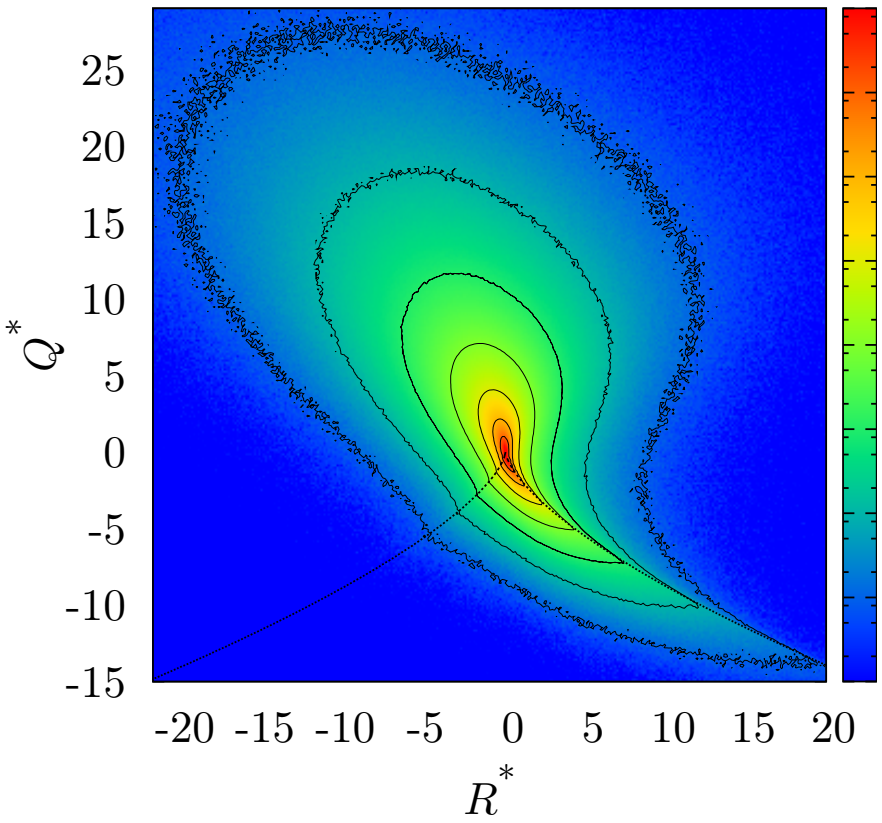

Figure 4.4.: Joint PDF of the velocity gradient tensor invariants (`sim_512`). The bulk of the PDF is located in the swirling regions of the flow and is elongated along the right branch of the Viellefosse line.

$\mathrm{TrA} = 0$. In this case the invariants take the form

$$Q' = -\frac{1}{2}\mathrm{TrA}^2 \tag{4.2a}$$

$$R' = -\frac{1}{3}\mathrm{TrA}^3 = -\mathrm{detA} \quad . \tag{4.2b}$$

Regarding the eigenvalues of A, a special role here is played by the so-called Viellefosse line, which is the discrimant of the characteristic polynomial of A,

$$D = \frac{27}{4}R'^2 + Q'^3 \tag{4.3}$$

as this line separates regions with purely real eigenvalues ($D < 0$) from regions with complex eigenvalues ($D > 0$). In this sense $D = 0$ separates regions with locally predominant strain from regions with locally predominant swirl (see, e.g., [Dav04] for a detailed discussion). Not only because of this simple interpretation the invariants of the velocity gradient tensor are a well-studied object and are the starting point for various modeling approaches [CPC90, Can92, MDV98, CPS99, CM06]. The joint PDF of $Q^* = \frac{Q'}{\langle \mathrm{Tr}S^2 \rangle}$ and $R^* = \frac{R'}{\langle \mathrm{Tr}S^2 \rangle^{\frac{3}{2}}}$ is shown in figure 4.4. It displays a peculiar teardrop shape, where the bulk of the PDF is located in the swirling regions of the R'-Q'-plane. Furthermore, one can observe a pronounced asymmetry, the PDF is elongated along the right branch of the Viellefosse line. As this asymmetry is absent in the case of Gaussian velocity statistics, it can be regarded as a typical signature of three-dimensional turbulence.

The dynamics of the invariants can be studied with the help of the equation of motion of the velocity gradient tensor (1.11). In the case of the Burgers equation the pressure Hessian, one of the main mathematical difficulties is absent, but an additional invariant, the divergence of the velocity field, comes into play. This will be studied analytically in the case of the n-dimensional Burgers equation in chapter 5.

4.1.2. Two-Point Statistics

Velocity Increment PDFs

A very common way to characterize the two-point statistics of the velocity field is the investigation of velocity increments, i.e. velocity differences separated by a distance vector $\boldsymbol{r}$. The longitudinal velocity increment is defined as

$$\delta v(r) = [\boldsymbol{u}(\boldsymbol{x} + \boldsymbol{r}) - \boldsymbol{u}(\boldsymbol{x})] \cdot \hat{\boldsymbol{r}} \quad . \tag{4.4}$$

One can choose two additional transversal directions, such that

$$\hat{\boldsymbol{r}} \perp \hat{\boldsymbol{s}} \perp \hat{\boldsymbol{t}} \quad . \tag{4.5}$$

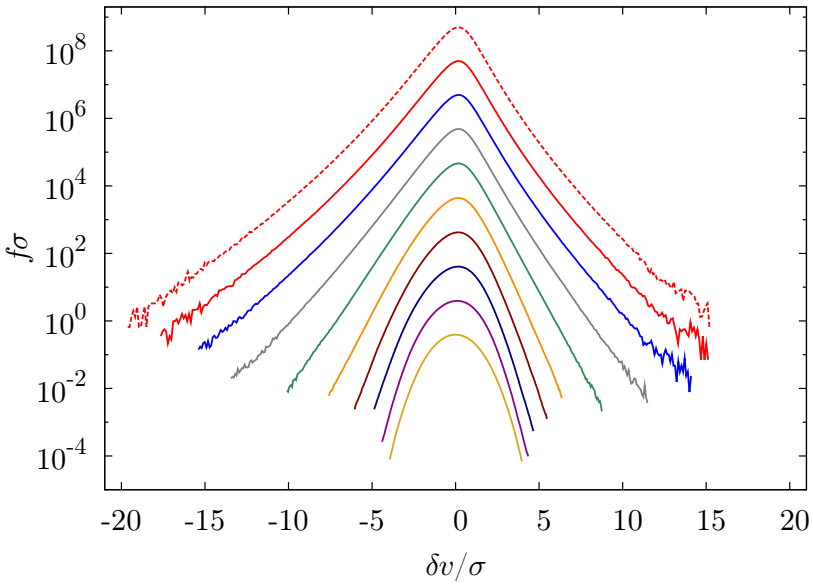

Figure 4.5.: Longitudinal velocity increment PDFs as a function of scale for $r \in \{1.2, 2.5, 4.9, 9.9, 19.8, 39.6, 79.1, 158.3, 316.6\}\,\eta$ (straight lines, from top to bottom). The dashed line corresponds to the PDF of a diagonal component of A (`sim_512`).

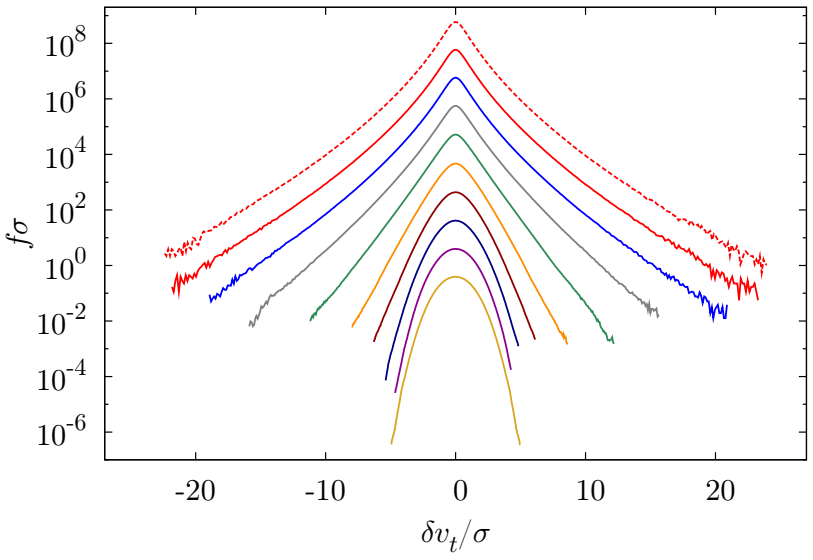

Figure 4.6.: Transversal velocity increment PDFs as a function of scale for $r \in \{1.2, 2.5, 4.9, 9.9, 19.8, 39.6, 79.1, 158.3, 316.6\}\,\eta$ (straight lines, from top to bottom). The dashed line corresponds to the PDF of an off-diagonal component of A (`sim_512`).

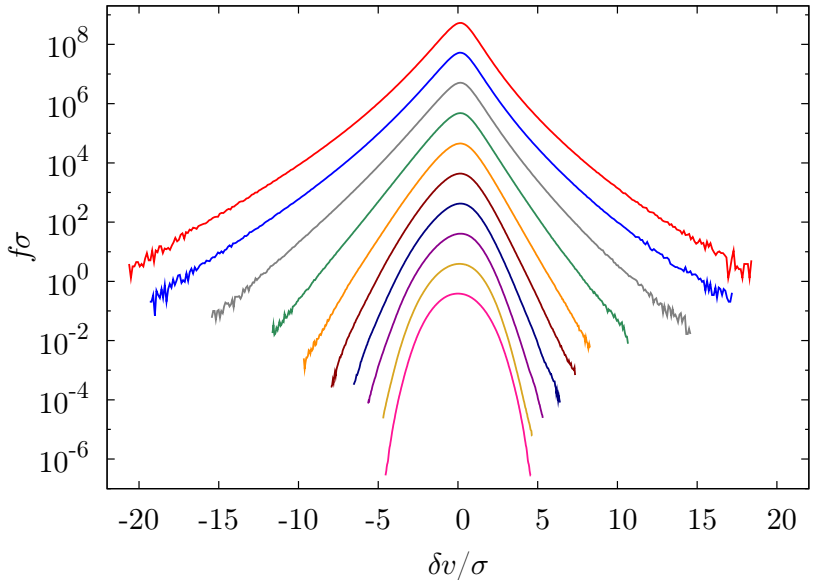

Figure 4.7.: Longitudinal velocity increment PDFs as a function of scale for $r \in \{1.6, 3.3, 6.5, 13.0, 26.0, 52.0, 104.1, 208.2, 416.3, 823.6\}\,\eta$ (from top to bottom, `sim_1024`).

With this one can define the two transversal velocity increments

$$\delta \boldsymbol{v}_s(r) = [\boldsymbol{u}(\boldsymbol{x}+\boldsymbol{r}) - \boldsymbol{u}(\boldsymbol{x}+\boldsymbol{r})] \cdot \hat{\boldsymbol{s}} \quad \text{and} \tag{4.6a}$$

$$\delta \boldsymbol{v}_t(r) = [\boldsymbol{u}(\boldsymbol{x}+\boldsymbol{r}) - \boldsymbol{u}(\boldsymbol{x}+\boldsymbol{r})] \cdot \hat{\boldsymbol{t}} \quad , \tag{4.6b}$$

which, however, exhibit the identical statistics due to isotropy. The PDFs of the longitudinal and transversal velocity increments are shown in figures 4.5 and 4.6. The PDFs evolve non-self-similar in scale, i.e., a continuous shape deformation over scale is observed. The PDFs are highly non-Gaussian with pronounced tails for small separations and tend to more Gaussian behavior for increasing separations. As the velocity increment is proportional to the velocity gradient for small separations, the statistics on the smallest scales almost coincides with the corresponding velocity gradient tensor PDFs, which are also shown for reference. The absence of a self-similar range is usually referred to as intermittency and shows that the simple reasoning of the K41 phenomenology is insufficient to characterize the statistics of fully developed turbulence. At second sight one can note that the longitudinal PDFs are strongly skewed, whereas the transversal PDFs are not. This skewness is related to the energy transfer in scale and will be discussed below. The longitudinal velocity increments for a higher Reynolds number ($R_\lambda = 225$ compared to $R_\lambda = 112$) are shown in figure 4.7. While the qualitative shape is comparable to the simulation at lower Reynolds number, the PDFs at small scales deviate even stronger from Gaussianity, indicating that the occurrence of extreme events

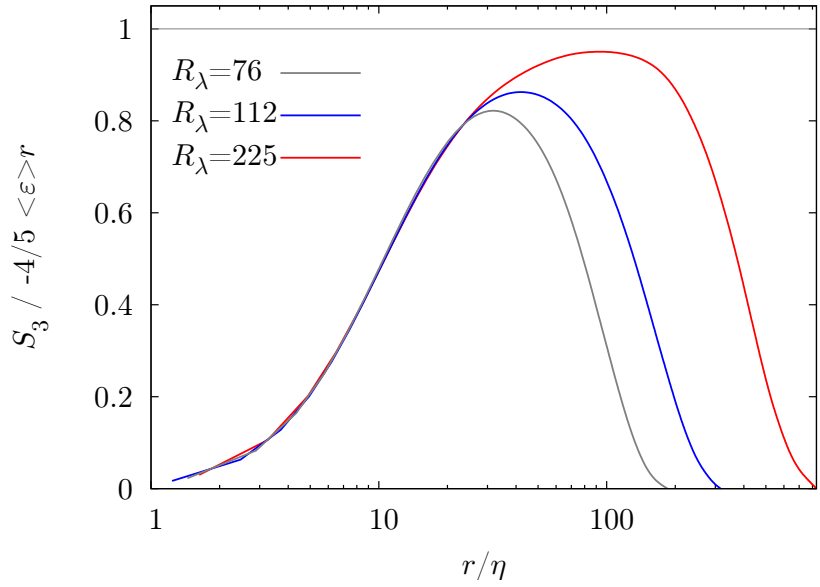

Figure 4.8.: Compensated third-order structure functions (`sim_256`, `sim_512`, `sim_1024_ext`).

becomes more probable for increasing Reynolds numbers. This observation will be made more precise in the following sections, when the fourth-order cumulants are studied.

The Direct Energy Cascade

Instead of considering the increment PDFs, one can also study their moments as a function of scale. These moments are the structure functions, which have already played a central role in the Kolmogorov phenomenology in chapter 2.4.3. The third-order structure function, which is related to the energy transfer in scale, is of considerable interest in this context, as the $4/5$-law (2.40) is derived rigorously from the Navier-Stokes equation and makes a prediction on its functional shape within the inertial range of scales. The third-order structure function has been evaluated from the direct numerical simulations for three different Reynolds numbers and is shown in figure 4.8. It has been compensated with the $4/5$-law, such that a plateau would indicate the inertial range. As can be seen, deviations occur, which decrease with increasing Reynolds number. The simulation with Reynolds number $R_\lambda = 225$ displays the slight onset of a scaling range, indicating that simulations at higher Reynolds numbers are needed to study inertial range statistics. These results are consistent with the findings presented in [GFN02], where we refer the reader to for an extended study of the Reynolds number dependence of the velocity statistics.

According to the K41 phenomenology, the energy spectrum is expected to display a $k^{-\frac{5}{3}}$ scaling range within the inertial range. It is shown in figure 4.9 for three different Reynolds numbers. No clear scaling range is found also here, consistent with the behavior

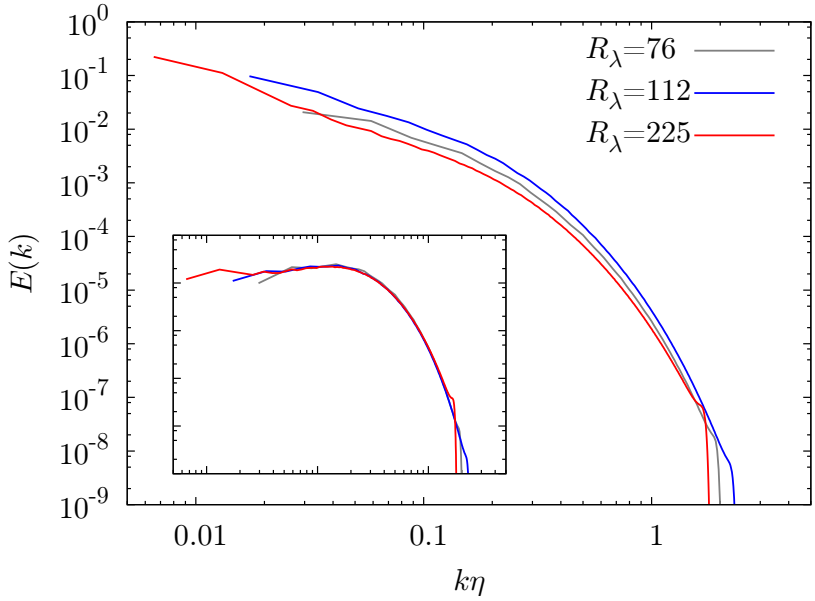

Figure 4.9.: Kinetic energy spectra (`sim_256`, `sim_512`, `sim_1024`). The inset shows the spectra compensated with the Kolmogorov prediction $E(k) \sim \langle\varepsilon\rangle^{\frac{2}{3}} k^{-\frac{5}{3}}$.

of the third-order structure function. It can be noted, though, that the wave vector band of excited modes increases with Reynolds numbers, so that the emergence of a clear scaling range may be expected for higher Reynolds numbers.

The simulations performed for this thesis are comparably well-resolved, as the statistical theory developed from chapter 6 on needs the investigation of derivatives of velocity and vorticity, which necessitates a good resolution of the fields. This can especially be seen from the energy spectra, which do not exhibit a strong spectral blocking for the high wave vectors. Simulations aimed at studying inertial range properties are usually under-resolved on the smallest scales, which make them inappropriate for our purposes. As studying inertial range properties of turbulence is not at the focus of this thesis, the absence of a clear inertial range scaling is unimportant for our investigations.

Structure Functions and Cumulants

After the last remarks it cannot be expected that the remaining structure functions exhibit a clear scaling range. Still a presentation is useful as a benchmark. Figure 4.10 shows the even longitudinal structure functions up to order eight. Beyond the dissipative range a clear change of the functional shape with an approximate scaling region can be seen. The scaling exponents have been estimated by compensating the structure functions and are plotted for reference. They clearly deviate from the K41 prediction $S_n(r) \sim (\langle\varepsilon\rangle r)^{n/3}$, indicating intermittency. The same observation can be made in the case of the transversal structure functions, which are displayed in figure 4.11. Here,

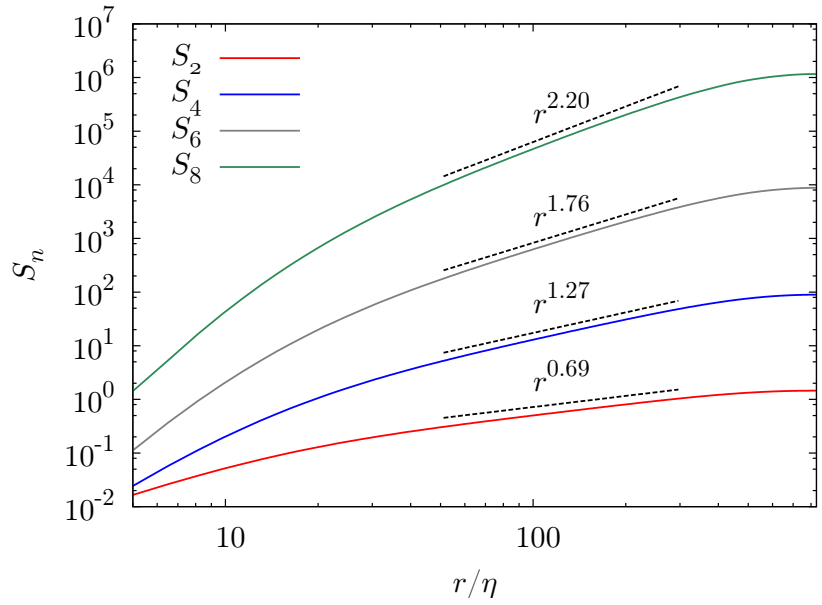

Figure 4.10.: Longitudinal velocity structure functions. The approximate scaling region clearly deviates from the K41 prediction. The structure functions have been shifted vertically (`sim_1024_ext`).

even stronger deviations from a self-similar behavior occur. Both the values for the longitudinal and transversal scaling exponent are in good agreement with the results reported in [GFN02].

Figure 4.12 shows the longitudinal structure function for the vorticity. Although these do not have the same physical meaning as the velocity structure function, a direct comparison with figure 4.10 reveals that they saturate quickly, which indicates that the correlations of the vorticity field decay faster than those of the velocity field. This is why the vorticity field is often referred to as a (comparably) short-range correlated quantity. The second-order correlations of velocity and vorticity will be focused on in the following section.

When it comes to characterizing the deformation of the PDFs across scales, it is convenient to investigate the skewness and the kurtosis of the increment PDFs. For instance, for the longitudinal velocity increments these quantities are defined as

$$K_3(r) = \frac{\langle \delta v^3 \rangle}{\langle \delta v^2 \rangle^{\frac{3}{2}}} \tag{4.7a}$$

$$K_4(r) = \frac{\langle \delta v^4 \rangle}{\langle \delta v^2 \rangle^2} - 3 \quad , \tag{4.7b}$$

where we have already made use of the fact that the mean velocity increment vanishes. In the case of a Gaussian distribution one finds $K_3(r) = 0$ and $K_4(r) = 0$, such

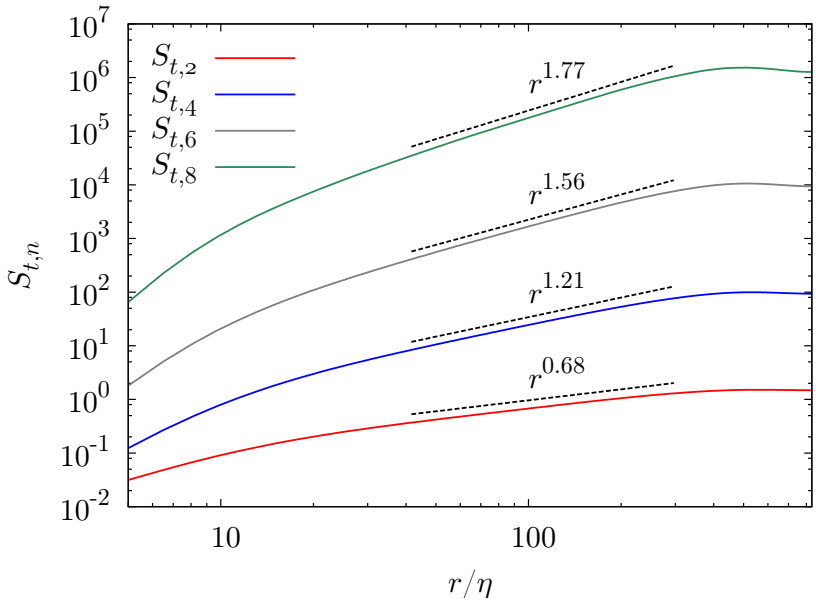

Figure 4.11.: Transversal velocity structure functions. The structure function have been shifted vertically (`sim_1024_ext`).

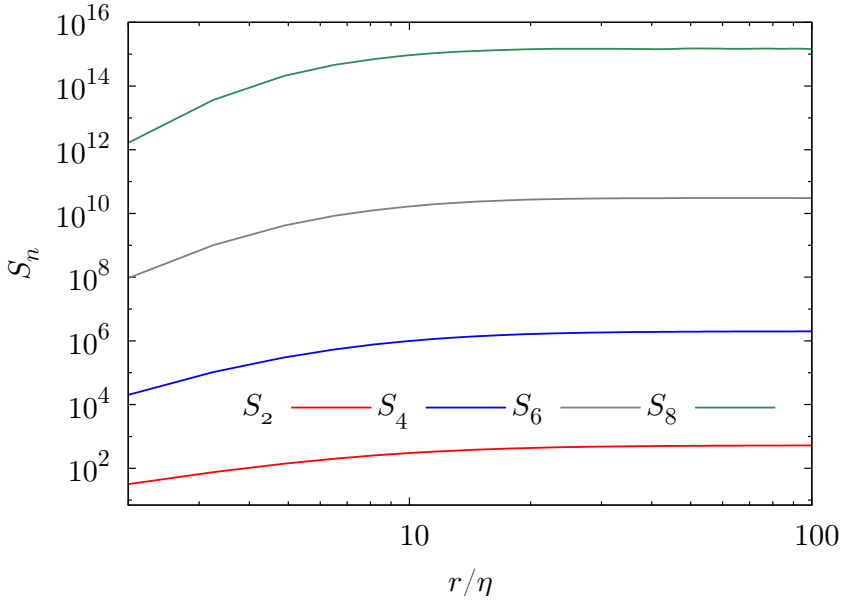

Figure 4.12.: Longitudinal vorticity structure functions. The structure functions saturate quickly, indicating that the vorticity is short-range correlated compared to the velocity (`sim_1024`).

that these quantities are particularly good measures for quantifying deviations from Gaussianity. The compensated cumulants are shown in figure 4.13 for three Reynolds numbers $R_\lambda \in \{76, 112, 225\}$. As already could be seen from figures 4.5 and 4.7, the velocity increment statistics is negatively skewed. The skewness seems to coincide for the smallest possible distances and tends to zero as the integral length scale is approached. The vanishing skewness for large length scales basically indicates that the single-point velocity PDF is symmetric. This interpretation is possible, as for large separations, where the two-point PDF of velocity becomes statistically independent, the increment PDF is the convolution of the single-point PDF. Turning to the kurtosis or flatness, this quantity decreases rapidly for small separations from highly non-Gaussian values, something which is often referred to as small-scale intermittency. The kurtosis increases as a function of Reynolds number, showing that deviations from Gaussianity increase with the Reynolds number. For integral separations the kurtosis drops below zero, indicating that the single-point velocity PDF will exhibit sub-Gaussian tails. Interestingly, this feature can already be observed in the measurements by Townsend presented in [Bat53], but up to today is subject to intense discussions.

Skewness and kurtosis are also evaluated for the transversal velocity increments in figure 4.14. As already indicated in figure 4.6 the skewness of this quantity vanishes. The kurtosis, however, takes higher values than in the case of the longitudinal increments, i.e., deviations from Gaussianity are stronger. As for the longitudinal velocity increments, these deviations increase with Reynolds number.

Finally, we present K_3 and K_4 for the longitudinal vorticity increments in figure 4.15. Here, also the skewness vanishes, as the vorticity increment PDFs are symmetric. The kurtosis decays rapidly from large values to an approximately constant behavior, which already has been highlighted in the discussion of the structure functions.

4.2. Eulerian Two-Point Correlations: Kinematic Relations and DNS Results

In this section we want to take a closer look at Eulerian two-point correlation functions. It turns out that relations for correlation functions of the velocity, vorticity and the velocity gradient tensor can be derived making use of the kinematics of solenoidal fields. We have already seen in chapter 2.3 how homogeneous isotropic turbulence allows to establish kinematic relations. It was shown that the longitudinal and transversal correlation functions of the two-point covariance tensor

$$R_{ij}^u(\boldsymbol{r}) = \langle u_i(\boldsymbol{x}_1)\, u_j(\boldsymbol{x}_2)\rangle = \frac{\langle \boldsymbol{u}^2\rangle}{3}\left[g_u\,\delta_{ij} + (f_u - g_u)\,\frac{r_i r_j}{r^2}\right] \tag{4.8}$$

obey the simple relation

$$g_u(r) = f_u(r) + \frac{1}{2} r f_u'(r) \quad , \tag{4.9}$$

which can be shown by exploiting solenoidality of R_{ij}^u. The longitudinal and transversal correlation functions can be used to define the corresponding integral length scales, e.g.,

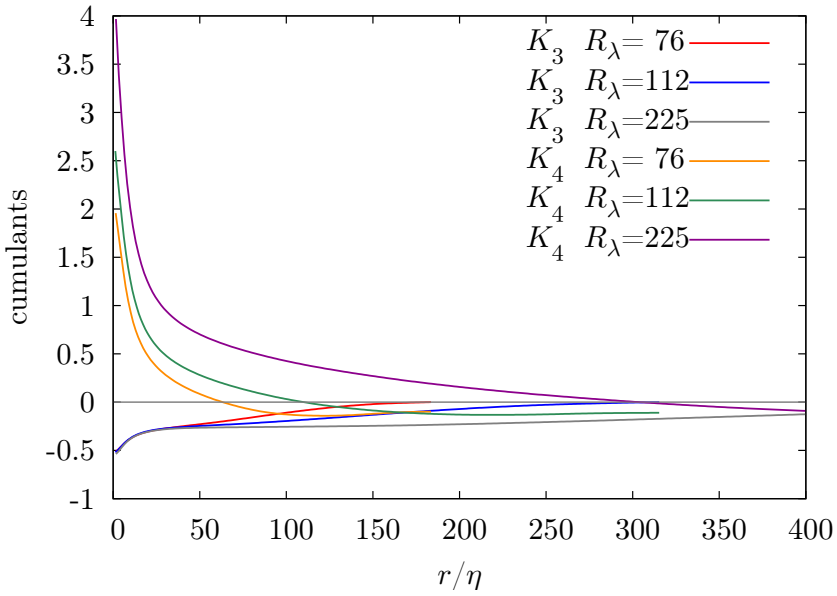

Figure 4.13.: Third and fourth cumulants for the longitudinal velocity increment at three different Reynolds numbers (`sim_256`, `sim_512`, `sim_1024_ext`).

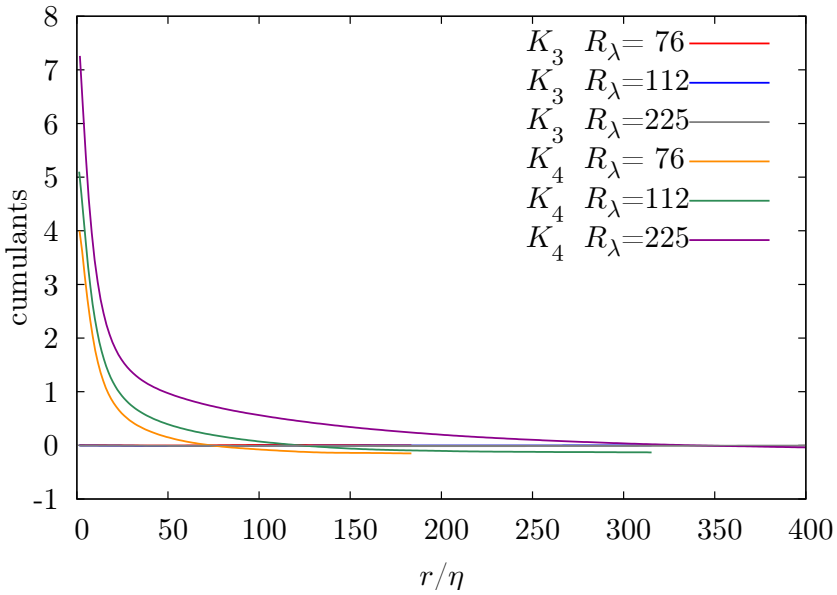

Figure 4.14.: Third and fourth cumulants for the transversal velocity increment at three different Reynolds numbers (`sim_256`, `sim_512`, `sim_1024_ext`).

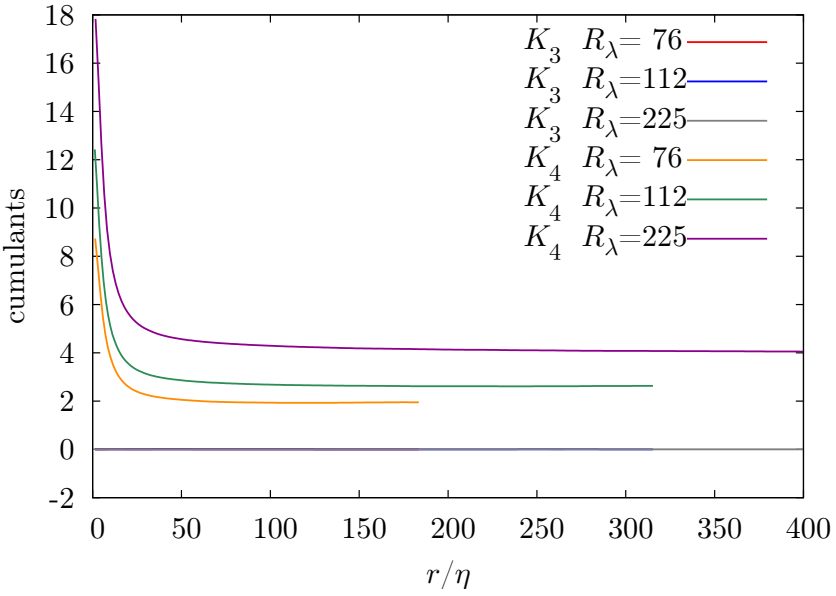

Figure 4.15.: Third and fourth cumulants for the longitudinal vorticity increment at three different Reynolds numbers (`sim_256`, `sim_512`, `sim_1024`).

the longitudinal integral length scale of the velocity is given by

$$L_{u,l} = \int_0^\infty \mathrm{d}r\, f_u(r) \quad . \tag{4.10}$$

Because of equation (4.9) the transversal integral length scale is not independent, however, by integration by parts we find the simple relationship

$$L_{u,t} = \int_0^\infty \mathrm{d}r\, g_u(r) = \int_0^\infty \mathrm{d}r\, \left(f_u(r) + \frac{1}{2} r f_u'(r) \right) = \frac{1}{2} L_{u,l} \quad . \tag{4.11}$$

We now want to establish further kinematic relations for the vorticity. To this end we first consider the two-point vorticity covariance tensor

$$R_{ij}^\omega(\boldsymbol{r}) = \langle \omega_i(\boldsymbol{x}_1)\, \omega_j(\boldsymbol{x}_2) \rangle = \frac{\langle \boldsymbol{\omega}^2 \rangle}{3} \left[g_\omega\, \delta_{ij} + (f_\omega - g_\omega)\, \frac{r_i r_j}{r^2} \right] \quad . \tag{4.12}$$

As also the vorticity field is solenoidal, we of course find the two correlation functions to be related according to

$$g_\omega(r) = f_\omega(r) + \frac{1}{2} r f_\omega'(r) \tag{4.13}$$

like in the case of the velocity covariance tensor. Furthermore, it is possible to establish a relation between the velocity correlations and the vorticity correlations as the vorticity

covariance tensor can be obtained from the velocity covariance tensor by taking the curl,

$$\begin{aligned} R^{\omega}_{ij}(\boldsymbol{r}) &= \epsilon_{ikl}\,\epsilon_{jmn}\,\frac{\partial}{\partial x_{1,k}}\,\frac{\partial}{\partial x_{2,m}}\,\langle u_l(\boldsymbol{x}_1)\,u_n(\boldsymbol{x}_2)\rangle \\ &= -\epsilon_{ikl}\,\epsilon_{jmn}\,\frac{\partial}{\partial r_k}\,\frac{\partial}{\partial r_m}\,R^{u}_{ln}(\boldsymbol{r}) \\ &= -\delta_{ij}\Delta R^{u}_{ll}(\boldsymbol{r}) + \frac{\partial^2}{\partial r_i \partial r_j} R^{u}_{ll}(\boldsymbol{r}) + \Delta R^{u}_{ij} \quad , \end{aligned} \tag{4.14}$$

a result, which has already been presented in [Bat53]. By explicitly evaluating the differentiation of the covariance tensor, this relation can be used to relate the correlation functions f_u and f_ω. And although these calculations likely have been carried out in the past, the author is not aware of any reference with the resulting relations. The calculation is straightforward and mainly involves book keeping and using the relation (4.9). The result reads

$$f_\omega(r) = \frac{\langle \boldsymbol{u}^2\rangle}{\langle \boldsymbol{\omega}^2\rangle}\left[-\frac{4}{r}f'_u(r) - f''_u(r)\right] \tag{4.15a}$$

$$g_\omega(r) = \frac{\langle \boldsymbol{u}^2\rangle}{\langle \boldsymbol{\omega}^2\rangle}\left[-\frac{2}{r}f'_u(r) - 3f''_u(r) - \frac{1}{2}r f'''_u(r)\right] \quad , \tag{4.15b}$$

showing that the full vorticity covariance tensor can be written as a function of the longitudinal velocity autocorrelation function only. It is readily checked that these relations also fulfill equation (4.13). It is furthermore evident that the integral length scales of the vorticity can be determined from the longitudinal velocity correlation function.

We now put this reasoning one step further and consider the two-point correlation tensor of the velocity gradients

$$R^{\mathrm{A}}_{ijkl}(\boldsymbol{r}) = \langle A_{ik}(\boldsymbol{x}_1)A_{jl}(\boldsymbol{x}_2)\rangle \quad . \tag{4.16}$$

Being a fourth-order tensor, its general structure will be of the form

$$\begin{aligned} R^{\mathrm{A}}_{ijkl}(\boldsymbol{r}) = {} & a_1\,\delta_{ik}\delta_{jl} + a_2\,\delta_{ij}\delta_{kl} + a_3\,\delta_{il}\delta_{jk} + a_4\,\delta_{ik}\frac{r_j r_l}{r^2} + a_5\,\delta_{jl}\frac{r_i r_k}{r^2} \\ & + a_6\,\delta_{ij}\frac{r_k r_l}{r^2} + a_7\,\delta_{kl}\frac{r_i r_j}{r^2} + a_8\,\delta_{il}\frac{r_j r_k}{r^2} + a_9\,\delta_{jk}\frac{r_i r_l}{r^2} + a_{10}\,\frac{r_i r_j r_k r_l}{r^4} \quad , \end{aligned} \tag{4.17}$$

where the prefactors $a_i(r)$ depend all on the absolute value of the distance vector. Because of solenoidality not all of the scalar functions are independent. We have the relations

$$\begin{aligned} R^{\mathrm{A}}_{ikjk}(\boldsymbol{r}) &= \big(3a_1 + a_2 + a_3 + a_4\big)\,\delta_{ij} + \big(3a_5 + a_6 + a_7 + a_8 + a_9 + a_{10}\big)\,\frac{r_i r_j}{r^2} = 0 \\ R^{\mathrm{A}}_{kikj}(\boldsymbol{r}) &= \big(3a_1 + a_2 + a_3 + a_5\big)\,\delta_{ij} + \big(3a_4 + a_6 + a_7 + a_8 + a_9 + a_{10}\big)\,\frac{r_i r_j}{r^2} = 0\,, \end{aligned} \tag{4.18}$$

which implies that all of the brackets have to vanish independently. Now choosing $\boldsymbol{r} = r\boldsymbol{e}_1$ (i.e., the index 1 corresponds to the longitudinal direction, whereas the indices 2 and 3 denote the two transversal directions) allows to determine which correlations contribute to the prefactors a_i. One obtains

$$a_1 = R^{\mathrm{A}}_{2323} \tag{4.19a}$$
$$a_2 = R^{\mathrm{A}}_{2233} \tag{4.19b}$$
$$a_3 = R^{\mathrm{A}}_{2222} - R^{\mathrm{A}}_{2323} - R^{\mathrm{A}}_{2233} \tag{4.19c}$$
$$a_4 = R^{\mathrm{A}}_{2121} - R^{\mathrm{A}}_{2323} \tag{4.19d}$$
$$a_5 = R^{\mathrm{A}}_{1212} - R^{\mathrm{A}}_{2323} \tag{4.19e}$$
$$a_6 = R^{\mathrm{A}}_{2211} - R^{\mathrm{A}}_{2233} \tag{4.19f}$$
$$a_7 = R^{\mathrm{A}}_{1122} - R^{\mathrm{A}}_{2233} \tag{4.19g}$$
$$a_8 = R^{\mathrm{A}}_{2112} - R^{\mathrm{A}}_{2222} + R^{\mathrm{A}}_{2323} + R^{\mathrm{A}}_{2233} \tag{4.19h}$$
$$a_9 = R^{\mathrm{A}}_{1221} - R^{\mathrm{A}}_{2222} + R^{\mathrm{A}}_{2323} + R^{\mathrm{A}}_{2233} \tag{4.19i}$$
$$a_{10} = R^{\mathrm{A}}_{1111} + R^{\mathrm{A}}_{2222} - R^{\mathrm{A}}_{2121} - R^{\mathrm{A}}_{1212} - R^{\mathrm{A}}_{2211} - R^{\mathrm{A}}_{1122} - R^{\mathrm{A}}_{1221} - R^{\mathrm{A}}_{2112} \quad . \tag{4.19j}$$

Following the same steps as in the case of the vorticity, this whole tensor is now expressed in terms of the longitudinal velocity autocorrelation function. To this end we evaluate

$$\begin{aligned} R^{\mathrm{A}}_{ijkl}(\boldsymbol{r}) &= \frac{\partial}{\partial x_{1,k}} \frac{\partial}{\partial x_{2,l}} \left\langle u_i(\boldsymbol{x}_1)\, u_j(\boldsymbol{x}_2) \right\rangle \\ &= -\frac{\partial}{\partial r_k} \frac{\partial}{\partial r_l} R^u_{ij}(\boldsymbol{r}) \end{aligned} \tag{4.20}$$

and make use of the relation (4.9). After collecting all terms we arrive at

$$a_1 = a_3 = \frac{\langle \boldsymbol{u}^2 \rangle}{6} \left[\frac{f_u'}{r} \right] \tag{4.21a}$$
$$a_2 = \frac{\langle \boldsymbol{u}^2 \rangle}{6} \left[-3\frac{f_u'}{r} - f_u'' \right] \tag{4.21b}$$
$$a_4 = a_5 = a_7 = a_8 = a_9 = \frac{\langle \boldsymbol{u}^2 \rangle}{6} \left[-\frac{f_u'}{r} + f_u'' \right] \tag{4.21c}$$
$$a_6 = \frac{\langle \boldsymbol{u}^2 \rangle}{6} \left[3\frac{f_u'}{r} - 3f_u'' - r f_u''' \right] \tag{4.21d}$$
$$a_{10} = \frac{\langle \boldsymbol{u}^2 \rangle}{6} \left[3\frac{f_u'}{r} - 3f_u'' + r f_u''' \right] \quad . \tag{4.21e}$$

Combining the relations (4.19) and (4.21) now allows to obtain the expressions for arbitrary components of R^{A}_{ijkl} and for the corresponding normalized correlation functions.

For example, one easily obtains

$$f_{\mathrm{A},1111}(r) = \frac{R^{\mathrm{A}}_{1111}(r)}{R^{\mathrm{A}}_{1111}(0)} = -5\frac{\langle \boldsymbol{u}^2\rangle}{\langle \boldsymbol{\omega}^2\rangle} f_u'' \tag{4.22a}$$

$$f_{\mathrm{A},2323}(r) = \frac{R^{\mathrm{A}}_{2323}(r)}{R^{\mathrm{A}}_{2323}(0)} = -5\frac{\langle \boldsymbol{u}^2\rangle}{\langle \boldsymbol{\omega}^2\rangle} \frac{f_u'}{r} \tag{4.22b}$$

$$f_{\mathrm{A},2233}(r) = \frac{R^{\mathrm{A}}_{2233}(r)}{R^{\mathrm{A}}_{2233}(0)} = \frac{5}{4}\frac{\langle \boldsymbol{u}^2\rangle}{\langle \boldsymbol{\omega}^2\rangle} \left[-3\frac{f_u'}{r} - f_u''\right] \quad , \tag{4.22c}$$

to explicitly evaluate only a few ones. Although the calculations of these results are straightforward but somewhat exhaustive, the author here also is unaware of any reference in the literature. Apart from the fact that these considerations allow for a very simple characterization of the two-point correlations of the velocity gradients, further interesting results can be obtained. For example, we obtain for the integral length scale of R^{A}_{1111}

$$L_{\mathrm{A},1111} = \int_0^\infty \mathrm{d}r\, f_{\mathrm{A},1111}(r) = -5\frac{\langle \boldsymbol{u}^2\rangle}{\langle \boldsymbol{\omega}^2\rangle} \left[f_u'(r)\right]_\infty^0 = 0 \quad , \tag{4.23}$$

which, as this correlation should be non-vanishing pointwise, allows to conclude that this correlation will exhibit a zero-crossing.

All of these kinematic relations can now be checked numerically. To this end we compute the correlation functions of the velocity, vorticity and velocity gradient directly from the data obtained by DNS and compare them to the kinematic relations by numerically differentiating the longitudinal velocity autocorrelation function. Some of the results are shown in figure 4.16. The longitudinal velocity correlation function decays slowly as a function of distance, the transversal correlation function shows the characteristic zero-crossing, which has been repeatedly reported (see, e.g., [MY75]). Compared to that, the correlation functions of the vorticity and velocity gradient tensor decay more rapidly, indicating that these quantities vary on much shorter scales. Regarding the kinematic relations for the small-scale quantities, i.e., the vorticity and the velocity gradient tensor, a perfect agreement is found with the correlation function obtained directly by DNS. The correlation function $f_{\mathrm{A},1111}(r)$ displays the predicted zero-crossing at about 12η. The kinematic relation for the transversal velocity shows slight deviations at large scales, which may be accounted for slight large-scale anisotropies of the simulation `sim_512`. We close this section with the remark that similar relations can be obtained for Lagrangian correlation tensors. While in the case of Eulerian correlations we may interchange spatial derivatives with ensemble averages, in the case of Lagrangian correlations temporal derivatives commute with ensemble averaging.

4.3. A Comparison of Turbulent and Random Fields

Up to now we have presented a collection of quantities typically used to characterize the statistical properties of fully developed turbulence. To highlight the typical features

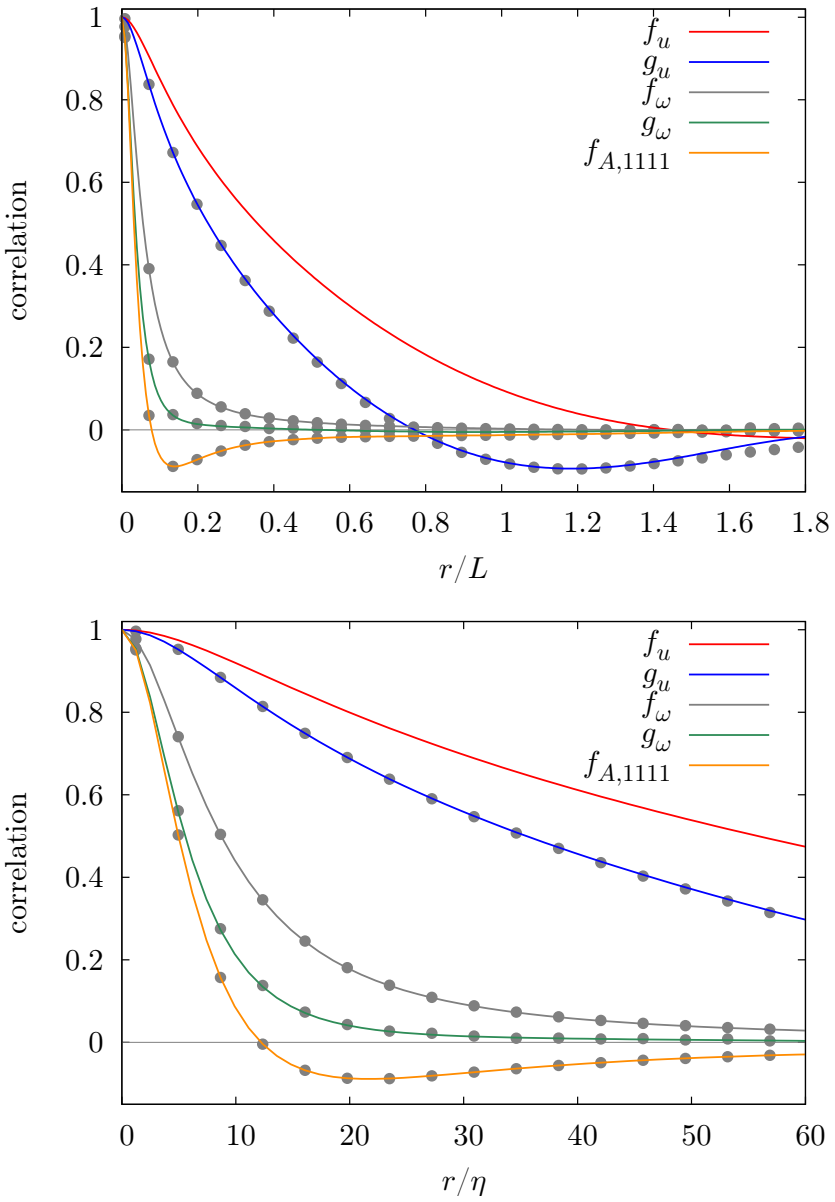

Figure 4.16.: Comparison of kinematic relations (points) with directly obtained DNS results (straight lines). The correlation functions for the vorticity and the velocity gradient tensor collapse perfectly with the correlation functions computed from the longitudinal velocity correlation function. Slight deviations are visible for the transversal velocity autocorrelation function, which may be accounted to large-scale anisotropies. The lower figure shows a zoom to clarify the behavior for small separations (`sim_512`).

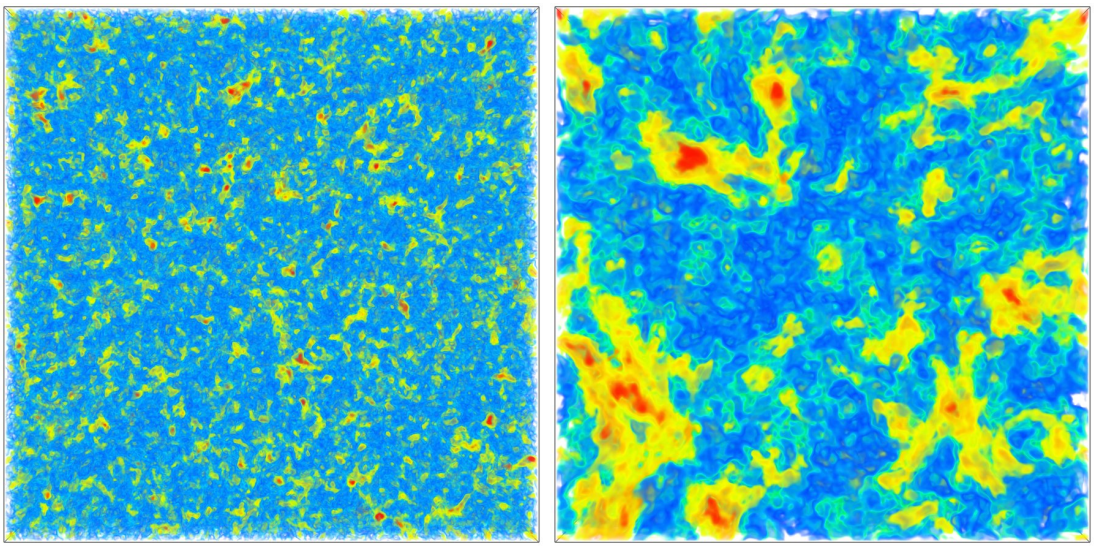

Figure 4.17.: Volume rendering of a randomized vorticity (left) and velocity field (right). The fields are the randomized versions of the fields presented in the upper panel of figure 1.1. The coherent structures of the vorticity field have vanished completely. However, it is still evident that the vorticity field varies on smaller scales than the velocity field.

of turbulence, it is useful to compare the results to the statistics of random fields, which are no solution of the Navier-Stokes equation. To this end we randomize a subensemble of the vorticity obtained in the simulation run `sim_512`.

4.3.1. Randomization Procedure

The randomization procedure makes use of the Fourier representation of the vorticity field

$$\boldsymbol{\omega}(\boldsymbol{x},t) = \frac{1}{(2\pi)^{\frac{3}{2}}} \sum_{\boldsymbol{k}} \tilde{\boldsymbol{\omega}}_{\boldsymbol{k}}(t)\, \mathrm{e}^{\mathrm{i}\boldsymbol{k}\cdot\boldsymbol{x}} \quad . \tag{4.24}$$

The vorticity field is real, which implies $\tilde{\boldsymbol{\omega}}_{-\boldsymbol{k}} = \tilde{\boldsymbol{\omega}}^*_{\boldsymbol{k}}$, and solenoidal, which means $\mathrm{i}\boldsymbol{k}\cdot\tilde{\boldsymbol{\omega}}_k = 0$. The randomization now is achieved by adding statistically independent, uniformly distributed random phases $\varphi_{\boldsymbol{k}}$ to each Fourier mode

$$\boldsymbol{\omega}^r(\boldsymbol{x},t) = \frac{1}{(2\pi)^{\frac{3}{2}}} \sum_{\boldsymbol{k}} \tilde{\boldsymbol{\omega}}_{\boldsymbol{k}}(t)\, \mathrm{e}^{\mathrm{i}(\boldsymbol{k}\cdot\boldsymbol{x}+\varphi_{\boldsymbol{k}})} \quad . \tag{4.25}$$

As the resulting field should be real, we have to impose $\varphi_{\boldsymbol{k}} = -\varphi_{-\boldsymbol{k}}$. Solenoidality is preserved by this transformation. The interesting property of this randomization procedure now is that it destroys all phase correlations in the field, which implies that in real space the coherent structures are destroyed. However, phase-independent quantities, like, e.g., the energy spectrum are conserved.

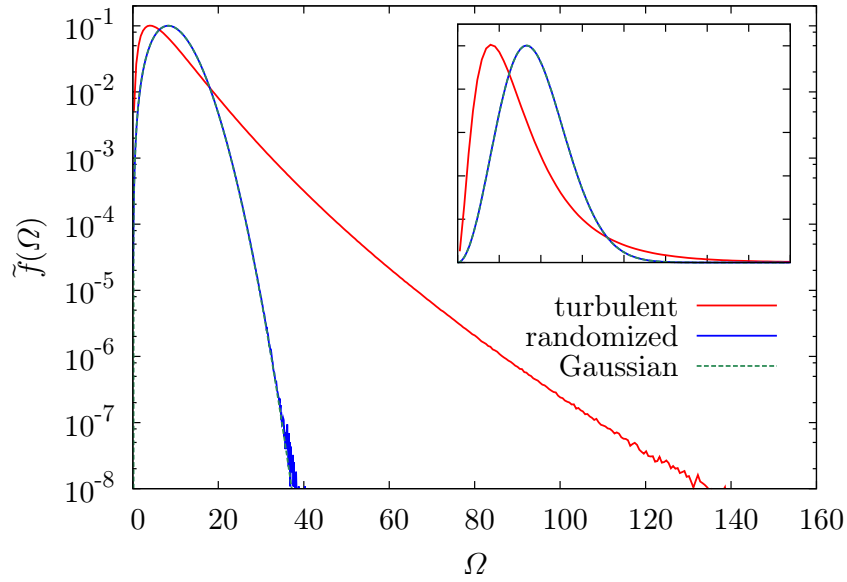

Figure 4.18.: Vorticity PDFs of turbulent and randomized fields. The randomized vorticity tends to a Gaussian distribution (`sim_512`).

To study velocity and velocity gradient statistics, the randomized velocity is obtained from the randomized vorticity by Biot-Savart's law

$$\boldsymbol{u}^r(\boldsymbol{x},t) = -\frac{1}{4\pi}\int \mathrm{d}\boldsymbol{x}' \, \frac{\boldsymbol{x}-\boldsymbol{x}'}{|\boldsymbol{x}-\boldsymbol{x}'|^3} \times \boldsymbol{\omega}^r(\boldsymbol{x}',t) \quad , \tag{4.26}$$

and the velocity gradient tensor is obtained by subsequent differentiation, $\mathrm{A}^r = \nabla \boldsymbol{u}^r$. It is now possible to study the statistics of typical turbulent properties in the case of the randomized fields.

4.3.2. DNS Results

Before turning to the statistical evaluation of the randomized fields, a visualization of the vorticity and velocity fields is shown in figure 4.17. The fields display the randomized version of the corresponding fields shown in chapter 1 in figure 1.1. A comparison of the vorticity field reveals that any signature of coherent structures is lost, no filamentary structures are visible in the randomized field. The field consists of fine blobs, where high and low values of vorticity are homogeneously distributed in space. The same goes for the velocity field, which, however, exhibits much slower decaying correlations. This comes due to the fact that the randomization procedure preserves the correlation tensors. The randomized velocity field is comparably similar to the turbulent velocity field shown in chapter 1, however, one can see that the fine-scale structure related to

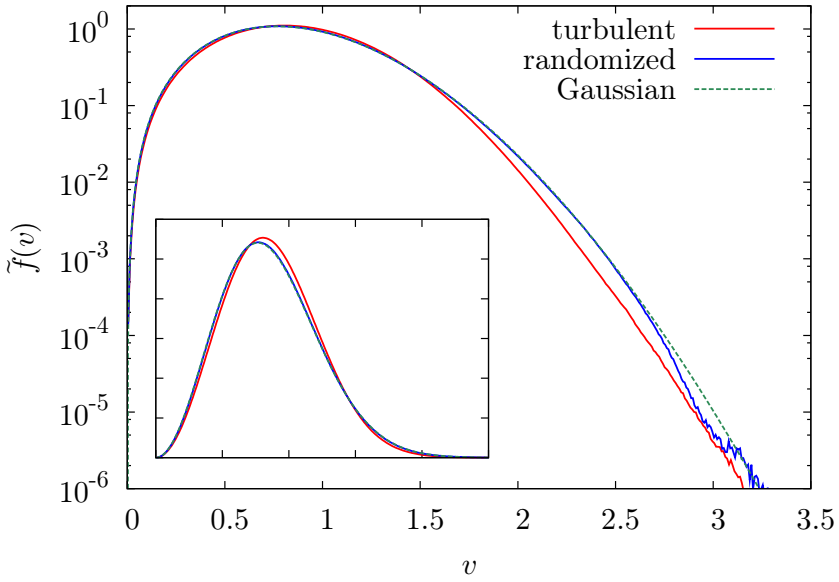

Figure 4.19.: Velocity PDFs of turbulent and randomized fields. In the randomized case the PDF is almost perfectly Gaussian, the sub-Gaussian behavior, as observed for the turbulent fields, vanishes (`sim_512`).

the gradients of the velocity is different. Gradients appear to be steeper in the turbulent fields, a sign for the intermittency found in turbulence.

Coming to the single point PDFs, the randomization procedure produces an almost perfect Gaussian vorticity PDF as can be seen in figure 4.18. The highly non-Gaussian behavior with the pronounced tail has completely vanished. In this sense, the vanishing of the coherent structures goes along with a more Gaussian behavior of the statistics.

The velocity PDFs of the turbulent and random fields compare quite well, as can be seen in figure 4.19. The randomized case is almost perfectly Gaussian, slight deviations can be accounted to limited statistical quality. The sub-Gaussianity has completely vanished and therefore can be seen as a typical signature of fully developed turbulence.

The PDFs of the different components of the velocity gradient tensor are presented in figure 4.20. While the diagonal and off-diagonal components exhibit different variances, they are perfectly Gaussian. The skewed and strongly non-Gaussian behavior of the tails is absent an therefore can be seen as a signature of turbulence as well. Turning to the joint PDF of the invariants of the velocity gradient tensor shown in figure 4.21, some striking similarities to the turbulent case shown in figure 4.4 can be observed. First, the bulk of the PDF lies in the upper half-plane and has a characteristic oval shape. Second, the Viellefosse line is also related to kinks in the isolines of the PDF in the lower half-plane. However, the joint PDF has much more rapidly decaying tails as compared to the turbulent case. Furthermore, any asymmetries regarding a reflection

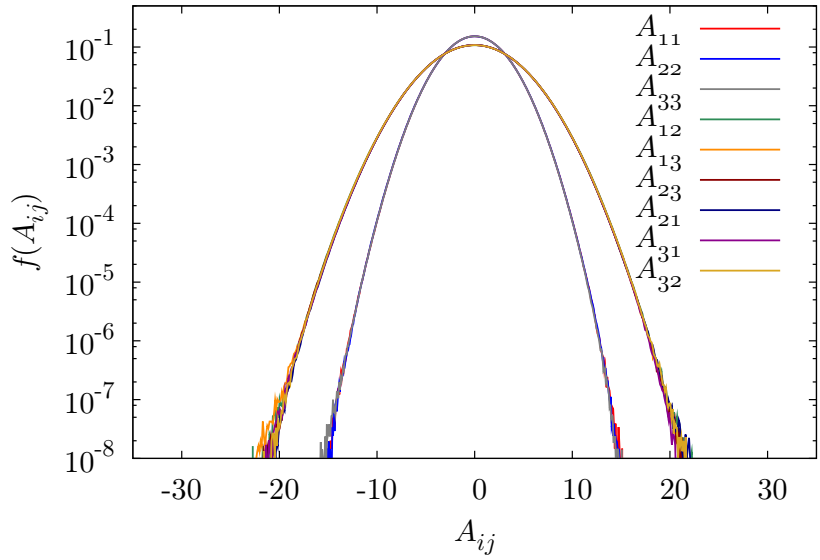

Figure 4.20.: PDFs of the velocity gradient tensor in randomized fields. As in the turbulent case, the diagonal components display a differing variance than the off-diagonal components. However, they become perfectly Gaussian (`sim_512`).

$R^* \mapsto -R^*$, distinctly present in the case of turbulent fields, vanish in the statistics of the randomized fields. Hence, the conclusion here is that while the gross features of the PDF survive for a randomized field, the asymmetry and pronounced tails are features typical for turbulent flows.

Our statistical analysis is completed by an investigation of the longitudinal velocity increment PDFs. As the velocity gradient is found to be Gaussian on the small scales and also the single-point velocity PDF exhibits a Gaussian shape, it is not surprising that also the velocity increment PDFs are found to be Gaussian and evolve perfectly self-similar in scale, as can be seen from figure 4.22. Hence the randomization procedure has destroyed any signature of intermittency. This diagnosis is also supported by figure 4.23, where the skewness and kurtosis are shown for both turbulent and randomized fields. As can be expected from the velocity increment PDFs, the randomized fields yield Gaussian values for the skewness and kurtosis across the scales.

4.3.3. Discussion

In conclusion, we have obtained Gaussian fields by randomizing the vorticity field. Gaussianity can be motivated from the fact that, for a fixed spatial position $\boldsymbol{x}$, equation (4.25) represents a sum of independent random variables with finite variances, such that the central limit theorem applies. By destroying all phase correlations in Fourier space, any sign of coherence is lost in real space, the filamentary vortex structures

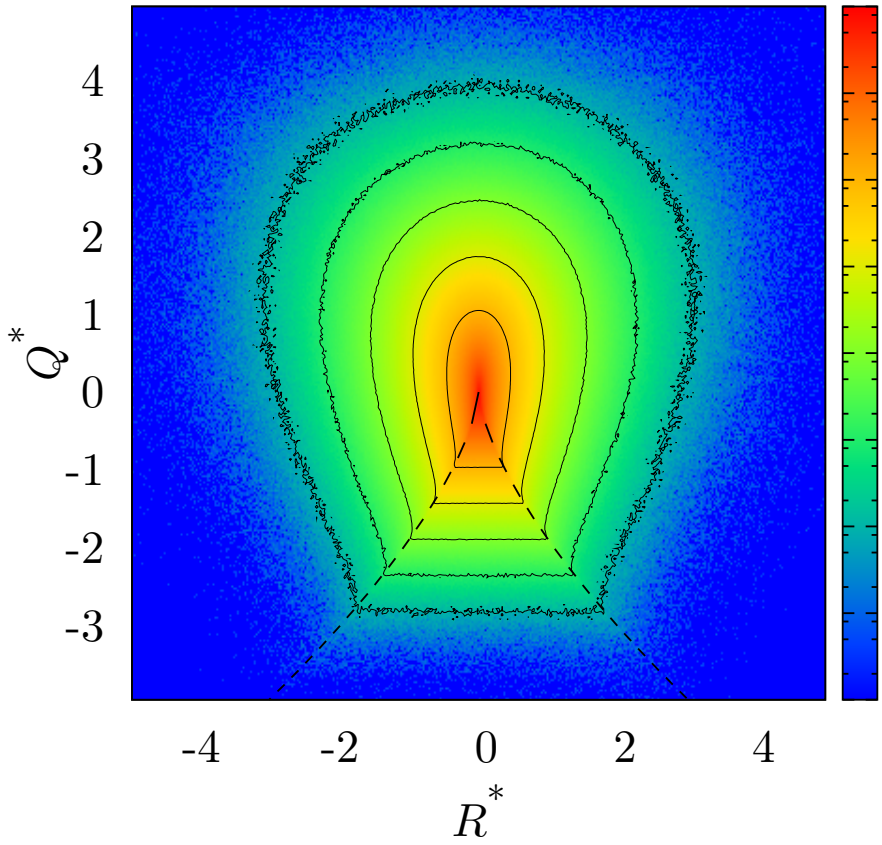

Figure 4.21.: Joint PDF of the velocity gradient tensor invariants for randomized fields. As for turbulent fields, the round shape in the upper half-plane is preserved and the bulk of the PDF lies in swirling regions in the flow. The isolines of the PDF also display kinks at the crossing with the Viellefosse line. However, the PDF displays much less pronounced tails and asymmetries have vanished (`sim_512`).

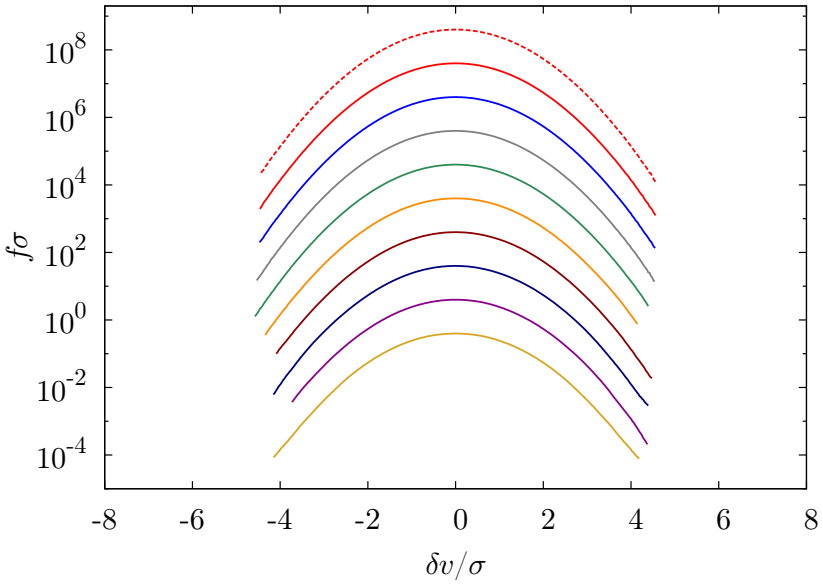

Figure 4.22.: Longitudinal velocity increment PDFs for randomized fields as a function of scale for $r \in \{1.2, 2.5, 4.9, 9.9, 19.8, 39.6, 79.1, 158.3, 316.6\}\,\eta$ (straight lines, from top to bottom). The dashed line corresponds to the PDF of a diagonal component of A. The PDFs evolve self-similar in scale (`sim_512`).

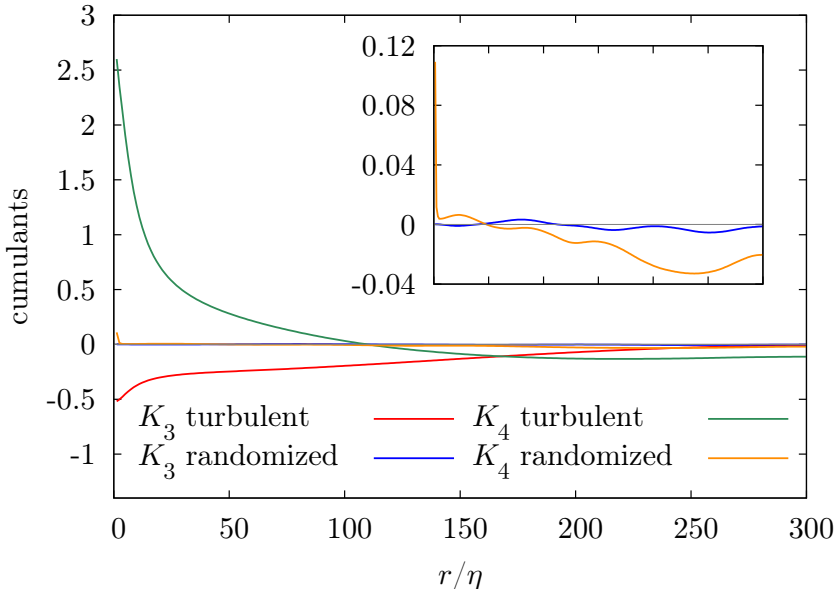

Figure 4.23.: Third and fourth cumulant for the longitudinal velocity increment in the case of turbulent and randomized fields. The cumulants of the randomized fields indicate a self-similar evolution in scale, any sign for intermittency present in turbulent fields, has vanished (`sim_512`).

vanish. In this sense this approach shows that non-Gaussian, non-self-similar statistics are related to the presence of the coherent structures. More precisely, it is evident that localized structures, which correspond to locally steep gradients are responsible for highly non-Gaussian values of, e.g., the flatness.

Admittedly, the presented approach may seem rather naïve and the results pretty obvious. Still, we think that the comparison is quite instructive as it helps to distinguish features that are typical for turbulent fields from features that are not. The investigation of the invariants of the velocity gradient tensor serves as a particularly suited example. Its investigation in randomized fields shows some remarkable similarities to real turbulent fields, such that it can be concluded that the typical features of turbulence are mirrored by the pronounced tails of the PDF and the strong asymmetries present.

4.4. DNS vs. Experiments

We close this chapter with a comparison of turbulence data sets obtained by experiments and numerics. The aim is to provide some benchmark results to convince that the statistical properties observed in direct numerical simulations to a good extent resemble the properties found in "real" experiments. We start with a discussions of the advantages and shortcomings of experiments and numerical simulations.

4.4.1. Pros and Cons for Experiments and DNS

Probably the most important argument in favor of turbulence experiments, of course, is that they undoubtedly represent "real" turbulence. For example, on the most fundamental level one can ascertain that experiments do not rely on the validity of the Navier-Stokes equation, which sometimes is discussed as these equations are derived assuming a number of material properties. And since some fundamental mathematical properties of this nonlinear, nonlocal equation remain to be understood, it is undoubtedly an advantage to compare to experimental results independent of this. Moreover, experiments are usually equipped with "natural" boundary conditions; the flow is usually limited by walls and turbulence is generated, e.g., by a mean flow passing a grid. This, of course, is at the same time a limitation to experiments, when trying to prepare the idealized case of homogeneous isotropic turbulence.

As we have seen in chapter 3, the Reynolds number achievable in numerical simulations is severely limited by the computational power available. The Reynolds numbers reached in turbulence experiments is usually much higher compared to that. While it is no fundamental problem to create a high Reynolds number flow in the laboratory, the Reynolds number accessible in experiments is still limited. This comes due to limitations of the sensors used, which have a finite spatial and temporal resolution and only yield reliable results in a certain range of velocities. This will become more clear in the following section. And although non-intrusive measurement techniques are available, measuring turbulent flow by placing a hot-wire anemometer in the flow remains the predominant Eulerian measurement technique for a number of technical reasons. This, however,

instantly brings up the problem that the flow will be disturbed by the sensor. While this is no problem for setups with a single sensor, it constrains the possibility to perform true two-point measurements. Furthermore, the sensors have to be calibrated carefully in order to measure the true velocity signal in the flow. For two-point measurements one usually relies on Taylor's frozen eddy hypothesis, which is only valid at comparably low turbulence intensities. Apart from the challenging technical demands on the sensors, data acquisition may restrict the measurements as both the length of the recorded time series as well as its sampling rate are limited by the hardware used.

Coming to direct numerical simulations of turbulence, one main advantage is that the "experimental" conditions are almost perfectly controllable and the numerical experiments performed are to a good extent reproducible. Maybe even more important, any quantity that can be calculated from the velocity field is available, such that observables inaccessible in experiments can be obtained by direct numerical simulations. Furthermore, as the full spatio-temporal record of the flow is available, any measurement configuration involving multiple points in space or time is accessible without disturbing the flow. At the same time the data sets obtained in simulations are usually much larger than the ones obtained in experiments allowing for an increased statistical quality. This, for example, allows for an investigation of the rare events that govern the tails of the PDFs.

On the other side, numerical simulations rely on the validity of the Navier-Stokes equations, as already mentioned above. A maybe more severe disadvantage is that the boundary conditions are usually unrealistic. The results presented in this thesis make use of periodic boundary conditions, something which is not met in reality. However, when the simulations are performed with care, the influence of the boundary conditions is well-controlled. Furthermore, to drive the flow into a statistically steady state, a forcing term has to be added to the Navier-Stokes equation as discussed in chapter 3. There it was made clear that these forcing methods are rather artificial, not resembling something like, for example, a grid generating the turbulence. This is why results are sometimes doubted and believed to be spoilt by the forcing techniques. By implementing and testing various different forcing methods, however, the influence of the forcing methods is characterizable.

As already stated, the Reynolds numbers accessible in DNS usually are lower than in experiments. And while numerics is far away from reaching the Reynolds numbers of real world flows, an overlap with laboratory experiments is available for a couple of decades now, allowing for a quantitative comparison of results.

In conclusion, experiments and direct numerical simulations should not be seen as opposing rivals, but rather as complementary approaches with complementary advantages and disadvantages.

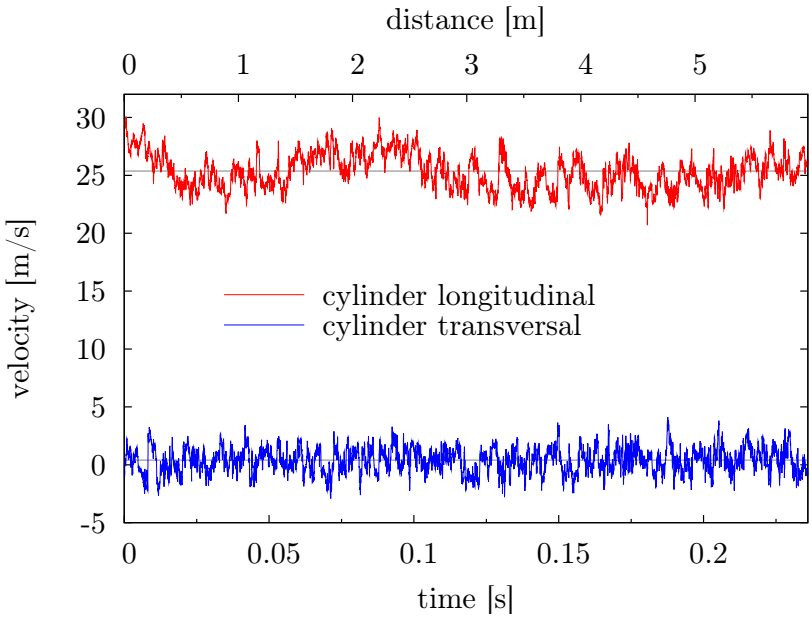

Figure 4.24.: Snapshot from an experimental longitudinal and transversal velocity time series from a cylinder wake. The longitudinal velocity component displays a pronounced mean flow and a slightly increased standard deviation. The lower x-axis indicates the actual temporal measurement, whereas the upper x-axis indicates the corresponding distance according to the Taylor frozen eddy hypothesis.

4.4.2. Some Words on Experimental Measurement Techniques

This being a theoretical work, we surely do not seek for a comprehensive characterization of the measurement techniques used in turbulence experiments. However, we would like to give a short overview how the experimental data sets presented in the following sections are obtained. We refer the reader to [Lüc01, RPF01, Ren02] for a detailed characterization of the measurements and to [TYF07] for a comprehensive account on various measurement techniques.

Both data sets were measured using hot-wire anemometry, which provides a good spatial and temporal resolution of the measured flow fields. The basic setup is a heated wire which is exposed to the flow. Due to the flow the wire is cooled altering its resistance, which can be measured using a Wheatstone bridge. As this resistance, or equivalently a voltage, can be shown to be directly related to the flow velocity (see, e.g., [Lüc01]), one effectively measures the desired velocity of the flow. It is clear that careful calibration measurements have to be performed, so that the measured voltage represents the velocity. Furthermore, it is evident that the smallest structures resolved by this technique depend on the size of the wire and the processing speed of the instrumentation, which limits the accessible Reynolds number. When a single wire is exposed to the flow, one mainly measures the downstream component of the flow. When also transversal directions shall

	Re	R_λ	L [mm]	λ [mm]	η [mm]	u_{mean} $[\frac{\text{m}}{\text{s}}]$	u_{rms} $[\frac{\text{m}}{\text{s}}]$	s [Hz]
free jet	27000	190	67	6.6	0.25	2.26	0.38	8000
cylinder	–	338	–	3.8	0.10	25.37	1.36	84746

Table 4.1.: Major experimental parameters. Reynolds number Re, Reynolds number based on the Taylor micro scale R_λ, integral length scale L, Taylor micro scale λ, Kolmogorov length scale η, mean flow velocity u_{mean}, longitudinal root mean square velocity u_{rms}, sampling rate s.

be measured, more complicated setups with crossed wires (X-wire anemometry) have to be used. This, of course, increases the experimental complexity as for example mutual disturbances have to be avoided.

With this instrumentation it is possible to measure a time series of velocity at a single point in space. To obtain spatially resolved statistics, Taylor's frozen eddy hypothesis has to be used. This hypothesis is supposed to work in the case of low turbulence intensity, which is defined as

$$I = \frac{u_{\text{rms}}}{u_{\text{mean}}} \quad , \tag{4.27}$$

where u_{rms} denotes the root mean square of the turbulent velocity fluctuations and u_{mean} is the velocity of the mean flow. For low turbulence intensities the root mean square fluctuations of the turbulent velocity are small compared to the velocity of the mean flow. In that sense the actual flow pattern can be regarded as "frozen" when being advected past the probe. Let $u^{\text{me}}(x_0, t)$ denote the measured velocity signal of a single probe at the spatial position x_0. The reconstructed spatial velocity profile $u^{\text{re}}(x, t)$ of this component then can be calculated with Taylor's hypothesis according to

$$u^{\text{re}}(x, t) = u^{\text{me}}(x_0 + u_{\text{mean}}\, t, t) \quad . \tag{4.28}$$

As this relation only holds for low to moderate turbulence intensities, this is another experimental restriction on the accessible Reynolds number.

4.4.3. Reference Data Sets

Two experimental data sets have been provided by the group of Joachim Peinke at the University of Oldenburg, each consisting $1.25 \cdot 10^7$ data points. The first data set was measured by Christoph Renner in a free jet experiment at the University in Oldenburg. The experiment has been performed with air being released through the nozzle from a high pressure reservoir. A hot-wire anemometer has been placed in a distance of $125D$ behind the nozzle, where $D = 8$mm is the diameter of the nozzle. The spatial resolution of the anemometer has been 1.25mm at a maximal temporal resolution of 30kHz. Further downstream a grid relaminizes the flow in order to suppress flow-wall interactions. A detailed description of this experimental setup is found in [RPF01, Ren02]. The main experimental parameters are summed up in table 4.1.

The second data set has been obtained by Stephan Lück during a stay at the University of Erlangen. The experimental flow is a turbulent wake behind a cylinder in a wind tunnel. For this measurement a X-wire anemometer was placed $100D$ behind the cylinder with diameter $D = 2\text{cm}$, allowing for a measurement of both longitudinal and transversal velocity components. The anemometer used displays a spatial resolution of 0.5mm. Compared to the first data set, the mean flow is more than an order of magnitude larger and the Reynolds number is much larger making a higher sampling rate necessary in order to maintain a fine spatial resolution. Again, the main experimental parameters are summarized in table 4.1, and a detailed description of the experimental setting can be found in [Lüc01]. A snapshot from this data set is shown in figure 4.24, where the longitudinal and transversal velocity component of the velocity signal is shown. The longitudinal component displays an offset due to the mean flow of this experiment. Additionally this component has a slightly increased standard deviation, indicating that this flow is not perfectly isotropic. The lower x-axis is labelled with the actual time span of the measured signal, whereas the upper x-axis is labelled with the corresponding distance, which is calculated by application of Taylor's hypothesis. The longitudinal component of the velocity seems to be sweeping in time, which might be related to vortex structures created behind the cylinder. This comparably slow sweeping is absent for the transversal component.

One should note that the Reynolds numbers characterizing these experiments cannot directly be compared to the Reynolds numbers given for our numerical simulations. The reason for that is that the precise definitions differ. For instance, in experiments the integral length scale L usually is given by the geometrical extents of the particular experiments rather than by the relation (3.62). Furthermore, for the present experiments the Taylor-based Reynolds number has been obtained by explicitly determining the Taylor length scale rather than using the relation (3.65).

4.4.4. Comparison of Statistical Results

Coming to the statistical quantities obtained from these data sets, figure 4.25 shows the single-point velocity PDFs. While all PDFs are close to a Gaussian probability density, they differ in details. The PDF from the free jet data set exhibits a pronounced asymmetry, which may be related to anisotropies caused by the mean flow. Compared to that, the PDFs from the cylinder experiment are more symmetric, however, the longitudinal PDF has a slightly different shape than the transversal PDF. While the longitudinal PDF exhibits sub-Gaussian tails, the transversal PDF is closer to a Gaussian. This shows that the two directions are statistically not fully equivalent and can be regarded as a signature of anisotropy.

The correlation functions of these signals are shown in figure 4.26. They all show qualitatively the behavior already observed in figure 4.16. All correlation functions originate with zero slope in $r = 0$ as theoretically expected. For increasing separations the longitudinal velocity components show a region with an approximately exponential decay. Compared to that, the transversal component from the cylinder experiment

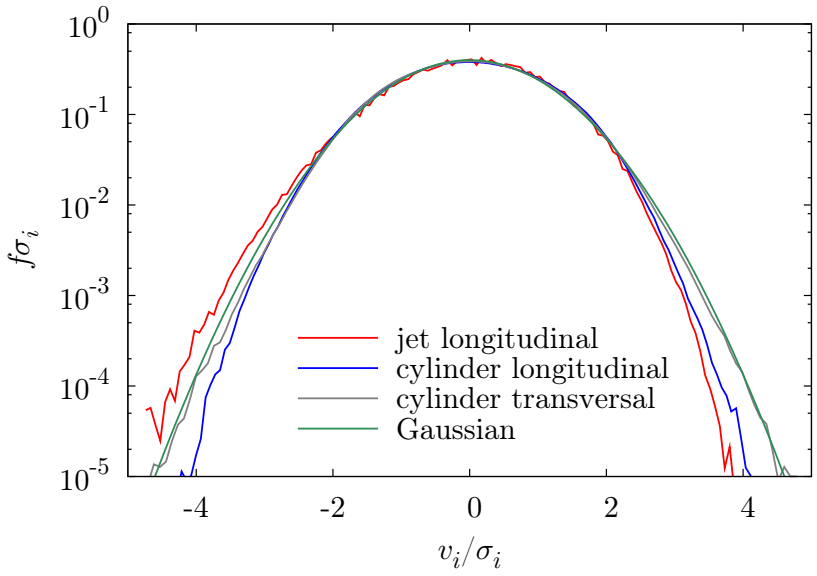

Figure 4.25.: Velocity PDFs from a free jet and a cylinder wake experiment. In the case of the free jet, the velocity PDF is asymmetric. The longitudinal component of the cylinder wake is slightly sub-Gaussian, whereas the transversal component has a more Gaussian shape.

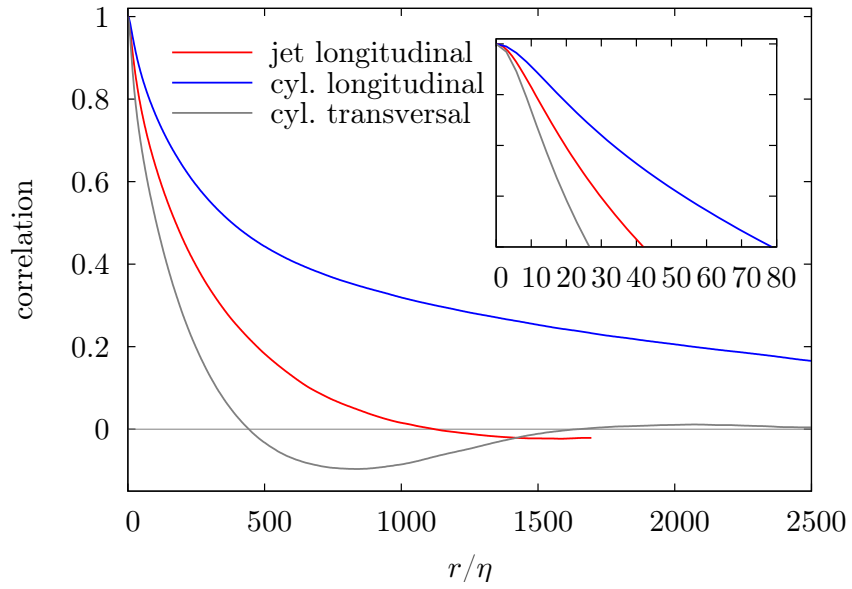

Figure 4.26.: Longitudinal and transversal velocity correlation functions from experimental data sets. The correlation functions behave similarly to the DNS results (see figure 4.16), the transversal components exhibits the characteristic zero-crossing. The inset highlights the behavior near zero.

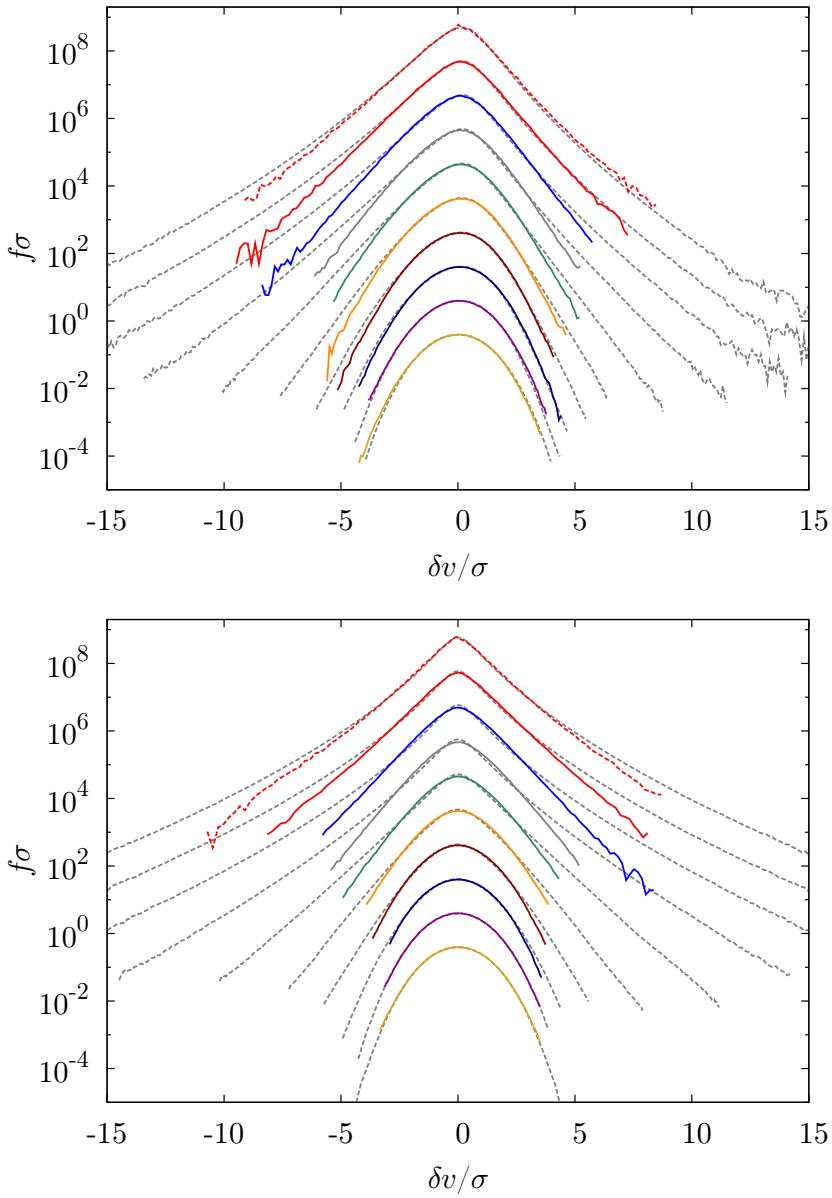

Figure 4.27.: Longitudinal and transversal velocity increment PDFs from the cylinder wake experiment as a function of scale for $r \in \{1.4, 2.8, 5.5, 10.4, 20.8, 41.6, 83.2, 166.5, 333.0\}\,\eta$ (straight lines, from top to bottom). The dashed red line corresponds to the PDF of the velocity gradient obtained by differentiation. The dashed gray lines correspond to the numerically obtained PDFs shown in figures 4.5 and 4.6 from the simulation `sim_512`. The PDFs correspond to approximately the same distances in scale, however, at a different Reynolds number.

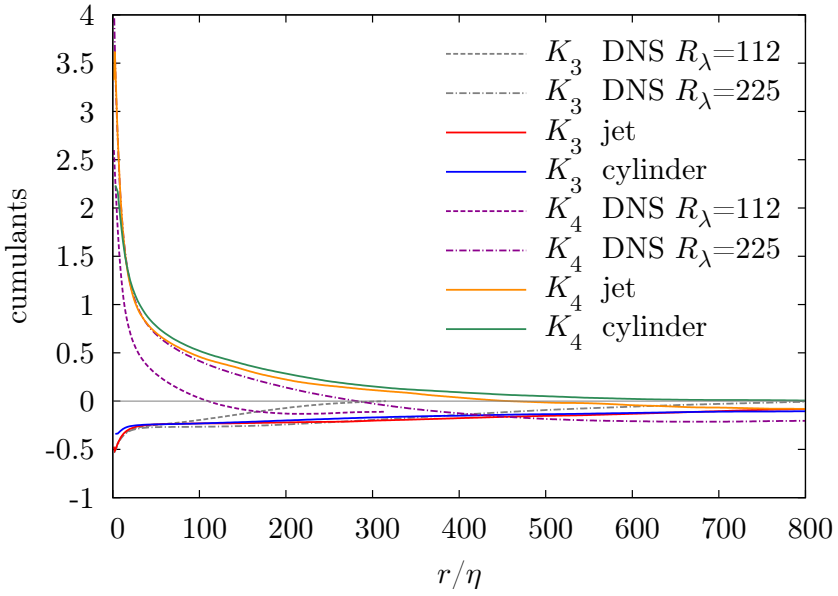

Figure 4.28.: Third and fourth longitudinal velocity cumulants for the jet and cylinder wake experiments. The dashed lines correspond to numerically obtained results from the simulations `sim_512` and `sim_1024_ext`.

exhibits the characteristic zero-crossing. However, the autocorrelations functions do not fulfill the relation (4.9), and it can be seen from the figure that also the integral length scales do not obey the simple relation (4.11), which is a hint on anisotropies of the flow. The differences in the statistical behavior could already be observed in the time series in figure 4.24 and in the velocity statistics in figure 4.25.

The velocity increment statistics of the cylinder experiment is shown in figure 4.27. The PDFs show the characteristic intermittent shape deformation from small scales to larger scales with the longitudinal component having a pronounced skewness. The numerically obtained velocity increment statistics at approximately the same spatial distances (in units of Kolmogorov length scales) already presented in figures 4.5 and 4.6 is drawn for comparison. It has to be stressed that the numerical simulation and the presented experimental result were obtained at very different Reynolds number in very different experimental settings, hence a collapse of the curves is not expected. Still, the PDFs show a remarkable similarity with the main features being robust. It appears especially from the transversal components that the PDFs from the numerical results have more slowly decaying tails, which is surprising in view of the lower Reynolds number. However, the statistical quality of the experimental data set does not allow for definite conclusions here. As it is quite easy to obtain large data sets with direct numerical simulations, the statistical quality here is more appropriate to study the far tails of the PDFs.

In order to draw further comparisons of the statistical evolution in scale, figure 4.28 shows the third- and fourth-order cumulants for the longitudinal velocities of the two experiments and two numerical simulations. The qualitative statistical features coincide; for example, all cumulants show a clear change beyond the dissipative range, where the slope strongly flattens. Being conducted, however, at very different Reynolds numbers in very different settings, the evolution in scale measured in multiples of the Kolmogorov length naturally differs. For example, the numerical simulations at low Reynolds numbers relax particularly fast to the stationary statistics as a clear separation of the smallest and largest scales in the flow is absent. Another interesting feature is that the behavior of the third-order cumulant does not differ as much over the different data sets as the fourth-order cumulant. It seems that the energy transfer mechanism between scales is more robust than the precise numerical values characterizing the flatness of the PDFs.

To conclude, the present section aimed at highlighting strengths and drawbacks of numerical and experimental investigations and to demonstrate the consistency of the statistical properties observed. Comparing data sets obtained in very different settings, the qualitative features like deviations from Gaussianity, spatial correlations and intermittency are found to be robust. It would be very interesting to perform joint experimental and numerical experiments with the goal to prepare more identical settings. For example, an experiment at moderate Reynolds number focussing on creating an isotropic flow could be compared in a more quantitative manner to numerical results.

5. Deterministic Aspects: the Burgers Equation

Apart from a few analytical solutions like the Lamb-Oseen or Burgers vortex, the Navier-Stokes equation is hardly accessible for a purely analytical treatment. Therefore it is of interest studying simplified models that maintain some features of the problem to a certain extent. One such model equation was introduced by Burgers [Bur39, Bur74], which up to today remains a well-studied equation in theoretical turbulence research. In this chapter we will study the n-dimensional inviscid Burgers equation taking focus on the velocity gradient evolution along Lagrangian trajectories. Although Burgers flows turn out to be very different from flows governed by the Navier-Stokes equation, we still think that the analytically obtained results are of interest when it comes to discuss the dynamics of incompressible flows.

5.1. The One-Dimensional Burgers Equation

The one-dimensional Burgers equation describes the evolution of a velocity field $u(x,t)$ on a line. The equation takes the form

$$\frac{\partial}{\partial t}u + u\frac{\partial}{\partial x}u = \nu\frac{\partial^2}{\partial x^2}u \quad , \tag{5.1}$$

showing a remarkable similarity to the Navier-Stokes equation (1.1); the velocity field is nonlinearly advected, and dissipation enters with the Laplacian of the velocity field. A huge difference, however, is the absence of the pressure gradient term, which for Navier-Stokes flows maintains the incompressibility according to equation (1.2). Thereby the nonlocality, which is the main mathematical difficulty in the case of the Navier-Stokes equation, is lacking. Apart from this being a strong simplification, one should note that studying incompressible flows on a line is somewhat boring. The Burgers equation models a perfectly compressible fluid, where any pressure-induced repulsive forces are absent. Typical compressible phenomena like the emergence of shocks hence can be observed in the dynamics of the Burgers equation.

An interesting property of the Burgers equation is that by introducing the transformation (found by Hopf and Cole in 1950 and 1951, respectively [Hop50, Col51])

$$u(x,t) = -2\nu\frac{\partial}{\partial x}\ln\varphi(x,t) \tag{5.2}$$

it is mapped onto the heat equation

$$\frac{\partial}{\partial t}\varphi = \nu \frac{\partial^2}{\partial x^2}\varphi \quad , \tag{5.3}$$

which, of course, can be solved analytically. Due to the nonlinear differential transformation, the solution for arbitrary initial conditions in general cannot be discussed easily. Still, having found a transformation onto a linear equation shows that the solutions of the Burgers equation are lacking any signature of chaoticity, something which is an important feature of the solutions of the Navier-Stokes equation. One can already conclude at this stage that the quadratic nonlinearity is not solely responsible for the complex dynamical behavior of turbulence, but nonlocal pressure contributions play an important role.

Solutions of the Burgers equation can also be discussed in the Lagrangian frame, for which the governing equations read

$$\frac{\mathrm{d}}{\mathrm{d}t}X(t,y) = [u(x,t)]_{x=X(t,y)} \tag{5.4a}$$

$$\frac{\mathrm{d}}{\mathrm{d}t}U(t,y) = \left[\nu \frac{\partial^2 u}{\partial x^2}(x,t)\right]_{x=X(t,y)} \quad . \tag{5.4b}$$

These equations, which describe the evolution of the field along a Lagrangian tracer particle, basically state that the particle moves with the velocity at its current position and is accelerated by viscous forces only. The pressure gradient, which strongly contributes to the Lagrangian particle acceleration in the case of incompressible flows, is absent.

5.2. Anomalies, Shocks and Singularities

Due to the viscous term on the right-hand side, kinetic energy is being dissipated in the course of the time. Multiplying equation (5.1) by u and averaging instantly yields the evolution of the kinetic energy $E_{\mathrm{kin}} = \langle \frac{1}{2}u^2 \rangle$. Assuming homogeneous statistics we obtain

$$\dot{E}_{\mathrm{kin}}(t) = -\langle \varepsilon(t) \rangle = -\nu \left\langle \left(\frac{\partial u}{\partial x}\right)^2 (x,t) \right\rangle \quad , \tag{5.5}$$

from which it is apparent that the rate of energy dissipation depends on the viscosity and the average of the squared velocity gradients. A case often studied in turbulence research is the limit of infinite Reynolds number, which is achieved by taking the limit $\nu \to 0$. If the velocity gradients remain finite in this limit, the kinetic energy will be a conserved quantity. However, we will see in the following that they diverge, which eventually causes a finite dissipation also in the case of vanishing viscosity. This fact, known as dissipation anomaly, is also often discussed in the case the of the Navier-Stokes equation at infinite Reynolds number.

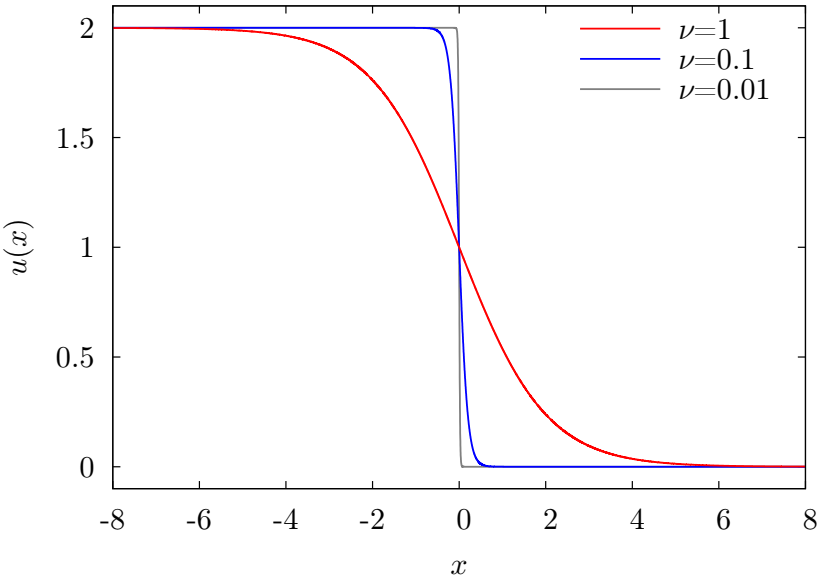

Figure 5.1.: Single shock solution (5.6) of the Burgers equation for $x_0 = 0$ and $u_0 = 1$ at $t = 0$. The slope of the shocks steepens with decreasing viscosity indicating a discontinuity of the velocity field in the limit of vanishing viscosity.

In the case of the Burgers equation the dissipation anomaly may be exemplified by considering the analytical solution

$$u(x,t) = u_0 \left[1 - \tanh\left(\frac{u_0(x - x_0 - u_0 t)}{2\nu}\right)\right] \quad , \tag{5.6}$$

which represents a travelling shock initially localized at x_0 travelling at the speed u_0. The slope of the shock depends besides the velocity on the viscosity as illustrated in figure 5.1, with decreasing viscosity the shock steepens. In the limit of vanishing viscosity the velocity field will eventually become discontinuous, and the velocity gradient diverges. If such a discontinuity develops from smooth initial conditions, this behavior is often referred to as a finite-time singularity. For finite viscosity we can calculate the dissipation field of the solution (5.6) obtaining

$$\varepsilon(x,t) = \nu \left(\frac{\partial u}{\partial x}\right)^2 (x,t) = u_0^4 \left[4\nu \cosh\left(\frac{u_0(x - x_0 - u_0 t)}{2\nu}\right)^4\right]^{-1} \quad . \tag{5.7}$$

The cumulative rate of energy dissipation of the whole field becomes independent both of time and viscosity,

$$\bar{\varepsilon} = \int_{-\infty}^{\infty} \mathrm{d}x\, \varepsilon(x,t) = \frac{2}{3} u_0^3 \quad , \tag{5.8}$$

demonstrating a finite rate of energy dissipation in the limit of vanishing viscosity.

Now having seen that the Burgers equation has an analytical shock solution, it is interesting to investigate its tendency to develop shock solutions from smooth initial conditions. To this end we consider the velocity gradient tensor evolution equation, which can be obtained from equation (5.1) by taking the spatial derivative. Defining the velocity derivative as $A = \frac{\partial u}{\partial x}$ we obtain

$$\frac{\partial}{\partial t}A + u\frac{\partial}{\partial x}A = -A^2 + \nu\frac{\partial^2}{\partial x^2}A \quad . \tag{5.9}$$

Apart from viscous diffusion and advection this equation explicitly reveals the self-amplification/depletion of the velocity gradient on the right-hand side of the equation. Now taking the limit of vanishing viscosity, we first notice that according to the equations (5.4) the Lagrangian acceleration along the trajectory of a fluid particle is zero, which allows to integrate the ordinary differential for the Lagrangian particle path yielding

$$X(t, y) = y + U(0, y)\, t \quad . \tag{5.10}$$

This so-called naïve Lagrangian map [BK07] shows that in smooth regions of the velocity field Lagrangian particle paths are straight lines. Studying the velocity gradient along these lines yields the ODE

$$\dot{A}(t, y) = -A^2(t, y) \quad , \tag{5.11}$$

which is solved by differentiating $1/A$. The solution is

$$A(t, y) = \frac{1}{\frac{1}{A(0,y)} + t} = \frac{A(0, y)}{1 + A(0, y)t} \tag{5.12}$$

and has a number of interesting properties. First of all, one can note that if $A(0) > 0$ the velocity gradient will decay over time, i.e., positives slopes will be depleted. If, however, $A(0) < 0$, the solution develops a singularity in finite time, negative velocity gradients will steepen and eventually diverge. Since the velocity gradient corresponds to the divergence of the velocity field, sources of the velocity field will decay over time while the sinks will be amplified and eventually diverge. The time the singularity develops is given by

$$t^*(y) = -\frac{1}{A(0, y)} \quad , \tag{5.13}$$

determining the moment of birth of a shock. Considering the whole field, the time

$$T^* = \min\{t^*(x) \,|\, x \in \mathbb{R}\} = \min\left\{ -\frac{1}{A(0, x)} \,\middle|\, x \in \mathbb{R} \right\} \tag{5.14}$$

indicates the time the first shock is born in the field. Steepening of the velocity gradients basically means that two "neighboring" fluid particles with differing velocities become closer and closer. The singularity happens when the two particle positions coincide. Consequently, the birth of a shock corresponds to the breakdown of the naïve Lagrangian

map (5.4). When two particle paths cross, this map becomes non-invertible. It can be shown, but also motivated from the analytical solution (5.6), that the shock speed is given by a Rankine-Hugoniot condition, i.e., given by the arithmetic mean of the field taken infinitesimally left and right of the shock. This furthermore shows that in the moment the shock develops an acceleration acts on the fluid particle, giving further evidence for the breakdown of the naïve Lagrangian map. Being related to the change of velocity along the fluid particles, one can see that shocks are related to dissipative events in the field.

Studying the velocity increment PDFs of fully developed three-dimensional turbulence, we have observed skewed velocity increment statistics in figures 4.5 and 4.7. In this context the one-dimensional Burgers equation may give a simple explanation of this observation: The different behavior of the velocity gradient depending on the sign of the initial value gives a dynamical picture how self-amplification or depletion of velocity gradients may cause skewed or more generally asymmetric velocity gradient and velocity increment statistics.

5.3. The Multi-Dimensional Burgers Equation

The Burgers equation can easily be generalized to higher dimensions, where it takes the form

$$\frac{\partial}{\partial t}\boldsymbol{u} + \boldsymbol{u}\cdot\nabla\boldsymbol{u} = \nu\Delta\boldsymbol{u} \quad . \tag{5.15}$$

The velocity field now is an n-dimensional vector. If the velocity field is potential, $\boldsymbol{u} = \nabla\varphi$, the problem can again be treated with the Hopf-Cole transformation, which is generalized to

$$\boldsymbol{u}(\boldsymbol{x},t) = -2\nu\nabla\ln\varphi(\boldsymbol{x},t) \quad , \tag{5.16}$$

which now, of course, leads to the heat equation in n dimensions

$$\frac{\partial}{\partial t}\varphi = \nu\Delta\varphi \quad . \tag{5.17}$$

For non-potential (i.e. rotational) initial conditions no closed general solution of the Burgers equation can be formulated. However, the qualitative behavior still can be discussed within the Lagrangian frame governed by

$$\frac{\mathrm{d}}{\mathrm{d}t}\boldsymbol{X}(t,\boldsymbol{y}) = \left[\boldsymbol{u}(\boldsymbol{x},t)\right]_{\boldsymbol{x}=\boldsymbol{X}(t,\boldsymbol{y})} \tag{5.18a}$$

$$\frac{\mathrm{d}}{\mathrm{d}t}\boldsymbol{U}(t,\boldsymbol{y}) = \left[\nu\Delta\boldsymbol{u}(\boldsymbol{x},t)\right]_{\boldsymbol{x}=\boldsymbol{X}(t,\boldsymbol{y})} \tag{5.18b}$$

describing the evolution of tracer particles in n dimensions. In the inviscid case the solution of these equations reads

$$\boldsymbol{X}(t,\boldsymbol{y}) = \boldsymbol{y} + \boldsymbol{U}(0,\boldsymbol{y})t \tag{5.19}$$

as in the one-dimensional case. Of course, this equation only holds, as long as the naïve Lagrangian map is valid. Whether the individual particle is overrun by a shock, depends on the initial configuration of the whole field and cannot be determined by this local consideration. Finding straight lines as Lagrangian particle paths outside the shocks shows that the dynamics is very different from incompressible flows. For two- and three-dimensional Navier-Stokes flows the presence of vorticity will induce spiraling motion to nearby trajectories. From the solution of the Lagrangian equations of motion it is clear that this behavior is not expected for compressible Burgers flows. The reason for this is that in the case of Navier-Stokes dynamics the vorticity fully determines the velocity field according to the Poisson equations (1.6) together with equation (1.5). In the case of the Burgers equation one additionally has to consider the temporal evolution of the divergence of the velocity field for a full specification. With the definition $P(\boldsymbol{x}, t) = \nabla \cdot \boldsymbol{u}(\boldsymbol{x}, t)$ we obtain its evolution equation by taking the divergence of equation (5.15). We find

$$\frac{\partial}{\partial t} P + \boldsymbol{u} \cdot \nabla P = -P^2 + \nu \Delta P \quad , \tag{5.20}$$

which has the same structure as the evolution of the velocity gradient for the one-dimensional Burgers equation (5.9). The presence of the self-amplification/depletion term on the right hand side is related to the emergence of shocks, as we will see in the following.

5.4. Lagrangian Velocity Gradient Evolution

After these introductory remarks into the phenomena encountered in a perfectly compressible flow, we now want to study the temporal evolution along Lagrangian tracer particles for the inviscid Burgers equation. As we have seen for the one-dimensional equation, taking the limit $\nu \to 0$ goes along with the emergence of finite-time singularities due to undamped steepening of velocity gradients. Although we will only obtain analytical solutions in the case of the inviscid limit, it can be expected from the considerations in the one-dimensional case that viscosity smoothens out the singularity and that the qualitative behavior of the inviscid case carries over to the viscid case.

5.4.1. Formal Solution and Breakdown of the Naïve Lagrangian Map

The consideration of the one-dimensional velocity gradient governed by the ODE (5.11) can be generalized to the multi-dimensional case in a straightforward manner. In this case the matrix-valued ordinary differential equation

$$\frac{\mathrm{d}}{\mathrm{d}t} \mathrm{A}(t, \boldsymbol{y}) = -\mathrm{A}(t, \boldsymbol{y})^2 \tag{5.21}$$

has to be solved. The solution involves the inverse of A. Without loss of generality we can assume the existence of A^{-1}, because if A is not invertible, we have $\det \mathrm{A} = 0$. As

we will see in the following sections, this corresponds to the case that the dynamics is restricted to a lower dimensionality. Hence we can always find A^{-1} by considering a lower-dimensional problem. As in the one-dimensional case, differentiating A^{-1} yields

$$\frac{\mathrm{d}}{\mathrm{d}t}\mathrm{A}^{-1} = -\mathrm{A}^{-2}\frac{\mathrm{d}}{\mathrm{d}t}\mathrm{A} = \mathrm{E} \quad , \tag{5.22}$$

where E denotes the unit matrix. This is easily integrated yielding

$$\mathrm{A}^{-1}(t, \boldsymbol{y}) = \mathrm{A}^{-1}(0, \boldsymbol{y}) + \mathrm{E}\, t \quad , \tag{5.23}$$

which by inversion yields the desired result

$$\mathrm{A}(t, \boldsymbol{y}) = (\mathrm{A}^{-1}(0, \boldsymbol{y}) + \mathrm{E}\, t)^{-1} \quad . \tag{5.24}$$

That means, the problem of solving equation (5.21) reduces to the inversion of matrix on the right-hand side of equation (5.24). While this may become a tedious task in arbitrary dimensions, we will present an alternative approach by examining the invariants of A later on. Of course, now the question has to be posed, whether $\mathrm{A}^{-1}(\boldsymbol{y}, 0) + \mathrm{E}\, t$ is invertible at all. This is not possible if

$$\det(\mathrm{A}^{-1}(0, \boldsymbol{y}) + \mathrm{E}\, t) = 0 \quad . \tag{5.25}$$

Introducing $\lambda = -t$ this equation is obviously related to the characteristic equation of A^{-1}. As a consequence, the negative real eigenvalue $\tilde{\lambda}_{\min}(\boldsymbol{y})$ of A^{-1} with the smallest absolute value defines the time at which the invertibility of $\mathrm{A}^{-1}(\boldsymbol{y}, 0) + \mathrm{E}\, t$ breaks down. This is exactly the time at which a shock is born. Taking the global minimum

$$\lambda_{\min} = \min_{\boldsymbol{x}} \left\{ \tilde{\lambda}_{\min}(\boldsymbol{x}) \middle| \boldsymbol{x} \in \mathbb{R}^n \right\} \tag{5.26}$$

identifies the global breakdown time of the naïve Lagrangian map. As the eigenvalues of A are the inverse eigenvalues of A^{-1}, the negative real eigenvalue of A with the largest absolute value determines this time. This is the extension to the one-dimensional observation, where the steepest slope of the velocity field (which simply is the only eigenvalue of the velocity gradient tensor in one dimension) determines the global breakdown time.

At this stage one should note that an extension beyond this time makes it necessary to replace the *naïve Lagrangian map* with the *proper Lagrangian map* for which we refer the reader to, e.g., [BK07] for further details. However, we will restrict our investigation in the following to the time before the first singularity appears.

In what follows, we will study the invariants of A, which we define in this context as the prefactors of the characteristic polynomial. As we have motivated in chapter 4.1, these objects are often studied in the case of the three-dimensional Navier-Stokes equation. Before investigating the ordinary differential equations for all the invariants, it is useful to consider the determinant of A as its evolution is closely related to the

above considerations. First of all, we define the characteristic polynomial of the matrix A according to

$$\Pi_{\mathrm{A}}(\lambda) = \det(\lambda \mathrm{E} - \mathrm{A}) \quad . \tag{5.27}$$

Additionally, the characteristic polynomial of a matrix is related to the characteristic polynomial of its inverse according to

$$\Pi_{\mathrm{A}^{-1}}(\lambda) = \frac{(-\lambda)^n}{\det \mathrm{A}} \Pi_{\mathrm{A}} \left(\frac{1}{\lambda} \right) \quad . \tag{5.28}$$

Taking the determinant of equation (5.24), this relation yields after some manipulation the temporal evolution of the determinant of A in terms of its characteristic polynomial,

$$\det \mathrm{A}(t) = \left[\frac{(-t)^n}{\det \mathrm{A}(0)} \Pi_{\mathrm{A}} \left(-\frac{1}{t} \right) \right]^{-1} \quad . \tag{5.29}$$

That means, we can quantify the temporal evolution of the determinant by knowledge of the characteristic polynomial and the initial conditions. As the characteristic polynomial involves all the invariants of the matrix, the temporal evolution of the determinant depends on the initial conditions of all of these quantities.

5.4.2. Evolution of the Velocity Gradient Tensor Invariants

For the physical discussion it is particularly useful to study the relevant cases of two and three dimensions first before we proceed to the general n-dimensional case.

Two-Dimensional Flows

We start with considering the two-dimensional case, for which the invariants are defined according to

$$P = \mathrm{Tr}\mathrm{A} \tag{5.30a}$$

$$Q = \frac{1}{2} \left((\mathrm{Tr}\mathrm{A})^2 - \mathrm{Tr}\mathrm{A}^2 \right) = \det \mathrm{A} \quad . \tag{5.30b}$$

As already indicated above, P corresponds to the divergence of the velocity field, where sinks are related to regions of developing shocks and sources correspond to regions from which fluid particles stream away. By decomposing the velocity gradient tensor into its symmetric and antisymmetric part, $\mathrm{A} = \mathrm{S} + \mathrm{W}$, the invariant Q can be expressed as $Q = \sigma_1 \sigma_2 + \frac{1}{4}\omega^2$, where σ_1 and σ_2 are the real eigenvalues of S and ω is the vorticity. In incompressible flows, where we always have $\sigma_1 \sigma_2 < 0$, an investigation of the sign of Q allows to discriminate strain dominated regions from regions of strong vorticity. In the case of compressible flows such a simple discrimination is unfortunately not possible.

With these definitions the characteristic polynomial of A takes the form

$$\lambda^2 - P\lambda + Q = 0 \quad . \tag{5.31}$$

We now want to study the dynamics of the velocity gradient tensor invariants. Due to the quadratic nonlinearity of the velocity gradient tensor evolution, third powers of the velocity gradient tensor appear in these calculations. These powers can be reduced with the help of Caley-Hamilton's theorem according to

$$\mathrm{A}^2 = P\mathrm{A} - Q\mathrm{E} \quad . \tag{5.32}$$

We now differentiate the definitions (5.30) with respect to time and exploit equation (5.32), finally obtaining a nonlinear system of ordinary differential equations

$$\dot{P} = 2Q - P^2 \tag{5.33a}$$

$$\dot{Q} = -PQ \quad . \tag{5.33b}$$

One can already see from these ordinary differential equations that if $Q(0) = 0$ the equations reduce to the one-dimensional case of (5.21), in which the 1×1 velocity gradient tensor is itself the only invariant. That means, a fluid particle starting in the $Q(0) = 0$–plane is confined to this plane forever. For non-vanishing Q a particle starting in the $P(0) = 0$–plane leaves this plane, indicating the compressible character of the Burgers dynamics.

Beyond this qualitative discussion one can find a general solution of this system by exploiting the relation (5.29) or differentiating $1/Q$ twice. The solution reads

$$P(t) = \frac{2t + a}{t^2 + at + b} \tag{5.34a}$$

$$Q(t) = \frac{1}{t^2 + at + b} \tag{5.34b}$$

with $a = P(0)/Q(0)$ and $b = 1/Q(0)$ being fixed by the initial conditions. As in the one-dimensional case, we find rational functions as solutions, however, with a higher degree as we are considering the two-dimensional case. Correspondingly, we can investigate the emergence of possible singularities by examining the zeros of the denominator (i.e., the poles of equation (5.34)) given by

$$t_{1,2} = \frac{-P(0) \pm \sqrt{P(0)^2 - 4Q(0)}}{2Q(0)} \quad . \tag{5.35}$$

Given an initial condition at $t = 0$ a singularity develops along the trajectory if there is a $t_{1,2} > 0$. A simple analysis shows that a singularity is reached if

$$Q(0) < 0 \quad \text{or} \tag{5.36a}$$

$$P(0)^2 > 4Q(0) > 0 \tag{5.36b}$$

with the trajectories diverging toward $P(t) \to -\infty$. Under these conditions a shock will develop along the considered particle path. Alternatively this result can be obtained from the general expression of the characteristic polynomial of A according to equation (5.29).

These analytical results are visualized in figure 5.2, where the two-dimensional vector field of the ODE system (5.33) together with some trajectories is shown. The green and orange trajectories diverge toward $P \to -\infty$, indicating that shocks will form along these trajectories. However, the invariant Q will diverge to $-\infty$ for the green trajectories and to ∞ for the orange trajectories. The remaining red trajectories perform a loop in the upper half plane and asymptotically reach the origin of the P, Q–plane, indicating that these trajectories will not develop a singularity.

Having found analytical solutions for the velocity gradient tensor invariants, it is now interesting to seek for solutions of the full velocity gradient tensor. To this end we note that differentiation and taking into account that equation (5.32) transforms equation (5.21) into a second-order linear system of ordinary differential equations with non-constant coefficients, once the solutions for P and Q are known,

$$\ddot{\mathrm{A}} + 2P\dot{\mathrm{A}} + 2Q\mathrm{A} = 0 \quad . \tag{5.37}$$

This differential equation has the solution

$$\mathrm{A}(t) = (\mathrm{C}_0 + \mathrm{C}_1 t)Q(t) \tag{5.38}$$

with $\mathrm{C}_0 = \frac{\mathrm{A}(0)}{Q(0)}$ and $\mathrm{C}_1 = \frac{-\mathrm{A}^2(0)+P(0)\mathrm{A}(0)}{Q(0)} = \mathrm{E}$ (due to the Cayleigh-Hamilton theorem). By this we finally have obtained a complete local characterization of the velocity gradient tensor evolution along a Lagrangian particle path.

Three-Dimensional Flows

We now proceed to three-dimensional flows, for which the invariants have been studied extensively in the case of the Navier-Stokes equation (see, e.g., [MDV98, CPS99, CPC90, Can92, CM06, Dav04] for some recent works and further references). Two major differences occur compared to the case of the inviscid Burgers equation. As already mentioned, we have to include the divergence of the velocity field in this discussion. Second, and more importantly, the arising system of differential equations is closed in the case of the Burgers equation as the terms related to the pressure Hessian are absent. This allows for a fully analytical study in the case of the Burgers equation without resorting to closure assumptions.

The characteristic polynomial in three dimensions takes the form

$$\lambda^3 - P\lambda^2 + Q\lambda - R = 0 \quad , \tag{5.39}$$

where the tensor invariants are defined according to

$$P = \mathrm{TrA} \tag{5.40a}$$

$$Q = \frac{1}{2}\left[(\mathrm{TrA})^2 - \mathrm{TrA}^2\right] \tag{5.40b}$$

$$R = \det \mathrm{A} \quad . \tag{5.40c}$$

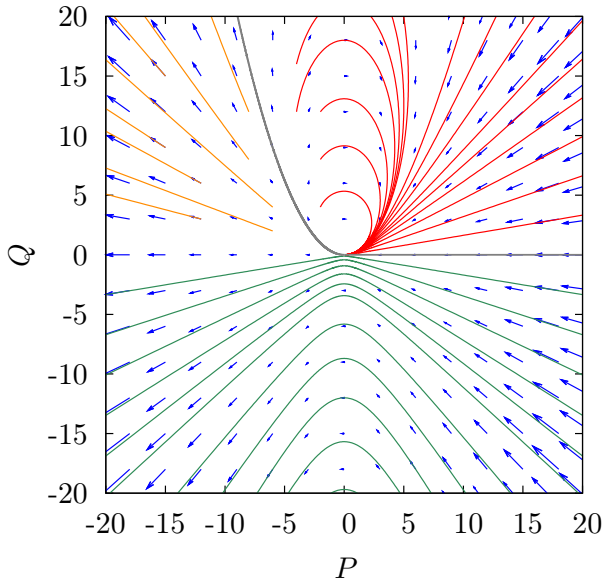

Figure 5.2.: Vector field for the velocity gradient tensor invariants of the two-dimensional Burgers equation. The red lines converge to the origin, while the green and orange lines diverge toward $P \to -\infty$, $Q \to -\infty$ and $P \to -\infty$, $Q \to \infty$, respectively. The gray line separates diverging from converging regions.

By differentiating the definitions, we obtain the evolution equations

$$\dot{P} = 2Q - P^2 \tag{5.41a}$$

$$\dot{Q} = 3R - PQ \tag{5.41b}$$

$$\dot{R} = -PR \quad . \tag{5.41c}$$

As in the two-dimensional case, we here have used Cayleigh-Hamilton's theorem to express higher powers of A in terms of a sum of lower powers according to

$$\mathrm{A}^3 = P\mathrm{A}^2 - Q\mathrm{A} + R\mathrm{E} \quad . \tag{5.42}$$

As in the one- and two-dimensional case a fluid at rest, i.e. $P = Q = R = 0$, is a solution, but for non-vanishing initial conditions a dynamical solution develops. Again, if $R(0) = 0$, the solution is restricted to the P–Q–plane, and if additionally $Q(0) = 0$, the dynamics of the one-dimensional Burgers equation is recovered. Also the three-dimensional ODE system can be solved analytically, either by inserting equation (5.29) and subsequently calculating the remaining solutions or by differentiating $1/R$ thrice

and using the ODE set (5.41). The result reads

$$P(t) = \frac{3t^2 + 2at + b}{t^3 + at^2 + bt + c} \tag{5.43a}$$

$$Q(t) = \frac{3t + a}{t^3 + at^2 + bt + c} \tag{5.43b}$$

$$R(t) = \frac{1}{t^3 + at^2 + bt + c} \tag{5.43c}$$

with $a = {}^{Q(0)}/_{R(0)}$, $b = {}^{P(0)}/_{R(0)}$ and $c = {}^{1}/_{R(0)}$. As in the one- and two-dimensional case, we obtain rational functions as solutions. The time at which a singularity develops along the trajectory of a fluid particle can be determined by investigating the roots of the denominator. In the case of three dimensions this is doable, but already exhaustive. The zeros of the denominator can be explicitly determined with Cardano's method resulting in the expression

$$\begin{aligned} t^* &= -\frac{v}{3u} + u - \frac{a}{3} \quad \text{with} \\ u &= \left(-\frac{w}{2} \pm \sqrt{\frac{w^2}{4} + \frac{v^3}{27}} \right)^{1/3} \quad , \\ v &= b - \frac{a^2}{3} \quad \text{and} \\ w &= c + \frac{2}{27}a^3 - \frac{ab}{3} \quad . \end{aligned} \tag{5.44}$$

Starting from $t = 0$, any initial condition with a positive real solution will end in a singularity. If one seeks to calculate the time the singularity occurs, one has to undertake the tedious task of analyzing these roots in detail. However, if one is only interested *if* a singularity develops *at all*, the investigation of $R(t)$ allows some simple observations. For example, if $R(0) < 0$, there always exists a $t^* > 0$ for which a singularity is reached. For the case of $R(0) > 0$ the polynomial in the denominator has to be analyzed. If the polynomial displays no local extrema, no $t^* > 0$ exists. In case the polynomial exhibits local extrema (which is the case if $a^2 - 3b > 0$), it has to be checked whether the minimum $t_{\min} > 0$ and $f(t_{\min}) \leq 0$. The position of the minimum is given by

$$t_{\min} = \frac{1}{3}\left(-a + \sqrt{a^2 - 3b}\right) \quad \text{with} \tag{5.45a}$$

$$f(t_{\min}) = \frac{1}{27}\left(2a^3 - 9ab + 27c - 2(a^2 - 3b)\sqrt{a^2 - 3b}\right) \quad . \tag{5.45b}$$

An evaluation of these formulas for given initial conditions then shows whether a singularity forms. These analytical investigations are supplemented with a visualization in figure 5.3, where the vector field of the ODE system (5.41) is shown. The green region marks the set of initial conditions that will develop a singularity. One can especially see how the characteristics of the two-dimensional system are recovered in the $R = 0$ plane.

In the two lower panels diverging and converging trajectories are shown in red and blue, respectively. For $R < 0$ trajectories are observed that perform a loop in the upper half of the volume, but finally diverge toward $P \to -\infty$ and $Q \to -\infty$. In the lower half of the volume the trajectories also behave similar to the two-dimensional case shown in figure 5.2, however with a tilt in R-direction. The blue trajectories all converge to $P = Q = R = 0$ with some of them performing a loop in the upper half of the volume and others converging in a straight manner.

As a side remark we note that in all cases considered so far we have observed that a singularity is formed if the "highest" invariant, i.e. the determinant, is negative. This just mirrors the fact that the occurrence of a singularity is related to the existence of a negative eigenvalue of A(0). Alternatively this issue, of course, can also be discussed by analyzing the spectrum of A using equation (5.29).

According to the two-dimensional situation, the nonlinear velocity gradient evolution can be transformed to a linear ODE system also in three dimensions. The resulting equation takes the form

$$\mathrm{A}^{(3)} + 3P\mathrm{A}^{(2)} + 6Q\mathrm{A}^{(1)} + 6R\mathrm{A} = 0 \quad . \tag{5.46}$$

The ODE (5.46) is solved by

$$\mathrm{A}(t) = (\mathrm{C}_0 + \mathrm{C}_1 t + \mathrm{C}_2 t^2) R(t) \tag{5.47}$$

with $\mathrm{C}_0 = \frac{\mathrm{A}(0)}{R(0)}$, $\mathrm{C}_1 = \frac{-\mathrm{A}^2(0)+P(0)\mathrm{A}(0)}{R(0)}$ and $\mathrm{C}_2 = \frac{1}{R(0)}\left[\mathrm{A}^3(0) - P(0)\mathrm{A}^2(0) + Q(0)\mathrm{A}(0)\right]$ $= \mathrm{E}$. As the invariants can be calculated from A(0), and the derivatives have been replaced by powers of A(0), the initial conditions only depend on A(0). A remarkable property of the presented solution is that it can be found by only investigating the invariants P, Q and R, as it is known that they are insufficient to fully characterize the local geometry of the flow [Dav04]. A full characterization can, for example, be given by investigating the invariants of both the symmetric and antisymmetric parts of A, and it turns out that P, Q and R are expressed as combinations of these invariants. The consequences of this observations, however, remain to be understood (at least for the author).

Relation to the Restricted Euler Model

In this section we want to make a short excursion and compare the results obtained so far to an important model for the velocity gradient tensor evolution in three-dimensional incompressible Navier-Stokes dynamics. Taking the inviscid limit, the Lagrangian velocity gradient tensor evolution takes the form

$$\frac{\mathrm{d}}{\mathrm{d}t}\mathrm{A}(\boldsymbol{y}, t) = -\mathrm{A}^2(\boldsymbol{y}, t) - \mathrm{H}(\boldsymbol{y}, t) \quad , \tag{5.48}$$

where additionally the pressure Hessian $H_{ij} = \frac{\partial^2}{\partial x_i \partial x_j} p$ evaluated along a Lagrangian tracer particle shows up. Due to incompressibility the trace of the velocity gradient

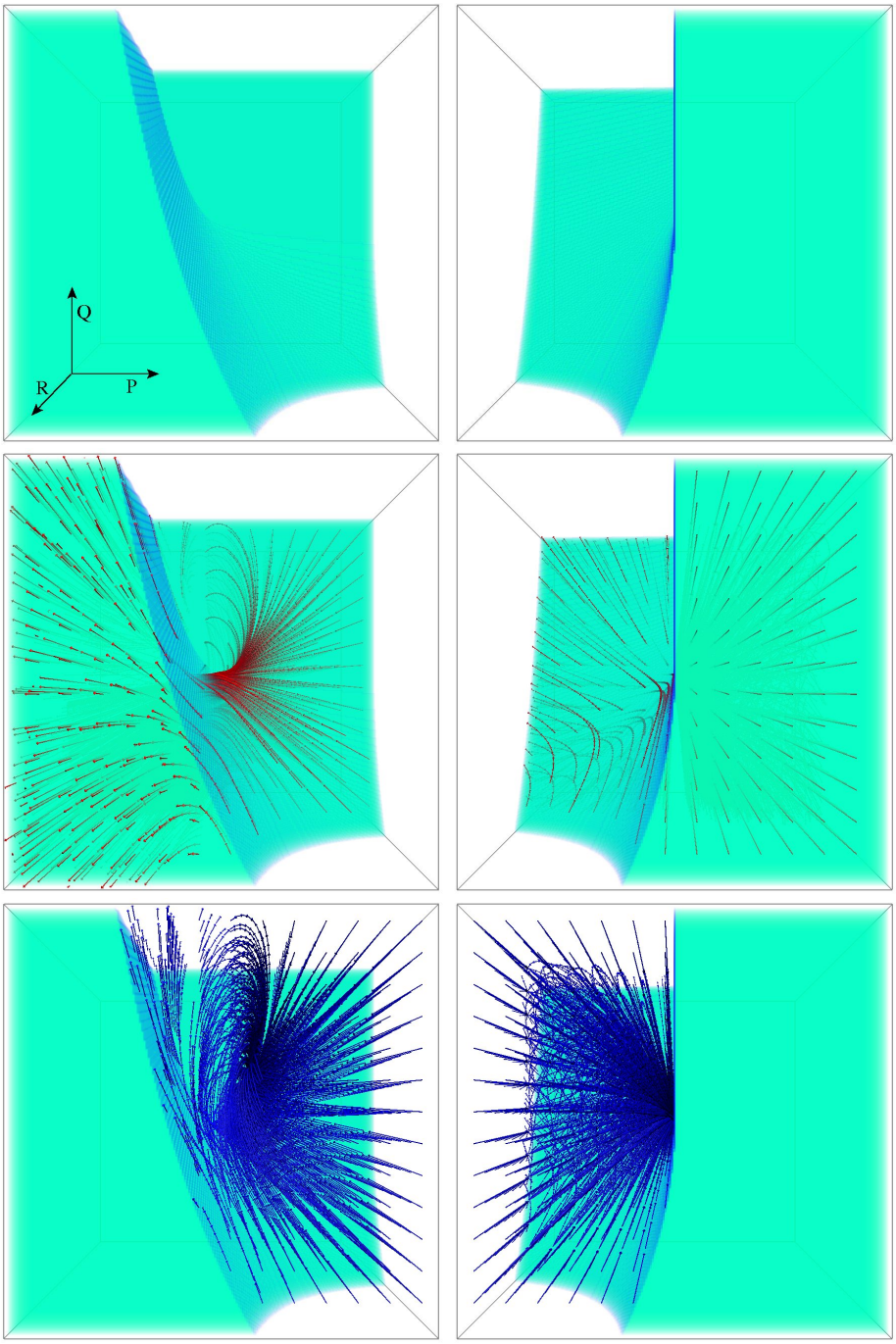

Figure 5.3.: Visualization of the three-dimensional vector field of the invariants P, Q and R from two different views. The region of initial conditions developing a singularity is colored in green. The red trajectories will diverge, whereas the blue will converge to the origin.

tensor and hence the first invariant vanishes

$$P' = \mathrm{TrA} = 0 \quad , \tag{5.49}$$

such that only the remaining two invariants Q' and R' are dynamically active. With this constraint Q' and R' may be defined as

$$Q' = -\frac{1}{2}\mathrm{TrA}^2 \tag{5.50a}$$

$$R' = -\frac{1}{3}\mathrm{TrA}^3 \quad . \tag{5.50b}$$

Note that compared to the definition of R in (5.40) we have included a sign, in order to stay compliant with the standard literature. With these definitions the characteristic polynomial takes the form

$$\lambda^3 + Q'\lambda + R' = 0 \quad . \tag{5.51}$$

By differentiating these definitions and employing equation (5.48) one obtains the evolution equations for Q' and R'

$$\dot{Q}' = -3R' - \mathrm{Tr(AH)} \tag{5.52a}$$

$$\dot{R}' = 2Q' - \mathrm{Tr(A^2H)} \quad , \tag{5.52b}$$

where again the Cayleigh-Hamilton theorem has been invoked to reduce powers of A. While the diffusive term neglected in equation (5.48) is assumed mainly to have a damping influence, which is often modeled linearly (see, for instance, [MDV98]), the main challenge in this context is to formulate an appropriate model for the unclosed pressure Hessian. This term introduces a coupling between fluid particles and in this way induces nonlocal fluctuations to a single trajectory. Here the term *fluctuation* does not imply that a simple stochastic modeling is appropriate, as recently highlighted in [Dai09], but rather that most of the nonlocal information missing, when only a single fluid particle is considered, accumulates here. It can be argued further that this nonlocal information is to a good extent contained within the off-diagonal components of this tensor, as the role of its trace mainly is to preserve solenoidality of the velocity field. This can be seen by taking the trace of equation (5.48) yielding

$$\dot{P}' = 2Q' - \mathrm{TrH} \quad . \tag{5.53}$$

This shows that for an initial condition with $P'(0) = 0$ incompressibility is preserved by

$$\mathrm{TrH} = 2Q' \quad . \tag{5.54}$$

Hence the most simple choice for a model of the pressure Hessian is to assume it to be

$$H_{ij} = \frac{1}{3}\mathrm{TrH}\,\delta_{ij} = \frac{2}{3}Q'\,\delta_{ij} \quad , \tag{5.55}$$

which exactly is the constituting approximation for the restriced Euler model [Vie82, Vie84, Can92]. Insertion into (5.52) yields the Restricted Euler model

$$\frac{\mathrm{d}}{\mathrm{d}t}Q' = -3R' \tag{5.56a}$$

$$\frac{\mathrm{d}}{\mathrm{d}t}R' = \frac{2}{3}Q'^2 \quad . \tag{5.56b}$$

This set of equations takes a very different form than the invariant dynamics of the Burgers equation (5.41), which also can be seen from the visualization in figure 5.4. Here the vector field of the Restricted Euler system as well as the Viellefosse line along with some sample trajectories is shown. Above the Viellefosse line, which separates swirling regions of the flow from straining regions, the trajectories perform a loop and then diverge toward $R' \to \infty$ and $Q' \to -\infty$. Below the Viellefosse line the trajectories first move in direction of the origin but then make a bended curve and diverge in the same direction as the trajectories above the Viellefosse line. That means that all trajectories eventually encounter a singularity, which, of course, is not observed in real turbulent flows, where the solutions remain finite. This, on the one hand, can be attributed to the neglected viscous effects, as including damping terms actually removes the singularity. However, the trajectories then spiral toward the origin, such that no stationary statistics can be obtained from these models. And while the trajectories above the Viellefosse line show a qualitative agreement with experimentally and numerically obtained results, the second and maybe more severe shortcoming is that the trajectories of the Restricted Euler model below the Viellefosse line differ completely from numerical or experimental results, having opposite directions in some of the regions (see, e.g., [Dai09]). The reason for this is that the effects of the pressure Hessian are not captured by the simple approximation used for the model, as recently shown in a number of works [CMBT08, Dai09]. It is shown in these works that the pressure Hessian counteracts the self-amplification of the velocity gradient and helps to prevent the formation of a singularity. One should stress at this point that the formation of a singularity in the Restricted Euler model is an artifact of inappropriate modeling assumptions. In contrast to that, the appearance of singularities in the case of the Burgers equation is a physical phenomenon and part of the dynamics of inviscid, perfectly compressible flows.

Though the Burgers dynamics appears to be very different from the invariant dynamics of the Restricted Euler model for incompressible flows, still a relation between both dynamical systems can be established. To this end we formally include the pressure Hessian into the Burgers dynamics according to

$$\frac{\mathrm{d}}{\mathrm{d}t}\mathrm{A}(t,\boldsymbol{y}) = -\mathrm{A}(t,\boldsymbol{y})^2 - \mathrm{H}(t,\boldsymbol{y}) \tag{5.57}$$

but still maintain P as a dynamical variable. One should note that a more elaborate way to establish this connection would be to start from the compressible Navier-Stokes equation and include the density field into the considerations. However, at this point

this slightly inconsistent approach suffices. The inclusion of the pressure Hessian gives a number of additional terms to the ODE system of the invariants yielding

$$\dot{P} = 2Q - P^2 - \mathrm{TrH} \tag{5.58a}$$

$$\dot{Q} = 3R - PQ - \mathrm{Tr}\left[(P - \mathrm{A})\mathrm{H}\right] \tag{5.58b}$$

$$\dot{R} = -PR - \mathrm{Tr}\left[(\mathrm{A}^2 - P\mathrm{A} + Q)\mathrm{H}\right] \quad . \tag{5.58c}$$

Like it should, the original system (5.41) is recovered by the choice $\mathrm{H} = 0$. We now have two options to derive the Restricted Euler model equations from this set of equations. The first one is to simply apply the approximation (5.55), which results in

$$\dot{P} = -P^2 \tag{5.59a}$$

$$\dot{Q} = 3R - PQ \tag{5.59b}$$

$$\dot{R} = -PR - \frac{2}{3}Q \quad . \tag{5.59c}$$

If we additionally demand $\dot{P} = 0$ and consider the initial condition $P(0) = 0$, we recover the Restricted Euler model (5.56), when the different sign in the definitions of R and R' are taken into account. An alternative way is to alter the approximation which leads to the model according to

$$H_{ij} = \frac{1}{3}\mathrm{TrH}\,\delta_{ij} = \frac{1}{3}(2Q - P^2)\,\delta_{ij} \quad . \tag{5.60}$$

Considering solutions with the initial conditions $P(0) = 0$ also yields the Restricted Euler model. These considerations might be taken as a starting point for future Restricted Euler modeling of compressible flows.

The General Case of n-dimensional Flows

After considering the physically interesting cases of two- and three-dimensional flows, we now want to study the general case of n-dimensional flows. The motivation comes from the fact that the two- and three-dimensional cases indicate a systematic structure, which should become more clear when the general case is investigated. In the n-dimensional case we have to consider the invariants $I_1 \ldots I_n$, which are defined such that the characteristic polynomial takes the form

$$\lambda^n + I_1\lambda^{n-1} + I_2\lambda^{n-2} + \cdots + I_{n-1}\lambda + I_n = 0 \quad . \tag{5.61}$$

Our next aim is to derive evolution equations for all the invariants. Although in principle possible, it is lengthy to proceed like in the two- and three-dimensional case and derive each invariant individually. Alternatively one can make use of the Cayleigh-Hamilton theorem which yields

$$\mathrm{A}^n + I_1\mathrm{A}^{n-1} + I_2\mathrm{A}^{n-2} + \cdots + I_{n-1}\mathrm{A} + I_n\mathrm{E} = 0 \quad . \tag{5.62}$$

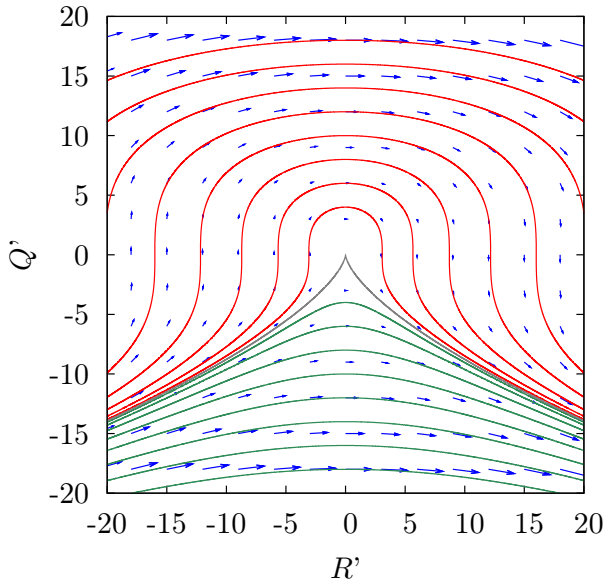

Figure 5.4.: Vector field for the velocity gradient tensor invariants of the Restricted Euler model. The trajectories above the gray Viellefosse line perform a loop in the upper half plane, whereas the trajectories in the lower half plane are bended curves. All trajectories diverge along the Viellefosse line toward $R' \to \infty$, $Q' \to -\infty$.

In what follows, we first derive this expression with respect to time and use the Burgers dynamics (5.21). The highest appearing power, $n+1$, is reduced again invoking the Cayleigh-Hamilton theorem, and we obtain the expression

$$I_1 \mathrm{A}^n + (\dot{I}_1 + 2I_2)\,\mathrm{A}^{n-1} + (\dot{I}_2 + 3I_2)\,\mathrm{A}^{n-2} + \cdots + (\dot{I}_{n-1} + nI_n)\,\mathrm{A} + \dot{I}_n \mathrm{E} = 0 \quad . \tag{5.63}$$

Now subtracting the expression (5.61) times I_1 eliminates the leading term yielding

$$\begin{aligned} &(\dot{I}_1 + 2I_2 - I_1 I_2)\,\mathrm{A}^{n-1} + (\dot{I}_2 + 3I_2 - I_1 I_3)\,\mathrm{A}^{n-2} \\ &+ \ldots \\ &+ (\dot{I}_{n-1} + nI_n - I_1 I_{n-1})\,\mathrm{A} + (\dot{I}_n - I_1 I_n)\,\mathrm{E} = 0 \quad . \end{aligned} \tag{5.64}$$

That means, we have found a polynomial of degree $n-1$ which yields the zero matrix when A is inserted. When we consider the generic case of n different eigenvalues, the only possible conclusion is that all the terms in brackets vanish. This situation actually is generic, because it is obtained from degenerate one by infinitesimal perturbations of the eigenvalues. By this we obtain the system of ODEs

$$\dot{I}_k = I_1 I_k - (k+1) I_{k+1} \quad \text{with} \quad 1 \le k \le n \quad , \tag{5.65}$$

where the case $k = n$ is formally included as $I_{n+1} = 0$ in a n-dimensional system. This result, of course, is consistent with the ODEs obtained in the one-, two- and

three-dimensional case and actually highlights the algebraic structure of the invariant dynamics; the evolution of each invariant couples to the next higher one and to the first one. The solution for this set of equations reads

$$I_k(t) = \frac{(-1)^k}{k!} \frac{p^{(k)}(t)}{p(t)} \quad , \tag{5.66}$$

where the polynomial $p(t)$ is given by

$$p(t) = \sum_{l=0}^{n} (-1)^l \, \frac{I_{n-l}(0)}{I_n(0)} \, t^{n-l} \quad . \tag{5.67}$$

This polynomial obviously is related to the characteristic polynomial of A, which can be seen easily by considering equation (5.66) for the case $k = n$, which (depending on the dimension up to a sign) corresponds to the solution already given in equation (5.29). Consideration of equations (5.28) and (5.29) yields the relation

$$p(t) = \Pi_{\mathrm{A}^{-1}}(-t) = \frac{t^n}{\det \mathrm{A}(0)} \Pi_{\mathrm{A}} \left(-\frac{1}{t} \right) = (-1)^n \det \mathrm{A}(t) \quad . \tag{5.68}$$

That means, the solution for *each* invariant can be obtained by differentiation of the solution for the determinant. Consequently, the solution given in equation (5.29) contains all information necessary to determine the temporal evolution of all invariants.

Motivated by the results of the two- and three-dimensional case, it is interesting to look for solutions for the full velocity gradient tensor also in n dimensions. By differentiation of the Burgers dynamics and taking into account the characteristic polynomial (5.63), we obtain a n-th-order differential equation for the velocity gradient,

$$\sum_{k=0}^{n} \frac{(-1)^{n-k}}{(n-k)!} \, I_k \, \mathrm{A}^{(n-k)} = 0 \tag{5.69}$$

with the convention $I_0 = 1$. Inspired by the solutions of the two- and three-dimensional case we look for solutions of the form

$$\mathrm{A}(t) = \mathrm{G}(t) \, I_n(t) \quad , \tag{5.70}$$

with an hitherto unspecified matrix-valued function G. It can be shown by induction that the k-th derivative of this ansatz obeys

$$\mathrm{A}^{(k)} = \mathrm{G}^{(k)} I_n - k! \sum_{m=0}^{k-1} \frac{(-1)^{k-m}}{m!} \, I_{k-m} \, \mathrm{A}^{(m)} \quad . \tag{5.71}$$

Insertion for $k = n$ into equation (5.69) results in a cancellation of all but one term giving the result

$$\mathrm{G}^{(n)} I_n = 0 \quad . \tag{5.72}$$

Considering only the "fully n-dimensional" case with $I_n \neq 0$ allows to integrate this equation yielding

$$\mathrm{A}(t) = I_n(t) \sum_{k=0}^{n-1} \mathrm{C}_k \, t^k \quad , \tag{5.73}$$

where the constants of integration are given by

$$\mathrm{C}_k = (-1)^k \sum_{m=0}^{k} \frac{I_{k-m}(0)}{I_n(0)} \, \mathrm{A}^{m+1}(0) \quad . \tag{5.74}$$

In case of $k = n-1$ this expression yields $\mathrm{C}_{n-1} = (-1)^n \mathrm{E}$ due to the Cayleigh-Hamilton theorem. In total the solution for the full velocity gradient tensor is given by the dynamics of the n-th invariant times a matrix-valued polynomial of order n in t, which depends on the initial condition $\mathrm{A}(0)$.

5.5. Summary

After introducing into the phenomenology of the Burgers equation, we have studied the evolution of the velocity gradients along Lagrangian trajectories with the goal to derive exact solutions. A detailed discussion of the two- and three-dimensional case has allowed for a classification of initial conditions that will develop a singularity in finite time. These cases are particularly useful to investigate the compressible character of the dynamics and the emergence of shocks. Turning to the general n-dimensional case then revealed the systematic structure of the ordinary differential equations governing the invariant dynamics. Solutions for the full velocity gradient tensor have been found in all dimensions and the n-dimensional case eventually has shown that they can be constructed by knowledge of the initial conditions and the determinant dynamics only. It has to be stressed that the presented solutions are valid also for non-potential initial conditions. In this sense, the results add insights to the generally poorly studied case of Burgers dynamics with non-potential initial conditions and comprise the first fully analytical study of the emergence of finite-time singularities in terms of the Lagrangian velocity gradient tensor.

One should also note that the presented solutions do not display any signatures of chaos, which is completely different for the Lagrangian dynamics in incompressible flows. This direct comparison shows that understanding the properties of the pressure Hessian is the major challenge for the understanding of fully developed incompressible turbulence; the local self-amplification or depletion can be well understood in terms of the Burgers equation or simplified models like the Restricted Euler model.

Part III.

A PDF Approach to Fully Developed Turbulence Based on First Principles

6. The Lundgren-Monin-Novikov Hierarchy

> From the point of view of theoretical physics, turbulence is the first clear-cut instance calling for a new form of statistical mathematics ...
>
> *(John von Neumann, 1949)*

6.1. Introduction and Historical Notes

In chapters 2 and 4 we have motivated that the problem of turbulence is a statistical one. The challenge of solving this problem has already been outlined by introducing the closure problem and presenting statistical evaluations of turbulence data. The striking feature typical for turbulence is the genuinely non-normal statistics going along with strong correlations. In this part of the thesis we will turn to a statistical formulation of turbulence in terms of probability density functions based on first principles. By "first principles" we mean that the derived statistical equations are not introduced on a phenomenological basis but are directly related to the basic equations of motion, i.e. the Navier-Stokes equation. Work on this topic has been initiated way back in the middle of the twentieth century and on a more general level even before, as we will outline in the following.

Tracing back the line of research we are following leads us to the foundations of kinetic theory which have been developed in the framework of statistical mechanics for a many body system. Considering a gas of N particles, it is a well-known result that the probability density $f(\boldsymbol{x}, \boldsymbol{p}, t)$ for the momentum $\boldsymbol{p}$ of a single gas atom (or molecule) to be found at space-time point $(\boldsymbol{x}, t)$ evolves according to [LP83]

$$\frac{\mathrm{d}}{\mathrm{d}t} f = \frac{\partial}{\partial t} f + \boldsymbol{v} \cdot \nabla f = \mathrm{Coll}[f] \quad . \tag{6.1}$$

Here Coll[·] denotes the collision operator, which takes into account the change of the PDF per time unit due to collisions of gas particles in the phase space volume $\mathrm{d}\boldsymbol{x}\,\mathrm{d}\boldsymbol{p}$ and depends on the interaction of the gas particles. If one considers a freely evolving, non-interacting gas, the collision operator is zero, and consequently the PDF evolves according to the Liouville theorem. The task now is to formulate a collision operator which captures the physical mechanisms that govern the statistical evolution of the system. One of the most prominent expressions for the collision operator has been

given by Ludwig Boltzmann in 1872 constituting his kinetic equation [LP83]. Taking into account two-particle collisions and assuming statistical independence of the two particles in every instance apart from the time of the collision yields

$$\mathrm{Coll}[f] = \int \mathrm{d}\tilde{\boldsymbol{p}}\,\mathrm{d}\boldsymbol{p}'\,\mathrm{d}\tilde{\boldsymbol{p}}'\; p(\boldsymbol{p},\tilde{\boldsymbol{p}}|\boldsymbol{p}',\tilde{\boldsymbol{p}}')\left[f'\tilde{f}' - f\tilde{f}\right] \quad , \tag{6.2}$$

where $\boldsymbol{p}$ and $\tilde{\boldsymbol{p}}$ denote the momenta of the first and second particle before the collision and $\boldsymbol{p}'$, and $\tilde{\boldsymbol{p}}'$ denote the momenta of the two particles after the collision. $p(\boldsymbol{p},\tilde{\boldsymbol{p}}|\boldsymbol{p}',\tilde{\boldsymbol{p}}')$ is the transition probability between these two states. In this sense the Boltzmann collision term simply specifies the gains and losses due to two-particle collisions to the phase space interval under consideration. One interesting property of the Boltzmann equation is that it has a unique stationary solution

$$f(\boldsymbol{p}) = (2\pi m k_B T)^{-\frac{3}{2}} \exp\left[-\frac{p^2}{2mk_BT}\right] \tag{6.3}$$

with m being the mass of the gas atom, T denoting the temperature of the gas and k_B denoting the Boltzmann constant. Thus under the assumption of a number of physical properties a collision term has been formulated which determines the equilibrium distribution for the momentum. Of course, it is not clear whether the assumptions fully take into account the physical properties of the gas. That is why it is desirable to develop a framework which yields the general structure of statistical equations without having to resort to modeling assumptions. Such a framework has been formulated by Bogoliubov, Born, Green, Kirk and Yvon and today is known as the BBKGY hierarchy [Bog66, LP83]. The idea here is the following: As the collision operator takes into account the interaction of multiple particles, it obviously incorporates information of the statistics of more than one particle. Taking into account *all* particles, the N-particle distribution function $f_N(\boldsymbol{x}_1,\ldots,\boldsymbol{x}_N,\boldsymbol{p}_1,\ldots,\boldsymbol{p}_N,t)$ contains the full information of the system at a given point in time. If the equations of motion specified by the interaction potentials are known for the system, a closed kinetic equation can be derived for f_N. If we assume for the moment that only two-particle interactions, which depend on the distance of the particles are physically relevant and higher order interactions are negligible, the Hamiltonian takes the form

$$H = \sum_{i=1}^{N} \frac{p_i^2}{2m} + \sum_{i<j=1}^{N} V(|\boldsymbol{x}_j - \boldsymbol{x}_i|) \quad . \tag{6.4}$$

This allows to derive the Liouville equation, an evolution equation for the N-particle distribution function leading to [LP83]

$$\frac{\partial}{\partial t} f_N + \sum_{i=1}^{N} \left\{ \boldsymbol{v}_i \cdot \nabla_{\boldsymbol{x}_i} f_N - \left(\nabla_{\boldsymbol{p}_i} f_N\right) \cdot \sum_{i<j=1}^{N} \nabla_{\boldsymbol{x}_i} V(|\boldsymbol{x}_j - \boldsymbol{x}_i|) \right\} = 0 \quad . \tag{6.5}$$

The evolution equations for less than N particles can then be obtained by integration over the coordinates and momenta of the particles not taken into account for the moment. For the single-particle PDF, for example, one obtains

$$\frac{\partial}{\partial t} f_1(\boldsymbol{x}_1, \boldsymbol{p}_1, t) + \boldsymbol{v}_1 \cdot \nabla_{\boldsymbol{x}_1} f_1(\boldsymbol{x}_1, \boldsymbol{p}_1, t) = M \int \mathrm{d}\boldsymbol{x}_2 \, \mathrm{d}\boldsymbol{p}_2 \, \left[\nabla_{\boldsymbol{p}_1} f_2(\boldsymbol{x}_1, \boldsymbol{x}_2, \boldsymbol{p}_1, \boldsymbol{p}_2, t)\right] \cdot \left[\nabla_{\boldsymbol{x}_1} V_{12}\right] . \tag{6.6}$$

Here $M = N - 1$ takes into account that particle 1 interacts with the remaining $N - 1$ particles in an identical manner. This expression explicitly demonstrates that the evolution of the single-particle distribution depends on the two-particle distribution. Of course, also the evolution equation for the two-particle statistics can be obtained. There, however, a coupling to the three-particle PDF appears. This hierarchy of evolution equations eventually stops on the N-particle level. Consequently, we have to deal with a closure problem when less than N particles are considered, and the Boltzmann collision integral actually is nothing else than a closure, which rests on the statistical independence of the two particles before and after the collision. The advantage of the formulation in terms of the BBGKY hierarchy, rather than starting from a phenomenological model for the collision operator, is that it allows to derive and study the statistical equations in a very conceptual manner allowing for well-defined closure approximations. This is not the only reasons why this approach to statistical mechanics up to today remains fundamental to a number of research fields. One of the most advanced fields in this respect is the statistical mechanics of plasmas, which is also studied in terms of kinetic equations.

When applied to the statistical turbulence problem, a number of difficulties arise. First of all, the equations of fluid motion are formulated for a continuum. Consequently the statistical equations have to be formulated for a whole field if the full information is supposed to be contained in the statistical description. The alternative would be to study the statistical problem of turbulence on the molecular level coming at the high price of giving up the advantages of the continuum description. For example, a turbulent velocity field is smooth below its dissipative length scale such that a continuum description is appropriate. Resolving this sub-Kolmogorov length scale on a molecular level would be a much more fine-grained description than necessary. The mathematical consequence is that the full information of the system cannot be contained within an N-point PDF, no matter how large N is, one rather has to formulate the statistics of the whole continuous field. As a side remark we note, however, that from a physical point of view a finite number of points should suffice to fully characterize the turbulent system if the field is sampled well below the dissipative length scales. Nevertheless, the mathematically complete approach has first been followed by Hopf in 1952 [Hop52] by formulating the evolution equation for the characteristic functional of the velocity field. This approach later on was also followed by Monin and has become textbook knowledge nowadays [MY71, MY75]. Although this approach proves to be very elegant and undoubtedly comprehensive, the mathematical complexity of the arising functional equations remains a major obstacle up to today. Apart from that, information on

single-point or two-point statistics of turbulence still would be very valuable, which motivates the investigation of N-point probability density functions. This actually has been pursued by a number of authors, and it is remarkable to note that all of these works have been published independently in 1967. Starting from a fine-grained PDF describing the velocity field at a single point in space, Lundgren derived the hierarchy of evolution equations for the velocity field. In addition to a very clear derivation of the equations this beautifully written paper ([Lun67], received June 9 1966, published May 1967) highlights the connection to the BBGKY hierarchy. The same set of equations has been obtained in a work by Monin ([Mon67], received August 17 1967, published 1967) from the characteristic functional together with the corresponding hierarchy of moment equations. As incompressible flows equivalently may be described in terms of the vorticity field, the hierarchy of evolution equations, of course, can also be formulated for the vorticity field, which has been done by Novikov for both Eulerian and Lagrangian PDFs ([Nov68], received on January 30 1967, published in November 1967 in Russian, the English translation appeared May 1968). And although the velocity field statistics is very different from the statistics of the vorticity field, the general structure of the equations is very similar, as we will demonstrate later on. Consequently we think that it is appropriate to call the hierarchy of evolution equations the Lundgren-Monin-Novikov (LMN) hierarchy. We will give a detailed review on the hierarchy of equations in the following sections of this chapter.

Shortly after these pioneering papers a work by Ulinich and Lyubimov appeared in 1969, in which also velocity increment distributions are considered and a perturbative treatment of the hierarchy is presented [UL69]. Later on, in the eighties it was shown by Pope that the kinetic equations can be taken as a good starting point for modeling when instead of the coupling to higher order PDFs the equations are formally truncated on the single-point level [PC93, Pop00]. This approach opened the whole field of PDF modeling, which up to today is of great interest in the context of applied turbulence research dealing with reacting flows [Pop00]. But also on the fundamental side work on the kinetic equations continued, e.g., a number of Japanese authors published various closure approximations in recent years (see, e.g., [TY04, Hos07, Hos08]).

Apart from the mathematical difficulties of the arising equations, the second major obstacle is that "simple" closures like the one suggested by Boltzmann do not yield meaningful results in the case of fully developed turbulence due to long-range correlations in the fluid. This is why up to today a general procedure to formulate a closure which does not miss fundamental properties of the statistics observed in experiments is lacking. Nevertheless, one should note that the PDF approach still is promising and comes along with a number of advantages. For example, it is especially suited to formulate closure assumptions as it guarantees physically realizable solutions of the resulting equations, something which often is violated for closures of moment equations.

After these introductory remarks the overall situation seems somewhat challenging; the basic equations have been derived decades ago, and a fully satisfactory statistical treatment is apparently out of reach at the moment. Hence it is appropriate to wonder what kind of questions can be sought after within this framework. This brings us to

the motivation and outline of this part of the thesis. The main strategy here is the following. Going through the literature one can first of all note that only limited effort has been spent on investigating the unclosed terms of the PDF equations by numerical or experimental means. As we *a priori* do not know how to formulate an appropriate closure, one consequently should first try to gather data from experiments or numerics. Numerical evaluations turn out to be especially useful in this context as they allow to calculate almost any desirable physical quantity in an outstanding statistical quality (at least for simple statistical quantities). Hence we have performed simulations of fully developed homogeneous isotropic turbulence in order to obtain this information for both the velocity and vorticity field. One should note at this point that also Novikov has worked in this direction in the case of the vorticity equation [Nov93, ND94, MDN96], and we will take some of his works as a starting point for deeper investigations in the later chapters.

Coming to the outline of this and the following chapters, we first of all will introduce the basic definitions and highlight some constraints the PDFs have to fulfill. We then will give a detailed review on how the PDF equations may be derived for the velocity field. Here we will follow Lundgren's approach and will first derive the evolution equations for the fine-grained PDF and then obtain the full PDF equation by ensemble averaging. Once the equations are set up, the second thing to notice is that only few attempts have been made to simplify the mathematical structure of the equations of the hierarchy. It turns out that drastic simplifications arise when homogeneous isotropic turbulence is studied. We will close this chapter with some remarks on this topic, but the exploitation of statistical symmetries will be of central interest in the following chapters as well.

After introducing the basic techniques, chapters 7 and 8 are devoted to a detailed joint analytical and numerical investigation of the single-point statistics of the velocity and the vorticity. One of the most interesting results here will be that exploiting statistical symmetries eventually allows to find solutions of single-point PDF equations that highlight the dependence of the functional forms of the PDFs on averaged dynamical properties of the flow. A detailed characterization of the unclosed terms will be given with the help of DNS results in these chapters.

While the single-point statistics can be treated in a comprehensive manner by joint analytical and numerical efforts, this approach becomes unpracticable for multi-point statistics. The reason for this is that the statistical quantities under consideration are numerically inaccessible due to their high dimensionality. However, we will use the information gathered on the single-point level to study possible closure schemes. Chapters 9 and 10 will be devoted to approach the closure problem from two different sides. in chapter 9 we will try to calculate the unclosed terms analytically in the framework of the Twisted Gaussian Approximation, which will be introduced then. In contrast to that, we will analyze in chapter 10 the PDF equations with respect to the question which information of the two-point PDF has to be contained in a model in order to correctly close the single-point equation.

6.2. Basic Concepts

6.2.1. Definitions and Constraints on PDFs

To introduce the basic concepts in deriving evolution equations of PDFs, we are following Lundgren [Lun67] as the author thinks that his derivation is particularly clear and comprehensible. More details on the derivation can also be found in Pope's book [Pop00]. The approach makes extensive use of the properties of Dirac's delta distribution, such that we list some of the most important properties in appendix A.1. As already introduced in chapter 2, the fine-grained probability density function for a velocity field may be defined as

$$\hat{f}_1(\boldsymbol{v}_1; \boldsymbol{x}_1, t) = \delta(\boldsymbol{u}(\boldsymbol{x}_1, t) - \boldsymbol{v}_1) \quad , \tag{6.7}$$

where $\boldsymbol{u}(\boldsymbol{x}, t)$ is a realization of the velocity field and $\boldsymbol{v}_1$ denotes the corresponding sample space variable. The notation here implies that $\hat{f}_1$ is a probability density with respect to the sample space variable $\boldsymbol{v}_1$ and a function with respect to the variables $\boldsymbol{x}_1$ and t. The term "fine-grained" refers to the fact that this PDF is sharply peaked in the sense that, given a realization $\boldsymbol{u}(\boldsymbol{x}_1, t)$, the PDF only gives a non-vanishing probability density if $\boldsymbol{v}_1 = \boldsymbol{u}(\boldsymbol{x}_1, t)$ for each point $(\boldsymbol{x}_1, t)$. Thus knowing the fine-grained PDF for each point $\boldsymbol{x}_1$ of a particular realization is equivalent to knowing the realization itself. Now taking into account an ensemble of velocity fields lets us obtain the "full" PDF from the fine-grained PDF by ensemble averaging according to

$$f_1(\boldsymbol{v}_1; \boldsymbol{x}_1, t) = \langle \hat{f}_1(\boldsymbol{v}_1; \boldsymbol{x}, t) \rangle = \langle \delta(\boldsymbol{u}(\boldsymbol{x}_1, t) - \boldsymbol{v}_1) \rangle \quad . \tag{6.8}$$

By taking this average, we have turned to a statistical description in which the information on the individual realization is lost. In the following we will usually omit the index 1 if only single-point PDFs are considered. Of course, this definition can be extended to multiple points according to

$$\begin{aligned} f_N(\boldsymbol{v}_1, \ldots, \boldsymbol{v}_N; \boldsymbol{x}_1, \ldots, \boldsymbol{x}_N, t) &= \langle \hat{f}_N(\boldsymbol{v}_1, \ldots, \boldsymbol{v}_N; \boldsymbol{x}_1, \ldots, \boldsymbol{x}_N, t) \rangle \\ &= \left\langle \prod_{i=1}^{N} \delta(\boldsymbol{u}(\boldsymbol{x}_i, t) - \boldsymbol{v}_i) \right\rangle \quad , \end{aligned} \tag{6.9}$$

which allows for a statistical characterization of N points in space. For example, the investigation of f_2 is necessary to study the statistical properties of velocity increments.

The PDFs are subject to a number of constraints appearing due to the fact that a physical field at N points is considered. First of all, the PDFs have to fulfill the *reduction property*

$$\int \mathrm{d}\boldsymbol{v}_N \, f_N = f_{N-1} \quad , \tag{6.10}$$

which means that by integration one can project from the N-point to the $N-1$-point PDF. The normalization condition

$$\int \mathrm{d}\boldsymbol{v}_1 \, f_1 = 1 \tag{6.11}$$

can be seen as a special case of this property. Furthermore, the PDFs have to fulfill the *separation property*

$$\lim_{|\boldsymbol{x}_2-\boldsymbol{x}_1|\to\infty} f_2(\boldsymbol{v}_1,\boldsymbol{v}_2;\boldsymbol{x}_1,\boldsymbol{x}_2,t) = f_1(\boldsymbol{v}_1;\boldsymbol{x}_1,t)\, f_1(\boldsymbol{v}_2;\boldsymbol{x}_2,t) \quad , \tag{6.12}$$

here exemplified for the two-point PDF. The separation property just takes into account the fact that the velocities at two points in space have to become statistically independent if their separation is large enough. Conversely, if the separation between two points is becoming infinitesimally small, we have to obtain the same value for $\boldsymbol{v}_1$ and $\boldsymbol{v}_2$, which imposes the *coincidence property*

$$\lim_{|\boldsymbol{x}_2-\boldsymbol{x}_1|\to 0} f_2(\boldsymbol{v}_1,\boldsymbol{v}_2;\boldsymbol{x}_1,\boldsymbol{x}_2,t) = f_1(\boldsymbol{v}_1;\boldsymbol{x}_1,t)\, \delta(\boldsymbol{v}_2-\boldsymbol{v}_1) \quad . \tag{6.13}$$

As we are considering solenoidal fields, the statistical quantities have to be consistent with that. The consequence is that incompressibility does not only have to be fulfilled pointwise, $\nabla_{\boldsymbol{x}_1}\cdot\boldsymbol{u}(\boldsymbol{x}_1,t)=0$, but also on the statistical average. This yields

$$0 = \langle \nabla_{\boldsymbol{x}_1}\cdot\boldsymbol{u}(\boldsymbol{x}_1,t)\rangle = \nabla_{\boldsymbol{x}_1}\cdot\langle\boldsymbol{u}(\boldsymbol{x}_1,t)\rangle = \nabla_{\boldsymbol{x}_1}\cdot\int \mathrm{d}\boldsymbol{v}_1\, \boldsymbol{v}_1 f_1(\boldsymbol{v}_1;\boldsymbol{x}_1,t) \quad . \tag{6.14}$$

This *continuity property* also applies to higher order PDFs, which can be seen by considering

$$\begin{aligned} 0 &= \left\langle \left[\int \mathrm{d}\boldsymbol{v}_1\, \delta(\boldsymbol{u}(\boldsymbol{x}_1,t)-\boldsymbol{v}_1)\right] \ldots \delta(\boldsymbol{u}(\boldsymbol{x}_N,t)-\boldsymbol{v}_N)\, \nabla_{\boldsymbol{x}_1}\cdot\boldsymbol{u}(\boldsymbol{x}_1,t)\right\rangle \\ &= \nabla_{\boldsymbol{x}_1}\cdot\int \mathrm{d}\boldsymbol{v}_1 \left\langle \delta(\boldsymbol{u}(\boldsymbol{x}_1,t)-\boldsymbol{v}_1)\ldots\delta(\boldsymbol{u}(\boldsymbol{x}_N,t)-\boldsymbol{v}_N)\,\boldsymbol{u}(\boldsymbol{x}_1,t)\right\rangle \\ &= \nabla_{\boldsymbol{x}_1}\cdot\int \mathrm{d}\boldsymbol{v}_1\, \boldsymbol{v}_1\, f_N(\boldsymbol{v}_1,\ldots,\boldsymbol{v}_N;\boldsymbol{x}_1,\ldots,\boldsymbol{x}_N,t) \quad . \end{aligned} \tag{6.15}$$

This property, of course, may be formulated for any $\boldsymbol{v}_i$. All of these properties have to be fulfilled by the N-point PDFs describing turbulent flows. It can be shown that this actually is the case for PDFs of the Lundgren-Monin-Novikov hierarchy [Lun67], and they can be used as a guideline when models for PDF closures are developed, which we will demonstrate in chapter 10. There we will also introduce some additional constraints which arise from statistical symmetries.

6.2.2. Evolution Equations for Fine-Grained PDFs

To obtain the equations of the LMN hierarchy, we will now take derivatives of the fine-grained PDF (6.7) and use the Navier-Stokes equation (1.1) to re-express some of the terms. We start with taking the partial derivative with respect to time,

$$\frac{\partial}{\partial t}\hat{f}_1(\boldsymbol{v}_1;\boldsymbol{x}_1,t) = \frac{\partial}{\partial t}\delta(\boldsymbol{u}(\boldsymbol{x}_1,t)-\boldsymbol{v}_1) = -\nabla_{\boldsymbol{v}_1}\cdot\left[\frac{\partial\boldsymbol{u}}{\partial t}(\boldsymbol{x}_1,t)\,\hat{f}_1(\boldsymbol{v}_1;\boldsymbol{x}_1,t)\right] \quad . \tag{6.16}$$

We can, of course, proceed in the same manner with spatial derivatives, such that we obtain

$$\frac{\partial}{\partial x_i}\hat{f}_1(\boldsymbol{v}_1;\boldsymbol{x}_1,t) = \frac{\partial}{\partial x_i}\delta(\boldsymbol{u}(\boldsymbol{x}_1,t)-\boldsymbol{v}_1) = -\nabla_{\boldsymbol{v}_1}\cdot\left[\frac{\partial \boldsymbol{u}}{\partial x_i}(\boldsymbol{x}_1,t)\,\hat{f}_1(\boldsymbol{v}_1;\boldsymbol{x}_1,t)\right] \quad . \tag{6.17}$$

If we additionally note that

$$\begin{aligned}\boldsymbol{u}(\boldsymbol{x}_1,t)\cdot\nabla_{\boldsymbol{x}_1}\hat{f}_1(\boldsymbol{v}_1;\boldsymbol{x}_1,t) &= \nabla_{\boldsymbol{x}_1}\cdot\Big[\boldsymbol{u}(\boldsymbol{x}_1,t)\hat{f}_1(\boldsymbol{v}_1;\boldsymbol{x}_1,t)\Big]\\ &= \nabla_{\boldsymbol{x}_1}\cdot\Big[\boldsymbol{v}_1\hat{f}_1(\boldsymbol{v}_1;\boldsymbol{x}_1,t)\Big]\\ &= \boldsymbol{v}_1\cdot\nabla_{\boldsymbol{x}_1}\hat{f}_1(\boldsymbol{v}_1;\boldsymbol{x}_1,t) \quad ,\end{aligned} \tag{6.18}$$

where we made use of incompressibility and the sifting property of the delta distribution, we obtain the evolution equation for the fine-grained PDF

$$\begin{aligned}&\frac{\partial}{\partial t}\hat{f}_1(\boldsymbol{v}_1;\boldsymbol{x}_1,t) + \boldsymbol{v}_1\cdot\nabla_{\boldsymbol{x}_1}\hat{f}_1(\boldsymbol{v}_1;\boldsymbol{x}_1,t)\\ &\qquad= -\nabla_{\boldsymbol{v}_1}\cdot\left[\left(\frac{\partial \boldsymbol{u}}{\partial t}(\boldsymbol{x}_1,t)+\boldsymbol{u}(\boldsymbol{x}_1,t)\cdot\nabla_{\boldsymbol{x}_1}\boldsymbol{u}(\boldsymbol{x}_1,t)\right)\hat{f}_1(\boldsymbol{v}_1;\boldsymbol{x}_1,t)\right]\\ &\qquad= -\nabla_{\boldsymbol{v}_1}\cdot\left[\big(-\nabla_{\boldsymbol{x}_1}p(\boldsymbol{x}_1,t)+\nu\Delta_{\boldsymbol{x}_1}\boldsymbol{u}(\boldsymbol{x}_1,t)+\boldsymbol{F}(\boldsymbol{x}_1,t)\big)\hat{f}_1(\boldsymbol{v}_1;\boldsymbol{x}_1,t)\right] \quad .\end{aligned} \tag{6.19}$$

Here we have used the Navier-Stokes equation (1.1) to replace the terms of its left-hand side by the terms of its right-hand side. To move on to the evolution for the full PDF, we take the ensemble average of the last equation and make use of the fact that we can interchange the temporal derivative as well as the advective term with the ensemble average. This leads us to

$$\begin{aligned}&\frac{\partial}{\partial t}f_1(\boldsymbol{v}_1;\boldsymbol{x}_1,t) + \boldsymbol{v}_1\cdot\nabla_{\boldsymbol{x}_1}f_1(\boldsymbol{v}_1;\boldsymbol{x}_1,t)\\ &\qquad= -\nabla_{\boldsymbol{v}_1}\cdot\left\langle\big(-\nabla_{\boldsymbol{x}_1}p(\boldsymbol{x}_1,t)+\nu\Delta_{\boldsymbol{x}_1}\boldsymbol{u}(\boldsymbol{x}_1,t)+\boldsymbol{F}(\boldsymbol{x}_1,t)\big)\hat{f}_1(\boldsymbol{v}_1;\boldsymbol{x}_1,t)\right\rangle \quad .\end{aligned} \tag{6.20}$$

The first thing to note is that this equation is formally very similar to (6.1) if the collision operator is identified with the right-hand side. Hence the task here is also to specify this collision operator, which turns out to be a severe problem. The reason for that is that the terms of the right-hand side of equation (6.20) cannot be expressed in terms of $\boldsymbol{v}_1$ and f_1 only, i.e., we are facing the closure problem of turbulence. To close the unclosed terms

$$\left\langle -\nabla_{\boldsymbol{x}_1}p(\boldsymbol{x}_1,t)\,\hat{f}_1(\boldsymbol{v}_1;\boldsymbol{x}_1,t)\right\rangle \tag{6.21a}$$

$$\left\langle \nu\Delta_{\boldsymbol{x}_1}\boldsymbol{u}(\boldsymbol{x}_1,t)\,\hat{f}_1(\boldsymbol{v}_1;\boldsymbol{x}_1,t)\right\rangle \tag{6.21b}$$

$$\left\langle \boldsymbol{F}(\boldsymbol{x}_1,t)\,\hat{f}_1(\boldsymbol{v}_1;\boldsymbol{x}_1,t)\right\rangle \quad , \tag{6.21c}$$

unknown information on the joint statistics of the velocity with the pressure gradient, the diffusive terms and the external forcing is necessary, and there are several options how to proceed in the following with these terms.

6.2.3. Coupling to Higher Orders vs. Conditional Averaging

It turns out that the diffusive term and the term involving the pressure gradient can be expressed in terms of the two-point PDF $f_2(\boldsymbol{v}_1, \boldsymbol{v}_2; \boldsymbol{x}_1, \boldsymbol{x}_2, t)$. To illustrate this fact, we start with the diffusive term, where the coupling can be seen especially easily. To this end we use the identity

$$\int \mathrm{d}\boldsymbol{v}_2 \, \delta(\boldsymbol{u}(\boldsymbol{x}_2, t) - \boldsymbol{v}_2) = 1 \tag{6.22}$$

and treat the diffusive term according to

$$\begin{aligned}
\big\langle \big(\nu \Delta_{\boldsymbol{x}_1} \boldsymbol{u}(\boldsymbol{x}_1, t)\big) \, \hat{f}_1(\boldsymbol{v}_1; \boldsymbol{x}_1, t) \big\rangle &= \lim_{\boldsymbol{x}_2 \to \boldsymbol{x}_1} \big\langle \nu \Delta_{\boldsymbol{x}_2} \boldsymbol{u}(\boldsymbol{x}_2, t) \, \hat{f}_1(\boldsymbol{v}_1; \boldsymbol{x}_1, t) \big\rangle \\
&= \lim_{\boldsymbol{x}_2 \to \boldsymbol{x}_1} \nu \Delta_{\boldsymbol{x}_2} \big\langle \boldsymbol{u}(\boldsymbol{x}_2, t) \, \hat{f}_1(\boldsymbol{v}_1; \boldsymbol{x}_1, t) \big\rangle \\
&= \lim_{\boldsymbol{x}_2 \to \boldsymbol{x}_1} \nu \Delta_{\boldsymbol{x}_2} \int \mathrm{d}\boldsymbol{v}_2 \, \big\langle \boldsymbol{u}(\boldsymbol{x}_2, t) \, \hat{f}_2(\boldsymbol{v}_1, \boldsymbol{v}_2; \boldsymbol{x}_1, \boldsymbol{x}_2, t) \big\rangle \\
&= \lim_{\boldsymbol{x}_2 \to \boldsymbol{x}_1} \nu \Delta_{\boldsymbol{x}_2} \int \mathrm{d}\boldsymbol{v}_2 \, \boldsymbol{v}_2 \, f_2(\boldsymbol{v}_1, \boldsymbol{v}_2; \boldsymbol{x}_1, \boldsymbol{x}_2, t) \quad .
\end{aligned} \tag{6.23}$$

This shows that the coupling of the diffusive term is "almost local"; we only need to know the velocity field in an infinitesimal small region around $\boldsymbol{x}_1$, such that we can compute the second derivatives. In this sense the diffusive term depends on the local geometry of the velocity field.

Things are different for the pressure gradient term as the pressure is determined as an integral over the whole domain as indicated in equation (1.4). Consequently, the pressure gradient term is written as

$$\begin{aligned}
&\big\langle \big(- \nabla_{\boldsymbol{x}_1} p(\boldsymbol{x}_1, t)\big) \hat{f}_1(\boldsymbol{v}_1; \boldsymbol{x}_1, t) \big\rangle \\
&= \left\langle - \frac{1}{4\pi} \int \mathrm{d}\boldsymbol{x}_2 \left(\nabla_{\boldsymbol{x}_1} \frac{\nabla_{\boldsymbol{x}_2} \cdot [\boldsymbol{u}(\boldsymbol{x}_2, t) \cdot \nabla_{\boldsymbol{x}_2} \boldsymbol{u}(\boldsymbol{x}_2, t)]}{|\boldsymbol{x}_2 - \boldsymbol{x}_1|} \right) \delta(\boldsymbol{u}(\boldsymbol{x}_1, t) - \boldsymbol{v}_1) \right\rangle \\
&= \left\langle - \frac{1}{4\pi} \int \mathrm{d}\boldsymbol{x}_2 \left(\nabla_{\boldsymbol{x}_1} \frac{\mathrm{Tr}\left[(\nabla_{\boldsymbol{x}_2} \nabla_{\boldsymbol{x}_2}^T)(\boldsymbol{u}(\boldsymbol{x}_2, t) \boldsymbol{u}^T(\boldsymbol{x}_2, t)) \right]}{|\boldsymbol{x}_2 - \boldsymbol{x}_1|} \right) \times \right. \\
&\qquad \left. \delta(\boldsymbol{u}(\boldsymbol{x}_1, t) - \boldsymbol{v}_1) \left(\int \mathrm{d}\boldsymbol{v}_2 \, \delta(\boldsymbol{u}(\boldsymbol{x}_2, t) - \boldsymbol{v}_2) \right) \right\rangle \\
&= - \frac{1}{4\pi} \int \mathrm{d}\boldsymbol{x}_2 \, \mathrm{d}\boldsymbol{v}_2 \left(\nabla_{\boldsymbol{x}_1} \frac{1}{|\boldsymbol{x}_2 - \boldsymbol{x}_1|} \right) (\boldsymbol{v}_2 \cdot \nabla_{\boldsymbol{x}_2})^2 \, f_2(\boldsymbol{v}_1, \boldsymbol{v}_2; \boldsymbol{x}_1, \boldsymbol{x}_2, t) \quad .
\end{aligned} \tag{6.24}$$

For this series of rearrangements we made use of the identity (6.22), the solenoidality of the velocity field and the sifting property of the delta distribution. This expression

shows that the pressure contains information about the two-point PDF f_2 at any point $\boldsymbol{x}_2$ for fixed $\boldsymbol{x}_1$. As a side remark one should note that the diffusive term is a linear function of $\boldsymbol{v}_2$, whereas the pressure gradient term is a quadratic one.

The forcing term cannot generally be expressed in terms of the two-point PDF, this term rather depends on how the velocity field reacts on the external forcing. Maybe that is the reason why it generally is not considered in the works on the LMN hierarchy dealing with the velocity field. In general one will expect that the correlation length and the amplitude of the forcing will influence the velocity field. Things can be made more precise if a stochastic forcing term is considered. If we assume a Gaussian random forcing which is delta correlated in time

$$\langle F_i(\boldsymbol{x},t)\, F_j(\boldsymbol{x}',t')\rangle = Q_{ij}(\boldsymbol{x}-\boldsymbol{x}')\,\delta(t-t') \tag{6.25}$$

with the covariance tensor

$$Q_{ij}(\boldsymbol{r}) = \frac{Q_0}{3}\left[c_\perp(r)\delta_{ij} + (c_\parallel - c_\perp)(r)\,\frac{r_i r_j}{r^2}\right] \quad \text{with} \quad \boldsymbol{r} = \boldsymbol{x}-\boldsymbol{x}' \quad , \tag{6.26}$$

it is possible to obtain an explicit expression for the derivative of the joint average of the fine-grained PDF and the external forcing in the context of stochastic processes. Here Q_0 denotes the amplitude of the forcing, whereas $c_\parallel$ and $c_\perp$ denote the normalized longitudinal and transversal correlation functions of the forcing field, respectively. The results reads [Hak78, Ris96]

$$\frac{\partial}{\partial v_{1,i}}\big\langle F_i(\boldsymbol{x}_1,t)\,\hat{f}_1(\boldsymbol{v}_1;\boldsymbol{x}_1,t)\big\rangle = \frac{1}{2}Q_{ij}(\boldsymbol{0})\frac{\partial^2}{\partial v_{1,i}\,\partial v_{1,j}}f_1 = \frac{1}{2}Q_0\Delta_{\boldsymbol{v}_1}f_1 \quad , \tag{6.27}$$

i.e., a diffusive term with respect to the sample space variable, which depends on the amplitude of the forcing term, is obtained. This shall remain a side remark at this point as a stochastic forcing term has not been used for the DNS results presented in this thesis.

With these results one can write down the single-point PDF equation (6.20) in terms of its coupling to the two-point PDF and obtain

$$\begin{aligned}
&\frac{\partial}{\partial t}f_1 + \boldsymbol{v}_1\cdot\nabla_{\boldsymbol{x}_1}f_1 \\
&\quad = -\nabla_{\boldsymbol{v}_1}\cdot\Bigg[-\frac{1}{4\pi}\int \mathrm{d}\boldsymbol{x}_2\,\mathrm{d}\boldsymbol{v}_2\left(\nabla_{\boldsymbol{x}_1}\frac{1}{|\boldsymbol{x}_2-\boldsymbol{x}_1|}\right)(\boldsymbol{v}_2\cdot\nabla_{\boldsymbol{x}_2})^2\, f_2 \\
&\qquad\qquad + \lim_{\boldsymbol{x}_2\to\boldsymbol{x}_1}\nu\Delta_{\boldsymbol{x}_2}\int \mathrm{d}\boldsymbol{v}_2\,\boldsymbol{v}_2\, f_2 + \langle \boldsymbol{F}_1\,\hat{f}_1\rangle\Bigg] \quad ,
\end{aligned} \tag{6.28}$$

where we have dropped arguments in favor of clarity and used the notation $\boldsymbol{F}_1 = \boldsymbol{F}(\boldsymbol{x}_1,t)$. Note that this equation is formally very similar to (6.6) when the unclosed terms on the right-hand side are regarded as interaction potentials. However, no simple closures are expected to work in this case as, for example, the integral related to the pressure

gradient introduces slowly decaying long-range correlations. This whole procedure can naturally be extended to obtain an evolution equation for f_2. Going through all the steps of the derivation yields

$$\begin{aligned}
&\frac{\partial}{\partial t} f_2 + \boldsymbol{v}_1 \cdot \nabla_{\boldsymbol{x}_1} f_2 + \boldsymbol{v}_2 \cdot \nabla_{\boldsymbol{x}_2} f_2 \\
&\quad = -\nabla_{\boldsymbol{v}_1} \cdot \Bigg[-\frac{1}{4\pi} \int \mathrm{d}\boldsymbol{x}_3 \, \mathrm{d}\boldsymbol{v}_3 \left(\nabla_{\boldsymbol{x}_1} \frac{1}{|\boldsymbol{x}_3 - \boldsymbol{x}_1|} \right) (\boldsymbol{v}_3 \cdot \nabla_{\boldsymbol{x}_3})^2 \, f_3 \\
&\qquad\qquad + \lim_{\boldsymbol{x}_3 \to \boldsymbol{x}_1} \nu \Delta_{\boldsymbol{x}_3} \int \mathrm{d}\boldsymbol{v}_3 \, \boldsymbol{v}_3 \, f_2 + \langle \boldsymbol{F}_1 \, \hat{f}_2 \rangle \Bigg] \\
&\qquad -\nabla_{\boldsymbol{v}_2} \cdot \Bigg[-\frac{1}{4\pi} \int \mathrm{d}\boldsymbol{x}_3 \, \mathrm{d}\boldsymbol{v}_3 \left(\nabla_{\boldsymbol{x}_2} \frac{1}{|\boldsymbol{x}_3 - \boldsymbol{x}_2|} \right) (\boldsymbol{v}_3 \cdot \nabla_{\boldsymbol{x}_3})^2 \, f_3 \\
&\qquad\qquad + \lim_{\boldsymbol{x}_3 \to \boldsymbol{x}_2} \nu \Delta_{\boldsymbol{x}_3} \int \mathrm{d}\boldsymbol{v}_3 \, \boldsymbol{v}_3 \, f_2 + \langle \boldsymbol{F}_2 \, \hat{f}_2 \rangle \Bigg] \quad ,
\end{aligned} \tag{6.29}$$

which gives an impression of how the hierarchy of evolution equations looks like. On the left-hand side "advective" terms with respect to the different points in space appear, and on the right-hand side the collision operators with respect to the sample space variables $\boldsymbol{v}_1$ and $\boldsymbol{v}_2$ have to be taken into account. Note that the whole expression is symmetric with respect to an interchange $(\boldsymbol{x}_1, \boldsymbol{v}_1) \leftrightarrow (\boldsymbol{x}_2, \boldsymbol{v}_2)$ as none of the spatial points should be distinguished by notation.

A second way of treating the unclosed terms has been put forward by Pope in the context of PDF equation modeling [Pop00]. For this approach one makes use of the fact that the conditional probability of two random variables is defined by the relation

$$f_2(\boldsymbol{v}_1, \boldsymbol{v}_2; \boldsymbol{x}_1, \boldsymbol{x}_2, t) = p(\boldsymbol{v}_2 | \boldsymbol{v}_1, \boldsymbol{x}_1, \boldsymbol{x}_2, t) f_1(\boldsymbol{v}_1; \boldsymbol{x}_1, t) \quad , \tag{6.30}$$

where we have introduced the transition probability $p(\boldsymbol{v}_2 | \boldsymbol{v}_1, \boldsymbol{x}_1, \boldsymbol{x}_2, t)$. With this definition it is possible to evaluate conditional averages according to

$$\langle \boldsymbol{u}(\boldsymbol{x}_2, t) | \boldsymbol{v}_1 \rangle = \int \mathrm{d}\boldsymbol{v}_2 \, \boldsymbol{v}_2 \, p(\boldsymbol{v}_2 | \boldsymbol{v}_1, \boldsymbol{x}_1, \boldsymbol{x}_2, t) \quad . \tag{6.31}$$

This allows to express the joint averages of the unclosed terms as

$$\big\langle \big(-\nabla_{\boldsymbol{x}_1} p(\boldsymbol{x}_1, t) \big) \, \hat{f}_1(\boldsymbol{v}_1; \boldsymbol{x}_1, t) \big\rangle = \big\langle -\nabla_{\boldsymbol{x}_1} p(\boldsymbol{x}_1, t) \big| \boldsymbol{v}_1, \boldsymbol{x}_1, t \big\rangle \, f_1(\boldsymbol{v}_1; \boldsymbol{x}_1, t) \tag{6.32a}$$

$$\big\langle \big(\nu \Delta_{\boldsymbol{x}_1} \boldsymbol{u}(\boldsymbol{x}_1, t) \big) \, \hat{f}_1(\boldsymbol{v}_1; \boldsymbol{x}_1, t) \big\rangle = \big\langle \nu \Delta_{\boldsymbol{x}_1} \boldsymbol{u}(\boldsymbol{x}_1, t) \big| \boldsymbol{v}_1, \boldsymbol{x}_1, t \big\rangle \, f_1(\boldsymbol{v}_1; \boldsymbol{x}_1, t) \tag{6.32b}$$

$$\big\langle \boldsymbol{F}(\boldsymbol{x}_1, t) \, \hat{f}_1(\boldsymbol{v}_1; \boldsymbol{x}_1, t) \big\rangle = \big\langle \boldsymbol{F}(\boldsymbol{x}_1, t) \big| \boldsymbol{v}_1, \boldsymbol{x}_1, t \big\rangle \, f_1(\boldsymbol{v}_1; \boldsymbol{x}_1, t) \quad . \tag{6.32c}$$

These expressions explicitly show that not the full joint PDF of, e.g., the pressure gradient and the velocity has to be known in order to close the first equation of the hierarchy, it rather suffices to know the local correlations of the two quantities in form of the conditional average. With these expressions we may write it down as

$$\frac{\partial}{\partial t} f_1 + \boldsymbol{v}_1 \cdot \nabla_{\boldsymbol{x}_1} f_1 = -\nabla_{\boldsymbol{v}_1} \cdot \Big[\big\langle -\nabla p + \nu \Delta \boldsymbol{u} + \boldsymbol{F} \big| \boldsymbol{v}_1 \big\rangle \, f_1 \Big] \quad , \tag{6.33}$$

showing that it takes a particularly simple form, where the left-hand side of the equation indicates an advective transport of the probability and the right-hand side contains gains and losses of probability induced by the correlations of the velocity with the dynamical quantities arising in the right-hand side of the Navier Stokes equation. This form of formulating the kinetic equation turns out to be particularly easy to interpret as the closure problem may be cast in form of questions like, e.g., which value the pressure gradient will take on average given a fixed velocity.

Something not explicitly stressed in the literature is the fact that the introduction of conditional averages cannot only be done on the single-point level, but rather at any given level. If we formally denote the coupling exemplified in equations (6.28) and (6.29) of the evolution for the k-point PDF to the $k+1$-point PDF with $\mathcal{C}_k\big[f_{k+1}, \boldsymbol{F}_1, \ldots, \boldsymbol{F}_k\big]$ and introduce the conditional averages on the N-point level, the hierarchy takes the form

$$\begin{aligned}
\frac{\partial}{\partial t} f_1 + \boldsymbol{v}_1 \cdot \nabla_{\boldsymbol{x}_1} f_1 &= \mathcal{C}_1\big[f_2, \boldsymbol{F}_1\big] \\
\frac{\partial}{\partial t} f_2 + \boldsymbol{v}_1 \cdot \nabla_{\boldsymbol{x}_1} f_2 + \boldsymbol{v}_2 \cdot \nabla_{\boldsymbol{x}_2} f_2 &= \mathcal{C}_2\big[f_3, \boldsymbol{F}_1, \boldsymbol{F}_2\big] \\
&\vdots \\
\frac{\partial}{\partial t} f_{N-1} + \sum_{i=1}^{N-1} \boldsymbol{v}_i \cdot \nabla_{\boldsymbol{x}_i} f_{N-1} &= \mathcal{C}_{N-1}\big[f_N, \boldsymbol{F}_1, \ldots, \boldsymbol{F}_{N-1}\big] \\
\frac{\partial}{\partial t} f_N + \sum_{i=1}^{N} \boldsymbol{v}_i \cdot \nabla_{\boldsymbol{x}_i} f_N &= -\sum_{i=1}^{N} \nabla_{\boldsymbol{v}_i} \cdot \big\{ \big\langle -\nabla_{\boldsymbol{x}_i} p_i + \nu \Delta_{\boldsymbol{x}_i} \boldsymbol{u}_i + \boldsymbol{F}_i \big| \boldsymbol{v}_1, \ldots, \boldsymbol{v}_N \big\rangle f_N \big\}
\end{aligned} \tag{6.34}$$

i.e., the hierarchy up to the N-th level will be closed if the N-point conditional averages are known. If one now assumes that N is large enough to provide a sufficiently fine-meshed sampling of the spatial domain, such that the Kolmogorov length scale is adequately resolved, one could actually argue that a closed system of PDF equations on the N-point level would contain all physically necessary information.

We should note at this point that a formally closed set of equations will not automatically give a constructive procedure to calculate the PDFs, something which we will see when the single-point statistics of velocity and vorticity will be investigated in chapters 7 and 8. However, the hierarchy in the form of (6.34) may formally be solved with the method of characteristics, which allows to recast the system of equations in terms of ordinary partial differential equations for the variables $\boldsymbol{x}_i$ and $\boldsymbol{v}_i$. Let $\boldsymbol{X}_i(t, \boldsymbol{x}_{0,i}, \boldsymbol{v}_{0,i})$ and $\boldsymbol{V}_i(t, \boldsymbol{x}_{0,i}, \boldsymbol{v}_{0,i})$ denote the characteristic curves with

$$\boldsymbol{X}_i(t_0, \boldsymbol{x}_{0,i}, \boldsymbol{v}_{0,i}) = \boldsymbol{x}_{0,i} \tag{6.35a}$$

$$\boldsymbol{V}_i(t_0, \boldsymbol{x}_{0,i}, \boldsymbol{v}_{0,i}) = \boldsymbol{v}_{0,i} \quad . \tag{6.35b}$$

These curves obey the characteristic equations

$$\begin{aligned}
\frac{\mathrm{d}}{\mathrm{d}t}\boldsymbol{X}_1 &= \boldsymbol{V}_1 \\
\frac{\mathrm{d}}{\mathrm{d}t}\boldsymbol{X}_2 &= \boldsymbol{V}_2 \\
&\vdots \\
\frac{\mathrm{d}}{\mathrm{d}t}\boldsymbol{X}_N &= \boldsymbol{V}_N \\
\frac{\mathrm{d}}{\mathrm{d}t}\boldsymbol{V}_1 &= \big\langle -\nabla_{\boldsymbol{x}_1} p_1 + \nu\Delta_{\boldsymbol{x}_1}\boldsymbol{u}_1 + \boldsymbol{F}_1 \big| \boldsymbol{v}_1,\ldots,\boldsymbol{v}_n\big\rangle_{[\boldsymbol{x}_i=\boldsymbol{X}_i(t),\,\boldsymbol{v}_i=\boldsymbol{V}_i(t)]} \\
\frac{\mathrm{d}}{\mathrm{d}t}\boldsymbol{V}_2 &= \big\langle -\nabla_{\boldsymbol{x}_2} p_2 + \nu\Delta_{\boldsymbol{x}_2}\boldsymbol{u}_2 + \boldsymbol{F}_2 \big| \boldsymbol{v}_1,\ldots,\boldsymbol{v}_n\big\rangle_{[\boldsymbol{x}_i=\boldsymbol{X}_i(t),\,\boldsymbol{v}_i=\boldsymbol{V}_i(t)]} \\
&\vdots \\
\frac{\mathrm{d}}{\mathrm{d}t}\boldsymbol{V}_N &= \big\langle -\nabla_{\boldsymbol{x}_N} p_N + \nu\Delta_{\boldsymbol{x}_N}\boldsymbol{u}_N + \boldsymbol{F}_N \big| \boldsymbol{v}_1,\ldots,\boldsymbol{v}_n\big\rangle_{[\boldsymbol{x}_i=\boldsymbol{X}_i(t),\,\boldsymbol{v}_i=\boldsymbol{V}_i(t)]} \quad , \qquad (6.36)
\end{aligned}$$

and the PDF $f_N\big(\boldsymbol{V}_1(t),\ldots\boldsymbol{V}_N(t);\boldsymbol{X}_1(t),\ldots,\boldsymbol{X}_N(t),t\big)$ evolves along the solution of these curves according to

$$\frac{\mathrm{d}}{\mathrm{d}t}f_N = \left[-\sum_{i=1}^{N}\nabla_{\boldsymbol{v}_i}\cdot\big\langle -\nabla_{\boldsymbol{x}_i}p_i + \nu\Delta_{\boldsymbol{x}_i}\boldsymbol{u}_i + \boldsymbol{F}_i\big|\boldsymbol{v}_1,\ldots,\boldsymbol{v}_n\big\rangle\right]_{[\boldsymbol{x}_i=\boldsymbol{X}_i(t),\,\boldsymbol{v}_i=\boldsymbol{V}_i(t)]} f_N \quad . \qquad (6.37)$$

The interesting fact about this equation is that it can be formally integrated once the characteristic curves are known, leading to

$$f_N\big(\boldsymbol{V}_1(t),\ldots,\boldsymbol{V}_N(t);\boldsymbol{X}_1(t),\ldots,\boldsymbol{X}_N(t),t\big) = f_N\big(\boldsymbol{v}_{0,1},\ldots,\boldsymbol{v}_{0,N};\boldsymbol{x}_{0,1},\ldots,\boldsymbol{x}_{0,N},t_0\big)\times$$
$$\exp\left\{-\int_{t_0}^{t}\mathrm{d}t'\left[-\sum_{i=1}^{N}\nabla_{\boldsymbol{v}_i}\cdot\big\langle -\nabla_{\boldsymbol{x}_i}p_i + \nu\Delta_{\boldsymbol{x}_i}\boldsymbol{u}_i + \boldsymbol{F}_i\big|\boldsymbol{v}_1,\ldots,\boldsymbol{v}_n\big\rangle\right]_{[\boldsymbol{x}_i=\boldsymbol{X}_i(t'),\,\boldsymbol{v}_i=\boldsymbol{V}_i(t')]}\right\}. \qquad (6.38)$$

Of course, obtaining an explicit solution for the general N-point case will be very hard, however, the method of characteristics can be used for a qualitative understanding of the evolution of the PDF in probability space and will turn out to be particularly useful when studying decaying turbulence.

We close this section with the remark that up to now we have encountered three different types of closure problems. When the Friedman-Keller hierarchy of moments is considered, the closure problem comes in terms of a coupling to higher moments. This, for example, has been illustrated in chapter 2 in the context of the Kármán-Howarth equation. In the framework of the Lundgren-Monin-Novikov hierarchy the closure problem appears in two alternative ways. One may either formulate the unclosed expressions in terms of a coupling to PDFs at an increasing number of spatial points or in terms of local correlations in the shape of conditional averages.

6.2.4. The Role of Statistical Symmetries

The kinetic equations have been formulated for the most general situation of a turbulent fluid without further assumptions. As indicated in chapter 2.3, turbulence research often considers the idealized case of homogeneous isotropic turbulence. In the same chapter we have motivated how homogeneity and isotropy may be used to simplify statistical quantities like probability density functions and correlation functions. Of course, these arguments can also be applied to the conditional averages appearing in the hierarchy of evolution equations, and we will make extensive use of these simplifications in the following chapters. Beyond simplifying the description, some of the results only become possible when these symmetries will be taken into account. The homogeneous and stationary solutions of the single-point PDF equations for the velocity and vorticity, that will be derived in chapters 7 and 8, are maybe the most important ones to note in this context. Instead of giving a general discussion of all arising relations at this point, we will introduce them in the following chapters when appropriate.

7. Single-Point Statistics of the Turbulent Velocity

7.1. Motivation

In this chapter we turn to a closer investigation of the single-point velocity PDF $f(\boldsymbol{v}; \boldsymbol{x}, t)$ in both stationary and decaying turbulence. One might argue at this point that the single-point velocity PDF of fully developed turbulence is not a very interesting quantity. Turbulence research has often focused on the two-point characteristics of the velocity field in terms of velocity increment statistics, and a number of phenomenological theories exist describing the intermittent behavior we have observed in chapter 4. We refer the reader, for example, to [Fri95] for an overview of the different theories. Furthermore, since the middle of the twentieth century experimental data exists demonstrating that the velocity PDF displays a nearly Gaussian behavior. For example, some classical measurements by Townsend are presented in [Bat53]. Maybe due to the closeness to Gaussianity the functional shape of the velocity PDF is often regarded as rather trivial, and Gaussianity is often assumed on a phenomenological basis sometimes utilizing hand-waving arguments involving the central limit theorem. Careful numerical and experimental investigations, however, indicate that slight deviations from Gaussianity exist, see, e.g., the works by [VM91, NWL$^+$97, GFN02], which show that the PDF has slightly sub-Gaussian tails. Interestingly this observation can also be made for Townsend's data presented in [Bat53], where the kurtosis of the longitudinal velocity increment is shown. Since this value drops below the Gaussian value beyond the integral length scale, it can be concluded that the single-point velocity PDF should also be sub-Gaussian. These findings are consistent with the DNS results presented in this thesis, as can be seen from figure 4.1.

On the theoretical side the shape of the velocity PDF has been discussed by a number of authors. Jimenez suggests sub-Gaussian tails taking into account the precise shape of the energy spectrum [Jim98], while the instanton formalism is used by Falkovich and Lebedev [FL97] to argue in favor of sub-Gaussian tails depending strongly on the external forcing. In contrast to that, Gaussian PDFs have been found in the case of decaying turbulence by Ulinich and Lyubimov [UL69] and later by Hosokawa [Hos08] or in the case of the cross-independence hypothesis by Tatsumi and coworkers [TY04]. The latter works make use of the statistical framework of the Lundgren-Monin-Novikov hierarchy [Lun67, Nov68, Mon67] with additional closure approximations.

Hence the motivation for this chapter of the thesis is to examine the shape of probably the most simple PDF one can consider in the framework of the LMN hierarchy, especially

focusing on deviations from Gaussianity. The strategy will be the following. First of all we will go for a deeper investigation of the single-point velocity PDF. We will especially examine the simplifications that arise due to statistical symmetries and will present closed expressions for the single-point velocity PDF for both homogeneous and stationary turbulence. Furthermore, the relation to moment equations is considered and the theoretical part of this chapter will present possible analytical closures of the PDF equations. The second part of the chapter then will consult DNS results to gain information on the unclosed terms. These results will lead to insights into the correlation of the dynamical quantities arising in the kinetic equation and will allow for a physical interpretation of the different terms. This analysis will especially highlight the limitations of analytical closure approaches and will motivate refined closures. As a check for consistency the homogeneous and stationary solutions of the PDF equations will be evaluated with these terms. The properties of decaying turbulence will also be studied in this context. This chapter represents joint work with Anton Daitche. Some of the results can also be found in [Dai09] and will be published in [WDF10a, WDF10b].

7.2. The Single-Point Velocity PDF Equation

7.2.1. Application of Statistical Symmetries

As introduced in the preceding chapter, the single-point PDF equation may be written down taking the form

$$\frac{\partial}{\partial t} f + \boldsymbol{v} \cdot \nabla f = -\nabla_{\boldsymbol{v}} \cdot \left[\left\langle -\nabla p + \nu \Delta \boldsymbol{u} + \boldsymbol{F} \middle| \boldsymbol{v} \right\rangle f \right] \quad , \tag{7.1}$$

i.e., the closure problem comes in the shape of the unknown conditional averages of the pressure gradient, the diffusive term and the external forcing. In the case of decaying turbulence the forcing term is absent, and it is not possible to maintain a statistically stationary flow. We will omit the subscript 1 in this chapter as no confusion with higher order PDFs has to be expected.

For homogeneous turbulence all statistical quantities should be invariant with respect to spatial translations $\boldsymbol{x} \mapsto \boldsymbol{x} + \boldsymbol{r}$. For the single-point PDF $f(\boldsymbol{v}; \boldsymbol{x}, t)$ the consequence is that it cannot depend on $\boldsymbol{x}$, such that the advective term on the left-hand-side vanishes. By this simplification the kinetic equation takes the form of a continuity equation for the probability density

$$\frac{\partial}{\partial t} f = -\nabla_{\boldsymbol{v}} \cdot \left[\left\langle -\nabla p + \nu \Delta \boldsymbol{u} + \boldsymbol{F} \middle| \boldsymbol{v} \right\rangle f \right] \quad , \tag{7.2}$$

where the conditionally averaged right-hand side of the Navier-Stokes equation times the PDF defines the probability current. Homogeneity furthermore allows to derive relations between various conditional averages. The most simple relation can be obtained by calculating the Laplacian of the fine-grained PDF and taking the ensemble average.

This average vanishes due to homogeneity, and by introducing conditional averages we obtain the relation

$$\frac{\partial^2}{\partial x_k^2} f = 0 = -\frac{\partial}{\partial v_i}\left\langle \frac{\partial^2 u_i}{\partial x_k^2}\middle| \boldsymbol{v}\right\rangle f + \frac{\partial}{\partial v_i}\frac{\partial}{\partial v_j}\left\langle \frac{\partial u_i}{\partial x_k}\frac{\partial u_j}{\partial x_k}\middle| \boldsymbol{v}\right\rangle f \quad . \tag{7.3}$$

Here and in the following Einstein's summation convention will be applied. With this relation the diffusive term in (7.2) can be replaced, such that the equation takes the form

$$\frac{\partial}{\partial t} f = -\frac{\partial}{\partial v_i}\left\langle -\frac{\partial}{\partial x_i} p + F_i \middle| \boldsymbol{v}\right\rangle f - \frac{\partial}{\partial v_i}\frac{\partial}{\partial v_j}\left\langle \nu \frac{\partial u_i}{\partial x_k}\frac{\partial u_j}{\partial x_k}\middle| \boldsymbol{v}\right\rangle f \quad . \tag{7.4}$$

By this the so-called conditional (pseudo-)dissipation tensor

$$D_{ij}(\boldsymbol{v}) = \left\langle \nu \frac{\partial u_i}{\partial x_k}\frac{\partial u_j}{\partial x_k}\middle| \boldsymbol{v}\right\rangle \tag{7.5}$$

has entered the equation. This nomenclature will become more clear in the following. It should be mentioned that similar equations have been studied by Pope [Pop00] for turbulence with mean flow, where they have been used as a starting point for PDF modeling. The interesting fact here is that exploitation of the homogeneity relation (7.3) alters the mathematical structure of the kinetic equation such that second derivatives enter. We will see in the following that both versions of the kinetic equation are useful for different purposes. For example, the structure of equation (7.4) allows to derive a unique stationary solution, something which is not possible for equation (7.2). To exemplify the mathematical structure of equation (7.4) further, let us consider the case of decaying turbulence. In this case the only two terms in equation (7.4) governing the evolution of the velocity PDF are the conditionally averaged pressure gradient and the conditional dissipation tensor. While the former takes the form of a drift induced by the nonlocal pressure contributions, the latter term may be interpreted as a diffusive term, however with a negative sign. This sign has a physically plausible origin as for a diffusion process an initially localized concentration spreads over time, eventually being dispersed over a large domain. Regarding the decay of the velocity field of a turbulent fluid, the opposite takes place; an initially broad distribution of velocity contracts as the velocity field dies away. When the fluid has come to rest, the PDF is localized sharply in probability space, $\lim_{t\to\infty} f(\boldsymbol{v}, t) = \delta(\boldsymbol{v})$, expressing that we have probability one to find a vanishing velocity.

We now want to study the simplifications possible due to isotropy. As introduced in chapter 2, isotropy implies invariance of statistical quantities under arbitrary rotations and reflections[1] of the coordinate system. As we have seen there, this implies

$$f(\mathrm{R}\boldsymbol{v}) = f(\boldsymbol{v}) \quad \forall\, \mathrm{R} \in \mathrm{SO}(3) \quad , \tag{7.6}$$

[1] For the current presentation we only make use of invariance under rotations.

such that the PDF can only depend on the magnitude of the velocity. This allows to establish the simple relation

$$\tilde{f}(v) = 4\pi v^2 f(\boldsymbol{v}) \quad , \tag{7.7}$$

where $\tilde{f}$ denotes the PDF of the magnitude of velocity, i.e., the investigation of this quantity suffices to characterize the PDF of the vector. In experiments and numerical simulations often the PDFs of the components of the velocity, v_x, v_y and v_z are investigated. These may be obtained from the PDF of the vector simply by integration, for example,

$$f(v_x) = \int \mathrm{d}v_y \, \mathrm{d}v_z \, f(\boldsymbol{v}) \tag{7.8}$$

and may also be obtained directly from $\tilde{f}(v)$. This can be seen by introducing cylindrical coordinates, where v_x is chosen as z-axis. A short calculation yields the result

$$f(v_x) = \int_{|v_x|}^{\infty} \mathrm{d}v \, \frac{\tilde{f}(v)}{v} \quad . \tag{7.9}$$

This relation can also be inverted by differentiation resulting in

$$\tilde{f}(v) = \left[2v_x \frac{\mathrm{d}}{\mathrm{d}v_x} f(v_x) \right]_{v_x = v} \quad . \tag{7.10}$$

These considerations demonstrate that for isotropic turbulence the single-point statistics can fully be characterized in terms of the PDF of the velocity vector, the magnitude of the velocity or a single component. We choose the PDF of the magnitude as the resulting equations are especially easy to handle.

The kinetic equation (7.1) contains vectors conditionally averaged with respect to the vectorial velocity. Isotropy here implies

$$\langle \boldsymbol{a} | \mathrm{R}\boldsymbol{v} \rangle = \mathrm{R} \langle \boldsymbol{a} | \boldsymbol{v} \rangle \quad \forall \, \mathrm{R} \in \mathrm{SO}(3) \quad , \tag{7.11}$$

which, according to chapter 2, leads to the general form

$$\langle \boldsymbol{a} | \boldsymbol{v} \rangle = \alpha(v) \hat{\boldsymbol{v}} \quad \text{with} \quad \alpha(v) = \langle \hat{\boldsymbol{u}} \cdot \boldsymbol{a} | v \rangle \quad , \tag{7.12}$$

where, for example, $\hat{\boldsymbol{v}}$ denotes the direction of the $\boldsymbol{v}$ vector. Note that the scalar function α depends on the magnitude of the velocity vector only, which is a strong simplification with respect to the numerical evaluation later on. This allows to express the conditional vectors in the kinetic equations (7.2) and (7.4) in terms of the scalar functions Π, Λ and Φ according to

$$\left\langle -\nabla p \middle| \boldsymbol{v} \right\rangle = \Pi(v) \hat{\boldsymbol{v}} \qquad \Pi(v) = \left\langle -\hat{\boldsymbol{u}} \cdot \nabla p \middle| v \right\rangle \tag{7.13a}$$

$$\left\langle \nu \Delta \boldsymbol{u} \middle| \boldsymbol{v} \right\rangle = \Lambda(v) \hat{\boldsymbol{v}} \qquad \Lambda(v) = \left\langle \nu \hat{\boldsymbol{u}} \cdot \Delta \boldsymbol{u} \middle| v \right\rangle \tag{7.13b}$$

$$\left\langle \boldsymbol{F} \middle| \boldsymbol{v} \right\rangle = \Phi(v) \hat{\boldsymbol{v}} \qquad \Phi(v) = \left\langle \hat{\boldsymbol{u}} \cdot \boldsymbol{F} \middle| v \right\rangle \quad . \tag{7.13c}$$

As a result the knowledge of the three scalar functions suffices to close the kinetic equation (7.2). To simplify the structure of the conditional dissipation tensor, we take into account that for second order tensors isotropy implies

$$\mathrm{D}(\mathrm{R}\boldsymbol{v}) = \mathrm{R}\mathrm{D}(\boldsymbol{v})\mathrm{R}^T \quad \forall\, \mathrm{R} \in \mathrm{SO}(3) \quad . \tag{7.14}$$

We have motivated in chapter 2 that under these conditions the most general form of the tensor (which is symmetric) will be [Rob40, Bat53, Dai09]

$$D_{ij}(\boldsymbol{v}) = \mu(v)\,\delta_{ij} + \big[\lambda(v) - \mu(v)\big]\frac{v_i v_j}{v^2} \quad , \tag{7.15}$$

where μ and λ are the eigenvalues of D depending only on the magnitude of velocity. For a given matrix D they can simply be determined by the relations

$$\mathrm{Tr}(\mathrm{D}) = \lambda(v) + 2\mu(v) \tag{7.16a}$$

$$\hat{\boldsymbol{v}}\mathrm{D}\hat{\boldsymbol{v}} = \lambda(v) \quad . \tag{7.16b}$$

To find out their physical meaning, we first note that the trace of D is determined by the conditional averages of the local rate of energy dissipation $\varepsilon = 2\nu\mathrm{Tr}(\mathrm{S}^2)$ and the squared vorticity ω^2,

$$\mathrm{Tr}(\mathrm{D}) = \nu\left\langle \mathrm{Tr}(\mathrm{S}^2) - \mathrm{Tr}(\mathrm{W}^2)\middle| v\right\rangle = \frac{1}{2}\left\langle \varepsilon + \nu\omega^2\middle| v\right\rangle \quad . \tag{7.17}$$

The second scalar quantity needed to determine D is

$$\hat{\boldsymbol{v}}\mathrm{D}\hat{\boldsymbol{v}} = \left\langle \nu\,\hat{\boldsymbol{u}}\mathrm{A}\mathrm{A}^T\hat{\boldsymbol{u}}\middle| v\right\rangle = \left\langle \nu(\mathrm{A}^T\hat{\boldsymbol{u}})^2\middle| v\right\rangle \quad . \tag{7.18}$$

This rather formally looking quantity has a simple physical interpretation. As A may be decomposed in symmetric and antisymmetric parts, we write $\mathrm{A}^T\hat{\boldsymbol{u}} = (\mathrm{S} - \mathrm{W})\hat{\boldsymbol{u}}$. The last term may also be written as $\mathrm{W}\hat{\boldsymbol{u}} = \frac{1}{2}\boldsymbol{\omega} \times \hat{\boldsymbol{u}}$ due to the relation $W_{ij} = -\frac{1}{2}\epsilon_{ijk}\omega_k$. Hence, the conditional average appearing in (7.18) involves the absolute value of the difference between the rate of stretching in the direction of the velocity vector and the rate of rotation of the unit vector $\hat{\boldsymbol{u}}$. Summing up, the conditional dissipation tensor D in isotropic turbulence has the form

$$D_{ij}(\boldsymbol{v}) = \mu(v)\,\delta_{ij} + [\lambda(v) - \mu(v)]\frac{v_i v_j}{v^2} \tag{7.19a}$$

$$\mu(v) = \frac{1}{4}\left\langle \varepsilon + \nu\omega^2\middle| v\right\rangle - \frac{1}{2}\left\langle \nu(\mathrm{A}^T\hat{\boldsymbol{u}})^2\middle| v\right\rangle \tag{7.19b}$$

$$\lambda(v) = \left\langle \nu(\mathrm{A}^T\hat{\boldsymbol{u}})^2\middle| v\right\rangle \quad . \tag{7.19c}$$

We will see in the context of the energy budget equation that only the trace of D is associated with the dissipation of kinetic energy. Hence the remaining terms may be interpreted as a redistribution of kinetic energy between the different components of velocity. Now having expressed all terms arising in equations (7.2) and (7.4) in terms

of scalar functions depending on the magnitude of velocity only, these terms can be inserted into the kinetic equations, which yields further simplifications. For example, the terms involving conditionally averaged vectors take the simple form

$$\begin{aligned}\frac{\partial}{\partial v_i}\langle a_i|\boldsymbol{v}\rangle f(\boldsymbol{v}) &= \frac{\partial}{\partial v_i}\alpha(v)\frac{v_i}{4\pi v^3}\tilde{f}(v) \\ &= \frac{1}{4\pi v^2}\frac{\partial}{\partial v}\alpha(v)\tilde{f}(v) \quad .\end{aligned} \tag{7.20}$$

For the conditional dissipation tensor we proceed in a similar manner and obtain

$$\frac{\partial}{\partial v_i}\frac{\partial}{\partial v_j}D_{ij}(\boldsymbol{v})f(\boldsymbol{v}) = \frac{1}{4\pi v^2}\left[\frac{\partial^2}{\partial v^2}\lambda(v)\tilde{f}(v) - \frac{\partial}{\partial v}\frac{2}{v}\mu(v)\tilde{f}(v)\right] \quad . \tag{7.21}$$

If we now insert these relations into our original kinetic equations, they take (what we call) the isotropic form of the equations (7.2), (7.3) and (7.4)

$$\frac{\partial}{\partial t}\tilde{f} = -\frac{\partial}{\partial v}\left(\Pi + \Lambda + \Phi\right)\tilde{f} \tag{7.22a}$$

$$0 = -\frac{\partial}{\partial v}\left(\Lambda + \frac{2\mu}{v}\right)\tilde{f} + \frac{\partial^2}{\partial v^2}\lambda\tilde{f} \tag{7.22b}$$

$$\frac{\partial}{\partial t}\tilde{f} = -\frac{\partial}{\partial v}\left(\Pi + \Phi - \frac{2\mu}{v}\right)\tilde{f} - \frac{\partial^2}{\partial v^2}\lambda\tilde{f} \quad . \tag{7.22c}$$

The important observation now is that these equations depend only on the magnitude of the velocity vector, any explicit dependence on components of the velocity has vanished. That means that the problem is hereby mathematically reduced to a one-dimensional one, which will allow for a number of important conclusions. For example, if we consider stationary turbulence, the left-hand side of (7.22a) vanishes, such that we obtain

$$0 = \frac{\partial}{\partial v}\left(\Pi + \Lambda + \Phi\right)\tilde{f} \quad . \tag{7.23}$$

By integrating this equation and choosing the integration constant to be zero (which is corresponds to the generic case) we obtain

$$0 = \Pi(v) + \Lambda(v) + \Phi(v) \quad . \tag{7.24}$$

This conditional balance shows that in stationary homogeneous isotropic turbulence the contributions of the pressure gradient, the diffusive term and the external forcing cancel. Note that this holds in the *conditional* sense, which is stricter than the corresponding relation for ordinary averages. Of course, the latter relation is included in this relation and may be obtained by integration. This relation basically states that the probability current of the right-hand side of equation (7.22a) vanishes for stationary turbulence. This also shows that it is not possible to compute a meaningful stationary solution for $\tilde{f}$ directly from equation (7.22a).

7.2.2. Homogeneous and Stationary PDF

The second important property of the equations (7.22b) and (7.22c) is that explicit expressions for the velocity PDF in the case of homogeneous or additionally stationary isotropic turbulence may be obtained. For the case of homogeneous turbulence equation (7.22b) may be integrated, and we obtain

$$\tilde{f}(v;t) = \frac{\mathcal{N}}{\lambda(v,t)} \exp \int_{v_0}^{v} \mathrm{d}v' \, \frac{\Lambda(v',t) + \frac{2}{v'}\mu(v',t)}{\lambda(v',t)} \quad , \tag{7.25}$$

where $\mathcal{N}$ denotes a normalization constant, which depends on the integration limit v_0. This expression shows that the precise shape of the PDF of the magnitude of velocity depends on the conditional average related to the diffusive term Λ and the two eigenvalues of the conditional dissipation tensor μ and λ. As this relation is only based on homogeneity and isotropy, it also holds for decaying turbulence, such that all of the quantities may depend on time.

If we assume stationary statistics, the left-hand side of equation (7.22c) vanishes, and the equation then may be solved in exactly the same manner. The solution reads

$$\tilde{f}(v) = \frac{\mathcal{N}}{\lambda(v)} \exp \int_{v_0}^{v} \mathrm{d}v' \, \frac{-\Pi(v') - \Phi(v') + \frac{2}{v'}\mu(v')}{\lambda(v')} \quad , \tag{7.26}$$

i.e., the stationary PDF depends on the conditionally averaged pressure gradient and external forcing as well as on the eigenvalues of the conditional dissipation tensors. Note that this result can also be obtained from the homogeneous solution (7.25) by exploiting the conditional balance (7.24). Of course, the functional form of the conditional averages cannot be explicitly computed at this point without further assumptions, but the expression reveals that the shape of the probability density function depends on the correlations between the velocity and the different dynamical effects on the single-point level. For example, the stationary solution depends on how energy is injected into the system by the forcing on the large scales, redistributed by the pressure gradient and finally dissipated on the small scales. Due to this interpretation we think that these results are more than just formal solutions. We will demonstrate in section 7.2.5 how, based on physical arguments, closures may be formulated leading to closed expressions for the PDF. Furthermore one can argue that, although these expressions involve unknown terms, still meaningful insights can be gained. For instance, this procedure explicitly reveals which correlations influence the functional shape of the single-point velocity PDF.

7.2.3. The Method of Characteristics For Decaying Turbulence

The shape of the PDF can be determined in the non-stationary situation by evaluating the homogeneous solution (7.25). Here, the conditional averages Λ, λ and μ have to be known as a function of time. Another possibility to study non-stationary situations is with the help of the method of characteristics as indicated in chapter 6. In the case of

the single-point velocity PDF in homogeneous isotropic turbulence things turn out to be particularly simple as we only have to consider the sample space evolution of the magnitude of the velocity vector. Let $V(t, v_0)$ denote a characteristic curve which starts from v_0, i.e. $V(t_0, v_0) = v_0$. The method of characteristics then yields the following equations

$$\frac{\mathrm{d}}{\mathrm{d}t} V(t, v_0) = \left[\Pi(v, t) + \Lambda(v, t)\right]_{v=V(t,v_0)} \tag{7.27a}$$

$$\frac{\mathrm{d}}{\mathrm{d}t} \tilde{f}(V(t, v_0); t) = \left[-\frac{\partial}{\partial v}\big(\Pi(v, t) + \Lambda(v, t)\big)\right]_{v=V(t,v_0)} \tilde{f}(V(t, v_0); t) \quad . \tag{7.27b}$$

The first equation here describes how a sample space velocity evolves over time due to the pressure gradient and viscous diffusion. In terms of the PDF, this equation describes the stretching of the v-axis. The second equation is easily integrated. We obtain the evolution of $\tilde{f}$ along the characteristic curves

$$\tilde{f}(V(t, v_0); t) = \tilde{f}(v_0; t_0) \exp\left[-\int_{t_0}^{t} \mathrm{d}t' \left[\frac{\partial}{\partial v}\big(\Pi(v, t') + \Lambda(v, t')\big)\right]_{v=V(t',v_0)}\right] \quad . \tag{7.28}$$

The effect of the exponential factor in this solution is two-fold. First, it preserves normalization when the v-axis is stretched according to equation (7.27a). Second, it contributes to the deformation of the PDF in addition to the deformation of the v-axis. This formal solution describes the evolution of the PDF along the characteristic curves. Of course, we are more interested in the temporal evolution of $f(v; t)$ instead of $f(V(t, v_0); t)$. This mapping can be achieved with the inverse function of $V(t, v_0)$, which is defined by

$$V^{-1}(t, V(t, v_0)) = v_0 \quad . \tag{7.29}$$

Thus the temporal evolution of the PDF of the magnitude of velocity is given by $\tilde{f}(v; t) = \tilde{f}(V(t, V^{-1}(t, v)); t)$, such that we obtain

$$\tilde{f}(v; t) = \tilde{f}(V^{-1}(t, v); t_0) \exp\left[-\int_{t_0}^{t} \mathrm{d}t' \left[\frac{\partial}{\partial v'}\big(\Pi(v', t') + \Lambda(v', t')\big)\right]_{v'=V(t',V^{-1}(t,v))}\right] . \tag{7.30}$$

As a consequence, the temporal evolution of the PDF is known, when the solution of the characteristic curve $V(t, v)$ is available for arbitrary initial conditions v. This procedure allows to discuss the evolution of a PDF in a very intuitive way. We want to exemplify this with the particularly simple case of a self-similar evolution of the PDF, which is characterized by

$$\tilde{f}(v; t) = \frac{\sigma(t_0)}{\sigma(t)} \tilde{f}\left(\frac{\sigma(t_0)}{\sigma(t)} v; t_0\right) \quad , \tag{7.31}$$

where

$$\sigma(t) = \sqrt{\frac{2}{3} E_{\mathrm{kin}}(t)} \tag{7.32}$$

denotes the standard deviation of the vectorial PDF related to the kinetic energy of the flow. By comparison of (7.31) and (7.30) it is clear that a self-similar solution can only be obtained if the characteristics are of the form

$$V(t, v_0) = \frac{\sigma(t)}{\sigma(t_0)} v_0 \quad , \tag{7.33}$$

i.e., the stretching of the v-axis is a linear function of time. The interesting consequence is that this behavior implies

$$\Pi(v,t) + \Lambda(v,t) = v \, \frac{\mathrm{d}}{\mathrm{d}t} \ln \left[\frac{\sigma(t)}{\sigma(t_0)} \right] = -\frac{1}{2} \frac{\langle \varepsilon \rangle (t)}{E_{\mathrm{kin}}(t)} \, v \quad . \tag{7.34}$$

That means, the observation of a self-similar evolution of the PDF implies that the sum of the conditional averages related to the pressure gradient and the Laplacian is a linear function of v with a negative slope proportional to the ratio of the rate of energy dissipation and the kinetic energy. In this sense the assumption (or observation) of a self-similar decay leads to a closure of the kinetic equation for decaying turbulence if the temporal evolution of the kinetic energy and the rate of energy dissipation are known by additional modeling or experimental or numerical input.

7.2.4. Relation to Moment Equations

The PDF $f(\boldsymbol{v}; \boldsymbol{x}, t)$ contains the information for all moments $\langle v_x^{n_1} \, v_y^{n_2} \, v_z^{n_3} \rangle$ which can be obtained by integration according to

$$\langle v_x^{n_1} \, v_y^{n_2} \, v_z^{n_3} \rangle = \int \mathrm{d}\boldsymbol{v} \, v_x^{n_1} \, v_y^{n_2} \, v_z^{n_3} \, f(\boldsymbol{v}; \boldsymbol{x}, t) \quad . \tag{7.35}$$

As a consequence, the evolution equation for the PDF should also contain evolution equations for all the moments. In fact, these can be obtained by multiplying the PDF equation by the moment of interest and subsequent integration with respect to the velocity. This procedure can be applied to the kinetic equation of the "original" form (7.1) but to also the kinetic equations (7.2), (7.4), (7.22a) and (7.22c) after exploiting the statistical symmetries. To exemplify this issue, we would like to take equation (7.4) for the case of decaying turbulence as a starting point and deduce the law of energy decay. To this end we multiply equation (7.4) by $\frac{\boldsymbol{v}^2}{2}$ and integrate over $\boldsymbol{v}$,

$$\frac{\partial}{\partial t} E_{\mathrm{kin}} = \int \mathrm{d}\boldsymbol{v} \, \frac{\boldsymbol{v}^2}{2} \frac{\partial}{\partial t} f = -\int \mathrm{d}\boldsymbol{v} \, \frac{v_k v_k}{2} \left[\frac{\partial}{\partial v_i} \left\langle -\frac{\partial}{\partial x_i} p \middle| \boldsymbol{v} \right\rangle f + \frac{\partial}{\partial v_i} \frac{\partial}{\partial v_j} \left\langle \nu \frac{\partial u_i}{\partial x_k} \frac{\partial u_j}{\partial x_k} \middle| \boldsymbol{v} \right\rangle f \right] . \tag{7.36}$$

The right-hand side may be integrated by parts. Assuming a sufficiently rapid decay of the PDF, one finds

$$\begin{aligned} \frac{\partial}{\partial t} E_{\mathrm{kin}} &= \int \mathrm{d}\boldsymbol{v} \left[-\langle \boldsymbol{u} \cdot \nabla p | \boldsymbol{v} \rangle f - \left\langle \nu \frac{\partial u_i}{\partial x_k} \frac{\partial u_i}{\partial x_k} \middle| \boldsymbol{v} \right\rangle f \right] \\ &= -\langle \boldsymbol{u} \cdot \nabla p \rangle - \frac{1}{2} \langle \varepsilon + \nu \omega^2 \rangle \\ &= -\langle \varepsilon \rangle \quad . \end{aligned} \tag{7.37}$$

The last equality comes from the fact that the pressure related average vanishes due to homogeneity and incompressibility and that the rate of energy dissipation and squared vorticity (multiplied by ν) have the same spatial and consequently also the same ensemble average. Hence the result is the well-known law of energy decay. We stress once more that any other moment equation may be obtained in the same manner from the kinetic equations. This example demonstrates that the PDF approach is rather comprehensive as, for example, applying closure hypotheses on the level of the PDF equation corresponds to applying a closure to *all* moment equations simultaneously. This has a number of advantages, of which the most important one might be the fact that by this realizability of the resulting PDF is guaranteed.

7.2.5. Analytical Closure Approximations

Before we proceed to the evaluation of the DNS results to obtain further information on the unclosed terms, we want to seek for plausible analytical closure approximations of the kinetic equations. To this end it is useful to note that the unknown conditional averages are subject to a number of integral constraints. First of all, it is a well-known result that the average pressure gradient times the velocity vanishes for homogeneous isotropic turbulence, which we have already used in the preceding section. This yields the relation

$$0 = \langle \boldsymbol{u} \cdot \nabla p \rangle = \int_0^\infty \mathrm{d}v \, \left\langle \boldsymbol{u} \cdot \nabla p \middle| v \right\rangle \tilde{f}(v) = - \int_0^\infty \mathrm{d}v \, v \, \Pi(v) \tilde{f}(v) \quad . \tag{7.38}$$

Furthermore, the dissipative terms of the kinetic equations should yield the average rate of energy dissipation when multiplied with the PDF of velocity and integrated. This leads to

$$- \langle \varepsilon \rangle = \langle \nu \boldsymbol{u} \cdot \Delta \boldsymbol{u} \rangle = \int_0^\infty \mathrm{d}v \, v \, \Lambda(v) \tilde{f}(v) \tag{7.39a}$$

$$\langle \varepsilon \rangle = \langle \mathrm{Tr(D)} \rangle = \int_0^\infty \mathrm{d}v \, [\lambda(v) + 2\mu(v)] \tilde{f}(v) \quad . \tag{7.39b}$$

In the stationary case the rate of energy dissipation is on average balanced by the external forcing and yields the constraint

$$\langle \varepsilon \rangle = \langle \boldsymbol{u} \cdot \boldsymbol{F} \rangle = \int_0^\infty \mathrm{d}v \, v \, \Phi(v) \tilde{f}(v) \quad . \tag{7.40}$$

Any reasonable closure ansatz for the conditional averages has to fulfill these integral constraints. Now a very simple argument can be introduced to close the set of equations, which assumes statistical independence of large-scale and small-scale fields. We have seen in chapter 4 that the correlation function of the velocity decays slowly compared to the correlation functions related to the gradients of velocity. The same goes for the pressure gradient, which is usually assumed to be a strongly fluctuating quantity. In this sense one is apt to assume that when averaging over regions of nearly identical velocities, the

dissipation and pressure gradient fields fluctuate strongly such that averaging over these regions is approximately the same as averaging over the whole field. This *decoupling* argument is rather typical for analytical studies of turbulence and has, for example, been recently used in [FFO10]. On the other hand, as the forcing and the velocity both vary on large scales, statistical correlations are expected. A *linear response* of the velocity field to the external forcing here is the most simple ansatz. With these arguments the conditional averages of equation (7.22a) take the form

$$\Pi_0(v) = 0 \tag{7.41a}$$

$$\Phi_0(v) = \frac{\langle\varepsilon\rangle}{3\sigma^2} v \tag{7.41b}$$

$$\Lambda_0(v) = -\frac{\langle\varepsilon\rangle}{3\sigma^2} v \quad , \tag{7.41c}$$

showing that this assumption leads to vanishing pressure contributions and a linear dependence of the diffusive and forcing term on the velocity. Note that the relation for Λ_0 is a direct result of the conditional balance (7.24) for stationary turbulence and equations (7.41a) and (7.41b). If decoupling is assumed for the conditional dissipation tensor, it has to simplify to an isotropic tensor of rank two, which is determined by its trace only. Consequently we obtain

$$\lambda_0(v) = \mu_0(v) = \frac{\langle\varepsilon\rangle}{3} \quad , \tag{7.42}$$

i.e., the eigenvalues coincide and may be expressed in terms of the average rate of kinetic energy dissipation. Inserting these approximations into the solutions of the PDF equation (7.25) or (7.26) yields

$$\tilde{f}(v;t) = \sqrt{\frac{2}{\pi}} \frac{v^2}{\sigma(t)^3} \exp\left(-\frac{1}{2}\frac{v^2}{\sigma(t)^2}\right) \quad , \tag{7.43}$$

which is the angle-integrated Gaussian distribution[2], i.e., the velocity *vector* is distributed according to a Gaussian

$$f(\boldsymbol{v};t) = \frac{1}{(2\pi\sigma(t)^2)^{3/2}} \exp\left(-\frac{1}{2}\frac{\boldsymbol{v}^2}{\sigma(t)^2}\right) \quad . \tag{7.44}$$

One should be aware of the fact that this result is no proof for Gaussianity as it is not clear at this point whether the approximations made are appropriate for real turbulent flows. It shall rather point out that deviations from Gaussianity should be expected if these simple assumptions are not found to be true. In fact, we will find non-negligible deviations from these approximations when the DNS results are considered. Furthermore,

[2] This distribution is also known as Maxwell distribution. Whenever we loosely speak in this thesis of a Gaussian PDF in the context of a magnitude of a vector, Gaussianity refers to the statistics of the vector, which results in a Maxwellian for the magnitude.

we would like to point out that the results arrived at coincide with the results obtained, for example, by [UL69, Hos08]. In these works, however, the closure assumptions are introduced on the level of the two-point PDF. Although the results do not differ, we think that introducing closure approximations on the level of the conditional averages helps to formulate physically sound and well-controlled closures.

The physical reasoning introduced so far can be made mathematically more precise if functional constraints imposed by isotropy are studied. To this end one considers equations (7.11) and (7.12) for the special case of $\boldsymbol{v} = \boldsymbol{0}$. This implies

$$\left\langle -\nabla p \middle| \boldsymbol{v} = \boldsymbol{0} \right\rangle = \boldsymbol{0} \quad \Rightarrow \quad \Pi(0) = 0 \tag{7.45a}$$

$$\left\langle \nu \Delta \boldsymbol{u} \middle| \boldsymbol{v} = \boldsymbol{0} \right\rangle = \boldsymbol{0} \quad \Rightarrow \quad \Lambda(0) = 0 \tag{7.45b}$$

$$\left\langle \boldsymbol{F} \middle| \boldsymbol{v} = \boldsymbol{0} \right\rangle = \boldsymbol{0} \quad \Rightarrow \quad \Phi(0) = 0 \quad , \tag{7.45c}$$

showing that the conditional averages of the kinetic equation (7.22a) have to vanish at the origin. A similar observation can be made for the eigenvalues of D. As δ_{ij} is the only isotropic tensor of rank two in three dimensions, we can conclude

$$D_{ij}(\boldsymbol{v} = \boldsymbol{0}) \sim \delta_{ij} \quad \Rightarrow \quad \lambda(0) = \mu(0) \quad , \tag{7.46}$$

i.e., the eigenvalues have to coincide at the origin. Additional information can be gained by considering the derivatives of the conditional averages. We start with taking the second derivative of the scalar function α determining the conditional vector $\boldsymbol{a}$ in (7.12)

$$\frac{\mathrm{d}^2 \alpha}{\mathrm{d}v^2}(v) = \left[\frac{\partial}{\partial v_i} \frac{\partial}{\partial v_j} a_k(\boldsymbol{v}) \right] \frac{v_i \, v_j \, v_k}{v^3} \quad . \tag{7.47}$$

The expression $\frac{\partial}{\partial v_i} \frac{\partial}{\partial v_j} a_k(\boldsymbol{v})$ constitutes a tensor of rank three, which is symmetric in i and j. Now evaluating this expression for $\boldsymbol{v} = \boldsymbol{0}$ yields an isotropic tensor of rank three symmetric in i and j. Such a tensor, however, does not exist. We can conclude that this expression has to vanish, which implies

$$\left. \frac{\mathrm{d}^2 \alpha}{\mathrm{d}v^2} \right|_{v=0} = 0 \quad . \tag{7.48}$$

The same argumentation applies to higher derivatives, as for isotropic statistics no isotropic tensors of odd rank exist. This leads to the conclusion

$$\left. \frac{\mathrm{d}^n \Pi}{\mathrm{d}v^n} \right|_{v=0} = \left. \frac{\mathrm{d}^n \Lambda}{\mathrm{d}v^n} \right|_{v=0} = \left. \frac{\mathrm{d}^n \Phi}{\mathrm{d}v^n} \right|_{v=0} = 0 \,, \quad \text{if } n \text{ is even} \quad . \tag{7.49}$$

This strategy, of course, can also be applied to the conditional dissipation tensor. Here, however, D_{ij} is symmetric in i and j, such that the argumentation already applies for the first derivative. One, for example, obtains

$$\frac{\mathrm{d}\lambda}{\mathrm{d}v}(v) = \left[\frac{\partial}{\partial v_k} D_{ij}(\boldsymbol{v}) \right] \frac{v_i \, v_j \, v_k}{v^3} \tag{7.50}$$

which has the consequence

$$\left.\frac{\mathrm{d}\lambda}{\mathrm{d}v}\right|_{v=0} = 0 \quad . \tag{7.51}$$

When higher derivatives are considered we obtain

$$\left.\frac{\mathrm{d}^n\lambda}{\mathrm{d}v^n}\right|_{v=0} = \left.\frac{\mathrm{d}^n\mu}{\mathrm{d}v^n}\right|_{v=0} = 0\,, \quad \text{if } n \text{ is odd} \quad . \tag{7.52}$$

The relations (7.49) and (7.52) have the interesting implication that if the conditional averages are expanded in powers of v around $v = 0$, the expansion for Π, Λ and Φ only contains odd powers, whereas the expansion of λ and μ only contains even powers. In this sense the physical approximation introduced in this section represents a lowest-order approximation, which is consistent with the integral constraints (7.38)-(7.40).

7.3. DNS results

After this theoretical investigation of the kinetic equations we turn to the numerical evaluation of the unclosed terms. We would like to stress that an appropriate simulation should be both well-resolved and long. The resolution of the fine scales is important as derivatives of the velocity field like, for example, the rate of kinetic energy dissipation are considered. The duration of the simulation is particularly important to obtain homogeneous isotropic statistics as we have demonstrated at the end of chapter 3. Consequently, in view of limited computational ressources it is better to use data from a long 512^3 simulation at a rather moderate Reynolds number than from a short 1024^3 simulation at higher Reynolds number. If not stated differently, the following results are obtained from the simulation `sim_512`.

7.3.1. Role of the Pressure Gradient, External Forcing and Diffusion

We start with considering the conditional averages appearing in the kinetic equation (7.22a) in figure 7.1. The conditional forcing term represented by $\Phi(v)$ is positively correlated with the velocity, indicating that for given velocity v a fluid particle will on average be accelerated due to this term. The dependence of different forcing mechanisms has been tested and the results proved to be robust. It is not clear at this point how this finding is consistent with the results presented in [FL97], who find that the tails of the PDF depend strongly on the precise forcing mechanism. The diffusive term represented by $\Lambda(v)$ is negatively correlated with the velocity and consequently tends to decelerate a fluid particle on average. These observations are physically intuitive as the forcing is supposed to inject energy into the fluid, whereas the diffusive term dissipates energy. The pressure gradient term has a particularly interesting shape exhibiting a zero-crossing. The interpretation is that a fluid particle will be decelerated due to this term for low to moderate velocities, but will be accelerated for higher velocities beyond this zero-crossing. The zero-crossing can already be expected from the theoretical

considerations above; since the pressure has to fulfill the integral constraint (7.38), this term either has to vanish or has to display at least one zero-crossing. One should stress at this point that the pressure term is neglected in a number of theoretical works on the subject [Hos08, TY04], such that there the closure of the single-point equation reduces to specifying the dissipative terms. At least in [Hos08] it becomes clear that this term is neglected due to a bug in the mathematical argumentation, when the gradient of the pressure term is taken. From the theoretical derivation presented above there is no reason to expect a vanishing of this term, however, a zero contribution is at least consistent with the integral constraint (7.38). Our numerical results explicitly show that the pressure contribution is not negligible, and so this term contributes to the functional shape of the PDF. The second thing to be stressed is that the conditional averages obtained by the DNS differ strongly from the analytical Gaussian closure approximations (7.41a), (7.41b) and (7.41c). In this approximation the pressure term is assumed to vanish and the forcing is a linear function in v, however, with a different slope than found for the roughly linear function from the DNS data. It is furthermore clear that (7.41c) yields a poor match for the bended shape of Λ.

Taking all three conditional averages together they add up according to the conditional balance (7.24) showing that the conditional acceleration exerted on a fluid particle is zero in stationary turbulence. In fact, we have calculated the forcing contribution exploiting this balance. The reason for that is that the forcing is applied implicitly to the velocity field as described in chapter 3. As a consequence, it is not available as an additive field that we can average over.

Having investigated these terms, the information needed to close the kinetic equation (7.22a) is in principle available. However, apart from the interesting functional form of each of the terms, the only conclusion that can be drawn from this formulation is that the conditional acceleration vanishes. To determine the shape of the PDF with the help of the homogeneous or stationary solutions (7.25) and (7.26), the eigenvalues of the conditional dissipation tensor have to be investigated.

7.3.2. Structure of the Conditional Energy Dissipation Tensor

The eigenvalues of the conditional dissipation tensor are displayed in figure 7.2. First one can note that the functional form of both eigenvalues is very similar; for low values of velocity the conditional averages are approximately constant and increase strongly for high values. The similarity of both eigenvalues indicates only weak directional correlations of both fields ($\mathrm{A}\mathrm{A}^T$ and $\boldsymbol{u}$). To explain this in more detail, one can assume that the projection of the conditional dissipation tensor onto a unit vector in direction of the velocity coincides with projection onto a random direction $\hat{\boldsymbol{d}}$, which yields the relation

$$\hat{\boldsymbol{v}}\,\mathrm{D}(\boldsymbol{v})\,\hat{\boldsymbol{v}} = \left\langle \nu(\mathrm{A}^T\hat{\boldsymbol{u}})^2 \middle| \boldsymbol{v} \right\rangle = \left\langle \nu(\mathrm{A}^T\hat{\boldsymbol{d}})^2 \middle| \boldsymbol{v} \right\rangle = \frac{1}{3}\mathrm{Tr}\mathrm{D}(v)\,\mathrm{E} \quad . \tag{7.53}$$

The last equality mirrors the fact that the average projection of a matrix of the form (7.19a) onto a random direction yields one third of its trace times the unit matrix. This

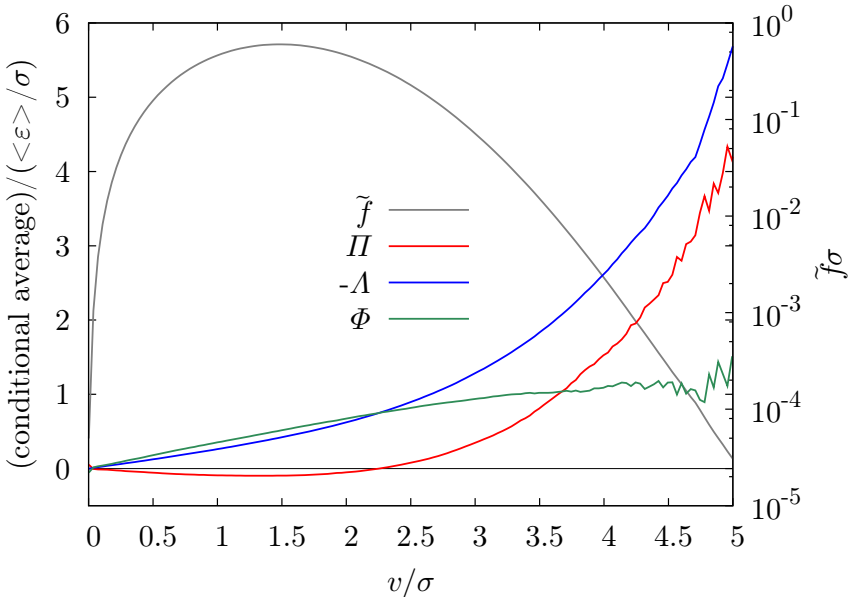

Figure 7.1.: Conditional averages Π, Λ and Φ from the kinetic equation (7.22a). The pressure term Π exhibits a zero-crossing, whereas the forcing term Φ is purely positively correlated with the velocity and the diffusive term Λ is purely negatively correlated with the velocity.

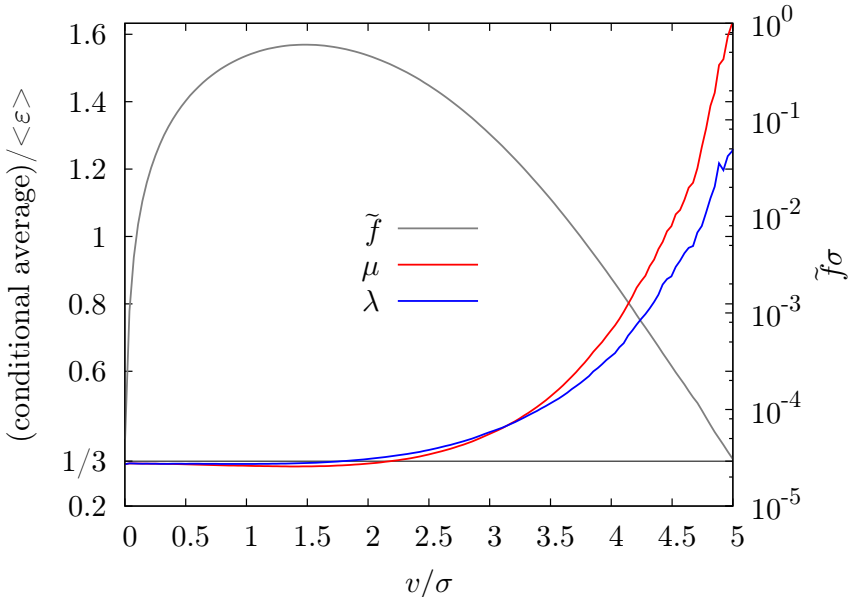

Figure 7.2.: Eigenvalues μ and λ of the conditional dissipation tensor D. For low velocities the eigenvalues are approximately constant. Stronger correlations with the velocity appear for higher values of v.

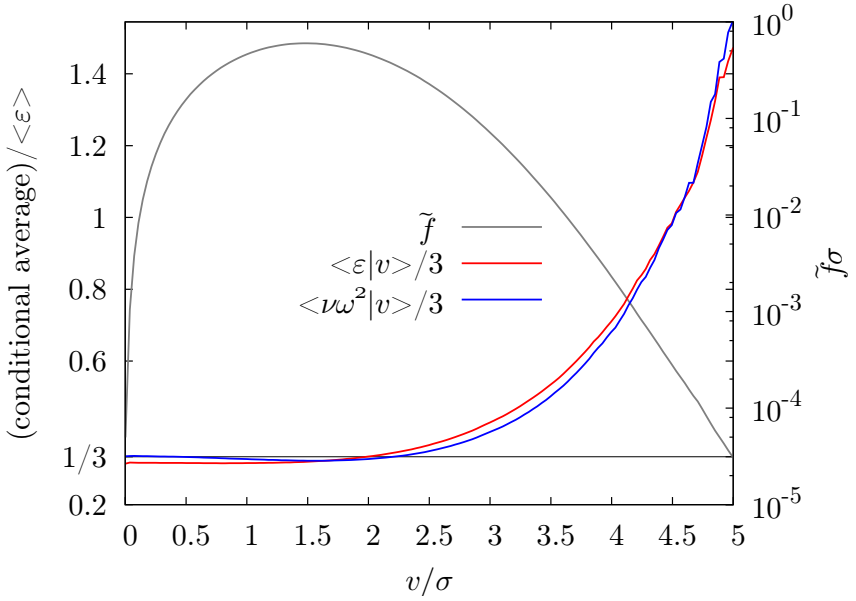

Figure 7.3.: Conditional rate of energy dissipation and squared vorticity times ν. For low values of velocity both functions are approximately constant indicating only minor statistical correlations in this range. For higher values strong correlations exist.

in turn implies $\lambda(v) = \mu(v)$.

Furthermore, the approximately constant behavior of the two eigenvalues for low to moderate values of velocity shows that the dissipative terms and the velocity are almost uncorrelated in this range. However, it can be seen that correlations become important for higher velocities, which may be regarded as a signature of intermittency.

These observations are qualitatively consistent with figure 1.1, where both the velocity and the dissipation field are shown. It is clear to see that the velocity varies on a much larger scale than the fine-scaled dissipation field, which makes the decoupling argument presented in section 7.2.5 appear as a rather reasonable approximation for the conditional dissipation tensor when low velocities corresponding to the core of the PDF are considered.

Seeking for possible approximations of the conditional dissipation tensor, one can conclude that ignoring directional correlations, but maintaining the dependence on the magnitude of velocity, which corresponds to the choice $\lambda = \mu$, leads to a reasonable approximation. In this case the conditional dissipation tensor is specified by its trace only, which may be expressed as

$$\mathrm{TrD} = \lambda(v) + 2\mu(v) = \langle \varepsilon + \nu\omega^2 | v \rangle \quad . \tag{7.54}$$

On the other hand, it is a well-known fact that for homogeneous turbulence the equality

$$\langle \varepsilon \rangle = \langle \nu\omega^2 \rangle \tag{7.55}$$

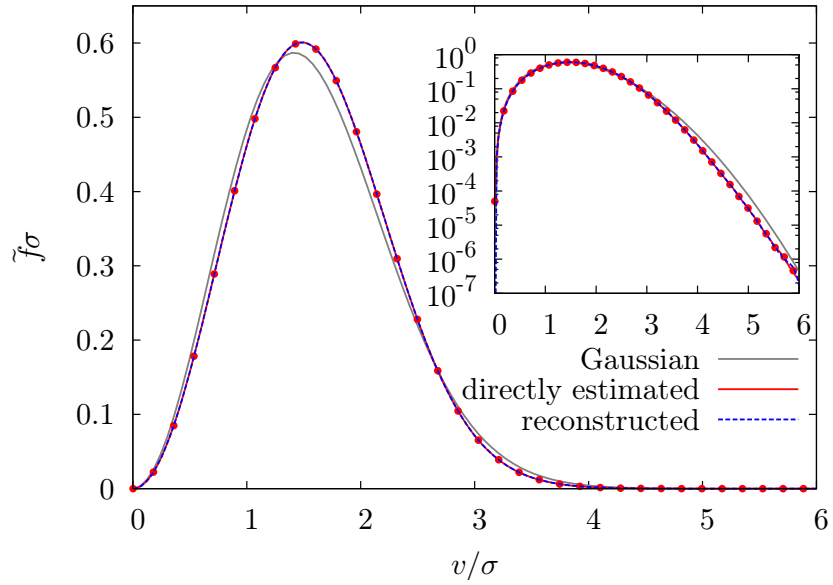

Figure 7.4.: Directly estimated and reconstructed velocity PDF according to equation (7.25) and (7.26) along with an angle-integrated Gaussian. The agreement is perfect demonstrating the consistency of the theoretical framework. Significant deviations from the Gaussian shape are observed in the form of sub-Gaussian tails.

holds, such that the obvious question can be raised whether this equality also holds in a stricter, conditionally averaged sense. This question can be answered with figure 7.3, where $\langle\varepsilon|v\rangle$ and $\langle\nu\omega^2|v\rangle$ are shown demonstrating that this equality approximately also holds for the conditionally averaged quantities. It can be seen from figure 1.1, however, that both quantities do not coincide pointwise in space, but only on the single-point level. Taking these results together, the conditional dissipation tensor can be approximated as

$$D_{ij}(\boldsymbol{v}) = \frac{1}{3}\langle\varepsilon|v\rangle\,\delta_{ij} \quad . \tag{7.56}$$

Note that, in contrast to the "lowest-order" approximation presented in section 7.2.5, here the *conditionally* averaged rate of energy dissipation is used.

7.3.3. Reconstruction of the Homogeneous and Stationary PDFs

We now come to the explicit evaluation of equations (7.25) and (7.26), where we insert the numerically obtained conditional averages. The result is depicted in figure (7.4), from which a perfect agreement between the PDF obtained directly from the DNS data and the theoretical results is apparent. It should be stressed that this is not very surprising as the homogeneous and stationary solutions are directly derived from the basic equation of motion and the unknown terms have been determined directly from

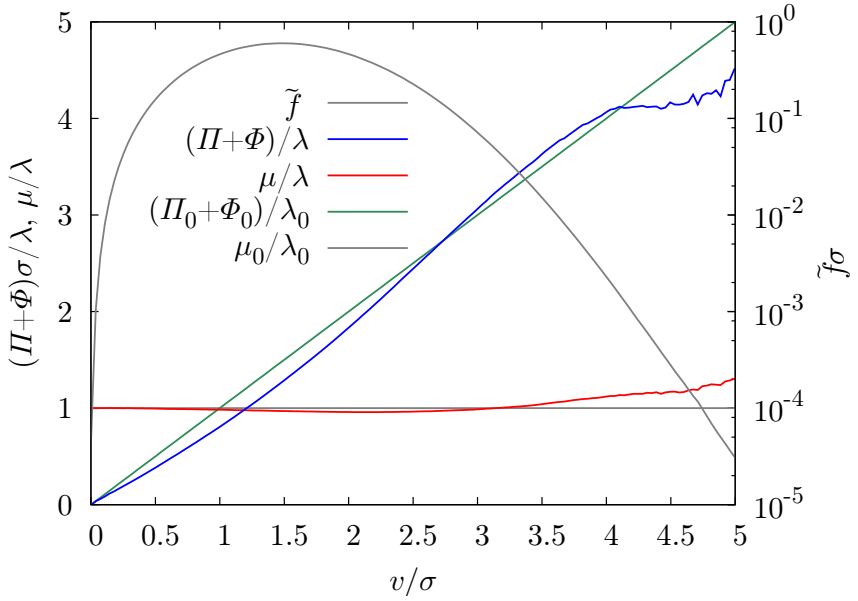

Figure 7.5.: The quotients $(\Pi + \Phi)/\lambda$ and μ/λ appearing in equation (7.26) show an approximately linear and constant functional form, respectively. The corresponding quotients expected from the analytical Gaussian closure approximation (7.41a)–(7.42) are shown for comparison.

the DNS data. Still, the agreement serves as a check for consistency. Furthermore, as both the DNS data and the homogeneous (or stationary) solution deviate significantly from the Gaussian form, it can be concluded that these deviations come due to the subtle interplay of the statistical correlations observed for the conditional averages.

In view of this result two questions are rather obvious: Why does the analytical Gaussian closure presented in section 7.2.5 not fail completely, although the individual conditional averages differ strongly from the ones observed in DNS? How do the observed rather pronounced statistical dependences coact, leading to rather moderate deviations from Gaussianity of the velocity PDF? Both questions can be answered by a closer investigation of the homogeneous and stationary solutions (7.25) and (7.26), where we choose the latter equation to discuss the issue. It can be seen from this equation that Gaussian solutions are obtained if $(\Pi + \Phi)/\lambda$ is linear, $\mu = \lambda$ and $\lambda = \text{const}$. The first relation causes a quadratically decaying exponential factor, the second will give the v^2 prefactor of the angle-integrated Gaussian (cf. equation (7.43)). With these two relations the Gaussian shape is already obtained. The third relation ensures that the prefactor in (7.26) does not lead to further deviations. It can be noted that these conditions are met in the case of the analytical closure approximation, which consequently yields a Gaussian distribution. The numerically obtained conditional averages $(\Pi + \Phi)/\lambda$ and μ/λ are presented in figure 7.5 along with the corresponding quantities for the Gaussian closure approximation. It can be seen that the pronounced statistical correlations observed in

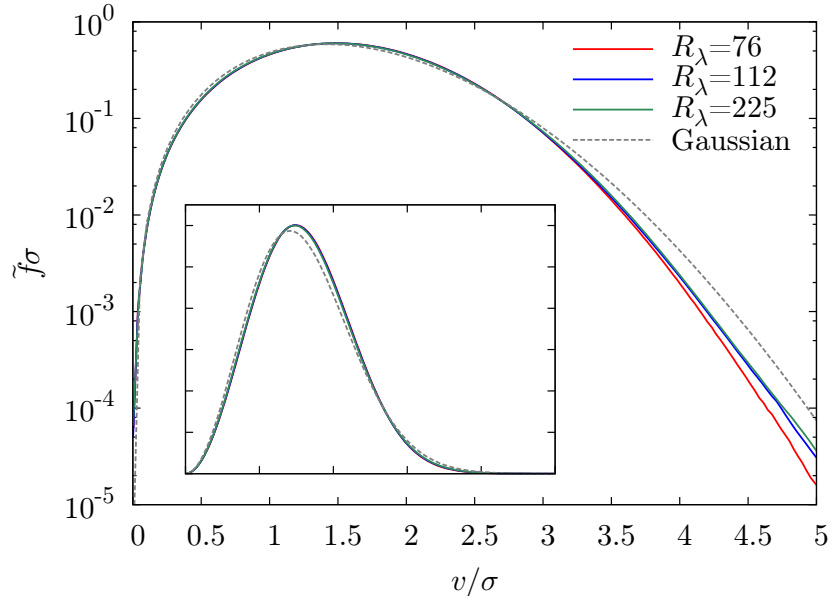

Figure 7.6.: Velocity PDFs for different Reynolds numbers (`sim_256`, `sim_512`, `sim_1024`). All PDFs deviate systematically from a Gaussian shape.

figures 7.1 and 7.2 cancel to a good extent, such that the conditions for a Gaussian shape are nearly met. The remaining deviations then lead to the deviation from the Gaussian shape of the PDF. These deviations are further modified by the functional form of λ shown in figure 7.2 due to the non-constant behavior of λ for large v. While the comparison of the conditional averages obtained within the closure approximations with the numerically obtained ones in the last two sections performed poorly, their combinations as appearing in equation (7.26) compare much better, which explains both the nearly Gaussian behavior of the velocity PDF itself as well as the observation that the analytical Gaussian closure approximation yields reasonable results.

7.3.4. Reynolds Number Dependence

A rather obvious question we would like to pursue in this section is the Reynolds number dependence of the results presented so far. To this end we compare the PDFs and conditional averages of the simulations `sim_256`, `sim_512` and `sim_1024` with the Taylor-based Reynolds numbers $R_\lambda = 76$, $R_\lambda = 112$ and $R_\lambda = 225$, respectively. It should be mentioned as a word of caution that these simulations do not only differ in Reynolds number, but, for example, are differently well resolved. Furthermore, the statistical quality varies between the three runs. Additionally the range of Reynolds numbers covered is rather small, but this is the best we can do at present.

We start with an inspection of the velocity PDFs in figure 7.6 from which can be seen that the PDFs display deviations from Gaussianity in all three cases. Interestingly, the

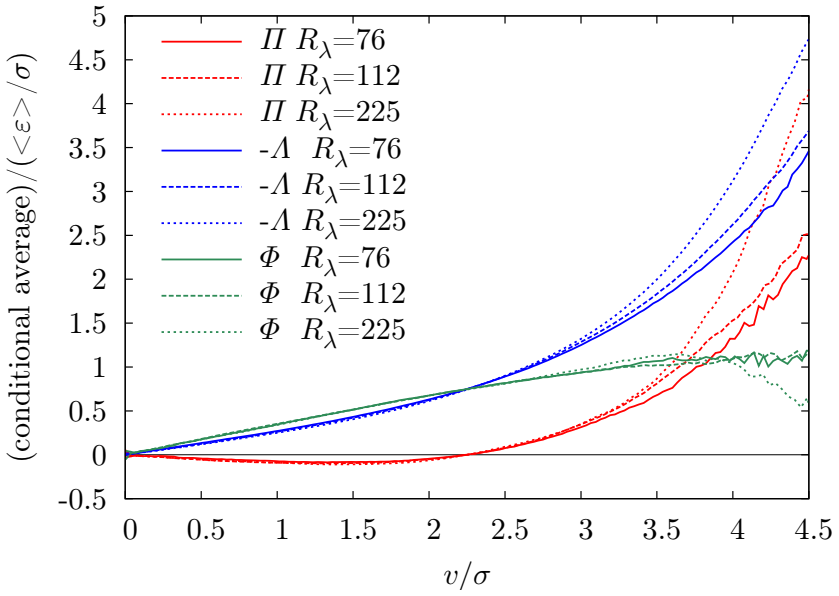

Figure 7.7.: Conditional averages Π, Λ and Φ from the kinetic equation (7.22a) for different Reynolds numbers (`sim_256`, `sim_512`, `sim_1024`).

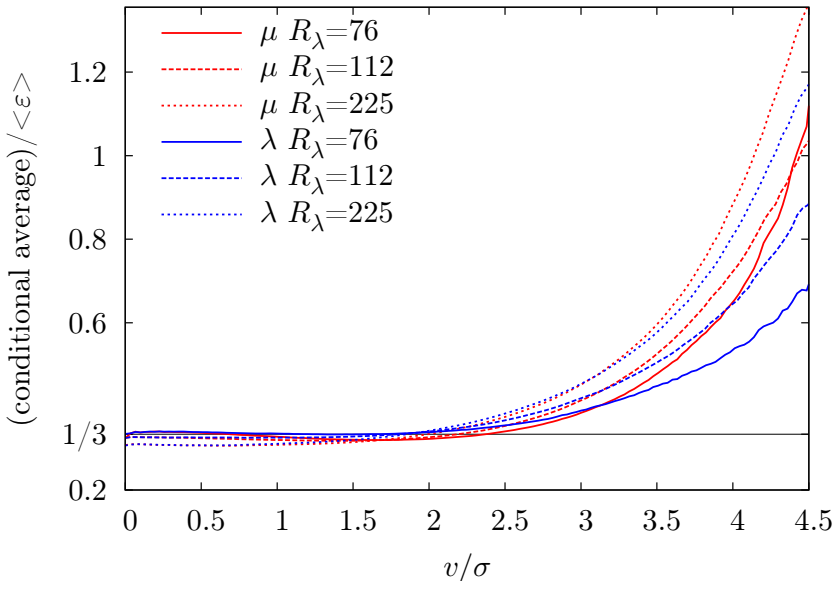

Figure 7.8.: Eigenvalues μ and λ of the conditional dissipation tensor D for different Reynolds numbers (`sim_256`, `sim_512`, `sim_1024`).

run at the lowest Reynolds number $R_\lambda = 76$ displays the strongest deviations in the tail, however, this trend is not continued for the higher Reynolds number runs. In the non-logarithmic inset the PDFs do not show any significant differences, such that the dependence of the PDF on the Reynolds number, both in shape and range of covered velocities, seems weak.

The conditional averages Π, Λ and Φ from the kinetic equation (7.22a) are shown in figure 7.7. First of all, one can note that the conditional averages nearly collapse for low to moderate values of velocity. For higher values it appears that the statistical correlations of the diffusive and the pressure gradient term increase with the Reynolds number, while the forcing appears to be less dependend on the Reynolds number. Due to the limited statistical quality it is, however, not possible to draw definite conclusions here.

A similar behavior can be observed for the eigenvalues of the conditional dissipation tensor shown in figure 7.8. For moderate values of velocity these statistical quantities do not change much with the Reynolds number. For higher values of velocity the deviations from statistical independence increase with the Reynolds number.

Based on these numerical results, it appears as if the shape of the velocity PDF does not vary strongly with the Reynolds number. This fact is accompanied by the observation that the conditional pressure and dissipative terms display statistical dependences on the velocity which slightly increase with the Reynolds number without changing the shape of the velocity PDF too much, i.e., they cancel to a good extent. A broader study of different numerical results including simulations at much higher Reynolds number would interesting at this point.

7.3.5. Decaying Turbulence

We now want to turn to an investigation of decaying turbulence. Apart from being interesting on its own, it helps to further clarify the origin of the deviations of the velocity PDF from Gaussianity. It was reasoned by Falkovich and Lebedev [FL97] that deviations from Gaussianity may originate from the external forcing. Conversely, it was hypothesized by Hosokawa [Hos08] that decaying turbulence may be profoundly different from stationary turbulence and, as discussed above, Gaussian solutions have been found under certain closure approximations.

For the case of decaying turbulence it is of course not allowed to take a temporal average over a run as the statistics is non-stationary. To obtain statistically convergent results, we have taken twelve statistically independent initial conditions from a run identical to the run `sim_512` and let them decay for about five large-eddy turnover times (in terms of the initial turnover times). During this decay the energy is decreased by more than one order of magnitude.

The first question to investigate, of course, is how the PDF of the velocity evolves over the time. This is shown in figure 7.9 where several PDFs separated by $0.35T$ are shown. The variance of the PDFs decreases over time as the kinetic energy is dissipated. The temporal evolution of the kinetic energy and the rate of kinetic energy dissipation

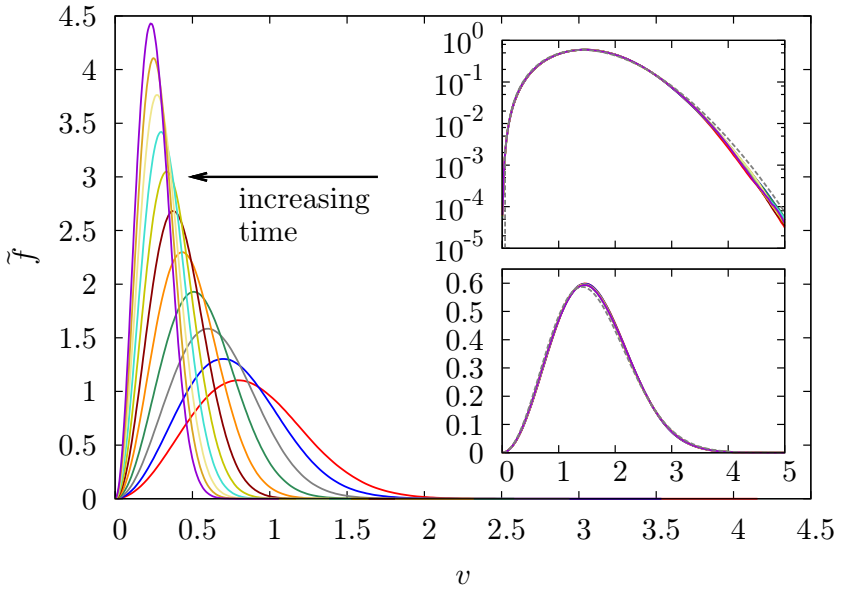

Figure 7.9.: Velocity PDFs for decaying turbulence separated by $0.35T$. As kinetic energy is dissipated, the variance decreases over time. When rescaled to unit variance, the PDFs collapse, indicating a self-similar decay, in which deviations from Gaussianity are apparent. The dashed gray line in the insets corresponds to an angle-integrated Gaussian.

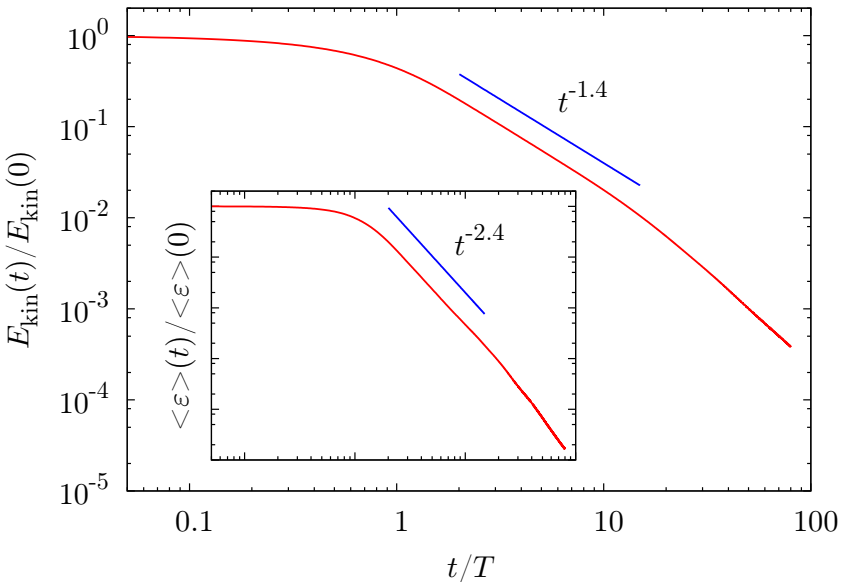

Figure 7.10.: Decay of kinetic energy and the rate of energy dissipation. After a short transient an algebraic decay regime can be observed.

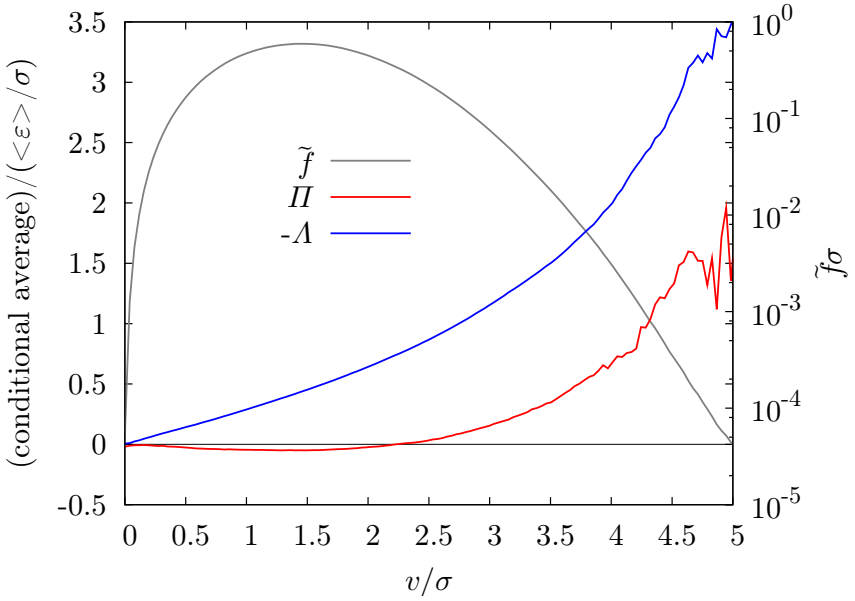

Figure 7.11.: Conditional averages Π and Λ from the kinetic equation (7.22a) for decaying turbulence after $1.4T$. The behavior is very similar to the stationary case.

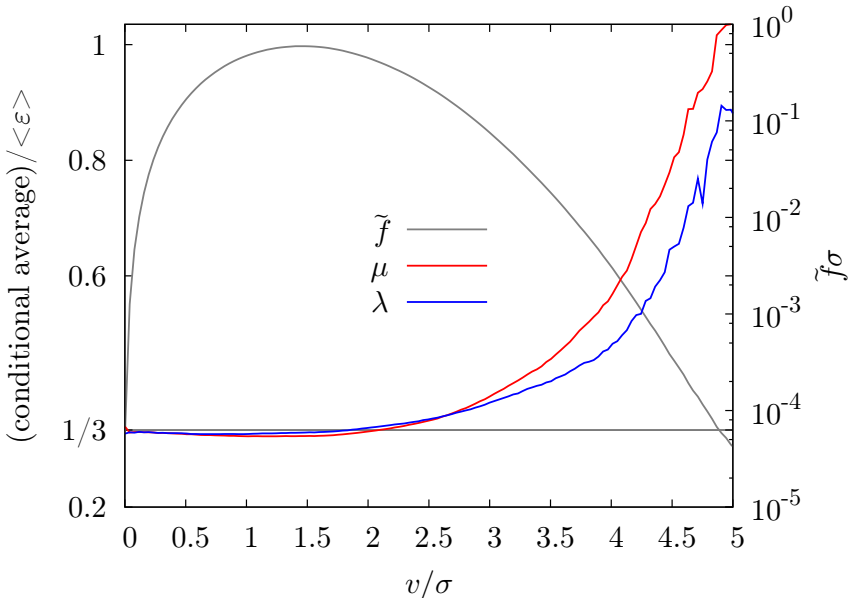

Figure 7.12.: Eigenvalues μ and λ of the conditional dissipation tensor D for decaying turbulence after $1.4T$. Also the conditional dissipation tensor is very similar to the one in the stationary case.

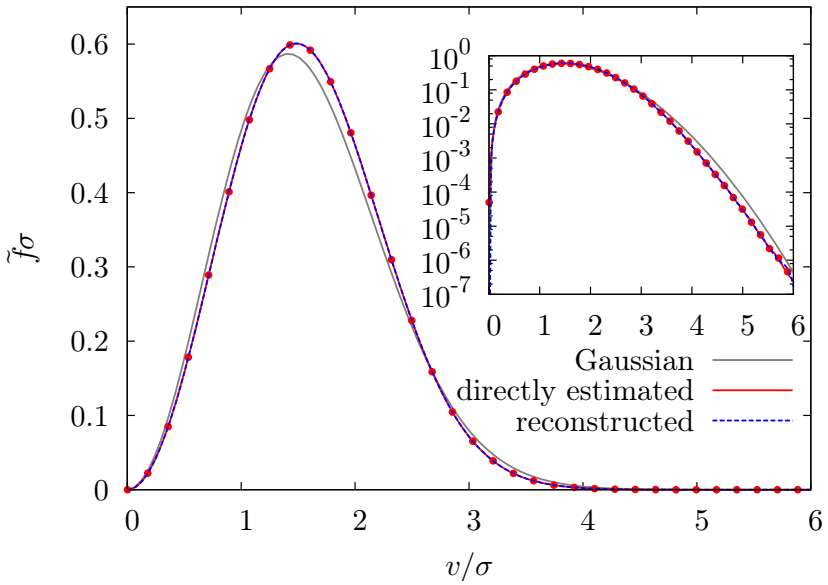

Figure 7.13.: Directly estimated and reconstructed velocity PDF according to equation (7.25) for decaying turbulence after $1.4T$.

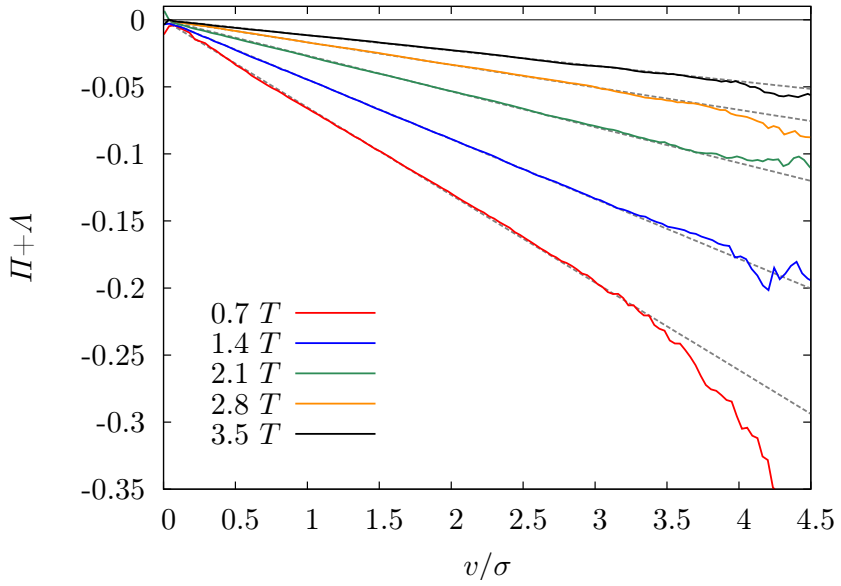

Figure 7.14.: Conditional acceleration $\Pi+\Lambda$ in decaying turbulence together with the analytical result (7.34). The conditional acceleration is a linear function of the velocity, slight deviations are apparent for the tails for high values of velocity. The dashed gray lines indicate the analytical prediction (7.34).

are shown in figure 7.10, where it can be seen that both the kinetic energy as well as the dissipation follow an algebraic decay with exponents of approximately 1.4 and 2.4, respectively, after a short transient. This transient indicates that turbulence somehow has to "relax" from the forced regime to the freely evolving decaying regime. Under the assumption of a purely algebraic decay the exponents for the kinetic energy and the dissipation are not independent and linked by the law of energy decay (7.37). This explains the observed difference of the two exponents of one. Slight deviations can be seen from figure 7.10, which may originate from the fact that the decay is not perfectly algebraic. Beyond this time a third regime may be surmised from figure 7.10, in which the energy has decayed to less than one percent of the initial value. It may be hypothesized that this regime corresponds to the final period of decay, in which most nonlinear interactions already have ceased.

When the PDFs are rescaled to unit variance, they collapse, indicating a self-similar decay regime (see figure 7.9). During this regime deviations from Gaussianity similar to the stationary case are apparent as a comparison with a Gaussian (dashed gray lines) shows. Hence our simulations do not confirm Hosokawa's hypothesis that decaying turbulence in general is expected to yield Gaussian single-point velocity statistics. This observation can be made more precise by studying the conditional averages that appear in the kinetic equations. The conditional pressure term and the diffusive term are shown in figure 7.11, whereas the eigenvalues of the conditional dissipation tensor are presented in figure 7.12. The results presented were obtained after a decay time of $1.4T$ and may serve as a representative example here. Compared to the evaluations for stationary turbulence in figures 7.1 and 7.2, the investigation of decaying turbulence yields very similar results, the observed statistical correlations do not display a qualitatively different functional form. It can be concluded that the observations regarding the statistical quantities carry over to the decaying case. This can be additionally supported by checking the homogeneous solution (7.25) against the directly obtained PDF, which is done in figure 7.13. The reconstruction performs as well as in the stationary case, showing that the velocity PDF also in decaying turbulence is the result of the interplay of the different conditional averages. Although this does not seem very surprising at this point, these results imply that the functional shape of the PDF is not strongly influenced by the type of forcing, as opposed to the suggestions by Falkovich and Lebedev [FL97], because this term is absent in the decaying case. One should note that it only makes sense to evaluate the homogeneous solution (7.25) in the decaying case as the turbulence is non-stationary.

In the theoretical section 7.2.3 we have derived an exact expression for the conditional acceleration for the case of a self-similar decay of the velocity field. The relation (7.34) predicts a linear function in v with the slope depending on the ratio of the rate of kinetic energy dissipation and the kinetic energy. As our numerical results suggest a self-similar decay, the relation can be compared to our simulation data. The results are presented in figure 7.14, in which a good agreement between the expected analytical relation and the DNS data is found. Slight deviations appear in regions of poor statistics. We stress once more that only the observation of a self-similar decay suffices to deduce this relation,

which in a sense reduces the closure problem of the single-point PDF equation to specify the temporal evolution of the kinetic energy and the rate of energy dissipation. If additionally an algebraic decay of the kinetic energy is assumed, the temporal behavior of the rate of energy dissipation is fixed, as explained above, simplifying the problem even more.

Altogether the results of this section document that the single-point velocity statistics in decaying turbulence does not fundamentally differ from forced stationary turbulence.

7.4. Summary

In this chapter we have investigated the single-point velocity statistics in turbulence both analytically and numerically. The presented approach allows for a unified description of decaying and stationary turbulence within the exact theoretical framework of the LMN hierarchy. On the theoretical side we have used statistical symmetries to simplify the kinetic equations. This especially allows to derive new exact formal expressions for the PDF for homogeneous and stationary turbulence, which can be regarded as one of the main results of this chapter. Furthermore, the PDF equation has been investigated for the case of decaying turbulence, where a relation for the conditional acceleration could be derived under the assumption of a self-similar decay.

A deeper analysis has pointed out functional and integral constraints which narrow down the possible functional shapes of the unclosed terms in the PDF equation. Based on these constraints and paralleled by physical arguments, an analytical closure has been suggested that yields Gaussian statistics. The scope of this closure, however, is not to claim the velocity statistics to be Gaussian, but to demonstrate which assumptions lead to this kind of statistics.

The theoretical investigations then have been supplemented and completed by extensive numerically obtained results for stationary turbulence at different Reynolds numbers as well as for decaying turbulence. All simulations indicate pronounced statistical correlations of the quantities determining the shape and evolution of the velocity PDF with the velocity. In particular, pronounced differences to the analytical closures have been found. It has been shown that the combination of these statistical correlations eventually leads to the sub-Gaussian shape of the PDF. It should be stressed that only the *joint* numerical and analytical investigation of the PDF equation has permitted this comprehensive analysis.

8. Single-Point Statistics of the Turbulent Vorticity

8.1. Motivation

Our theoretical and numerical investigations so far have been focussed on the description of fully developed turbulence in terms of the velocity field. Incompressible flows, however, can also be described in terms of the vorticity as explained in chapter 1. Moreover, it has been motivated that the vorticity field tends to be more localized than the velocity field. This either can be understood intuitively by identifying coherent structures, as exemplified in figures 1.1 and 1.4, but is also mirrored by statistical quantities like the correlation functions determining the vorticity covariance tensor presented in figure 4.16. These observations foster hope that the vorticity is maybe "more fundamental" than the velocity field in the sense that it might be more accessible to the application of physical arguments based on the study of individual coherent structures. The fact that analytical vortex solutions such as the Burgers vortex are available give further motivation for this view. On the statistical side the single-point vorticity PDF displays highly non-Gaussian tails, as presented in figure 4.2, indicating that strong vorticity events are much more likely in turbulence than for a Gaussian random field, which makes the vorticity statistics especially interesting to study.

In view of these remarks it is somewhat surprising that the statistical description of the vorticity field based on first principles has not been given nearly as much attention as the statistical theory of the velocity field. The vorticity field has been studied more deeply in the context of coherent structures (see, e.g., [SJO90]) and many phenomenological theories have been developed studying turbulence in terms of an ensemble of vortex structures [Tow51, Lun82, HK97, MHK03, MHK04, WJF08]. Hence it is of central interest to develop a statistical theory of turbulence based on the vorticity field. Work on this has been initiated by Novikov already decades ago and was continued up to the recent past [Nov68, Nov93, ND94, MDN96]. Interestingly, these works have not been paid much attention by the part of the community dealing with kinetic equations for the velocity field [Lun08], which also can be concluded from the fact that the corresponding works of Novikov are not often cited.

As we will demonstrate in the following, the two hierarchies have formally very much in common, and we will actually use Lundgren's approach to derive the hierarchy of evolution equations for the vorticity field. Still, some major differences stemming from the different spatial and consequently statistical structure of the turbulent fields make a combined study of the vorticity and velocity field particularly valuable. This brings

us to the outline of the present chapter. We first will derive the LMN hierarchy for the vorticity field, however, in a more condensed form than for the velocity field as many details have been given already in chapters 6 and 7. We then will turn to a closer investigation of the single-point vorticity PDF equation and again will exploit statistical symmetries to simplify its mathematical structure. Before we derive the homogeneous and stationary solutions of the PDF equation, the continuity version of the PDF equation will be discussed in more detail. As in the preceding chapter, we then will use simulation results to study the unclosed terms in more detail. Here, especially the conditional balance of the right-hand side of the vorticity equation will be of interest as well as the structure of the conditional enstrophy dissipation tensor.

Some of the results have been published in [WF09a].

8.2. LMN Hierarchy for the Vorticity

As for the case of the velocity, our derivation starts with the fine-grained PDF, now for the vorticity vector,

$$\hat{f}_1(\boldsymbol{\Omega}_1;\boldsymbol{x};t) = \delta(\boldsymbol{\omega}(\boldsymbol{x}_1,t) - \boldsymbol{\Omega}_1) \quad , \tag{8.1}$$

where $\boldsymbol{\omega}(\boldsymbol{x}_1,t)$, of course, denotes a realization of the vorticity field considered at a point $\boldsymbol{x}_1$ at time t and $\boldsymbol{\Omega}_1$ denotes the corresponding sample space variable. As usual, the single-point PDF is obtained by ensemble averaging,

$$f_1(\boldsymbol{\Omega}_1;\boldsymbol{x};t) = \langle \hat{f}_1(\boldsymbol{\Omega}_1;\boldsymbol{x};t)\rangle = \langle \delta(\boldsymbol{\omega}(\boldsymbol{x}_1,t) - \boldsymbol{\Omega}_1)\rangle \quad . \tag{8.2}$$

In favor of a simple presentation we choose not to introduce an additional subscript to distinguish the probability density of the velocity from the probability density of the vorticity. If confusion is likely to occur, we will explicitly write out all arguments of the PDF.

Now following exactly the same steps as in the derivation of the fine-grained evolution equation for the velocity in section 6.2.2, we obtain the corresponding equation for the single-point vorticity,

$$\begin{aligned}
&\frac{\partial}{\partial t}\hat{f}_1(\boldsymbol{\Omega}_1;\boldsymbol{x}_1,t) + \nabla_{\boldsymbol{x}_1}\cdot\left[\boldsymbol{u}(\boldsymbol{x}_1,t)\hat{f}_1(\boldsymbol{\Omega}_1;\boldsymbol{x}_1,t)\right] \\
&= -\nabla_{\boldsymbol{\Omega}_1}\cdot\left[\left(\frac{\partial\boldsymbol{\omega}}{\partial t}(\boldsymbol{x}_1,t) + \boldsymbol{u}(\boldsymbol{x}_1,t)\cdot\nabla_{\boldsymbol{x}_1}\boldsymbol{\omega}(\boldsymbol{x}_1,t)\right)\hat{f}_1(\boldsymbol{\Omega}_1;\boldsymbol{x}_1,t)\right] \\
&= -\nabla_{\boldsymbol{\Omega}_1}\cdot\left[\left(\mathrm{S}(\boldsymbol{x}_1,t)\boldsymbol{\omega}(\boldsymbol{x}_1,t) + \nu\Delta_{\boldsymbol{x}_1}\boldsymbol{\omega}(\boldsymbol{x}_1,t) + \nabla_{\boldsymbol{x}_1}\times\boldsymbol{F}(\boldsymbol{x}_1,t)\right)\hat{f}_1(\boldsymbol{\Omega}_1;\boldsymbol{x}_1,t)\right] \quad .
\end{aligned} \tag{8.3}$$

Direct comparison with the corresponding equation for the velocity field (6.19) reveals a very similar mathematical structure with a convective derivative of the fine-grained PDF on the left-hand side and the divergence of the right-hand side of the vorticity equation (1.8) times the fine-grained PDF on the right-hand side. The right-hand side

is now governed by the vortex stretching term, the diffusive term as well as the term involving the curl of the external forcing. One should note, however, that now already the advective term on the left-hand side appears unclosed as the velocity field cannot be determined by knowledge of the single-point vorticity statistics only. To obtain the evolution equation for the PDF $f_1(\boldsymbol{\Omega}_1; \boldsymbol{x}_1, t)$, we take the ensemble average and obtain

$$\begin{aligned}&\frac{\partial}{\partial t} f_1(\boldsymbol{\Omega}_1; \boldsymbol{x}_1, t) + \nabla_{\boldsymbol{x}_1} \cdot \left\langle \boldsymbol{u}(\boldsymbol{x}_1, t) \hat{f}_1(\boldsymbol{\Omega}_1; \boldsymbol{x}_1, t) \right\rangle \\ &= -\nabla_{\boldsymbol{\Omega}_1} \cdot \left\langle \big(\mathrm{S}(\boldsymbol{x}_1, t)\boldsymbol{\omega}(\boldsymbol{x}_1, t) + \nu \Delta_{\boldsymbol{x}_1} \boldsymbol{\omega}(\boldsymbol{x}_1, t) + \nabla_{\boldsymbol{x}_1} \times \boldsymbol{F}(\boldsymbol{x}_1, t) \big) \hat{f}_1(\boldsymbol{\Omega}_1; \boldsymbol{x}_1, t) \right\rangle \quad .\end{aligned} \tag{8.4}$$

Of course, we now again have the option to express the unclosed terms through a coupling to higher orders or to introduce conditional averages as unknown functions. To express the unclosed terms as functionals of $f_2(\boldsymbol{\Omega}_1, \boldsymbol{\Omega}_2; \boldsymbol{x}_1, \boldsymbol{x}_2, t)$, we start with the diffusive term, which can be treated exactly as in the case of the velocity field. We evaluate

$$\begin{aligned}\left\langle \big(\nu \Delta_{\boldsymbol{x}_1} \boldsymbol{\omega}(\boldsymbol{x}_1, t) \big) \, \hat{f}_1(\boldsymbol{\Omega}_1; \boldsymbol{x}_1, t) \right\rangle &= \lim_{\boldsymbol{x}_2 \to \boldsymbol{x}_1} \left\langle \nu \Delta_{\boldsymbol{x}_2} \boldsymbol{\omega}(\boldsymbol{x}_2, t) \, \hat{f}_1(\boldsymbol{\Omega}_1; \boldsymbol{x}_1, t) \right\rangle \\ &= \lim_{\boldsymbol{x}_2 \to \boldsymbol{x}_1} \nu \Delta_{\boldsymbol{x}_2} \int \mathrm{d}\boldsymbol{\Omega}_2 \, \boldsymbol{\Omega}_2 \, f_2(\boldsymbol{\Omega}_1, \boldsymbol{\Omega}_2; \boldsymbol{x}_1, \boldsymbol{x}_2, t) \quad .\end{aligned} \tag{8.5}$$

For the velocity as well as the rate-of-strain tensor we have to express the fields in terms of the vorticity with Biot-Savart's law. For the joint average of the velocity field and the fine-grained vorticity PDF we obtain

$$\begin{aligned}\left\langle \boldsymbol{u}(\boldsymbol{x}_1, t) \hat{f}_1(\boldsymbol{\Omega}_1; \boldsymbol{x}_1, t) \right\rangle &= \left\langle \frac{1}{4\pi} \int \mathrm{d}\boldsymbol{x}_2 \, \frac{\boldsymbol{\omega}(\boldsymbol{x}_2, t) \times (\boldsymbol{x}_1 - \boldsymbol{x}_2)}{|\boldsymbol{x}_1 - \boldsymbol{x}_2|^3} \, \hat{f}_1(\boldsymbol{\Omega}_1; \boldsymbol{x}_1, t) \right\rangle \\ &= \left\langle \frac{1}{4\pi} \int \mathrm{d}\boldsymbol{x}_2 \, \mathrm{d}\boldsymbol{\Omega}_2 \, \frac{\boldsymbol{\omega}(\boldsymbol{x}_2, t) \times (\boldsymbol{x}_1 - \boldsymbol{x}_2)}{|\boldsymbol{x}_1 - \boldsymbol{x}_2|^3} \, \hat{f}_2(\boldsymbol{\Omega}_1, \boldsymbol{\Omega}_2; \boldsymbol{x}_1, \boldsymbol{x}_2, t) \right\rangle \\ &= \frac{1}{4\pi} \int \mathrm{d}\boldsymbol{x}_2 \, \mathrm{d}\boldsymbol{\Omega}_2 \, \frac{\boldsymbol{\Omega}_2 \times (\boldsymbol{x}_1 - \boldsymbol{x}_2)}{|\boldsymbol{x}_1 - \boldsymbol{x}_2|^3} \, f_2(\boldsymbol{\Omega}_1, \boldsymbol{\Omega}_2; \boldsymbol{x}_1, \boldsymbol{x}_2, t) \quad ,\end{aligned} \tag{8.6}$$

which shows that the average involving the velocity field can only be obtained by integration of the two-point vorticity PDF over the whole spatial domain. The same goes for the velocity gradient tensor $\mathrm{S} = \frac{1}{2}(\mathrm{A} + \mathrm{A}^T)$, which also can be expressed in terms of the vorticity field by taking derivatives of the Biot-Savart kernel. We obtain

$$\begin{aligned}\left\langle S_{1,ij} \hat{f}_1 \right\rangle &= \left\langle \frac{3}{8\pi} \int \mathrm{d}\boldsymbol{x}_2 \, \epsilon_{ikl} \, \frac{(x_{1,k} - x_{2,k})(x_{1,j} - x_{2,j})}{|\boldsymbol{x}_1 - \boldsymbol{x}_2|^5} \, \omega_l(\boldsymbol{x}_2, t) \, \hat{f}_1 \right\rangle + (i \leftrightarrow j) \\ &= \left\langle \frac{3}{8\pi} \int \mathrm{d}\boldsymbol{x}_2 \, \mathrm{d}\boldsymbol{\Omega}_2 \, \epsilon_{ikl} \, \frac{(x_{1,k} - x_{2,k})(x_{1,j} - x_{2,j})}{|\boldsymbol{x}_1 - \boldsymbol{x}_2|^5} \, \omega_l(\boldsymbol{x}_2, t) \, \hat{f}_2 \right\rangle + (i \leftrightarrow j) \\ &= \frac{3}{8\pi} \int \mathrm{d}\boldsymbol{x}_2 \, \mathrm{d}\boldsymbol{\Omega}_2 \, \epsilon_{ikl} \, \frac{(x_{1,k} - x_{2,k})(x_{1,j} - x_{2,j})}{|\boldsymbol{x}_1 - \boldsymbol{x}_2|^5} \, \Omega_{2,l} \, f_2 + (i \leftrightarrow j) \quad ,\end{aligned} \tag{8.7}$$

where $(i \leftrightarrow j)$ indicates that the same expression with indices i and j interchanged has to be added. We omitted some of the arguments in favor of a clearer presentation. As a mathematical side remark we should mention that the above integrals have to be interpreted as Cauchy principal value integrals in order to assure a proper definition of the expressions. Like for the velocity the forcing term cannot be expressed in terms of the vorticity as it depends on the specifications of this external field.

Putting these results together, we can write down the evolution equation or the single-point vorticity PDF, which takes the form

$$\begin{aligned}\frac{\partial}{\partial t} f_1 + \frac{1}{4\pi} \nabla_{\boldsymbol{x}_1} \cdot \int \mathrm{d}\boldsymbol{x}_2 \, \mathrm{d}\boldsymbol{\Omega}_2 \, \frac{\boldsymbol{r}_{12} \times \boldsymbol{\Omega}_2}{r_{12}^3} \, f_2 \\ = -\nabla_{\boldsymbol{\Omega}_1} \cdot \left\{ \frac{3}{8\pi} \int \mathrm{d}\boldsymbol{x}_2 \, \mathrm{d}\boldsymbol{\Omega}_2 \left[\frac{(\boldsymbol{r}_{12} \times \boldsymbol{\Omega}_2)(\boldsymbol{r}_{12} \cdot \boldsymbol{\Omega}_1)}{r_{12}^5} + \frac{\boldsymbol{\Omega}_1 \cdot (\boldsymbol{r}_{12} \times \boldsymbol{\Omega}_2) \, \boldsymbol{r}_{12}}{r_{12}^5} \right] f_2 \right. \\ \left. + \lim_{\boldsymbol{x}_2 \to \boldsymbol{x}_1} \nu \Delta_{\boldsymbol{x}_2} \int \mathrm{d}\boldsymbol{\Omega}_2 \, \boldsymbol{\Omega}_2 \, f_2 + \left\langle \hat{f}_1 \nabla_{\boldsymbol{x}_1} \times \boldsymbol{F}_1 \right\rangle \right\} \quad , \end{aligned} \tag{8.8}$$

where we have introduced the notation $\boldsymbol{r}_{12} = \boldsymbol{x}_2 - \boldsymbol{x}_1$. This is easily generalized to the derivation of an evolution equation for the two-point PDF $f_2(\boldsymbol{\Omega}_1, \boldsymbol{\Omega}_2; \boldsymbol{x}_1, \boldsymbol{x}_2, t)$ yielding

$$\begin{aligned}\frac{\partial}{\partial t} f_2 + \frac{1}{4\pi} \nabla_{\boldsymbol{x}_1} \cdot \int \mathrm{d}\boldsymbol{x}_3 \, \mathrm{d}\boldsymbol{\Omega}_3 \, \frac{\boldsymbol{r}_{13} \times \boldsymbol{\Omega}_3}{r_{13}^3} \, f_3 + \frac{1}{4\pi} \nabla_{\boldsymbol{x}_2} \cdot \int \mathrm{d}\boldsymbol{x}_3 \, \mathrm{d}\boldsymbol{\Omega}_3 \, \frac{\boldsymbol{r}_{23} \times \boldsymbol{\Omega}_3}{r_{23}^3} \, f_3 \\ = - \nabla_{\boldsymbol{\Omega}_1} \cdot \left\{ \frac{3}{8\pi} \int \mathrm{d}\boldsymbol{x}_3 \, \mathrm{d}\boldsymbol{\Omega}_3 \left[\frac{(\boldsymbol{r}_{13} \times \boldsymbol{\Omega}_3)(\boldsymbol{r}_{13} \cdot \boldsymbol{\Omega}_1)}{r_{13}^5} + \frac{\boldsymbol{\Omega}_1 \cdot (\boldsymbol{r}_{13} \times \boldsymbol{\Omega}_3) \, \boldsymbol{r}_{13}}{r_{13}^5} \right] f_3 \right. \\ \left. + \lim_{\boldsymbol{x}_3 \to \boldsymbol{x}_1} \nu \Delta_{\boldsymbol{x}_3} \int \mathrm{d}\boldsymbol{\Omega}_3 \, \boldsymbol{\Omega}_3 \, f_3 + \left\langle \hat{f}_2 \nabla_{\boldsymbol{x}_1} \times \boldsymbol{F}_1 \right\rangle \right\} \\ - \nabla_{\boldsymbol{\Omega}_2} \cdot \left\{ \frac{3}{8\pi} \int \mathrm{d}\boldsymbol{x}_3 \, \mathrm{d}\boldsymbol{\Omega}_3 \left[\frac{(\boldsymbol{r}_{23} \times \boldsymbol{\Omega}_3)(\boldsymbol{r}_{23} \cdot \boldsymbol{\Omega}_2)}{r_{23}^5} + \frac{\boldsymbol{\Omega}_2 \cdot (\boldsymbol{r}_{23} \times \boldsymbol{\Omega}_3) \, \boldsymbol{r}_{23}}{r_{23}^5} \right] f_3 \right. \\ \left. + \lim_{\boldsymbol{x}_3 \to \boldsymbol{x}_2} \nu \Delta_{\boldsymbol{x}_3} \int \mathrm{d}\boldsymbol{\Omega}_3 \, \boldsymbol{\Omega}_3 \, f_3 + \left\langle \hat{f}_2 \nabla_{\boldsymbol{x}_2} \times \boldsymbol{F}_2 \right\rangle \right\} \quad . \end{aligned} \tag{8.9}$$

This indicates how the evolution equations couple to the next "level" of the hierarchy by the Biot-Savart integrals related to the velocity field and the rate-of-strain tensor. A closer look at these terms indicates that they depend linearly on the "additional" vorticity, a fact, which is different from the case of the velocity statistics. This will play a crucial role later on.

Of course, we can alternatively introduce conditional averages for the unclosed terms according to

$$\left\langle \boldsymbol{u}(\boldsymbol{x}_1, t) \hat{f}_1(\boldsymbol{\Omega}_1; \boldsymbol{x}_1, t) \right\rangle = \left\langle \boldsymbol{u}(\boldsymbol{x}_1, t) \middle| \boldsymbol{\Omega}_1 \right\rangle f_1(\boldsymbol{\Omega}_1; \boldsymbol{x}_1, t) \tag{8.10a}$$

$$\left\langle S_{ij}(\boldsymbol{x}_1, t) \hat{f}_1(\boldsymbol{\Omega}_1; \boldsymbol{x}_1, t) \right\rangle = \left\langle S_{ij}(\boldsymbol{x}_1, t) \middle| \boldsymbol{\Omega}_1 \right\rangle f_1(\boldsymbol{\Omega}_1; \boldsymbol{x}_1, t) \tag{8.10b}$$

$$\left\langle (\nu \Delta \boldsymbol{\omega}(\boldsymbol{x}_1, t)) \hat{f}_1(\boldsymbol{\Omega}_1; \boldsymbol{x}_1, t) \right\rangle = \left\langle (\nu \Delta \boldsymbol{\omega}(\boldsymbol{x}_1, t)) \middle| \boldsymbol{\Omega}_1 \right\rangle f_1(\boldsymbol{\Omega}_1; \boldsymbol{x}_1, t) \tag{8.10c}$$

$$\left\langle \nabla_{\boldsymbol{x}_1} \times \boldsymbol{F}(\boldsymbol{x}_1, t) \hat{f}_1(\boldsymbol{\Omega}_1; \boldsymbol{x}_1, t) \right\rangle = \left\langle \nabla_{\boldsymbol{x}_1} \times \boldsymbol{F}(\boldsymbol{x}_1, t) \middle| \boldsymbol{\Omega}_1 \right\rangle f_1(\boldsymbol{\Omega}_1; \boldsymbol{x}_1, t) \quad . \tag{8.10d}$$

As in the case of the velocity field, the single-point statistics of the vorticity field is determined by the local correlations of the vorticity field with the dynamical terms from the vorticity equation in form of the advecting velocity, the vortex stretching term, the diffusive term and the external forcing. With these definitions the single-point vorticity equation takes the simple form

$$\frac{\partial}{\partial t} f_1 + \nabla_{\boldsymbol{x}_1} \cdot \left[\left\langle \boldsymbol{u}_1 \middle| \boldsymbol{\Omega}_1 \right\rangle f_1 \right] = -\nabla_{\boldsymbol{\Omega}_1} \cdot \left[\left\langle \mathrm{S}_1 \boldsymbol{\omega}_1 + \nu \Delta_{\boldsymbol{x}_1} \boldsymbol{\omega}_1 + \nabla_{\boldsymbol{x}_1} \times \boldsymbol{F}_1 \middle| \boldsymbol{\Omega}_1 \right\rangle f_1 \right] \quad . \tag{8.11}$$

One should note at this point that the vortex stretching term may also be written as

$$\left\langle \mathrm{S}_1 \boldsymbol{\omega}_1 \middle| \boldsymbol{\Omega}_1 \right\rangle f_1 = \left\langle \mathrm{S}_1 \middle| \boldsymbol{\Omega}_1 \right\rangle \boldsymbol{\Omega}_1 f_1 \tag{8.12}$$

due to the sifting property of the fine-grained PDF. The introduction of conditional averages can be generalized to the case of multi-point statistics. If we truncate the hierarchy on the N-th level, the introduction of conditional averages allows to write

$$\begin{aligned}
\frac{\partial}{\partial t} f_1 &= \mathcal{C}_1 \left[f_2, \boldsymbol{F}_1 \right] \\
\frac{\partial}{\partial t} f_2 &= \mathcal{C}_2 \left[f_3, \boldsymbol{F}_1, \boldsymbol{F}_2 \right] \\
&\vdots \\
\frac{\partial}{\partial t} f_{N-1} &= \mathcal{C}_{N-1} \left[f_N, \boldsymbol{F}_1, \ldots, \boldsymbol{F}_{N-1} \right] \\
\frac{\partial}{\partial t} f_N &= -\sum_{i=1}^{N} \nabla_{\boldsymbol{x}_i} \cdot \left\{ \left\langle \boldsymbol{u}_i | \boldsymbol{\Omega}_1, \ldots, \boldsymbol{\Omega}_N \right\rangle f_N \right\} \\
&\quad - \sum_{i=1}^{N} \nabla_{\boldsymbol{\Omega}_i} \cdot \left\{ \left\langle \mathrm{S}_i \boldsymbol{\omega}_i + \nu \Delta_{\boldsymbol{x}_i} \boldsymbol{\omega}_i + \nabla_{\boldsymbol{x}_i} \times \boldsymbol{F}_i \middle| \boldsymbol{\Omega}_1, \ldots, \boldsymbol{\Omega}_N \right\rangle f_N \right\} \quad .
\end{aligned} \tag{8.13}$$

Compared to the velocity PDF hierarchy (6.34), the collision operators $\mathcal{C}_i$ now also contain the advective terms. Once the conditional averages on the N-point level are known, this set of equations becomes closed. As demonstrated for the velocity field, the method of characteristics can also be applied to the vorticity field in a straightforward manner, such that we refrain from a detailed presentation here. We note, however, that the major difference to the velocity case is that, besides the conditionally averaged right-hand side of the vorticity equation, also the conditional velocity field evaluated at the different points appears.

This theoretical introduction into the LMN hierarchy for the vorticity highlights the striking formal similarities compared to the velocity case. Up to now these derivations are based on purely mathematical arguments. Apart from the utilization of statistical symmetries, the following detailed analytical and numerical investigation will involve more physical arguments, which will allow to fully characterize the single-point vorticity statistics. Then also some deeper comparisons to the velocity statistics will be discussed.

8.3. The Single-Point Vorticity PDF Equation

8.3.1. Application of Statistical Symmetries

We now want to pursue a deeper investigation of the single-point vorticity PDF in homogeneous isotropic turbulence. To this end we start from the single-point PDF equation

$$\frac{\partial}{\partial t} f + \nabla \cdot \left[\left\langle \boldsymbol{u} \middle| \boldsymbol{\Omega} \right\rangle f \right] = -\nabla_{\boldsymbol{\Omega}} \cdot \left[\left\langle \mathrm{S}\boldsymbol{\omega} + \nu \Delta \boldsymbol{\omega} + \nabla \times \boldsymbol{F} \middle| \boldsymbol{\Omega} \right\rangle f \right] \quad . \tag{8.14}$$

Here and in the following we will omit the index 1 for a better presentation. We note first that due to homogeneity the advective term vanishes, as neither $\left\langle \boldsymbol{u} \middle| \boldsymbol{\Omega} \right\rangle$ nor f depend on $\boldsymbol{x}$. This yields

$$\frac{\partial}{\partial t} f = -\nabla_{\boldsymbol{\Omega}} \cdot \left[\left\langle \mathrm{S}\boldsymbol{\omega} + \nu \Delta \boldsymbol{\omega} + \nabla \times \boldsymbol{F} \middle| \boldsymbol{\Omega} \right\rangle f \right] \quad , \tag{8.15}$$

which again takes the form of a continuity equation for the probability density, where the conditional right-hand side of the vorticity equation times the PDF defines the probability current. We now introduce the conditional enstrophy dissipation tensor due to the homogeneity relation

$$\frac{\partial^2}{\partial x_k^2} f = 0 = -\frac{\partial}{\partial \Omega_i} \left\langle \frac{\partial^2 \omega_i}{\partial x_k^2} \middle| \boldsymbol{\Omega} \right\rangle f + \frac{\partial^2}{\partial \Omega_i \partial \Omega_j} \left\langle \frac{\partial \omega_i}{\partial x_k} \frac{\partial \omega_j}{\partial x_k} \middle| \boldsymbol{\Omega} \right\rangle f \quad . \tag{8.16}$$

This relation allows to express the diffusive term in equation (8.15) in terms of the conditional enstrophy dissipation tensor

$$D_{ij}(\boldsymbol{\Omega}) = \left\langle \nu \frac{\partial \omega_i}{\partial x_k} \frac{\partial \omega_j}{\partial x_k} \middle| \boldsymbol{\Omega} \right\rangle \quad , \tag{8.17}$$

such that the kinetic equation may be recast taking the form

$$\frac{\partial}{\partial t} f = -\frac{\partial}{\partial \Omega_i} \left\langle S_{ij}\omega_j + \epsilon_{ijk} \frac{\partial}{\partial x_j} F_k \middle| \boldsymbol{\Omega} \right\rangle f - \frac{\partial^2}{\partial \Omega_i \partial \Omega_j} \left\langle \nu \frac{\partial \omega_i}{\partial x_k} \frac{\partial \omega_j}{\partial x_k} \middle| \boldsymbol{\Omega} \right\rangle f \quad . \tag{8.18}$$

The mathematical structure of this partial differential equation will in the following allow for a stationary solution of the PDF when further simplifications due to isotropic statistics are taken into account. To this end we have to write down the isotropic forms of all the arising functions like already exemplified for the velocity statistics. First of all, we can express the PDF of the vorticity vector in terms of the PDF of the magnitude of vorticity as

$$\tilde{f}(\Omega) = 4\pi\Omega^2 f(\boldsymbol{\Omega}) \quad . \tag{8.19}$$

For the kinetic equation (8.15) we further have to specify the conditional averages of the rate-of-strain tensor, the diffusive term and the external forcing. Following the

argumentation in chapter 7, we arrive at

$$\left\langle S_{ij}\middle|\boldsymbol{\Omega}\right\rangle = \frac{1}{2}\Sigma(\Omega)\left(3\frac{\Omega_i\,\Omega_j}{\Omega^2} - \delta_{ij}\right) \qquad \Sigma(\Omega) = \left\langle \widehat{\boldsymbol{\omega}}\mathrm{S}\widehat{\boldsymbol{\omega}}\middle|\Omega\right\rangle \tag{8.20a}$$

$$\left\langle \nu\Delta\boldsymbol{\omega}\middle|\boldsymbol{\Omega}\right\rangle = \Lambda(\Omega)\,\widehat{\boldsymbol{\Omega}} \qquad \Lambda(\Omega) = \left\langle \nu\widehat{\boldsymbol{\omega}}\cdot\Delta\boldsymbol{\omega}\middle|\Omega\right\rangle \tag{8.20b}$$

$$\left\langle \nabla\times\boldsymbol{F}\middle|\boldsymbol{\Omega}\right\rangle = \Phi(\Omega)\,\widehat{\boldsymbol{\Omega}} \qquad \Phi(\Omega) = \left\langle \widehat{\boldsymbol{\omega}}\cdot(\nabla\times\boldsymbol{F})\middle|\Omega\right\rangle \quad . \tag{8.20c}$$

The conditional Laplacian Λ and the conditional forcing term Φ are denoted analogous to the case of the velocity in order to highlight their meaning. However, one should note that they represent different functions as, e.g., here the Laplacian of the *vorticity* is considered. When the danger of misinterpretation occurs, additional indices will be used. In contrast to the conditional enstrophy dissipation tensor, which will be analyzed next, the conditional rate-of-strain tensor may be expressed by a single scalar function Σ, the eigenvalue of the tensor, only. This comes due to the fact that the trace of this tensor

$$\left\langle S_{ii}\middle|\boldsymbol{\Omega}\right\rangle = \left\langle \frac{\partial u_i}{\partial x_i}\middle|\boldsymbol{\Omega}\right\rangle = 0 \tag{8.21}$$

vanishes due to incompressibility. The prefactors are chosen such that the function Σ corresponds to a (normalized) enstrophy production, which makes the interpretation especially easy. With this definition the conditional vortex stretching term takes the form

$$\left\langle \mathrm{S}\middle|\boldsymbol{\Omega}\right\rangle\boldsymbol{\Omega} = \Sigma(\Omega)\Omega\,\widehat{\boldsymbol{\Omega}} \quad , \tag{8.22}$$

such that this term in total has the functional form to be expected from a conditionally averaged vector. The general structure of the conditional enstrophy dissipation tensor is

$$D_{ij}(\boldsymbol{\Omega}) = \mu(\Omega)\,\delta_{ij} + \left[\lambda(\Omega) - \mu(\Omega)\right]\frac{\Omega_i\Omega_j}{\Omega^2} \quad , \tag{8.23}$$

where μ and λ are the eigenvalues of D depending only on the magnitude of velocity, which again can be obtained according to

$$\mathrm{Tr(D)} = \left\langle \nu\frac{\partial\omega_i}{\partial x_k}\frac{\partial\omega_i}{\partial x_k}\middle|\boldsymbol{\Omega}\right\rangle = \lambda(\Omega) + 2\mu(\Omega) \tag{8.24a}$$

$$\widehat{\boldsymbol{\Omega}}\mathrm{D}\widehat{\boldsymbol{\Omega}} = \left\langle \nu\widehat{\omega}_i\frac{\partial\omega_i}{\partial x_k}\frac{\partial\omega_j}{\partial x_k}\widehat{\omega}_j\middle|\boldsymbol{\Omega}\right\rangle = \lambda(\Omega) \quad . \tag{8.24b}$$

As we will see in the next section, the dissipative term of the enstrophy balance takes the form

$$\langle\nu\omega_i\Delta\omega_i\rangle = -\left\langle \nu\frac{\partial\omega_i}{\partial x_k}\frac{\partial\omega_i}{\partial x_k}\right\rangle \quad , \tag{8.25}$$

which makes clear that the eigenvalues on the one hand are related to the dissipation of enstrophy. On the other hand, the second term in (8.24) is related to the stretching and

turning of the vorticity vector due to the vorticity gradient tensor, which may be seen by

$$\left\langle \nu\widehat{\omega}_i \frac{\partial\omega_i}{\partial x_k}\frac{\partial\omega_j}{\partial x_k}\widehat{\omega}_j \middle| \mathbf{\Omega} \right\rangle = \left\langle \nu(\widehat{\boldsymbol{\omega}}\cdot\nabla\boldsymbol{\omega})^2 \middle| \mathbf{\Omega} \right\rangle \quad . \tag{8.26}$$

Now having expressed all relevant quantities as isotropic functions, we insert them into the kinetic equations (8.15) and (8.18) as well as into the homogeneity relation (8.16) and obtain, after some calculations very similar to the ones outlined in chapter 7, the isotropic versions of these equations,

$$\frac{\partial}{\partial t}\tilde{f} = -\frac{\partial}{\partial\Omega}\left(\Sigma\,\Omega + \Lambda + \Phi\right)\tilde{f} \tag{8.27a}$$

$$0 = -\frac{\partial}{\partial\Omega}\left(\Lambda + \frac{2\mu}{\Omega}\right)\tilde{f} + \frac{\partial^2}{\partial\Omega^2}\lambda\tilde{f} \tag{8.27b}$$

$$\frac{\partial}{\partial t}\tilde{f} = -\frac{\partial}{\partial\Omega}\left(\Sigma\,\Omega + \Phi - \frac{2\mu}{\Omega}\right)\tilde{f} - \frac{\partial^2}{\partial\Omega^2}\lambda\tilde{f} \quad . \tag{8.27c}$$

Of course, these equations show a remarkable similarity to the equations (7.22a)-(7.22c), however, the functional shape of the individual terms will turn out to be very different. This formulation of the problem will again allow to derive homogeneous and isotropic stationary solutions. Before coming to this point, we will further study the implications of equations (8.27a).

8.3.2. The Balance of Enstrophy Production and Dissipation

In the case of stationary turbulence equation (8.27a) takes the simple form

$$0 = \frac{\partial}{\partial v}\left(\Sigma\,\Omega + \Lambda + \Phi\right)\tilde{f} \quad . \tag{8.28}$$

Following the same reasoning as in the preceding chapter, we can conclude that also in the case of the vorticity field the conditional balance

$$0 = \Sigma(\Omega)\,\Omega + \Lambda(\Omega) + \Phi(\Omega) \tag{8.29}$$

holds, i.e., the vortex stretching term, the diffusive term and the term related to the external forcing tend to cancel on the single-point level. However, we will now seek for an even stronger conclusion. To this end we consider the enstrophy balance, which is obtained from the vorticity equation (1.8) by multiplying on $\boldsymbol{\omega}$ and subsequent averaging. We obtain

$$\frac{\partial}{\partial t}\left\langle\frac{\boldsymbol{\omega}^2}{2}\right\rangle + \nabla\cdot\left\langle\boldsymbol{u}\,\frac{\boldsymbol{\omega}^2}{2}\right\rangle = \left\langle\boldsymbol{\omega}\mathrm{S}\boldsymbol{\omega}\right\rangle + \left\langle\nu\boldsymbol{\omega}\cdot\Delta\boldsymbol{\omega}\right\rangle + \left\langle\boldsymbol{\omega}\cdot(\nabla\times\boldsymbol{F})\right\rangle \quad . \tag{8.30}$$

Considering the case of stationary homogeneous turbulence simplifies this equation to

$$0 = \left\langle\boldsymbol{\omega}\mathrm{S}\boldsymbol{\omega}\right\rangle + \left\langle\nu\boldsymbol{\omega}\cdot\Delta\boldsymbol{\omega}\right\rangle + \left\langle\boldsymbol{\omega}\cdot(\nabla\times\boldsymbol{F})\right\rangle \quad . \tag{8.31}$$

Of course, this equation can also be obtained from equation (8.29) by multiplying on Ω and $\tilde{f}$ and subsequent integration. Extending an analysis put forward by Tennekes and Lumley [TL83] and also by Novikov [Nov93], we now go for an order of magnitude estimation of the different terms with respect to the Reynolds number $Re = \frac{u_{\mathrm{rms}} L}{\nu}$. To find out how the terms scale with the Reynolds number, approximate dimensional estimates of the different quantities have to be made. One should stress that these estimates cannot be proven rigorously, such that caution in the derivation and interpretation of the results has to be taken. Based on the relation

$$\langle \nu \omega^2 \rangle = \langle \varepsilon \rangle \tag{8.32}$$

we estimate the enstrophy production term as

$$\big\langle \boldsymbol{\omega} \mathrm{S} \boldsymbol{\omega} \big\rangle \sim \langle \varepsilon \rangle^{\frac{3}{2}} \, \nu^{-\frac{3}{2}} \quad , \tag{8.33}$$

assuming that relation (8.32) also allows to estimate the rate-of-strain tensor. The term involving the forcing may be rewritten as

$$\big\langle \boldsymbol{\omega} \cdot (\nabla \times \boldsymbol{F}) \big\rangle = - \big\langle \boldsymbol{u} \cdot \Delta \boldsymbol{F} \big\rangle \tag{8.34}$$

by partial integration. As the large-scale forcing varies slowly in space, derivatives may be estimated to be of the order of L. Additionally noting that $\langle \boldsymbol{u} \cdot \boldsymbol{F} \rangle = \langle \varepsilon \rangle$ leads us to the estimate

$$\big\langle \boldsymbol{\omega} \cdot (\nabla \times \boldsymbol{F}) \big\rangle \sim \langle \varepsilon \rangle \, L^{-2} \quad . \tag{8.35}$$

For the dissipative term $\big\langle \nu \boldsymbol{\omega} \cdot \Delta \boldsymbol{\omega} \big\rangle$ no simple estimation can be given at this point as it is unclear which length scale is appropriate to estimate the Laplacian of the vorticity. To proceed, it is easy to calculate the ratio of the terms (8.35) and (8.33) which yields

$$\frac{\big\langle \boldsymbol{\omega} \cdot (\nabla \times \boldsymbol{F}) \big\rangle}{\big\langle \boldsymbol{\omega} \mathrm{S} \boldsymbol{\omega} \big\rangle} \sim \frac{\nu^{\frac{3}{2}}}{L^2 \langle \varepsilon \rangle^{\frac{1}{2}}} \sim Re^{-\frac{3}{2}} \quad , \tag{8.36}$$

where we have made use of the relation $\langle \varepsilon \rangle \sim u_{\mathrm{rms}}^3 \, L^{-1}$. This leads to the conclusion that the contribution of the forcing term to the enstrophy budget (8.29) decreases rapidly with Reynolds number and hence can be neglected asymptotically. To ensure a stationary balance, one can conclude a balance of enstrophy production and dissipation, i.e.,

$$0 = \big\langle \boldsymbol{\omega} \mathrm{S} \boldsymbol{\omega} \big\rangle - \big\langle \nu (\nabla \boldsymbol{\omega})^2 \big\rangle \quad , \tag{8.37}$$

where the diffusive term has been rewritten by partial integration. This expression shows that the dissipation of enstrophy is a strictly negative quantity, which implies that the mean enstrophy production is positive. The fact that the external forcing may be neglected indicates that the production of enstrophy, that means, e.g., the birth of vortex tubes, is a result of internal mechanisms of the Navier-Stokes dynamics and is expected to be independent of the external forcing. This result is consistent with the

common assumption that the small-scale statistics should become independent of the large-scale properties of the flow at sufficiently high Reynolds number, an important foundation of Kolmogorov's theory outlined in chapter 2.

As a side remark we would like to demonstrate that one can use this balance to determine the length scale on which the vorticity gradients vary. As this balance should hold at *any* sufficiently high Reynolds number one can demand the dissipative term to identically scale with the Reynolds number as the enstrophy production term. If we denote the unknown length scale as δ, equation (8.37) yields the relation

$$\left(\frac{\langle\varepsilon\rangle}{\nu}\right)^{\frac{3}{2}} \sim \frac{\langle\varepsilon\rangle}{\delta^2} \quad \Rightarrow \quad \delta \sim \left(\frac{\nu^3}{\langle\varepsilon\rangle}\right)^{\frac{1}{4}} = \eta \quad , \tag{8.38}$$

i.e., dimensional analysis indicates that the gradients of vorticity vary with the Kolmogorov length scale. It consequently has to be expected that the gradients of vorticity are strongly correlated with the vorticity itself, as the vorticity also varies on small scales. This will play an important role later on when the results from our DNS evaluation are interpreted.

We now come back to the *conditional* balance (8.29) and ask for the implications of the observations of the last paragraph on this stricter balance equation. To this end we note that the enstrophy budget (8.31) can be obtained from equation (8.29) by

$$\int \mathrm{d}\Omega\, \Omega\, [\Sigma(\Omega)\,\Omega + \Lambda(\Omega) + \Phi(\Omega)]\ \tilde{f}(\Omega) = \big\langle \boldsymbol{\omega}\mathrm{S}\boldsymbol{\omega}\big\rangle + \big\langle \nu\boldsymbol{\omega}\cdot\Delta\boldsymbol{\omega}\big\rangle + \big\langle \boldsymbol{\omega}\cdot(\nabla\times\boldsymbol{F})\big\rangle = 0\,. \tag{8.39}$$

Now the easiest way to achieve the asymptotically vanishing contribution of the forcing is to assume

$$\Phi(\Omega) \approx 0 \tag{8.40}$$

for sufficiently high Reynolds numbers. This in turn leads to the conditional balance of enstrophy production and dissipation only,

$$0 \approx \Sigma(\Omega)\,\Omega + \Lambda(\Omega) \quad . \tag{8.41}$$

This argumentation can be supported by a decoupling argument. As the forcing acts on the large scales and the vorticity is organized into slender vortex tubes, one could assume statistical independence leading to

$$\big\langle \widehat{\boldsymbol{\omega}}\cdot(\nabla\times\boldsymbol{F})\big|\Omega\big\rangle \approx \big\langle \widehat{\boldsymbol{\omega}}\cdot(\nabla\times\boldsymbol{F})\big\rangle = 0 \quad \Rightarrow \quad \Phi(\Omega) = 0 \quad . \tag{8.42}$$

It has to be stressed that these conclusions are not compellent, and we have seen for the case of the velocity statistics that similar arguments applied to the conditional pressure gradient lead to wrong results. For the moment we take the conditional balance of the terms related to enstrophy production and dissipation as a working hypothesis, which has to be verified with numerical or experimental data.

8.3.3. Homogeneous and Stationary PDF

The next interesting issue to study is the isotropic form (8.27c) of the kinetic equation as well as the homogeneity relation (8.27b). As we have seen in the case of the velocity field, the mathematical structure of this type of kinetic equation allows to derive homogeneous and stationary solutions for the PDF. Since the structure of the kinetic equations (8.27a)-(8.27c) is identical, this, of course, can also be achieved for the vorticity field.

The homogeneity relation (8.27b) is integrated yielding

$$\tilde{f}(\Omega;t) = \frac{\mathcal{N}}{\lambda(\Omega,t)} \exp \int_{\Omega_0}^{\Omega} \mathrm{d}\Omega' \, \frac{\Lambda(\Omega',t) + \frac{2}{\Omega'}\mu(\Omega',t)}{\lambda(\Omega',t)} \quad , \tag{8.43}$$

which has exactly the same structure as the homogeneous solution (7.25). However, the functional shape of the unclosed terms is expected to be very different from the velocity case. As both of the conditional averages in this expression contain derivatives of the vorticity, the fact that the vorticity is expected to be strongly correlated with the vorticity gradients will lead to a strong Ω-dependence of the conditional averages.

Proceeding to the stationary solution, integration of (8.27c) yields

$$\tilde{f}(\Omega) = \frac{\mathcal{N}}{\lambda(\Omega)} \exp \int_{\Omega_0}^{\Omega} \mathrm{d}\Omega' \, \frac{-\Sigma(\Omega')\,\Omega' - \Phi(\Omega') + \frac{2}{\Omega'}\mu(\Omega')}{\lambda(\Omega')} \quad , \tag{8.44}$$

which shows that the single-point vorticity PDF can be expressed in terms of the conditional vortex stretching term related to the enstrophy production, the external forcing term and the eigenvalues of the enstrophy dissipation tensor. If we assume that the approximate conditional balance (8.41) holds, we obtain

$$\tilde{f}(\Omega) \approx \frac{\mathcal{N}}{\lambda(\Omega)} \exp \int_{\Omega_0}^{\Omega} \mathrm{d}\Omega' \, \frac{-\Sigma(\Omega')\,\Omega' + \frac{2}{\Omega'}\mu(\Omega')}{\lambda(\Omega')} \quad . \tag{8.45}$$

This result is physically very appealing as it shows that the single-point vorticity PDF is fully determined by the enstrophy production and dissipation term and independent of the external forcing. This is very different from the velocity situation as we have seen that in this case the single-point velocity PDF depends on the external forcing, the pressure contributions and the dissipative effects, i.e., none of the terms can be neglected there. The DNS results will help us to verify this conjecture about the independence from the external forcing.

8.3.4. An Analytical Closure Approximation

The solutions (8.43), (8.44) and (8.45) of the PDF equations can in principle be treated with a decoupling argument like exemplified in the last chapter for the velocity leading to Gaussian solutions. As we have seen in chapter 4, the PDF deviates strongly from normality and has pronounced, slowly decaying tails. The reason for this can be seen

in the strong statistical correlations that have to be expected due to the similarity of the length scales that the vorticity, the rate-of-strain tensor and the gradients of vorticity vary on. Hence a "naïve" closure strategy resting on the assumption of statistical independence as proposed in the preceding chapter has to fail. On the other hand the complete opposite, i.e., the assumption of strong statistical correlations could work. We want to investigate this attempt deeper.

The assumption of "perfect" correlation can be regarded as reasonable only for the strong events of the vorticity, such that the following argumentation only applies to the tails of the PDF. We let us guide by the argumentation of the approximate enstrophy balance and assume first of all that the external forcing has a negligible influence. That means, we take the relation (8.45) as a starting point. To determine the shape of the PDF, we now have to specify the functional shape of the eigenvalues of the conditional rate-of-strain tensor as well as the conditional enstrophy dissipation tensor.

First of all, we can note that, as in the case of the velocity statistics, certain integral constraints have to be fulfilled. The relevant ones in this context are

$$\left\langle \boldsymbol{\omega} \mathrm{S} \boldsymbol{\omega} \right\rangle = \int \mathrm{d}\Omega \, \Sigma(\Omega) \Omega^2 \, \tilde{f}(\Omega) \tag{8.46a}$$

$$\left\langle \boldsymbol{\omega} \mathrm{S} \boldsymbol{\omega} \right\rangle = \int \mathrm{d}\Omega \, (\lambda + 2\mu) \, \tilde{f}(\Omega) \quad , \tag{8.46b}$$

where for the second one we have made use of the fact that the enstrophy production equals the enstrophy dissipation and that this quantity is obtained by averaging the trace of the conditional enstrophy dissipation tensor. To specify the functional form of the conditional averages, we first extend the above argument and assume that the rate-of-strain tensor is proportional to the vorticity. Hence the most simple estimate on dimensional grounds is

$$\Sigma_0(\Omega) = a \, \Omega \quad . \tag{8.47}$$

Furthermore, we have already estimated above that the vorticity gradients vary on a scale comparable to the vorticity itself. As the conditional enstrophy dissipation tensor is quadratic in the gradients of the vorticity, it is straightforward to assume

$$\lambda_0(\Omega) = b \, \Omega^2 \tag{8.48a}$$

$$\mu_0(\Omega) = c \, \Omega^2 \quad . \tag{8.48b}$$

As the strong events in the vorticity field tend to be organized into slender vortex tubes, strong directional correlations for the conditional dissipation tensor are likely, i.e., it is not expected that this tensor is isotropic, which would be the case if $\mu = \lambda$. Consequently, the fine-scale geometry imposes a relation

$$\lambda_0(\Omega) = d \, \mu_0(\Omega) \quad \Rightarrow \quad c = \frac{b}{d} \quad . \tag{8.49}$$

Inserting these ansatzes into the integral constraints (8.46a) and (8.46b) yields

$$a = \frac{\langle \boldsymbol{\omega} \mathrm{S} \boldsymbol{\omega} \rangle}{\langle \omega^3 \rangle} \tag{8.50a}$$

$$b = \left(1 + \frac{2}{d}\right)^{-1} \frac{\langle \boldsymbol{\omega} \mathrm{S} \boldsymbol{\omega} \rangle}{\langle \omega^2 \rangle} \tag{8.50b}$$

$$c = (d+2)^{-1} \frac{\langle \boldsymbol{\omega} \mathrm{S} \boldsymbol{\omega} \rangle}{\langle \omega^2 \rangle} \quad . \tag{8.50c}$$

With these results we can evaluate equation (8.45) and obtain

$$\tilde{f}(\Omega) \sim \Omega^{\frac{2}{d}-2} \exp\left[- \left(1 + \frac{2}{d}\right) \frac{\langle \omega^2 \rangle}{\langle \omega^3 \rangle} \Omega \right] \quad , \tag{8.51}$$

i.e., in this simple approximation the PDF decays exponentially with an algebraic prefactor and depends on the two moments $\langle \omega^2 \rangle$ and $\langle \omega^3 \rangle$ as well as on the local geometry of the field contained in the parameter d. As all of the quantities can be determined from the statistics of the vorticity field, this expression contains no fit parameter. For instance, we will see from the DNS data in the following that $d = 4$ is an appropriate choice. Of course, these approximations are "too simple to be true", such that we do not expect a perfect agreement with the numerical data later on. This analytical approximation rather highlights that under the assumption of strong statistical correlations highly non-Gaussian PDFs are obtained naturally.

8.3.5. A Simple Stochastic Interpretation

We have already indicated in chapter 7 that the kinetic equations, after introducing the homogeneity relation, show a remarkable formal similarity to a Fokker-Planck equation, however, with a negative diffusion coefficient. This negative sign, whose physical origin has been explained in the last chapter, for some researchers indicates the "ill-posedness" of the kinetic equations like equations (7.4) and (8.18), at least in a stochastic sense. In this short section we would like to demonstrate how a simple Langevin model for the stationary case still can be constructed. To this end we make use of the conditional balance (8.29) and neglect the external forcing,

$$\frac{\partial}{\partial t} f = - \frac{\partial}{\partial \Omega_i} \left\langle S_{ij} \middle| \boldsymbol{\Omega} \right\rangle \Omega_j \, f - \frac{\partial^2}{\partial \Omega_i \partial \Omega_j} \left\langle \nu \frac{\partial \omega_i}{\partial x_k} \frac{\partial \omega_j}{\partial x_k} \middle| \boldsymbol{\Omega} \right\rangle f \quad . \tag{8.52}$$

By introducing a change of variables

$$t^\star = -t \tag{8.53}$$

the kinetic equation (8.52) takes the form

$$\frac{\partial}{\partial t^\star} f = \frac{\partial}{\partial \Omega_i} \left\langle S_{ij} \middle| \boldsymbol{\Omega} \right\rangle \Omega_j \, f + \frac{\partial^2}{\partial \Omega_i \partial \Omega_j} \left\langle \nu \frac{\partial \omega_i}{\partial x_k} \frac{\partial \omega_j}{\partial x_k} \middle| \boldsymbol{\Omega} \right\rangle f \quad , \tag{8.54}$$

which simply means that we consider the kinetic equation backwards in time. As we are interested in stationary statistics and do not resolve any temporal statistics, this interpretation does not cause any further problems. If we now identify the terms

$$\boldsymbol{D}^1(\boldsymbol{\Omega}) = -\left\langle \mathrm{S} \middle| \boldsymbol{\Omega} \right\rangle \boldsymbol{\Omega} \tag{8.55a}$$

$$D^2_{ij}(\boldsymbol{\Omega}) = \left\langle \nu \frac{\partial \omega_i}{\partial x_k} \frac{\partial \omega_j}{\partial x_k} \middle| \boldsymbol{\Omega} \right\rangle \quad , \tag{8.55b}$$

the last equation formally takes the form of a Fokker-Planck equation

$$\frac{\partial}{\partial t^\star} f = -\frac{\partial}{\partial \Omega_i} D^1_i(\boldsymbol{\Omega})\, f + \frac{\partial^2}{\partial \Omega_i \partial \Omega_j} D^2_{ij}(\boldsymbol{\Omega})\, f \quad , \tag{8.56}$$

which by construction yields the same stationary PDF as equation (8.52). It is now easy to write down the corresponding Langevin equation

$$\mathrm{d}\boldsymbol{\Omega}(t^\star) = \boldsymbol{D}_1(\boldsymbol{\Omega})\, \mathrm{d}t^\star + \sqrt{2\mathrm{D}^2(\boldsymbol{\Omega})}\, \mathrm{d}\boldsymbol{W}(t^\star) \quad , \tag{8.57}$$

where $\mathrm{d}\boldsymbol{W}(t)$ denotes a delta-correlated white noise. For homogeneous isotropic turbulence we can make use of statistical symmetries and explicitly calculate the drift vector and diffusion matrix in terms of the scalar functions introduced in section 8.3.1. After a short calculation the Langevin equation takes the form

$$\mathrm{d}\Omega_i(t^\star) = -\Sigma(\Omega)\Omega_i\, \mathrm{d}t^\star + \sqrt{2}\left(\sqrt{\mu(\Omega)}\, \delta_{ij} + \left[-\sqrt{\mu(\Omega)} - \sqrt{\lambda(\Omega)} \right] \frac{\Omega_i \Omega_j}{\Omega^2} \right) \mathrm{d}W_j(t^\star) \quad . \tag{8.58}$$

One should stress at this point that this Langevin equation will by construction yield the correct single-point statistics, but it cannot be expected that, e.g., the temporal correlations of such a simple model will be the same as for the vorticity statistics measured at a single point. Still, this procedure shows that when setting up a Langevin model for the vorticity statistics, multiplicative noise naturally enters. We refrain from presenting a numerical implementation of this stochastic model at this point, further details on the model along with a numerical implementation can be found in [WF09b]. Instead, we proceed to the DNS results on the vorticity statistics and the unclosed terms.

8.4. DNS Results

8.4.1. The Conditional Balance of Enstrophy Production and Dissipation

We now come to the evaluation of the DNS data (`sim_512`) and start with the terms of the kinetic equation (8.27a) which are presented in figure 8.1. It can be seen that the conditional vortex stretching term $\Sigma\Omega$ is positively correlated with the vorticity and depends strongly on its magnitude. The nonlinear dependence mirrors the statistical

correlations between the rate-of-strain tensor and the vorticity. In the case of statistical independence of these two quantities the conditional vortex stretching term would be a linear function of the magnitude of vorticity with a slope determined by the integral constraint (8.46a). The fact that this function increases with the magnitude of vorticity indicates that stronger vortices are subject to a stronger vortex stretching. By multiplying this term with Ω one obtains the conditional enstrophy production, showing that it is enhanced for stronger vortices.

The diffusive term $\Lambda(\Omega)$ has the opposite effect because it is negatively correlated with the vorticity. As also this term is a nonlinear function of the magnitude of the vorticity, it is apparent that also the diffusive term and consequently the enstrophy dissipation are statistically correlated with the vorticity. This observation is consistent with the above order-of-magnitude estimate that the gradients of vorticity vary on a scale comparable to the vorticity itself.

The next important thing to note is that the conditional vortex stretching term and the (negative) diffusive term are almost identical. Consequently, the conditional forcing term $\Phi(\Omega)$ vanishes. This observation affirms the assumption that the small-scale vorticity statistics indeed is independent from the external forcing mechanisms, and the conditional balance (8.29) can be simplified to (8.41). Consequently, it is expected that the stationary solution of the vorticity PDF does not depend on the external forcing, such that the approximation (8.45) should yield good results. The fact that the conditional balance is independent from the external forcing shows that enstrophy production and dissipation can be seen as internal processes of the turbulent dynamics that do not depend on the details of the external forcing mechanism. This is an important difference compared to the velocity statistics, where we have seen how the external forcing contributes to the shape of the single-point PDF. It should be noted that this conditional balance has already been observed and theoretically discussed for decaying turbulence in [ND94]. Compared to this work the conditional balance holds better for our numerical data, which can be accounted to the well-resolved fields, the good statistical quality and maybe the increased Reynolds number.

8.4.2. The Structure of the Conditional Enstrophy Dissipation Tensor

Next we want to investigate the eigenvalues of the conditional enstrophy dissipation tensor, which are shown in figure 8.2. It can be seen that both eigenvalues depend strongly on the magnitude of vorticity, which has to be compared to the situation discussed for the velocity, where we have seen a nearly constant functional behavior for low values of velocity. This was accounted for by a scale separation argument for the velocity and the kinetic energy dissipation. It is clear that such an argument fails for the vorticity field as we have seen in the preceding paragraphs. A decoupling argument as used for the closure approximation in the case of the single-point velocity statistics would yield constant eigenvalues. In this sense the observation of the strong dependence of the eigenvalues on Ω fits well into the picture which is suggested by the order-of-magnitude

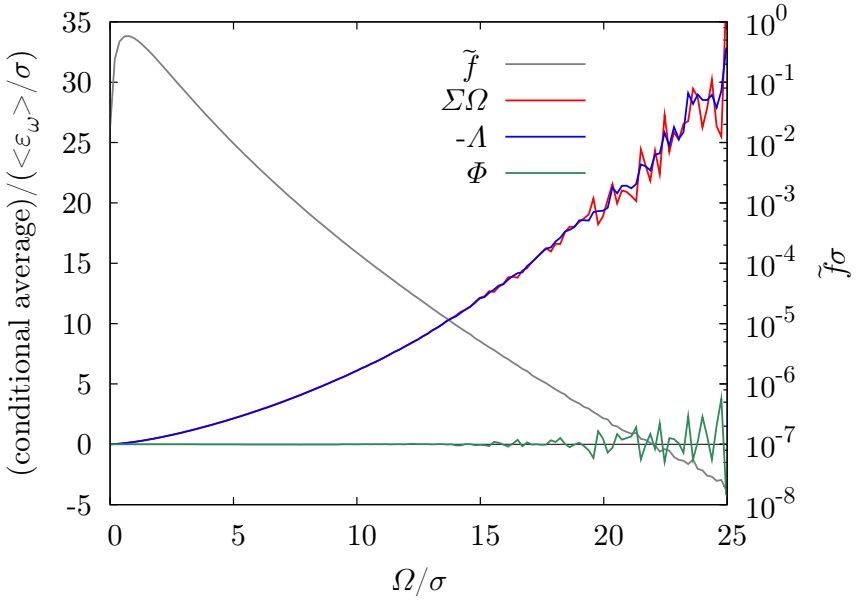

Figure 8.1.: Conditional averages $\Sigma\Omega$, Λ and Φ from the kinetic equation (8.27a). The fact that the first two functions approximately balance indicates that the external forcing does not contribute significantly to the enstrophy budget equation (8.29) (`sim_512`).

estimate for the vorticity gradients implying strong correlations of the vorticity gradients and the vorticity. This view can qualitatively be confirmed by figure 8.3, where the absolute value of vorticity as well as the trace of the enstrophy dissipation tensor are shown. It is clear to see that the gradients display slightly more fine structure than the vorticity itself, however, strong spatial correlations are visible. This has to be compared to the visualization of the velocity and kinetic energy dissipation in figure 1.1 which revealed a scale separation of the quantities.

The second important fact to be observed from figure 8.2 is that the eigenvalues are approximately proportional to each other by a factor of about four. This implies that the conditional enstrophy dissipation tensor is not isotropic and contains strong directional correlations. This conforms to the observation that the small-scale structure is governed by filamentary vortex structures, which cause strong gradients perpendicular to the filament axis.

8.4.3. Reconstruction of the Homogeneous and Stationary PDFs

Having estimated all terms that constitute the unclosed terms in the kinetic equations (8.27b) and (8.27c), we can evaluate the homogeneous and stationary solutions (8.43) and (8.44) as well as the solution (8.45), that assumes a negligible influence of the external forcing. All three PDFs are shown in figure 8.4 together with the PDF directly estimated from the DNS data and an angle-integrated Gaussian for comparison. All three

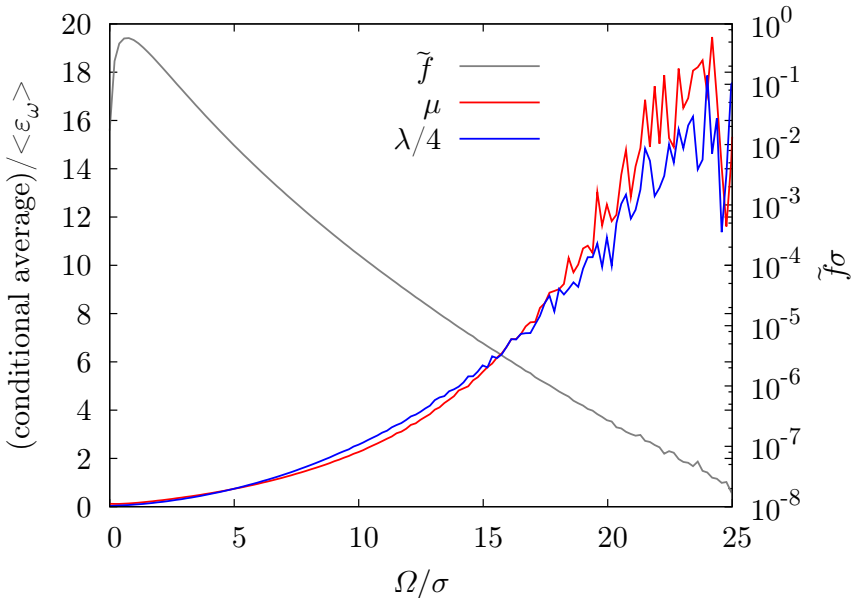

Figure 8.2.: Eigenvalues μ and λ of the conditional enstrophy dissipation tensor D. Both eigenvalues depend the magnitude of vorticity indicating pronounced statistical correlations. Note that $\frac{\lambda}{4}$ instead of λ is shown, such that the similar functional shape of $\frac{\lambda}{4}$ and μ implies that the enstrophy dissipation tensor is not isotropic. $\langle\varepsilon_\omega\rangle$ denotes the mean rate of enstrophy dissipation (`sim_512`).

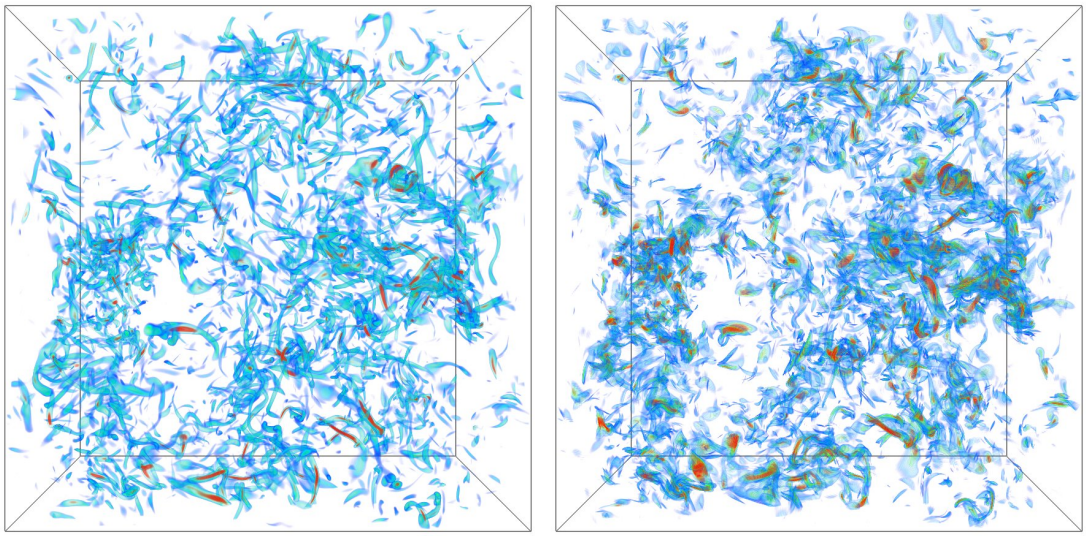

Figure 8.3.: Volume renderings of the absolute value of the vorticity and the trace of enstrophy dissipation tensor. Spatial correlations of the two quantities are apparent (simulation parameters identical to `sim_512`).

solutions agree perfectly with the highly non-Gaussian functional form of the vorticity PDF and indicate both the consistency of the theory as well as the validity of the approximate conditional balance of enstrophy production and dissipation. Additionally the tail dependence according to the analytical closure (8.51) is shown for reference. It can be observed that, although not delivering a perfect match, the approximate behavior of the PDF for large values of vorticity is captured quite well.

These observations again motivate the question how the interplay of the conditional averages leads to the observed highly non-Gaussian shape of the PDF. This can be answered with a closer look at the terms of, e.g., the stationary solution (8.45) together with figure 8.5, where the terms appearing in the integrand are shown. The approximately algebraic behavior of λ in the prefactor of equation (8.45) causes an algebraically decaying contribution to the functional shape of the PDF. The remaining two terms in the integrand contribute with a rather complicated functional shape. It can be seen that these two terms contribute very differently to the PDF. The fact that these functions are not linear or constant, respectively, altogether yields the slowly decaying (stretched) exponential tails of the PDF. Although a direct comparison (not shown) of the conditional averages Σ_0, λ_0 and μ_0 from the analytical closure approximation compares poorly to the ones estimated directly from the numerical data, the resulting approximation for the tail is quite decent. This can also be understood with figure 8.5, where the corresponding ratios are also shown for reference. It can be seen that for large values of vorticity the simple closure approximations yield a rough estimate for the ratios determined from DNS. While the estimate for the ratio of the two eigenvalues of the conditional dissipation tensor together with the prefactor in equation (8.45) yields an algebraic decay, the exponential contribution to the functional shape can be accounted to the ratio of the conditional vortex stretching term and the eigenvalue of the conditional enstrophy dissipation tensor. So the situation is similar to the Gaussian closure approximation in chapter 7, where the individual conditional averages of the approximates compared poorly to the ones estimated directly from DNS, and their ratios compared quite well.

8.4.4. Reynolds Number Dependence

The results for the vorticity statistics have also been investigated with respect to Reynolds number dependence for the simulations `sim_256`, `sim_512` and `sim_1024`. The vorticity PDF for different Reynolds numbers is shown in figure 8.6. It can be seen that the PDF displays strongly non-Gaussian, stretched exponential tails for all Reynolds numbers. For increasing Reynolds numbers the PDFs become increasingly stretched, showing that extreme values of vorticity become more probable. This probably results from the fact that the vorticity concentrates in finer and finer vortex structures with increasing Reynolds number. Recall that the tendency to develop more extreme values (in terms of standard deviations) with increasing Reynolds numbers has not been observed for the velocity, such that it can be concluded that, although the vorticity is getting more non-Gaussian, the vorticity field does not produce a more non-Gaussian

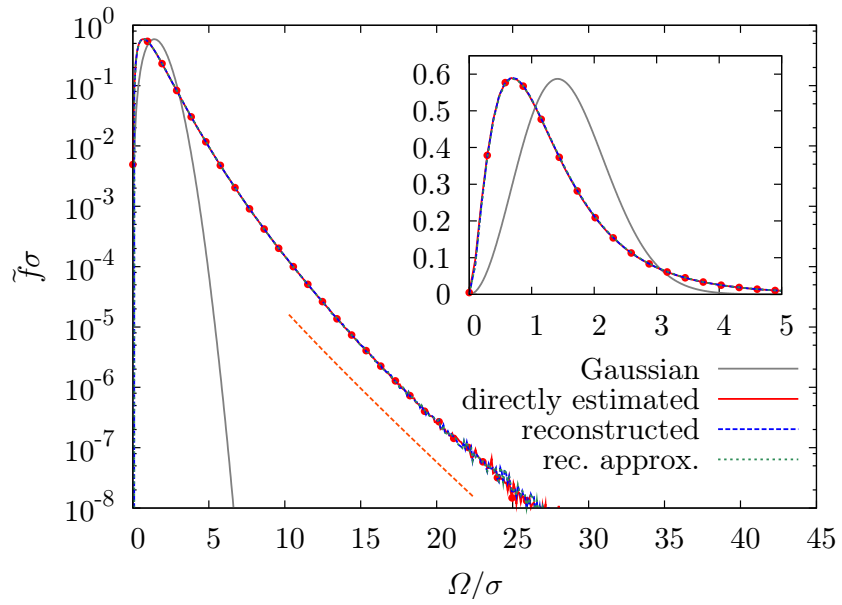

Figure 8.4.: Directly estimated and reconstructed vorticity PDF according to the exact relations (8.43) and (8.44) as well as the approximate relation (8.45). The agreement is perfect in all three cases demonstrating the consistency of the theoretical framework and the validity of the approximate conditional balance (8.41). The dashed orange line indicates the tail behavior of the analytical closure approximation (8.51) (`sim_512`).

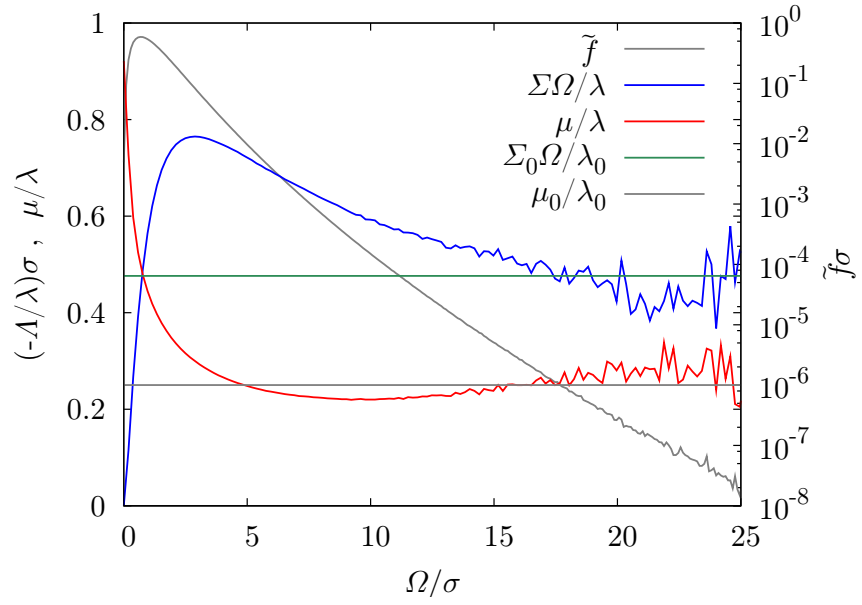

Figure 8.5.: The quotients $(\Sigma\Omega)/\lambda$ and μ/λ appearing in equation (8.45) (`sim_512`).

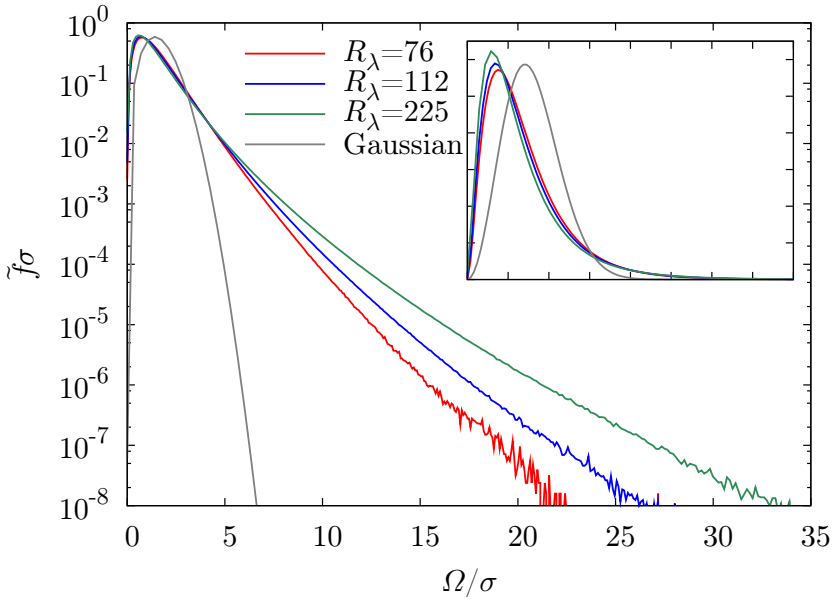

Figure 8.6.: Vorticity PDF for different Reynolds numbers. With increasing Reynolds number extreme vorticity events occur more frequently (`sim_256`, `sim_512`, `sim_1024`).

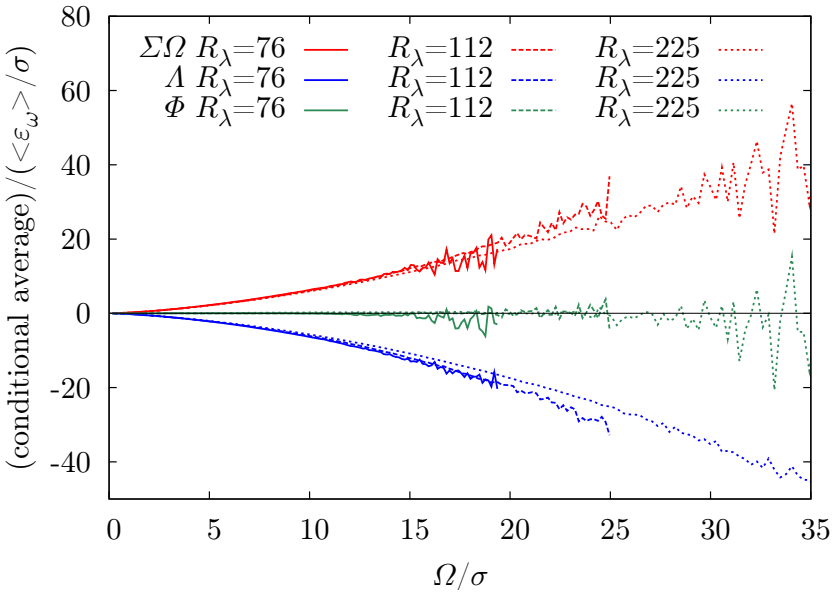

Figure 8.7.: Conditional averages $\Sigma\Omega$, Λ and Φ from the kinetic equation (8.27a) for different Reynolds numbers (`sim_256`, `sim_512`, `sim_1024`).

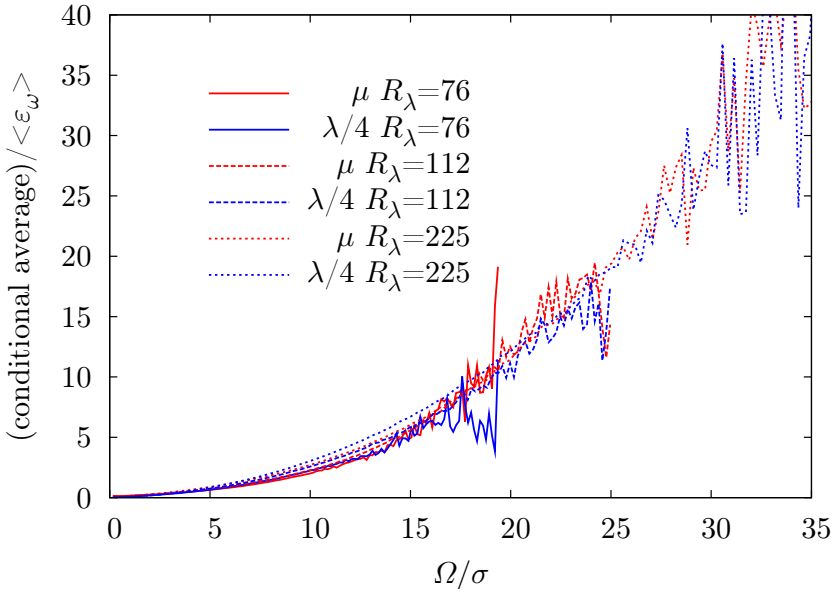

Figure 8.8.: Eigenvalues μ and λ of the conditional enstrophy dissipation tensor D for different Reynolds numbers (`sim_256`, `sim_512`, `sim_1024`).

velocity field on the single-point level.

Coming to the conditional averages that arise in the PDF equations, figure 8.7 shows the functions related to the vortex stretching and the diffusive term. It can be observed that the functional form does not vary strongly with the Reynolds number, and the balance of the vortex stretching term and the diffusive term does not change significantly. The major difference is that the range of values of the vorticity extends with the Reynolds number mirroring the appearance of more intense events. The same observation basically holds for the conditional averages related to the conditional enstrophy dissipation tensor, which are shown in figure 8.8. The ratio between the two eigenvalues of this tensor of about four proves to be robust for all Reynolds numbers, and it would be interesting to see if this observation carries over to even higher Reynolds numbers. If one would like to extract a trend form these figures, one could say that the slope of the conditional vortex stretching terms seems to decrease a little bit for increasing Reynolds number, whereas the slopes of the eigenvalues related to enstrophy dissipation increase with the Reynolds number. These two influences, together with the extension of the possible vorticity values, then lead to a more pronounced stretched exponential shape of the PDF.

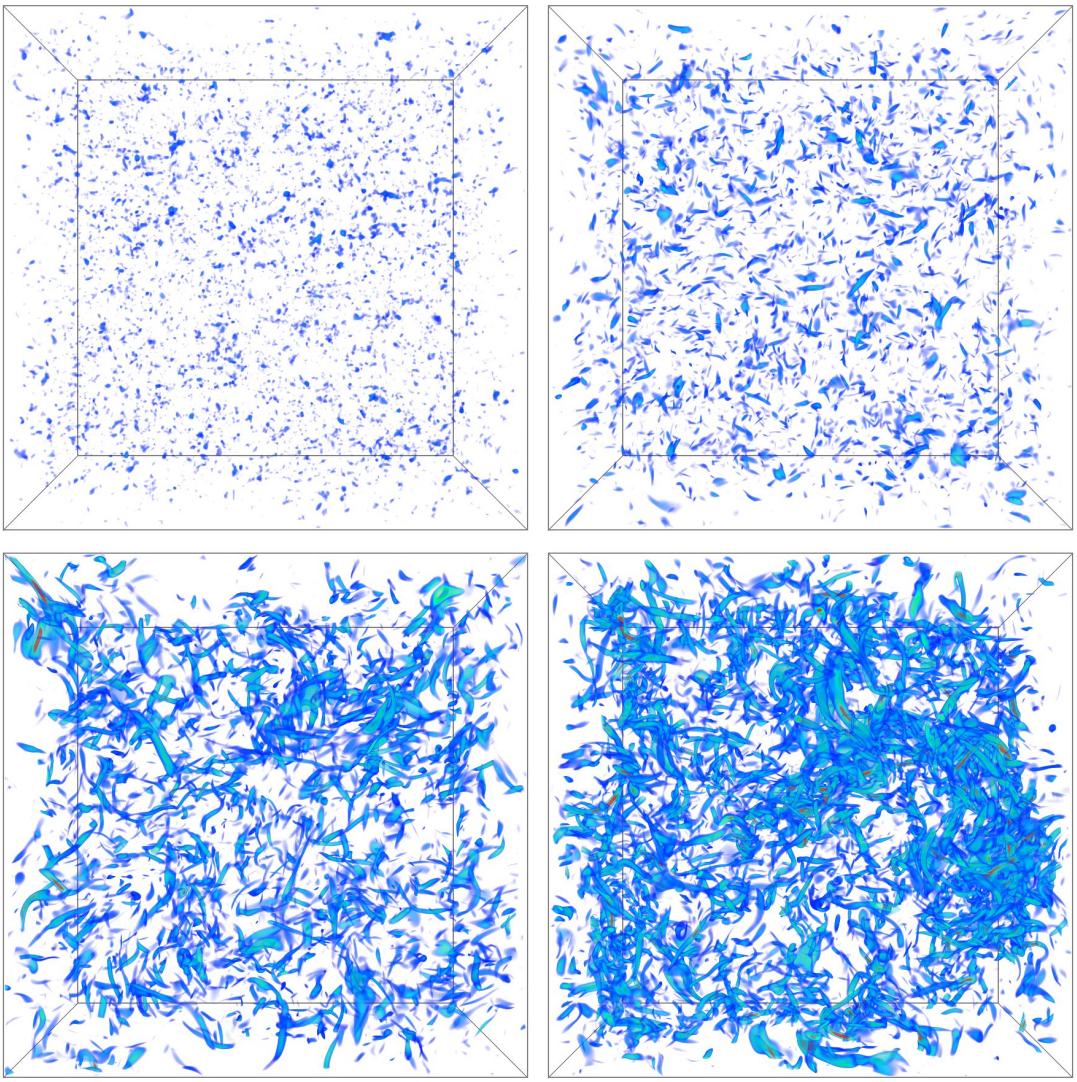

Figure 8.9.: Volume rendering of the magnitude of vorticity for a simulation with randomized initial conditions. The simulation time increases from upper left to lower right: $0.0T$, $0.07T$, $0.35T$ $3.5T$. The randomized initial condition does not contain any coherent vortex structures, but already after $0.07T$ the first vortices have emerged. In the course of time they grow stronger, eventually forming again a fully developed turbulent field.

8.4.5. Evolution of Non-Gaussian Statistics from Random Initial Conditions

After investigating the homogeneous and stationary solutions of the PDF as well as the conditional balance of vortex stretching and diffusion, we want to turn to a non-stationary situation in this section. In particular, we investigate the evolution of the vorticity field starting from random Gaussian initial conditions. To this end a subensemble of the run `sim_512` consisting of five independent fields has been randomized with the method described in chapter 4 before these fields have been taken as an initial conditions. Some snapshots of the temporal evolution of these simulations are shown in figure 8.9. It can be seen that the initial condition appears unstructured and does not contain any vortex tubes. This, however, changes soon as figure 8.9 shows that already after $0.07T$ the first structures have emerged. In the course of time these structures grow stronger, and already after $0.35T$ pronounced vortex tubes have developed. For even later stages of the simulation, the fully developed turbulent structure of the vorticity field like for a stationary simulation is recovered, where both the number as well as the strength of the vortex tubes has increased.

It is now interesting to study this scenario in the framework of the kinetic equation (8.27a) with the method of characteristics, which yields the set of equations

$$\frac{\mathrm{d}}{\mathrm{d}t}\widetilde{\Omega}(t,\Omega_0) = \left[\Sigma(\Omega,t)\Omega + \Lambda(\Omega,t)\right]_{\Omega=\widetilde{\Omega}(t,\Omega_0)} \tag{8.59a}$$

$$\frac{\mathrm{d}}{\mathrm{d}t}\tilde{f}(\widetilde{\Omega}(t,\Omega_0);t) = \left[-\frac{\partial}{\partial\Omega}\big(\Sigma(\Omega,t)\Omega + \Lambda(\Omega,t)\big)\right]_{\Omega=\widetilde{\Omega}(t,\Omega_0)} \tilde{f}(\widetilde{\Omega}(t,\Omega_0);t) \quad . \tag{8.59b}$$

For this presentation we take for granted that the conditional forcing Φ can be neglected even in this non-stationary situation, which has been checked by testing the results also for decaying turbulence. The conditional vortex stretching term $\Sigma(\Omega,t)\Omega$ as well as the conditional diffusive term $\Lambda(\Omega,t)$ are shown for different stages of the simulation in figure 8.10 along with the PDF of vorticity. The randomized Gaussian initial condition displays vanishing vortex stretching and a linear diffusive term. After a short time, corresponding to the first appearance of vortex tubes in figure 8.9, both nonlinear vortex stretching as well as vorticity diffusion have developed. Interpreting these conditional averages with equations (8.59a) and (8.59b) shows that the vorticity is, as observed before, depleted due to the dissipative term and amplified due to the vortex stretching term. However, dealing with a non-stationary situation, these two influences do not cancel. For the core of the PDF the diffusive term is dominant, such that the PDF is squeezed toward lower values of vorticity. For larger values, the vorticity is amplified due to unbalanced vortex stretching. At the same time equation (8.59b) additionally contributes to the change of shape of the PDF. By this an initially Gaussian PDF gradually develops exponential and finally stretched exponential tails, up to the time when the conditional balance (8.41) is recovered. Note that, as the evolution of the vorticity PDF is not self-similar, the right-hand side of (8.59a) is a nonlinear function, consistent with the discussion in chapter 7.

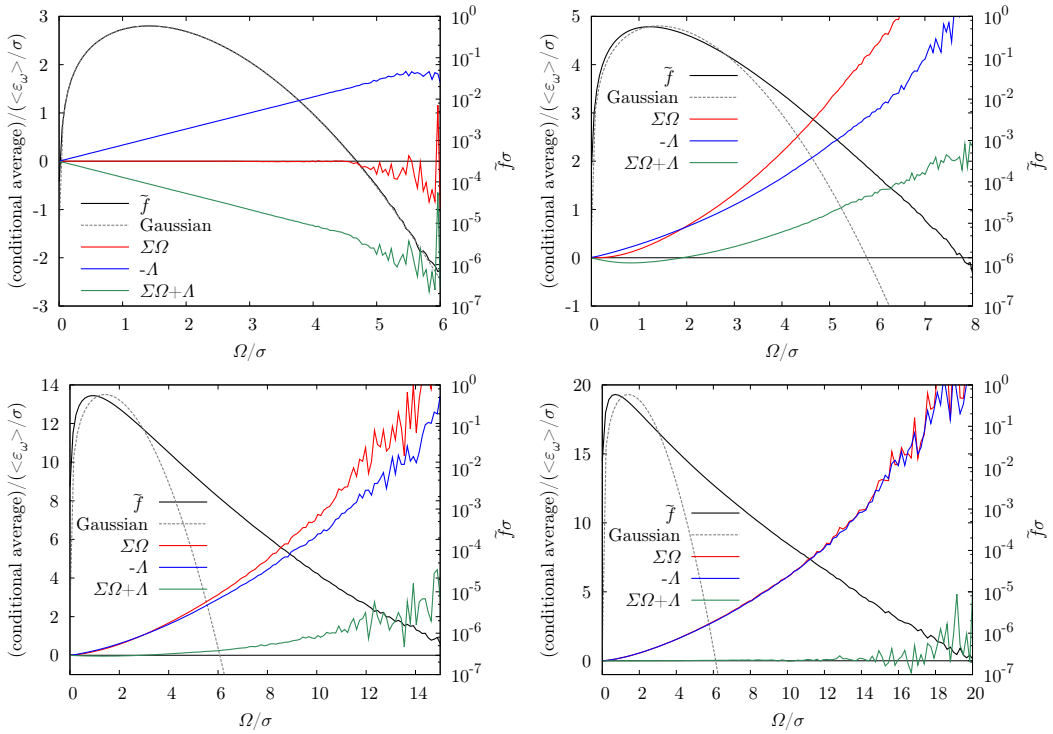

Figure 8.10.: Conditional vortex stretching and vorticity diffusion for simulations starting from Gaussian initial conditions. The random initial condition has vanishing vortex stretching (i.e. enstrophy production) and a linear diffusive term. Already after $0.07T$ nonlinear vortex stretching and vorticity diffusion have emerged, where the low values of the vorticity are diffusion dominated, whereas the high values are dominated by vortex stretching. After several large-eddy turnover times the conditional balance of the right-hand side of equation (8.27a) as observed for stationary statistics is recovered. The same instants as in figure 8.9 have been chosen.

Along with the visualizations in figure 8.10, the physical interpretation of these observations is straightforward. Small fluctuations in the random initial condition constitute the germs of vortex structures that emerge under the action of the vorticity equation. In the course of time the vorticity with low magnitude, which can be thought of as more unstructured, decays due to dominating dissipation. At the same time strong vortices will become even stronger due to unbalanced vortex stretching until the field finally relaxes to a statistically stationary state.

8.5. Ensemble of Burgers Vortices

The visualizations so far indicate that the vorticity field consists of a large number of filamentary coherent structures. It is therefore tempting to try to calculate the conditional averages arising in the kinetic equations from an ensemble of such vortices.

An analytically tractable vortex solution has already been introduced in chapter 1 in the form of the Burgers vortex. The vorticity field of such a vortex located at position $\boldsymbol{x}_0$ and pointing into the direction $\boldsymbol{e}_\parallel$ is given by

$$\boldsymbol{\omega}(\boldsymbol{x}) = \omega(r_\perp)\,\boldsymbol{e}_\parallel \quad \text{with} \quad \omega(r_\perp) = \frac{\Gamma a}{4\pi\nu}\,\exp\left[-\frac{a r_\perp^2}{4\nu}\right] \quad , \tag{8.60}$$

and the distance to the vortex axis $r_\perp$ is calculated according to

$$r_\perp = \left|\boldsymbol{x} - \boldsymbol{x}_0 - \left[(\boldsymbol{x}-\boldsymbol{x}_0)\cdot\boldsymbol{e}_\parallel\right]\,\boldsymbol{e}_\parallel\right| \quad . \tag{8.61}$$

Our ensemble shall consist of isolated, non-interacting vortex structures, such that we can calculate all terms of interest from a single vortex structure. In a sense we consider a "dilute Burgers vortex gas" at a fixed viscosity ν, where each Burgers vortex is characterized by the rate of strain a and the circulation Γ.

To calculate the terms of interest for an individual structure, we choose $\boldsymbol{x}_0 = \boldsymbol{0}$ and $\boldsymbol{e}_\parallel = \boldsymbol{e}_z$. To obtain the vortex stretching term, we first note that the rate-of-strain tensor may be decomposed into

$$\mathrm{S} = \mathrm{S}_{\mathrm{ext}} + \mathrm{S}_B \quad , \tag{8.62}$$

where the external contribution

$$\mathrm{S}_{\mathrm{ext}} = \begin{pmatrix} -\frac{a}{2} & 0 & 0 \\ 0 & -\frac{a}{2} & 0 \\ 0 & 0 & a \end{pmatrix} \tag{8.63}$$

is given by the potential flow related to the rate of strain a, and S_B is the strain locally induced by the vortex tube, which can be obtained by differentiating the velocity field (1.18) of the Burgers vortex. As only the vortex stretching term plays a role in the kinetic equations (8.27a) and (8.27c), it is useful to note that this term depends only on the external contribution to the rate-of-strain tensor such that

$$\mathrm{S}\boldsymbol{\omega} = \mathrm{S}_{\mathrm{ext}}\boldsymbol{\omega} = a\boldsymbol{\omega} \quad , \tag{8.64}$$

i.e., the vortex stretching field is directly proportional to the vorticity field. It is also straightforward to calculate the diffusive term for a single Burgers vortex yielding

$$\nu\Delta\boldsymbol{\omega} = \left[-a + \frac{a^2 r_\perp^2}{4\nu}\right]\boldsymbol{\omega} \quad , \tag{8.65}$$

showing that also this term depends linearly on the vorticity field. Finally, one can also calculate the enstrophy dissipation tensor, which takes the form

$$\left(\nu\frac{\partial\omega_i}{\partial x_k}\frac{\partial\omega_j}{\partial x_k}\right)_{1\le i,j\le 3} = \begin{pmatrix} 0 & 0 & 0 \\ 0 & 0 & 0 \\ 0 & 0 & \frac{a^2 r_\perp^2}{4\nu} \end{pmatrix}\boldsymbol{\omega}^2 \quad , \tag{8.66}$$

such that this tensor is quadratic in $\boldsymbol{\omega}$ and has only a single entry. The last point has an important implication as it can be seen that an ensemble of Burgers vortices is incapable of reproducing the ratio of the eigenvalues λ and μ which has been observed in the DNS data; each Burgers vortex contributes with $\mu = 0$ and $\lambda = \frac{a^2 r_\perp^2}{4\nu}\Omega^2$. On the one hand this may be seen as a disappointing statement as we cannot expect to calculate the "correct" statistics from such a simplified model. On the other hand the interesting conclusion to be drawn is that the coherent structures in turbulence display an inner structure which is not represented by the Burgers vortex.

Nevertheless, we would like to pursue the idea of a vortex ensemble a bit further as the last calculations have shown that, when we are considering an individual Burgers vortex, we can express the vortex stretching term, the diffusive term and the enstrophy dissipation tensor locally in terms of the vorticity field. This eventually allows to calculate the conditional averages analytically to a certain extent as we want to demonstrate now. To this end consider the general situation that we want to calculate the conditional average of a quantity $q(\boldsymbol{x})$ with respect to the vorticity $\boldsymbol{\omega}$. If Q denotes the corresponding sample space variable, this can be done via

$$\left\langle q \middle| \boldsymbol{\Omega} \right\rangle f(\boldsymbol{\Omega}) = \int \mathrm{d}Q \, Q \, f(Q, \boldsymbol{\Omega}) \quad . \tag{8.67}$$

Assuming that the considered volume is large enough to represent the ensemble average, the joint PDF $f(Q, \boldsymbol{\Omega})$ can be obtained by

$$f(Q, \boldsymbol{\Omega}) = \frac{1}{V} \int \mathrm{d}\boldsymbol{x} \, \delta(q(\boldsymbol{x}) - Q) \, \delta(\boldsymbol{\omega}(\boldsymbol{x}) - \boldsymbol{\Omega}) \quad . \tag{8.68}$$

By inserting this expression into (8.67), we readily arrive at

$$\begin{aligned} \left\langle q \middle| \boldsymbol{\Omega} \right\rangle f(\boldsymbol{\Omega}) &= \frac{1}{V} \int \mathrm{d}\boldsymbol{x} \, q(\boldsymbol{x}) \, \delta(\boldsymbol{\omega}(\boldsymbol{x}) - \boldsymbol{\Omega}) \\ &= \sum_i \frac{1}{V_i} \int_{V_i} \mathrm{d}\boldsymbol{x} \, q(\boldsymbol{x}) \, \delta(\boldsymbol{\omega}(\boldsymbol{x}) - \boldsymbol{\Omega}) \quad . \end{aligned} \tag{8.69}$$

For the second equality we have made use of the fact that the considered volume can be decomposed into disjoint volumes containing only single Burgers vortices. The interesting fact now is that all quantities of interest for the statistical equations can be expressed in terms of the vorticity field and a function containing parameters of the individual vortex and, if necessary, a spatial dependence. That means, for the i-th vortex we find

$$q(\boldsymbol{x}) = G(\Gamma_i, a_i, \boldsymbol{x}_0, \boldsymbol{e}_\parallel, \boldsymbol{x}) \, F(\boldsymbol{\omega}) \quad . \tag{8.70}$$

By inserting this expression into (8.69) and making use of the sifting property of the delta distribution, we obtain

$$\left\langle q \middle| \boldsymbol{\Omega} \right\rangle f(\boldsymbol{\Omega}) = F(\boldsymbol{\Omega}) \left[\sum_i \frac{1}{V_i} \int_{V_i} \mathrm{d}\boldsymbol{x} \, G(\Gamma_i, a_i, \boldsymbol{x}_0, \boldsymbol{e}_\parallel, \boldsymbol{x}) \, \delta(\boldsymbol{\omega}(\boldsymbol{x}) - \boldsymbol{\Omega}) \right] \quad . \tag{8.71}$$

This shows that the function $F(\boldsymbol{\Omega})$ can be separated, leaving an expression which depends on how in detail the ensemble is set up. Note that the integral term still may contain a functional dependence on $\boldsymbol{\Omega}$. A simple observation, however, can be made for the case that $G = c$ is a constant function. In that case we simply obtain

$$\langle q|\boldsymbol{\Omega}\rangle\, f(\boldsymbol{\Omega}) = F(\boldsymbol{\Omega}) \left[\sum_i \frac{1}{V_i} \int_{V_i} \mathrm{d}\boldsymbol{x}\, c\, \delta(\boldsymbol{\omega}(\boldsymbol{x}) - \boldsymbol{\Omega})\right] = c\, F(\boldsymbol{\Omega})\, f(\boldsymbol{\Omega}) \quad , \tag{8.72}$$

such that the conditional average is determined by c and F only. If we apply this reasoning to the individual terms relevant for the kinetic equations, we obtain

$$\langle \mathrm{S}\boldsymbol{\omega}|\boldsymbol{\Omega}\rangle f(\boldsymbol{\Omega}) = \boldsymbol{\Omega} \left[\sum_i \frac{1}{V_i} \int_{V_i} \mathrm{d}\boldsymbol{x}\, a_i\, \delta(\boldsymbol{\omega}(\boldsymbol{x}) - \boldsymbol{\Omega})\right] \tag{8.73a}$$

$$\langle \nu\Delta\boldsymbol{\omega}|\boldsymbol{\Omega}\rangle f(\boldsymbol{\Omega}) = \boldsymbol{\Omega} \left[\sum_i \frac{1}{V_i} \int_{V_i} \mathrm{d}\boldsymbol{x} \left[-a_i + \frac{a_i^2 r_{\perp,i}^2}{4\nu}\right] \delta(\boldsymbol{\omega}(\boldsymbol{x}) - \boldsymbol{\Omega})\right] \tag{8.73b}$$

$$\left\langle \nu \frac{\partial \omega_i}{\partial x_k} \frac{\partial \omega_i}{\partial x_k} \middle| \boldsymbol{\Omega} \right\rangle f(\boldsymbol{\Omega}) = \boldsymbol{\Omega}^2 \left[\sum_i \frac{1}{V_i} \int_{V_i} \mathrm{d}\boldsymbol{x}\, \frac{a_i^2 r_{\perp,i}^2}{4\nu}\, \delta(\boldsymbol{\omega}(\boldsymbol{x}) - \boldsymbol{\Omega})\right] \quad . \tag{8.73c}$$

From a formal point of view the problem is solved in this way, although an analytical evaluation of the remaining integral terms is impracticable. If one, however, assumes that the dependence on $\boldsymbol{\Omega}$ of these terms is weak, the general functional shape expected from such a vortex model can be seen from the prefactors.

8.6. Summary

In this chapter we have worked out the details of the single-point equation for the vorticity in the framework of the LMN hierarchy. To this end we first extended Lundgren's approach to the vorticity field and in this way obtained the hierarchy of PDF equations already introduced by Novikov. We then simplified the resulting equations by application of statistical symmetries, which eventually allowed to derive homogeneous and stationary solutions for the vorticity PDF, which is one of the main results of this chapter. Although these solutions are formally identical to the solutions in the velocity case, a very different single-point statistics is expected due to a different functional form of the conditional averages. This has been supported theoretically with a number of considerations. First, we have argued that the forcing is expected to have a negligible influence on the statistics, such that the conditional balance of vortex stretching and diffusion holds. This is a physically important result, as it indicates that the shape of the vorticity PDF is the result of the "pure" dynamics of the vorticity equation and is not influenced by the external forcing. Furthermore, we have argued that a simple scale separation argument, that leads to Gaussian results in the case of the velocity field, has to fail for the vorticity field. However, the complete opposite assumption, namely the assumption of strong

statistical correlations then was used to calculate an explicit expression for the tail behavior of the PDF. Apart from that, it has been demonstrated how the kinetic equation may be used to set up a simple Langevin model, which by construction yields the correct single-point statistics.

As for the velocity field, these theoretical points have been supplemented and verified by DNS results, which revealed strong statistical correlations of the arising conditional averages and the vorticity. A particularly interesting observation in this context has been the fact that the conditional enstrophy dissipation tensor exhibits non-vanishing off-diagonal elements, which is different from the conditional dissipation tensor for the kinetic energy. This observation originates from the fact that the presence of small-scale coherent structures induces directional correlations of the vorticity gradients and the vorticity itself. As for the velocity, the homogeneous and stationary solutions have been obtained also for the vorticity and a perfect agreement with the directly estimated PDF has been found. In this context we have also demonstrated the conditional balance of vortex stretching and vorticity diffusion, which has already been observed and predicted by Novikov. However, our results confirm his results at an unprecedented statistical quality and at higher Reynolds numbers. All of the statistical results have also been checked as a function of Reynolds number, showing that the stretched exponential character of the PDFs increases with increasing Reynolds number.

To investigate the influence of coherent structures on the statistical quantities, several attempts have been made. We first investigated the evolution of the conditional right-hand side of the vorticity equation for a flow starting from random Gaussian initial conditions. Interpreting these results with the method of characteristics revealed that strong vortices grow stronger due to unbalanced vortex stretching, whereas weak vorticity decays due to dominant dissipation. We then outlined how the unknown conditional averages can be calculated under the assumption that turbulence consists of an ensemble of Burgers vortices. The main outcome here is that, while these calculations in general will yield highly non-Gaussian vorticity statistics, the Burgers vortex itself is a too simple structure to explain the local conditional structure of turbulence. This observation will be a key point in the following chapter.

On a general level this and the preceding chapter have shown how a general framework describing and explaining the single-point statistics of fully developed homogeneous isotropic turbulence can be established by combining analytical and numerical efforts. Although the mathematical approach is very similar in the case of the velocity and the vorticity field, it has been shown how the differing topological structure of the fields eventually yields very different single-point statistics. Up to now the discussion has been led in terms of statistical correlations of the various dynamical quantities that arise in the Navier-Stokes and vorticity equation. In the following two chapters we will outline how the closure problem may be discussed and treated on the basis of two-point statistics.

9. Two-Point Enstrophy Statistics and the Closure Problem on the Level of Multi-Point Statistics

9.1. Motivation

Up to now we have treated the closure problem on the basis of a discussion of the local dynamical correlations of the right-hand side of the Navier-Stokes or the vorticity equation with the velocity or vorticity, respectively. This has allowed to physically interpret the arising terms, and eventually homogeneous and stationary solutions in terms of these quantities have been obtained. It is, of course, possible to proceed in this direction and apply the same strategy for two-point statistics, and in fact we will partly follow this path in the current chapter investigating the two-point enstrophy statistics in fully developed turbulence. To this end we will first discuss the two-point PDF equation for the vorticity and its relation to the two-point enstrophy PDF equation. As in the preceding chapters, the unclosed terms will be estimated from DNS data leading to a number of interesting observations.

We then, however, will seek for a connection of the results to the multi-point statistics of vorticity. This has already been discussed in chapters 6 and 8, where we have seen that the kinetic equations may be formulated in a way that the single-point equation couples to the two-point equation and so forth.

If one wants to treat the closure problem from this point of view, the two-point statistics of turbulence has to be understood and eventually modeled in order to yield a closure on the single-point level. To be more precise, closure here means to establish a model for the two-point statistics in a way that the conditional vortex stretching term and vorticity diffusion can be calculated. Accordingly, closing the two-point equations involves an investigation and understanding of three-point statistics.

With an increasing number of spatial points, the statistical quantities become more and more complex. It soon becomes clear that the dimensionality of the problem will prohibit a global numerical and analytical treatment of the problem, such that simplifying assumptions have to be made to study the multi-point statistics of fully developed turbulence and compare predictions to numerically obtained results.

These considerations are closely related to two works by Novikov [Nov93, MDN96], in which the analysis of the local conditional structure of the vorticity field in fully developed turbulence has been introduced. After reviewing and extending these works, we will take the multivariate Gaussian PDF as a guide how the multi-point statistics

can be treated analytically. It already becomes clear on the single-point level that the functional structure of Gaussian PDFs is incapable of explaining the observed vorticity statistics, such that we will construct an in a sense minimal model compatible with the mathematical structure of the kinetic equation. Hereby we will introduce the Twisted Gaussian Approximation, which is extendable to the statistics of multiple points in space. This concept then eventually will allow to study the two-point vorticity statistics in the Twisted Gaussian Approximation. These results then will be compared to DNS results and discussed.

9.2. Two-Point Enstrophy Statistics

9.2.1. The PDF Equations

The general procedure of setting up evolution equations for PDFs has already been introduced and exemplified in chapters 6, 7 and 8. Following these derivations, it is straightforward to write down the evolution equation for the two-point PDF $f_2(\boldsymbol{\Omega}_1, \boldsymbol{\Omega}_2; \boldsymbol{x}_1, \boldsymbol{x}_2, t)$. It takes the form

$$\begin{aligned}\frac{\partial}{\partial t} f_2 + \nabla_{\boldsymbol{x}_1} \cdot \left[\left\langle \boldsymbol{u}_1 \middle| \boldsymbol{\Omega}_1, \boldsymbol{\Omega}_2, \boldsymbol{r} \right\rangle f_2\right] + \nabla_{\boldsymbol{x}_2} \cdot \left[\left\langle \boldsymbol{u}_2 \middle| \boldsymbol{\Omega}_1, \boldsymbol{\Omega}_2, \boldsymbol{r} \right\rangle f_2\right] = \\ - \nabla_{\boldsymbol{\Omega}_1} \cdot \left[\left\langle \mathrm{S}_1 \boldsymbol{\omega}_1 + \nu \Delta_{\boldsymbol{x}_1} \boldsymbol{\omega}_1 + \nabla_{\boldsymbol{x}_1} \times \boldsymbol{F}_1 \middle| \boldsymbol{\Omega}_1, \boldsymbol{\Omega}_2, \boldsymbol{r} \right\rangle f_2\right] \\ - \nabla_{\boldsymbol{\Omega}_2} \cdot \left[\left\langle \mathrm{S}_2 \boldsymbol{\omega}_2 + \nu \Delta_{\boldsymbol{x}_2} \boldsymbol{\omega}_2 + \nabla_{\boldsymbol{x}_2} \times \boldsymbol{F}_2 \middle| \boldsymbol{\Omega}_1, \boldsymbol{\Omega}_2, \boldsymbol{r} \right\rangle f_2\right] \quad , \end{aligned} \tag{9.1}$$

i.e., the right-hand side of this PDF equation is similar to the single-point PDF equation (8.14), however, the different terms of the vorticity equation now have to be evaluated at the two spatial points $\boldsymbol{x}_1$ and $\boldsymbol{x}_2$ and are conditionally averaged with respect to the two sample space vorticities $\boldsymbol{\Omega}_1$ and $\boldsymbol{\Omega}_2$. On the left-hand side we have two advective terms. Due to homogeneity the statistics can only depend on $\boldsymbol{r} = \boldsymbol{x}_2 - \boldsymbol{x}_1$ such that we have

$$\nabla_{\boldsymbol{x}_1} = -\nabla_{\boldsymbol{r}} \quad \text{and} \quad \nabla_{\boldsymbol{x}_2} = \nabla_{\boldsymbol{r}} \quad . \tag{9.2}$$

As a consequence the two advective terms can be combined to yield

$$\begin{aligned}\nabla_{\boldsymbol{x}_1} \cdot \left[\left\langle \boldsymbol{u}_1 \middle| \boldsymbol{\Omega}_1, \boldsymbol{\Omega}_2, \boldsymbol{r} \right\rangle f_2\right] + \nabla_{\boldsymbol{x}_2} \cdot \left[\left\langle \boldsymbol{u}_2 \middle| \boldsymbol{\Omega}_1, \boldsymbol{\Omega}_2, \boldsymbol{r} \right\rangle f_2\right] \\ = \nabla_{\boldsymbol{r}} \cdot \left[\left\langle \boldsymbol{u}_2 - \boldsymbol{u}_1 \middle| \boldsymbol{\Omega}_1, \boldsymbol{\Omega}_2, \boldsymbol{r} \right\rangle f_2\right] \\ =: \nabla_{\boldsymbol{r}} \cdot \left[\left\langle \delta \boldsymbol{u} \middle| \boldsymbol{\Omega}_1, \boldsymbol{\Omega}_2, \boldsymbol{r} \right\rangle f_2\right] \quad , \end{aligned} \tag{9.3}$$

by which we have introduced the conditional velocity increment. Since we are considering two-point statistics, homogeneity does not imply a vanishing advective term. Accordingly, we have a probability flux in scale induced by a coupling of the advective term. An important implication is that the single-point balance (8.29) does not generally hold for the two-point vorticity statistics. The imbalance of the conditionally averaged right-hand

sides for fixed spatial distances is rather accompanied by a probability flux in scale. For the special case of $r \to \infty$, for which the statistics of the two points becomes independent, the single-point balance, however, is recovered.

Of course, this PDF equation can be simplified further under the assumption of isotropic statistics. Even under this assumption the two-point PDF $f_2(\boldsymbol{\Omega}_1, \boldsymbol{\Omega}_2; \boldsymbol{r}, t)$ still depends on six scalar quantities, which can be chosen as

$$\Omega_1,\, \Omega_2,\, r,\, \hat{\boldsymbol{r}} \cdot \widehat{\boldsymbol{\Omega}}_1,\, \hat{\boldsymbol{r}} \cdot \widehat{\boldsymbol{\Omega}}_2 \quad \text{and} \quad \widehat{\boldsymbol{\Omega}}_1 \cdot \widehat{\boldsymbol{\Omega}}_2$$

as already mentioned in the introductory chapter. Furthermore, the conditional averages appearing in the kinetic equation may statistically point in all possible directions which can be built from the vectors they depend on. This eventually prohibits to construct an orthonormal set of sample space vectors. Facing this situation, it is clear that the full information contained in the unclosed terms is numerically inaccessible. We thus seek for a lower-dimensional representation of the two-point vorticity statistics which is numerically tractable and still contains meaningful information.

One natural choice for such a lower-dimensional projection is the enstrophy statistics for several reasons. First of all, the enstrophy represents an invariant of the vorticity statistics. Second, the investigation of the enstrophy statistics has been at the center of a number of studies as it quantifies certain aspects of the small-scale structure of turbulence (see, for example, [Tsi09] and references therein). This probably is related to the fact that events of strong enstrophy can be discussed in the context of coherent vortex structures, which allows for an intuitive interpretation of the results. In the context of PDF methods, the enstrophy seems especially well-suited as the evolution for the enstrophy equation is readily obtained by multiplying the vorticity equation on the vorticity, which yields

$$\frac{\partial}{\partial t}\frac{\boldsymbol{\omega}^2}{2} + \boldsymbol{u} \cdot \nabla \frac{\boldsymbol{\omega}^2}{2} = \boldsymbol{\omega}\mathrm{S}\boldsymbol{\omega} + \nu \boldsymbol{\omega} \cdot \Delta \boldsymbol{\omega} + \boldsymbol{\omega} \cdot (\nabla \times \boldsymbol{F}) \quad . \tag{9.4}$$

As discussed in chapter 8, the terms on the right-hand side can be regarded as the local enstrophy production due to self-amplification, dissipation[1] and the local enstrophy production due to the external forcing. After the considerations of the preceding chapter the latter term can be assumed to have a negligible statistical impact. If we now denote z as the sample space variable corresponding to the enstrophy, we can define the two-point enstrophy PDF according to

$$f_2(z_1, z_2; \boldsymbol{x}_1, \boldsymbol{x}_2, t) = \left\langle \delta\!\left(\frac{\boldsymbol{\omega}^2}{2}(\boldsymbol{x}_1, t) - z_1\right) \delta\!\left(\frac{\boldsymbol{\omega}^2}{2}(\boldsymbol{x}_2, t) - z_2\right) \right\rangle \quad . \tag{9.5}$$

The corresponding evolution equation for the PDF can be derived in exactly the same manner as in the case of the velocity or vorticity PDF. Following the subsequent steps

[1] In this chapter we will speak of the diffusive term also loosely as dissipation.

of the derivation one finally obtains for homogeneous turbulence

$$\begin{aligned}\frac{\partial}{\partial t}f_2 + \nabla_{\boldsymbol{r}} \cdot \left[\left\langle \delta\boldsymbol{u}\middle| z_1, z_2, \boldsymbol{r}\right\rangle f_2\right] = &- \frac{\partial}{\partial z_1}\left[\left\langle \boldsymbol{\omega}_1 \mathrm{S}_1 \boldsymbol{\omega}_1 + \nu\boldsymbol{\omega}_1 \cdot \Delta_{\boldsymbol{x}_1}\boldsymbol{\omega}_1\middle| z_1, z_2, \boldsymbol{r}\right\rangle f_2\right] \\ &- \frac{\partial}{\partial z_2}\left[\left\langle \boldsymbol{\omega}_2 \mathrm{S}_2 \boldsymbol{\omega}_2 + \nu\boldsymbol{\omega}_2 \cdot \Delta_{\boldsymbol{x}_2}\boldsymbol{\omega}_2\middle| z_1, z_2, \boldsymbol{r}\right\rangle f_2\right] \quad .\end{aligned} \tag{9.6}$$

We have already omitted the terms related to the external forcing here. Due to isotropy only the longitudinal component of the velocity increment

$$\left\langle \delta u_l\middle| z_1, z_2, r\right\rangle = \left\langle \hat{\boldsymbol{r}} \cdot \delta\boldsymbol{u}\middle| z_1, z_2, r\right\rangle \tag{9.7}$$

contributes to the advective term, such that the PDF equation simplifies to

$$\begin{aligned}\frac{\partial}{\partial t}f_2 + \frac{1}{r}\frac{\partial}{\partial r} r\left[\left\langle \delta u_l\middle| z_1, z_2, r\right\rangle f_2\right] = &- \frac{\partial}{\partial z_1}\left[\left\langle \boldsymbol{\omega}_1 \mathrm{S}_1 \boldsymbol{\omega}_1 + \nu\boldsymbol{\omega}_1 \cdot \Delta_{\boldsymbol{x}_1}\boldsymbol{\omega}_1\middle| z_1, z_2, r\right\rangle f_2\right] \\ &- \frac{\partial}{\partial z_2}\left[\left\langle \boldsymbol{\omega}_2 \mathrm{S}_2 \boldsymbol{\omega}_2 + \nu\boldsymbol{\omega}_2 \cdot \Delta_{\boldsymbol{x}_2}\boldsymbol{\omega}_2\middle| z_1, z_2, r\right\rangle f_2\right] \quad .\end{aligned} \tag{9.8}$$

The evolution of the two-point enstrophy PDF hence is given by the conditional enstrophy production and dissipation terms at the two spatial points. The coupling between different scales is given by the longitudinal velocity increment. The velocity increment has to fulfill the additional constraint

$$0 = \left\langle \delta u_l\right\rangle = \int \mathrm{d}z_1\, \mathrm{d}z_2 \left\langle \delta u_l\middle| z_1, z_2\right\rangle f_2(z_1, z_2) \quad , \tag{9.9}$$

such that if the velocity increment is non-vanishing, zero-crossings will occur. That means, there will be different regions in the z_1-z_2-plane associated with a probability flux up- and downscale. The structure of the PDF equation implies for stationary turbulence that if the probability current on the right-hand side vanishes, also the probability flux in scale is zero. Consequently, the imbalance of enstrophy production and dissipation is a necessary condition for a coupling of the PDFs of various distances. Note that the equations are symmetric with respect to an exchange of z_1 and z_2, such that the vector field defined by the unclosed terms also will display this symmetry.

Although we have derived this equation starting from the definition of the fine-grained two-point enstrophy PDF, one could in principle also obtain this equation by projection of the two-point vorticity PDF equation (9.1). A second important thing to note is that, when only the single-point enstrophy PDF is considered, the PDF equation is completely equivalent to the single-point vorticity PDF (8.27a) for homogeneous isotropic turbulence. The reason for this is that for homogeneous isotropic turbulence the single-point vorticity PDF depends on the magnitude of vorticity, or equivalently the enstrophy, only. This especially means that for the limit of large spatial separations,

where we find statistical independence of z_1 and z_2, the well-known conditional balance (8.41) will be observed pointwise in sample space.

For the interpretation of the following DNS results it is useful to consider the characteristic equations corresponding to equation (9.8). If we denote $R(t, z_{1,0}, z_{2,0}, r_0)$, $Z_1(t, z_{1,0}, z_{2,0}, r_0)$ and $Z_2(t, z_{1,0}, z_{2,0}, r_0)$ as solutions of the characteristic equations, these solutions obey

$$\frac{\mathrm{d}}{\mathrm{d}t}R = \left[\left\langle \delta u_l \middle| z_1, z_2, r\right\rangle\right]_{[r=R(t),\, z_1=Z_1(t),\, z_2=Z_2(t)]} \tag{9.10a}$$

$$\frac{\mathrm{d}}{\mathrm{d}t}Z_1 = \left[\left\langle \boldsymbol{\omega}_1 \mathrm{S}_1 \boldsymbol{\omega}_1 + \nu \boldsymbol{\omega}_1 \cdot \Delta_{\boldsymbol{x}_1} \boldsymbol{\omega}_1 \middle| z_1, z_2, r\right\rangle\right]_{[r=R(t),\, z_1=Z_1(t),\, z_2=Z_2(t)]} \tag{9.10b}$$

$$\frac{\mathrm{d}}{\mathrm{d}t}Z_2 = \left[\left\langle \boldsymbol{\omega}_2 \mathrm{S}_2 \boldsymbol{\omega}_2 + \nu \boldsymbol{\omega}_2 \cdot \Delta_{\boldsymbol{x}_2} \boldsymbol{\omega}_2 \middle| z_1, z_2, r\right\rangle\right]_{[r=R(t),\, z_1=Z_1(t),\, z_2=Z_2(t)]} \tag{9.10c}$$

$$\begin{aligned}\frac{\mathrm{d}}{\mathrm{d}t}f_2 = -\Bigg[&\frac{1}{r}\frac{\partial}{\partial r} r \left\langle \delta u_l \middle| z_1, z_2, r\right\rangle \\ &+ \frac{\partial}{\partial z_1}\left\langle \boldsymbol{\omega}_1 \mathrm{S}_1 \boldsymbol{\omega}_1 + \nu \boldsymbol{\omega}_1 \cdot \Delta_{\boldsymbol{x}_1} \boldsymbol{\omega}_1 \middle| z_1, z_2, r\right\rangle \\ &+ \frac{\partial}{\partial z_2}\left\langle \boldsymbol{\omega}_2 \mathrm{S}_2 \boldsymbol{\omega}_2 + \nu \boldsymbol{\omega}_2 \cdot \Delta_{\boldsymbol{x}_2} \boldsymbol{\omega}_2 \middle| z_1, z_2, r\right\rangle\Bigg]_{[r=R(t),\, z_1=Z_1(t),\, z_2=Z_2(t)]} f_2 \quad .\end{aligned} \tag{9.10d}$$

Consequently, if we know the functional shape of the unclosed terms in the space spanned by z_1, z_2 and r, we can track their statistical evolution. At the same time the last equation determines the deformation of the PDF along these solutions.

9.2.2. DNS Results

For the numerical evaluation we take the data from the simulation `sim_512`. First of all, one can note that the statistics in the z_1-z_2-plane can equivalently be represented considering the statistics in the Ω_1-Ω_2-plane. The latter choice is particularly useful for a graphical representation as the coordinate axes are not as stretched as when choosing a representation in terms of the enstrophy. Accordingly, we evaluate $\tilde{f}_2(\Omega_1, \Omega_2; r)$ instead of $f_2(z_1, z_2; r)$. In fact, there is a simple relation between the two probability densities taking the form

$$\tilde{f}_2(\Omega_1, \Omega_2) = \left[(2z_1)^{\frac{1}{2}}\,(2z_2)^{\frac{1}{2}}\, f_2(z_1, z_2)\right]_{z_{1/2}=\frac{1}{2}\Omega_{1/2}^2} \quad . \tag{9.11}$$

This especially allows to make contact to the results presented in chapter 8. For example, the conditional averages of the right-hand side of equation (9.8) have to reduce to the ordinary balance (8.41) when projected onto the Ω_1- or Ω_2-axis. This is exemplified in figure 9.1 for $r = 2.5\eta$. Of course, this reduction property holds for arbitrary separations. When discriminated with respect to Ω_1 and Ω_2, in general no pointwise cancellation of the terms is expected. One example is shown in figure 9.2 for $r = 2.5\eta$, where the vector field spanned by the conditional enstrophy production

$$\left(\left\langle \boldsymbol{\omega}_1 \mathrm{S}_1 \boldsymbol{\omega}_1 \middle| \Omega_1, \Omega_2\right\rangle,\, \left\langle \boldsymbol{\omega}_2 \mathrm{S}_2 \boldsymbol{\omega}_2 \middle| \Omega_1, \Omega_2\right\rangle\right) \quad , \tag{9.12}$$

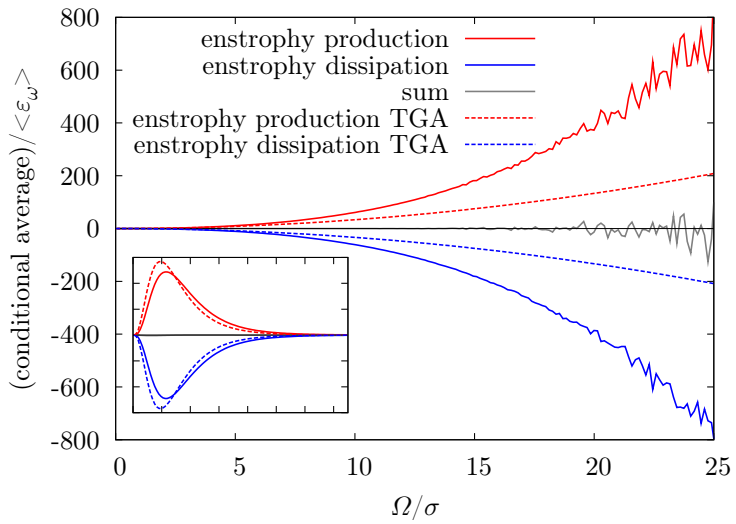

Figure 9.1.: Conditional balance of the single-point enstrophy production and dissipation obtained by projection of the two-point enstrophy statistics for $r = 2.5\eta$. As expected, the conditional production balances the conditional dissipation (`sim_512`). The analytical result for the Twisted Gaussian Approximation (discussed in section 9.5) is shown for reference. The inset shows the conditional averages times the PDF.

the conditional enstrophy dissipation

$$\left(\left\langle \nu\boldsymbol{\omega}_1 \cdot \Delta_{\boldsymbol{x}_1}\boldsymbol{\omega}_1 \middle| \Omega_1, \Omega_2 \right\rangle, \left\langle \nu\boldsymbol{\omega}_2 \cdot \Delta_{\boldsymbol{x}_2}\boldsymbol{\omega}_2 \middle| \Omega_1, \Omega_2 \right\rangle\right) \tag{9.13}$$

and their sum is shown. As in the single-point case, the vector field belonging to the enstrophy production points into the direction of larger values of vorticity and hence has an amplifying effect. The opposite effect is achieved by the dissipative terms, which produce a vector field pointing toward the origin. If the two vector fields are summed up, as in the PDF equation (9.8), they cancel to a good extent, only a small non-vanishing fraction remains. This is an important observation as it shows that enstrophy production and dissipation are strongly localized processes in sample space, which already almost balance pointwise in sample space.

In addition to the evolution in the Ω_1-Ω_2-plane one has to consider the evolution in scale, which is related to the conditional longitudinal velocity increment also shown in figure 9.2. Here, the first thing to note is that the velocity increment field changes sign in the Ω_1-Ω_2-plane. It takes a negative sign if Ω_1 strongly differs from Ω_2 and becomes positive if the two vorticities are roughly equal. If the conditional velocity increment is non-vanishing, this change of sign has to occur, because the increment has to fulfill the integral constraint (9.9). This observation adds another aspect to the interpretation of the statistical results. If two nearby vorticities differ strongly, they tend to be attracted on the statistical average and tend to separate if the two vorticities are roughly equal.

The statistics is presented as a function of scale in figures 9.3 and 9.4 along with the

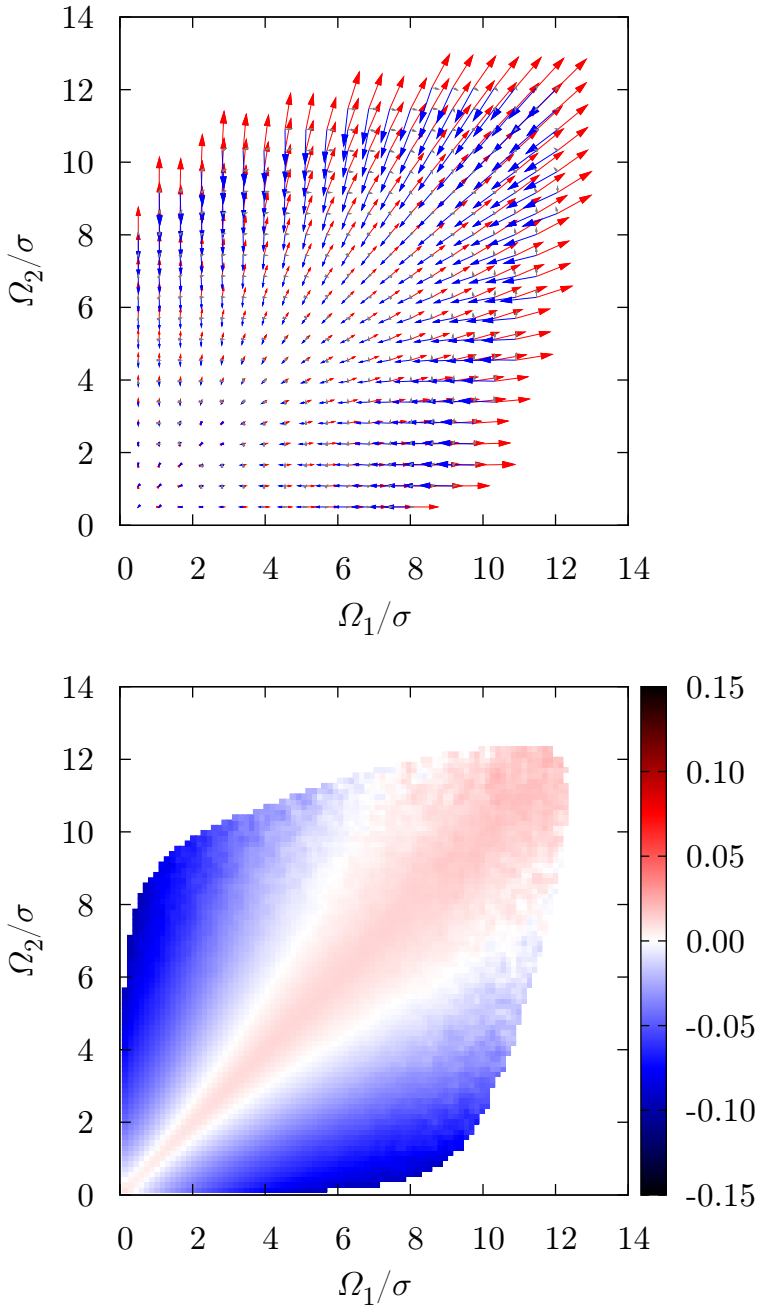

Figure 9.2.: Conditional averages of the two-point enstrophy PDF equation (9.8) for $r = 2.5\eta$. Upper figure: conditional enstrophy production $\langle \boldsymbol{\omega}_i \mathrm{S}_i \boldsymbol{\omega}_i | \Omega_1, \Omega_2 \rangle / \langle \varepsilon_\omega \rangle$ (red) and enstrophy dissipation $\langle \nu \boldsymbol{\omega}_i \cdot \Delta_{\boldsymbol{x}_i} \boldsymbol{\omega}_i | \Omega_1, \Omega_2 \rangle / \langle \varepsilon_\omega \rangle$ (blue) together with the small net vector field (gray), all vectors have been multiplied by a factor of 0.1. Lower figure: conditional longitudinal velocity increment $\langle \delta u_l | \Omega_1, \Omega_2 \rangle / \left(\frac{2}{3} \langle \boldsymbol{u}^2 \rangle \right)$ (`sim_512`).

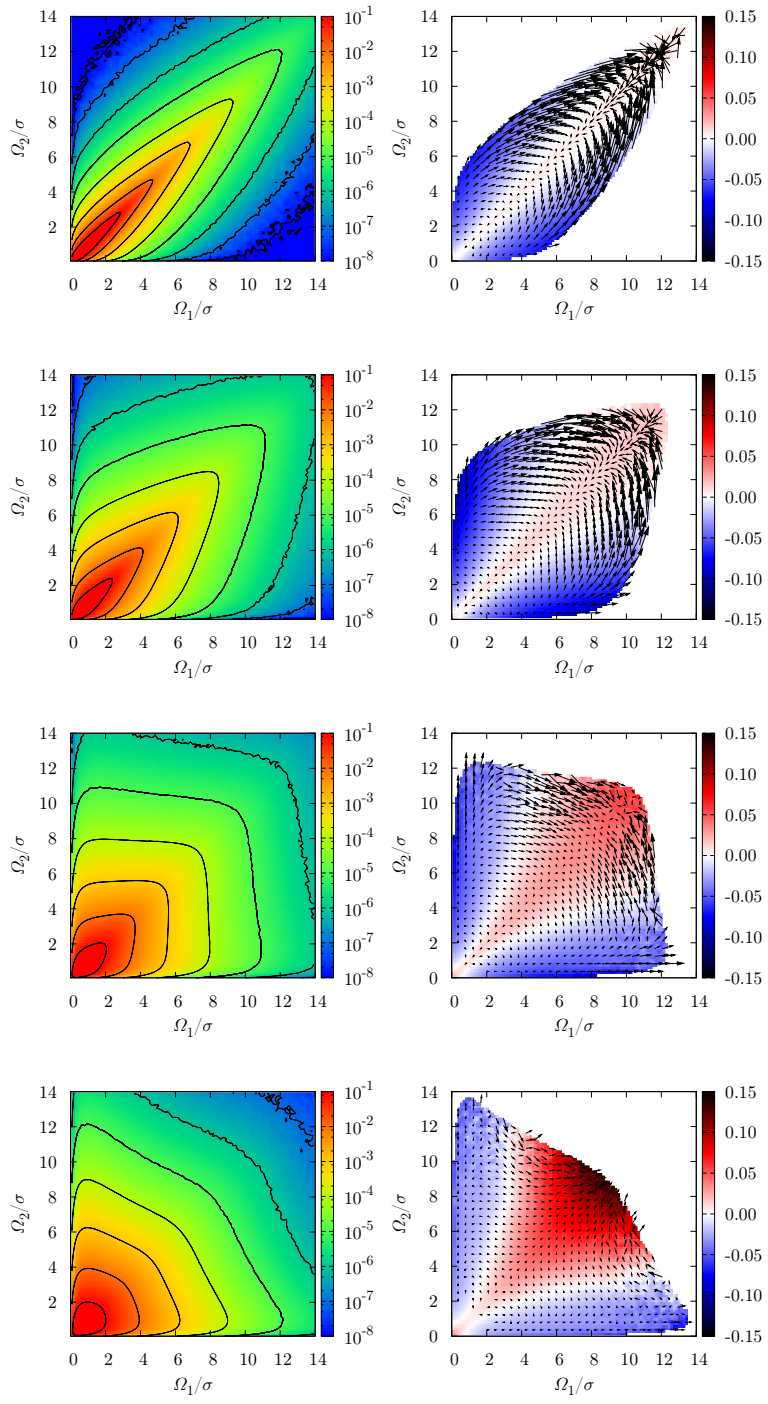

Figure 9.3.: Joint PDF $\tilde{f}_2(\Omega_1, \Omega_2; r)\sigma^2$ and conditional averages of the two-point enstrophy PDF equation (9.8) for $r \in \{1.2, 2.5, 4.9, 9.9\}\eta$ (`sim_512`).

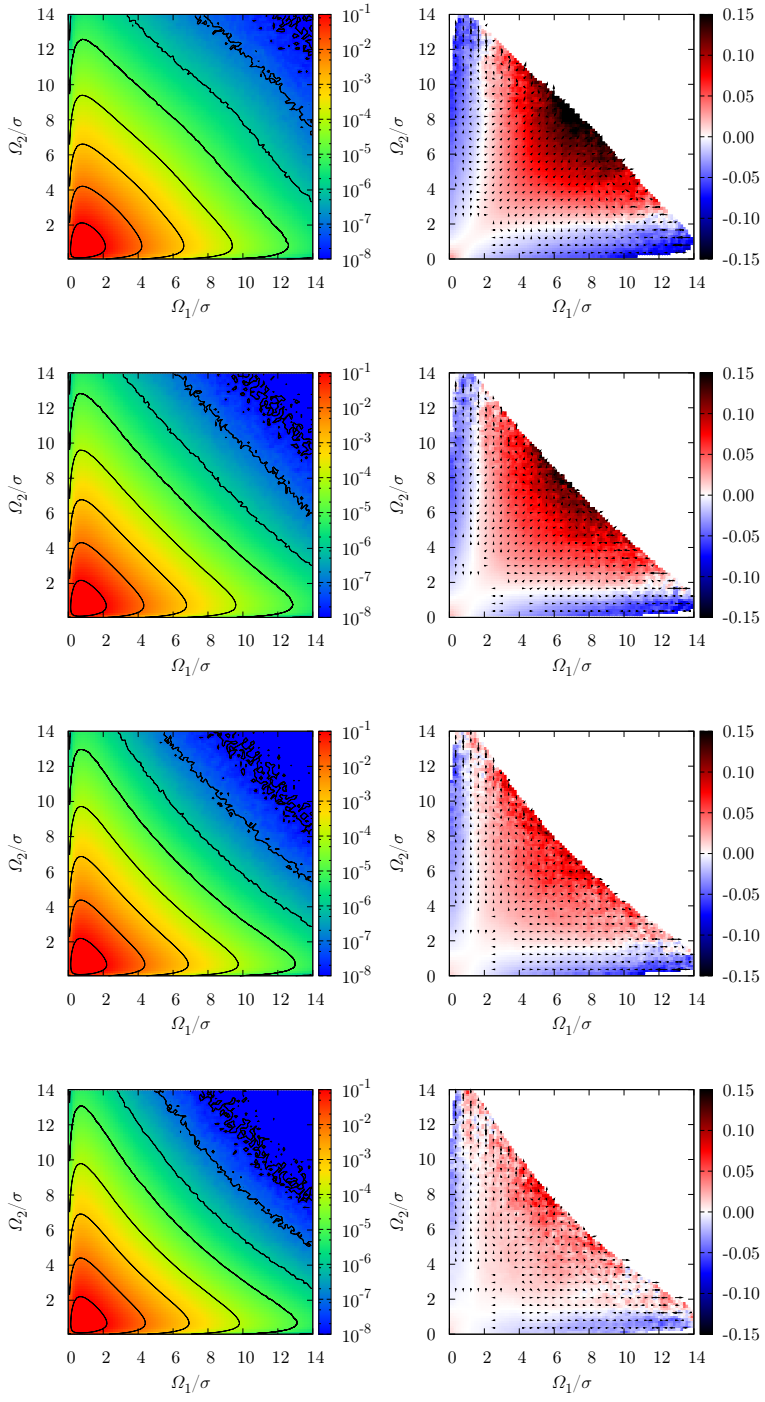

Figure 9.4.: Joint PDF $\tilde{f}_2(\Omega_1, \Omega_2; r)\sigma^2$ and conditional averages of the two-point enstrophy PDF equation (9.8) for $r \in \{19.8, 39.6, 79.1, 158.3\}\eta$ (`sim_512`).

joint PDF $\tilde{f}_2(\Omega_1, \Omega_2; r)$. The joint PDF, as expected, undergoes a transition from a very narrow shape for small separations to a broader shape for increasing separation. This just mirrors the fact that for vanishing separation the *coincidence property* has to be met, whereas for large distances the *separation property* has to hold.

Coming to the effective vector field spanned by the sum of the conditional enstrophy production and dissipation, this vector field is particularly strong for small separations and decreases in magnitude for larger separations. For small spatial separations the remaining vector field by and large has an amplifying effect if $\Omega_1 \not\approx \Omega_2$ and a depleting effect if $\Omega_1 \approx \Omega_2$, increasing nonlinearly with the magnitude of the two vorticities. This means, that if, on the statistical average, the enstrophy is not equal in two nearby points, turbulence tends to level this difference. Approximately equal enstrophies, however, are subject to a comparably slow decay. To put it differently, vortex stretching is especially active amplifying low vorticity in the neighborhood of strong vorticity, sometimes even amplifying the strong vorticity as can be seen from the details of the vector field. The dissipative effects are dominant when the two vorticities tend to coincide in magnitude. In a sense this reminds of the life cycle of a vortex structure generated by the vortex stretching of surrounding vorticity and eventually decaying after growing strong. For intermediate distances, for example at $r = 9.9\eta$, the almost pointwise cancellation of enstrophy production and dissipation is already observed for low vorticities. Events of strong vorticity, however, still are amplified due to dominant enstrophy production. This differing behavior of low and high magnitudes of vorticity could be a signature of the presence of coherent structures. While for small and weak structures the spatial correlation is already lost, particularly strong and elongated vortices found in the tails of the PDF are still subject to growth. For scale separations, where the joint PDF becomes statistically independent, the pointwise balance observed for the single-point enstrophy statistics is recovered. This is physically intuitive as two distant points should not influence each other.

The conditional longitudinal velocity increment displays a structure similar to the one already discussed for small scales. However, it takes the strongest positive and negative values at intermediate scales of the order of ten Kolmogorov micro scales. Due to the limiting properties of the statistics it has to vanish for vanishing separations and also for large ones. Additionally the region corresponding to a positive flux in scale increases with increasing separations.

These qualitative observations can be cast in a simple model for the characteristic equations (9.10), which captures the main features of the observed dynamics. The model reads

$$\frac{\mathrm{d}}{\mathrm{d}t} R = \alpha_1 \left[(Z_1 - \alpha_2 Z_2)(Z_2 - \alpha_2 Z_1) - \alpha_3 \right] \tag{9.14a}$$

$$\frac{\mathrm{d}}{\mathrm{d}t} Z_1 = Z_1 Z_2 \left[\beta_1 (Z_2 - Z_1) + \beta_2 (Z_1 + Z_2) + \beta_3 \right] + \beta_4 \left[Z_1^2 + Z_2^2 \right] \tag{9.14b}$$

$$\frac{\mathrm{d}}{\mathrm{d}t} Z_2 = Z_1 Z_2 \left[\beta_1 (Z_1 - Z_2) + \beta_2 (Z_1 + Z_2) + \beta_3 \right] + \beta_4 \left[Z_1^2 + Z_2^2 \right] \quad , \tag{9.14c}$$

where all prefactors α_i and β_i are functions of the spatial distance R. First of all, one can note that the model is symmetric with respect to a simultaneous change of Z_1 and Z_2. Depending on the choice of the parameters α_i, the transport in scale can be adjusted in a way that a probability flux upscale is found for $Z_1 \approx Z_2$ and downscale for $Z_1 \not\approx Z_2$. The extents of the corresponding regions can be fixed with the parameter α_2, which allows to model the scale dependent deformation observed in the DNS data. α_3 can be adjusted such that the model fulfills the integral constraint (9.9) by choosing

$$\alpha_3 = (1+\alpha_2^2)\langle Z_1 Z_2\rangle - \alpha_2\left(\langle Z_1^2\rangle + \langle Z_2^2\rangle\right) \quad . \tag{9.15}$$

The limiting behavior for small and large separations can be modeled by adjusting α_1. For example, choosing $\lim_{R\to\infty} \alpha_1 = 0$ leads to a vanishing probability flux in scale for large separations.

The dynamics is the Z_1-Z_2-plane can be understood best by considering limiting cases. For example, for $Z_1 = 0$ only the term involving β_4 is non-vanishing and leads to the characteristic amplification of enstrophy observed in the DNS data. For $Z_1 = Z_2$ the depleting effect for coinciding enstrophies can be modeled by choosing a negative β_3. β_2 can be adjusted in a way that the amplification of large enstrophies, observed in the DNS for intermediate distances, is captured. In between these two limiting cases the model vector field points toward the line corresponding to $Z_1 = Z_2$, such that in total the typical amplification for non-coinciding and the slight decay for coinciding enstrophies is found. For vanishing and infinite distances the limiting behavior $\dot{Z}_1 = \dot{Z}_2 = 0$ is met by choosing $\beta_i = 0$.

While the goal of this simple *ad hoc* model is to capture the topological structure of the vector field governing the evolution of the characteristics, it would be desirable to derive this type of model equations from a consideration of the two-point statistics, which is the topic of the following sections.

9.3. The Closure Problem in Terms of Conditional Moments

We now want to seek for an understanding of the unclosed expressions in terms of the multi-point vorticity statistics. The starting point of the analysis is the kinetic equation for the single-point PDF $f_1(\boldsymbol{\Omega}_1; \boldsymbol{x}_1, t)$ of the form

$$\begin{aligned}
&\frac{\partial}{\partial t} f_1 + \frac{1}{4\pi}\nabla_{\boldsymbol{x}_1} \cdot \int \mathrm{d}\boldsymbol{x}_0\, \mathrm{d}\boldsymbol{\Omega}_0\, \frac{\boldsymbol{r}_{10}\times\boldsymbol{\Omega}_0}{r_{10}^3}\, f_2 \\
&\quad = -\nabla_{\boldsymbol{\Omega}_1} \cdot \left\{ \frac{3}{8\pi} \int \mathrm{d}\boldsymbol{x}_0\, \mathrm{d}\boldsymbol{\Omega}_0 \left[\frac{(\boldsymbol{r}_{10}\times\boldsymbol{\Omega}_0)(\boldsymbol{r}_{10}\cdot\boldsymbol{\Omega}_1)}{r_{10}^5} + \frac{\boldsymbol{\Omega}_1\cdot(\boldsymbol{r}_{10}\times\boldsymbol{\Omega}_0)\,\boldsymbol{r}_{10}}{r_{10}^5} \right] f_2 \right. \\
&\quad \left. + \lim_{\boldsymbol{x}_0\to\boldsymbol{x}_1} \nu\Delta_{\boldsymbol{x}_0} \int \mathrm{d}\boldsymbol{\Omega}_0\, \boldsymbol{\Omega}_0 f_2 \right\} \quad ,
\end{aligned} \tag{9.16}$$

which couples to the two-point PDF $f_2(\boldsymbol{\Omega}_0, \boldsymbol{\Omega}_1; \boldsymbol{x}_0, \boldsymbol{x}_1, t)$. This PDF equation has already been introduced in chapter 8. Note that the spatial point integrated over and

the corresponding sample space vorticity are now denoted by the subscript 0 and we define $\boldsymbol{r}_{10} = \boldsymbol{x}_0 - \boldsymbol{x}_1$. This slight change in notation will eventually allow to generalize the results conveniently to multiple points in space. As discussed before, this equation explicitly reveals the coupling of the single-point PDF equation to the two-point PDF. Here and in the following the external forcing is neglected, which seems to be a reasonable approximation due to the results of the last chapter. The important point now is that the kinetic equation written down in the above form involves the sample space vorticity $\boldsymbol{\Omega}_0$ only linearly, an observation which has first been mentioned by Novikov [Nov93]. By expressing the two-point PDF in terms of the conditional PDF

$$f_2(\boldsymbol{\Omega}_0, \boldsymbol{\Omega}_1; \boldsymbol{x}_0, \boldsymbol{x}_1, t) = p(\boldsymbol{\Omega}_0|\boldsymbol{\Omega}_1, \boldsymbol{x}_0, \boldsymbol{x}_1, t)\, f_1(\boldsymbol{\Omega}_1; \boldsymbol{x}_1, t) \tag{9.17}$$

one recognizes that operations of the unclosed terms do not act on $f_1(\boldsymbol{\Omega}_1; \boldsymbol{x}_1, t)$. Additionally noting that

$$\int \mathrm{d}\boldsymbol{\Omega}_0\, \boldsymbol{\Omega}_0\, p(\boldsymbol{\Omega}_0|\boldsymbol{\Omega}_1, \boldsymbol{x}_0, \boldsymbol{x}_1, t) = \big\langle \boldsymbol{\omega}(\boldsymbol{x}_0, t) \big| \boldsymbol{\Omega}_1, \boldsymbol{x}_1 \big\rangle \quad , \tag{9.18}$$

it becomes clear that all the unclosed terms can be expressed in terms of the conditional vorticity field. By comparison with the kinetic equation (8.14) one actually recognizes that all the unknown averages (apart from the external forcing) arising in this equation can be obtained as a functional of $\big\langle \boldsymbol{\omega}(\boldsymbol{x}_0, t) \big| \boldsymbol{\Omega}_1, \boldsymbol{x}_1 \big\rangle$. For the velocity we explicitly obtain

$$\big\langle \boldsymbol{u}_1 \big| \boldsymbol{\Omega}_1 \big\rangle = -\frac{1}{4\pi} \int \mathrm{d}\boldsymbol{x}_0\, \frac{\boldsymbol{x}_1 - \boldsymbol{x}_0}{|\boldsymbol{x}_1 - \boldsymbol{x}_0|^3} \times \big\langle \boldsymbol{\omega}_0 \big| \boldsymbol{\Omega}_1 \big\rangle \quad , \tag{9.19}$$

i.e., we have to evaluate the Biot-Savart integral over the conditionally averaged vorticity field. In the same manner we can calculate the conditional rate-of-strain tensor as

$$\big\langle S_{1,ij} \big| \boldsymbol{\Omega}_1 \big\rangle = \frac{3}{8\pi} \int \mathrm{d}\boldsymbol{x}_0\, \epsilon_{ikl}\, \frac{(x_{1,k} - x_{0,k})(x_{1,j} - x_{0,j})}{|\boldsymbol{x}_1 - \boldsymbol{x}_0|^5} \big\langle \omega_{0,l} \big| \boldsymbol{\Omega}_1 \big\rangle + (i \leftrightarrow j) \quad , \tag{9.20}$$

where this integral again has to be understood as a Cauchy principal value integral. The dissipative term is also obtained easily as

$$\big\langle \nu \Delta_{\boldsymbol{x}_1} \boldsymbol{\omega}_1 \big| \boldsymbol{\Omega}_1 \big\rangle = \lim_{\boldsymbol{x}_0 \to \boldsymbol{x}_1} \nu \Delta_{\boldsymbol{x}_0} \big\langle \boldsymbol{\omega}_0 \big| \boldsymbol{\Omega}_1 \big\rangle \quad , \tag{9.21}$$

i.e., by differentiating the conditional vorticity field and taking the limit. That means, once the local conditional structure in terms of the first conditional moment of the vorticity is specified as a full field, all of the unclosed terms are specified. To put it differently, knowledge of the first conditional moment closes the single-point equation of the type (9.16). This eventually establishes the connection between the above type of kinetic equation and the ones involving conditional averages that we have dealt with in chapters 7 and 8. Compared to the latter equations, where knowledge of local correlations of different dynamical quantities at a single point in space is necessary, a closure now requires knowledge of a *whole field* as both integrals and derivatives of this

field have to be computed. In a sense the conditional averages on the single-point level considered in the preceding chapter contain condensed information of this conditional vorticity field. It has been noted by Novikov that the possibility to close the above kinetic equation in terms of the first conditional moment of the vorticity field is a unique property of the vorticity equation, as the pressure term in the Navier-Stokes equation is a quadratic functional of the velocity field. We would like to stress at this point that the kinetic equation presently discussed, however, does not allow to calculate the stationary solution of the single-point vorticity PDF. The corresponding version (equation (8.18)), for which a stationary solution has been presented in the preceding chapters, involves the conditional dissipation tensor which can be shown to depend on the second conditional moment. This will be the starting point of another modeling approach in the following chapter.

Of course, this whole procedure cannot only be applied to the single-point equation, but on an arbitrary level of the hierarchy. That means, the LMN hierarchy of the form (8.13) can be closed on the N-point level by knowledge of the conditional moment

$$\left\langle \boldsymbol{\omega}_0 \middle| \boldsymbol{\Omega}_1, \ldots, \boldsymbol{\Omega}_N \right\rangle \quad . \tag{9.22}$$

One additionally should note that the conditional fields in general obey a *reduction property* similar to the PDFs

$$\begin{aligned} &\left\langle \boldsymbol{\omega}_0 \middle| \boldsymbol{\Omega}_1, \ldots, \boldsymbol{\Omega}_{N-1} \right\rangle f_{N-1}(\boldsymbol{\Omega}_1, \ldots, \boldsymbol{\Omega}_{N-1}) \\ &= \int \mathrm{d}\boldsymbol{\Omega}_N \left\langle \boldsymbol{\omega}_0 \middle| \boldsymbol{\Omega}_1, \ldots, \boldsymbol{\Omega}_N \right\rangle f_N(\boldsymbol{\Omega}_1, \ldots, \boldsymbol{\Omega}_N) \end{aligned} \tag{9.23}$$

and eventually

$$\left\langle \boldsymbol{\omega}_0 \right\rangle = \int \mathrm{d}\boldsymbol{\Omega}_1 \ldots \mathrm{d}\boldsymbol{\Omega}_N \left\langle \boldsymbol{\omega}_0 \middle| \boldsymbol{\Omega}_1, \ldots, \boldsymbol{\Omega}_N \right\rangle f_N(\boldsymbol{\Omega}_1, \ldots, \boldsymbol{\Omega}_N) \quad . \tag{9.24}$$

For the two-point vorticity or enstrophy statistics, that we will study later on in this chapter, we will need to specify $\left\langle \boldsymbol{\omega}_0 \middle| \boldsymbol{\Omega}_1, \boldsymbol{\Omega}_2 \right\rangle$, and it is immediately clear that this term is inaccessible to a numerical study due to its dimensionality. Hence the strategy will be to explore the structure of the analytically and numerically accessible quantity $\left\langle \boldsymbol{\omega}_0 \middle| \boldsymbol{\Omega}_1 \right\rangle$, that closes the single-point equation, and take this as a starting point to formulate reasonable ansatzes for the vorticity field conditionally averaged with respect to two fixed vorticities. The results obtained in this way will eventually be compared to "condensed" statistics that is numerically accessible again.

9.4. The General Structure of the First Conditional Moment

After having emphasized the role of the first conditional moment of the vorticity field, we now want to investigate its possible functional form. To this end one has to note

that the expression $\langle \boldsymbol{\omega}(\boldsymbol{x}_0,t)\big|\boldsymbol{\Omega}_1,\boldsymbol{x}_1\rangle$ is a function of the time t, the two spatial points $\boldsymbol{x}_0$ and $\boldsymbol{x}_1$ and the sample space vorticity $\boldsymbol{\Omega}_1$. Considering stationary homogeneous isotropic turbulence, the functional form can be simplified. As usual, stationarity implies that the conditional field does not depend on time and homogeneity implies that the field depends only on the distance vector. To find the most general form for isotropic statistics, one first has to recognize that a complete set of invariants to be formed of $\boldsymbol{r}$ and $\boldsymbol{\Omega}_1$, for example, consists of r, Ω_1 and $\gamma := \hat{\boldsymbol{r}}\cdot\widehat{\boldsymbol{\Omega}}_1$, i.e., of the two magnitudes and the direction cosine of the two vectors. To find the statistical directions the conditional vorticity field may point to, we consider the transformation properties of the vector field

$$\mathrm{R}\langle \boldsymbol{\omega}_0\big|\boldsymbol{\Omega}_1,\boldsymbol{r}\rangle = \langle \boldsymbol{\omega}_0\big|\mathrm{R}\boldsymbol{\Omega}_1,\mathrm{R}\boldsymbol{r}\rangle \quad \forall\,\mathrm{R}\in\mathrm{O}(3) \quad , \tag{9.25}$$

which leads to the conclusion that possible directions for isotropic turbulence are $\hat{\boldsymbol{r}}$, $\widehat{\boldsymbol{\Omega}}_1$ and $\hat{\boldsymbol{r}}\times\widehat{\boldsymbol{\Omega}}_1$. However, for the following investigations it is more convenient to construct an orthonormal set of directions of these three vectors as was pointed out in [MDN96]. These can be chosen as

$$\widehat{\boldsymbol{\Omega}}_1 = \frac{\boldsymbol{\Omega}_1}{\Omega_1} \tag{9.26a}$$

$$\hat{\boldsymbol{\lambda}} = \frac{\hat{\boldsymbol{r}} - (\hat{\boldsymbol{r}}\cdot\widehat{\boldsymbol{\Omega}}_1)\widehat{\boldsymbol{\Omega}}_1}{\left[1-(\hat{\boldsymbol{r}}\cdot\widehat{\boldsymbol{\Omega}}_1)^2\right]^{\frac{1}{2}}} \tag{9.26b}$$

$$\hat{\boldsymbol{\tau}} = \widehat{\boldsymbol{\Omega}}_1\times\hat{\boldsymbol{\lambda}} \quad , \tag{9.26c}$$

such that the general structure of the conditional vorticity field will be of the form [MDN96]

$$\langle \boldsymbol{\omega}_0\big|\boldsymbol{\Omega}_1,\boldsymbol{r}\rangle = a(r,\Omega_1,\gamma)\,\widehat{\boldsymbol{\Omega}}_1 + b(r,\Omega_1,\gamma)\,\hat{\boldsymbol{\lambda}} + c(r,\Omega_1,\gamma)\,\hat{\boldsymbol{\tau}} \quad . \tag{9.27}$$

The scalar functions a, b and c are then easily obtained by projection according to

$$a(r,\Omega_1,\gamma) = \widehat{\boldsymbol{\Omega}}_1\cdot\langle \boldsymbol{\omega}_0\big|\boldsymbol{\Omega}_1,\boldsymbol{r}\rangle \tag{9.28a}$$

$$b(r,\Omega_1,\gamma) = \hat{\boldsymbol{\lambda}}\cdot\langle \boldsymbol{\omega}_0\big|\boldsymbol{\Omega}_1,\boldsymbol{r}\rangle \tag{9.28b}$$

$$c(r,\Omega_1,\gamma) = \hat{\boldsymbol{\tau}}\cdot\langle \boldsymbol{\omega}_0\big|\boldsymbol{\Omega}_1,\boldsymbol{r}\rangle \quad . \tag{9.28c}$$

Furthermore, the two scalar functions a and b cannot be chosen independently as the conditional vorticity field obeys solenoidality,

$$\frac{\partial}{\partial r_i}\langle \omega_{0,i}\big|\boldsymbol{\Omega}_1,\boldsymbol{r}\rangle = 0 \quad , \tag{9.29}$$

which yields the relation

$$r\gamma\left(\frac{\partial a}{\partial r}\right) + r\left[1-\gamma^2\right]^{\frac{1}{2}}\left(\frac{\partial b}{\partial r}\right) + \left[1-\gamma^2\right]\left(\frac{\partial a}{\partial \gamma}\right) - \gamma\left[1-\gamma^2\right]^{\frac{1}{2}}\left(\frac{\partial b}{\partial \gamma}\right) = 0 \tag{9.30}$$

after a short calculation. That means, we can choose the two scalar functions a and c independently to characterize the local structure of turbulence, the scalar function b then preserves solenoidality of the field. It is important to note that the term related to the scalar a statistically points into the direction of the vorticity, whereas the term related to c gives a twisting contribution to the vorticity field.

Of course, it is now interesting to investigate how these functions contribute to the conditional vortex stretching and diffusion term. Calculations on that have been performed in [Nov93] in Fourier space. We here rather obtain the results in real space as the calculations then are easier to follow.

We start with calculating the diffusive term from the kinetic equation (8.27a) which is obtained from the conditional vorticity field according to

$$\begin{aligned}
\Lambda(\Omega_1) &= \left\langle \nu \widehat{\boldsymbol{\omega}}_1 \cdot \Delta_{\boldsymbol{x}_1} \boldsymbol{\omega}_1 \middle| \boldsymbol{\Omega}_1 \right\rangle \\
&= \lim_{|\boldsymbol{x}_1 - \boldsymbol{x}_0| \to 0} \nu \, \widehat{\boldsymbol{\Omega}}_1 \cdot \left\langle \Delta_{\boldsymbol{x}_0} \omega_0 \middle| \boldsymbol{\Omega}_1 \right\rangle \\
&= \lim_{r \to 0} \nu \, \widehat{\boldsymbol{\Omega}}_1 \cdot \Delta_{\boldsymbol{r}} \left[a(r, \Omega_1, \gamma) \, \widehat{\boldsymbol{\Omega}}_1 + b(r, \Omega_1, \gamma) \, \hat{\boldsymbol{\lambda}} + c(r, \Omega_1, \gamma) \, \hat{\boldsymbol{\tau}} \right] \\
&= \lim_{r \to 0} \nu \, \widehat{\boldsymbol{\Omega}}_1 \cdot \Delta_{\boldsymbol{r}} \left[a(r, \Omega_1, \gamma) \, \widehat{\boldsymbol{\Omega}}_1 + b(r, \Omega_1, \gamma) \, \hat{\boldsymbol{\lambda}} \right] \quad . \qquad (9.31)
\end{aligned}$$

For the last equality we have made use of the fact that the terms related to the twist do not contribute when projected onto $\widehat{\boldsymbol{\Omega}}_1$. This means that the dissipative term of the kinetic equation is determined by the scalar functions a and b only. For example, the first term contributes with

$$\lim_{r \to 0} \widehat{\boldsymbol{\Omega}}_1 \cdot \Delta_{\boldsymbol{r}} \left[a(r, \Omega_1, \gamma) \, \widehat{\boldsymbol{\Omega}}_1 \right] = \lim_{r \to 0} \left[\left(\frac{\partial^2 a}{\partial r^2} \right) + \frac{2}{r} \left(\frac{\partial a}{\partial r} \right) - \frac{2\gamma}{r^2} \left(\frac{\partial a}{\partial \gamma} \right) + \frac{1 - \gamma^2}{r^2} \left(\frac{\partial^2 a}{\partial \gamma^2} \right) \right] . \qquad (9.32)$$

Hence the limiting behavior of the scalar functions in the origin determines the dissipative term. To calculate the scalar function related to the vortex stretching term, we evaluate

$$\begin{aligned}
\Sigma(\Omega_1) &= \left\langle \widehat{\boldsymbol{\omega}}_1 \mathrm{S}_1 \widehat{\boldsymbol{\omega}}_1 \middle| \boldsymbol{\Omega}_1 \right\rangle \\
&= \frac{3}{4\pi} \int \mathrm{d}\boldsymbol{x}_0 \, \frac{(\hat{\boldsymbol{r}} \cdot \widehat{\boldsymbol{\Omega}}_1)}{r^3} \left[\hat{\boldsymbol{r}} \times \left\langle \boldsymbol{\omega}_0 \middle| \boldsymbol{\Omega}_1 \right\rangle \right] \cdot \widehat{\boldsymbol{\Omega}}_1 \\
&= \frac{3}{4\pi} \int \mathrm{d}\boldsymbol{r} \, \frac{(\hat{\boldsymbol{r}} \cdot \widehat{\boldsymbol{\Omega}}_1)}{r^3} \left[\hat{\boldsymbol{r}} \times \left(a \, \widehat{\boldsymbol{\Omega}}_1 + b \, \hat{\boldsymbol{\lambda}} + c \, \hat{\boldsymbol{\tau}} \right) \right] \cdot \widehat{\boldsymbol{\Omega}}_1 \\
&= \frac{3}{4\pi} \int \mathrm{d}\boldsymbol{r} \, \frac{(\hat{\boldsymbol{r}} \cdot \widehat{\boldsymbol{\Omega}}_1) \, c}{r^3} \left[\hat{\boldsymbol{r}} \times \hat{\boldsymbol{\tau}} \right] \cdot \widehat{\boldsymbol{\Omega}}_1 \\
&= \frac{3}{4\pi} \int \mathrm{d}\boldsymbol{r} \, \frac{\gamma \, (1 - \gamma^2)^{\frac{1}{2}} \, c}{r^3} \quad , \qquad (9.33)
\end{aligned}$$

which shows that the enstrophy production is related to the twisted contribution only. Taking these observations together, we see that the scalar functions a and b are related to the dissipative terms of the field, whereas the scalar function c determines the enstrophy

production of the field. This is a very important result regarding the establishment of models for the local conditional structure of turbulence [Nov93, MDN96]. Any model lacking a twisting contribution will fail to fulfill the conditional balance of vortex stretching and vorticity diffusion. In fact, a consistent model has to fulfill

$$\lim_{r\to 0} \nu\, \widehat{\boldsymbol{\Omega}}_1 \cdot \Delta_{\boldsymbol{r}} \left[a\, \widehat{\boldsymbol{\Omega}}_1 + b\, \hat{\boldsymbol{\lambda}} \right] + \frac{3\Omega_1}{4\pi} \int \mathrm{d}\boldsymbol{r}\, \frac{\gamma\,(1-\gamma^2)^{\frac{1}{2}}\, c}{r^3} = 0 \tag{9.34}$$

and additionally satisfy the solenoidality relation (9.30) between a and b. These relations are highly nontrivial, and it is obviously not possible to make a simple guess for the scalar functions a, b and c. That is why we will follow a more systematic approach later on and start from Gaussian statistics to investigate the conditional structure of the field. The functional relations presented in this section then will guide the way to construct a consistent model. Before that, however, we will investigate the conditional structure of the velocity field with the help of DNS results.

9.4.1. The First Conditional Moment from DNS

The conditional vorticity field in terms of the scalar functions a, b and c has been evaluated from the DNS data (`sim_512`). A similar statistical evaluation is presented in [MDN96] at lower Reynolds numbers and with fewer statistics. As the conditional averages have to be taken with respect to three quantities, r, Ω_1 and γ, an extraordinarily high amount of data is needed. Additionally, only a small number of bins allows for statistically convergent results, such that, for example, the width of each Ω_1 bin is about three standard deviations.

Figure 9.5 shows the scalar functions a, b and c as a function of r and γ for different values of Ω_1. The scalar function a, which represents the amplitude of the field pointing into $\boldsymbol{\Omega}_1$-direction, decays rapidly. The function b peaks for larger values of r. Maybe the most striking feature is the non-vanishing twist term related to the scalar function c, which yields a helical contribution to the vorticity field. Also this function peaks for r around 10η, such that the twisting contribution peaks *near* the fixed vorticity. Considered as a function of γ, a is maximal for parallel and anti-parallel $\boldsymbol{\Omega}_1$ and $\boldsymbol{r}$, whereas the twist term is maximal for inclined situations. The twist term vanishes for $\gamma = 0$, i.e. for perpendicular $\boldsymbol{r}$ and $\boldsymbol{\Omega}_1$. It can be observed that all the functions increase with the magnitude of the vorticity, particularly indicating that the vorticity field is stronger twisted in regions of high vorticity.

These observations can be made more intuitive by investigating the conditional vorticity field for different magnitudes of vorticity fixed in z-direction, which is presented in figure 9.6. It appears that the conditional field shows an elongated twisted shape concentrated near the fixed vorticity and fanning out along the elongated direction. Thus the conditional vorticity field has a remarkable similarity to the vortex tubes observed in fully developed turbulence, compare figure 1.5. Note that the twisting contribution, which is related to the enstrophy production induced by the local conditional structure, can also be found by a careful inspection of vortex tubes. In this sense the conditional vorticity

field may be thought of as the "typical local structure" of the flow field reminiscent of the coherent structures present in the flow. It is evident that the axisymmetric Burgers vortex does not display a twisted spatial structure. As a consequence, the Burgers vortex is incapable of generating enstrophy. The enstrophy contribution of such a simplified vortex tube is rather induced by the external strain field. Hence it might be more appropriate to model the local structure of the vorticity field with strained spiral vortices like the famous Lundgren vortex [Lun82, Lun93].

9.5. Analytical Treatment of the Closure Problem

After having investigated the structure of the first conditional moment both analytically and numerically, we now want to study the possibility of an analytical treatment. To this end we start from Gaussian conditional expectations and subsequently obtain a model consistent with the local structure of turbulence. In view of the fact that the single-point statistics of the vorticity field has been found to be highly non-Gaussian in chapter 8, it may seem inappropriate to start analytical calculations from Gaussian statistics. However, the Gaussian distribution is maybe the only analytically tractable PDF on the multi-point level, such that we do not really have a choice. Second, as we are currently interested in the *conditional structure* of the vorticity field rather that in the precise *shape* of the PDF, taking Gaussian statistics as a starting point will turn out to be promising.

9.5.1. Gaussian Approximation and its Failure

We show in appendix A that the first conditional moment for a Gaussian random field takes the form

$$\left\langle \boldsymbol{\omega}_0 \middle| \boldsymbol{\Omega}_1, \boldsymbol{r} \right\rangle_G = \mathrm{C}(\boldsymbol{r})\boldsymbol{\Omega}_1 \quad , \tag{9.35}$$

where C is the two-point correlation tensor already encountered in the preceding chapters. It may be expressed in terms of the longitudinal and transversal correlation functions according to

$$C_{ij}(\boldsymbol{r}) = c_\perp(r)\,\delta_{ij} + \left[c_\parallel - c_\perp\right](r)\,\frac{r_i r_j}{r^2} \quad , \tag{9.36}$$

where we have slightly changed the usual notation of the correlation functions in order to avoid confusion with the notation for the PDFs. Comparing this result with the general expression (9.27) for the conditional vorticity field, this results corresponds to a choice of

$$a(r,\Omega_1,\gamma) = \left[c_\perp + (c_\parallel - c_\perp)\,\gamma^2\right]\,\Omega_1 \tag{9.37a}$$

$$b(r,\Omega_1,\gamma) = (1-\gamma^2)^{\frac{1}{2}}\,\gamma\,(c_\parallel - c_\perp)\,\Omega_1 \tag{9.37b}$$

$$c(r,\Omega_1,\gamma) = 0 \quad . \tag{9.37c}$$

This means that the Gaussian approximation does not contain any twisting contributions and is consequently not able to prevail the conditional balance (8.41) as enstrophy

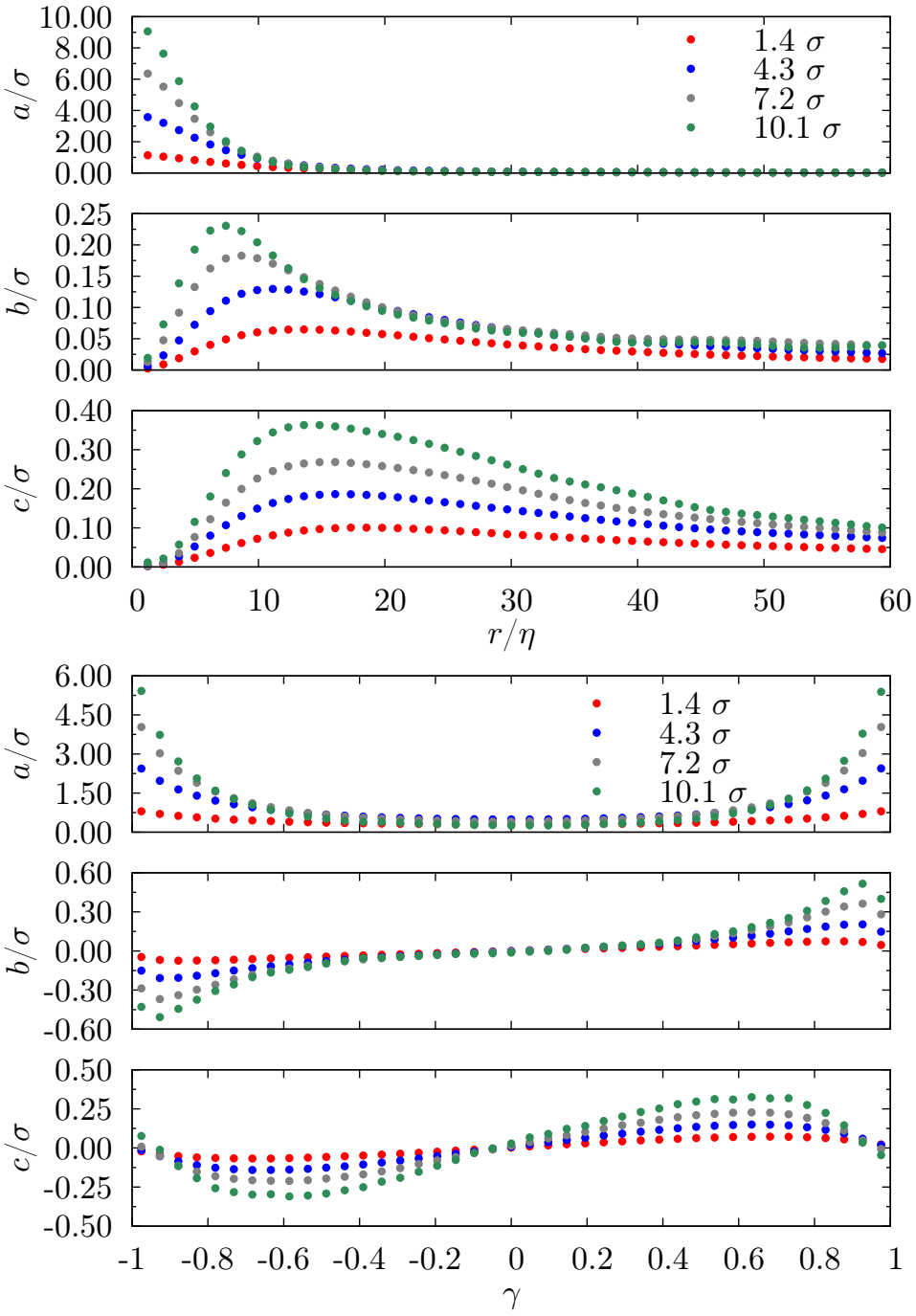

Figure 9.5.: Scalar functions a, b, c for different values of r,γ and Ω_1 (upper figure: fixed $\gamma = \frac{2}{3}$, lower figure: fixed $r = 9.9\,\eta$). The amplitude a corresponding to the $\mathbf{\Omega}_1$-direction decays monotonically, while the b and c peak for r around 10η. As a function of γ the angular dependence is resolved.

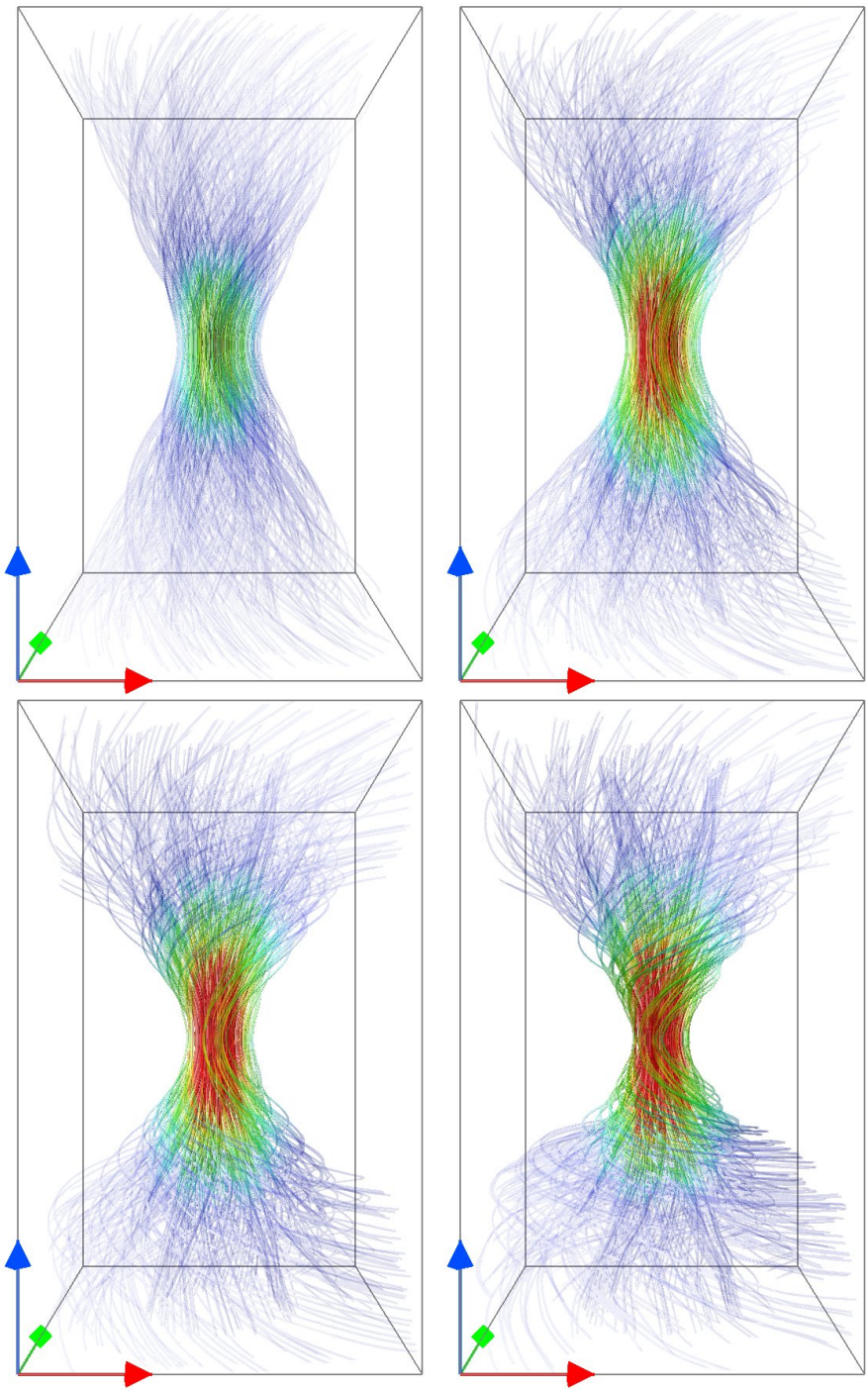

Figure 9.6.: Conditional vorticity field for different amplitudes Ω_1. From top left to bottom right $\Omega_1 \in \{1.4\sigma, 4.3\sigma, 7.2\sigma, 10.1\sigma\}$. The vorticity field gets increasingly intense (as indicated by the colors) and twisted.

production is missing. This, of course, can be also seen from an explicit calculation, which is demonstrated in the appendix A.

Still the Gaussian approximation can be used to compute the dissipative contribution, which is obtained as

$$\begin{aligned}\left\langle \Delta_{\boldsymbol{x}_1}\boldsymbol{\omega}(\boldsymbol{x}_1)\middle|\boldsymbol{\Omega}_1\right\rangle_G &= \lim_{|\boldsymbol{x}_1-\boldsymbol{x}_0|\to 0}\Delta_{\boldsymbol{x}_0}\left\langle \boldsymbol{\omega}_0\middle|\boldsymbol{\Omega}_1\right\rangle_G \\ &= \lim_{r\to 0}\Delta_{\boldsymbol{r}}\mathrm{C}(\boldsymbol{r})\boldsymbol{\Omega}_1 \quad ,\end{aligned} \tag{9.38}$$

i.e., the dissipative contribution is determined by the derivative of the correlation tensor in the origin. This derivative is readily calculated and yields

$$\Delta_{\boldsymbol{r}}C_{ij}(\boldsymbol{r}) = \left[c_\perp{}'' + \frac{2}{r}c_\perp' + \frac{2}{r^2}(c_\parallel - c_\perp)\right]\delta_{ij} + \left[(c_\parallel - c_\perp)'' + \frac{2}{r}(c_\parallel - c_\perp)' - \frac{6}{r^2}(c_\parallel - c_\perp)\right]\frac{r_i r_j}{r^2}\,. \tag{9.39}$$

Taking the limit requires invoking l'Hospital's rule. The result is

$$\lim_{r\to 0}\Delta_{\boldsymbol{r}}C_{ij}(\boldsymbol{r}) = (2c_\perp + c_\parallel)''(0)\,\delta_{ij} = \mathrm{TrC}''(\mathbf{0})\,\delta_{ij} \quad . \tag{9.40}$$

Thus we end up with the conditional dissipation term according to

$$\left\langle \nu\Delta_{\boldsymbol{x}_1}\boldsymbol{\omega}(\boldsymbol{x}_1)\middle|\boldsymbol{\Omega}_1\right\rangle_G = \nu\,\mathrm{TrC}''(\mathbf{0})\,\boldsymbol{\Omega}_1 \quad , \tag{9.41}$$

which finally yields a linear relation between the dissipative term and Ω_1,

$$\Lambda_G(\Omega_1) = \nu\,\mathrm{TrC}''(\mathbf{0})\,\Omega_1 \quad . \tag{9.42}$$

As Λ_G has to fulfill the integral constraint

$$-\left\langle \varepsilon_\omega\right\rangle = \int \mathrm{d}\Omega\,\Lambda_G(\Omega)\,\Omega\,\tilde{f}(\Omega) \quad , \tag{9.43}$$

we can conclude

$$\mathrm{TrC}''(\mathbf{0}) = -\frac{\left\langle \varepsilon_\omega\right\rangle}{3\nu\sigma^2} \quad . \tag{9.44}$$

Interestingly, this result is compliant with the lowest order closure approximation introduced for the velocity in chapter 7. While the qualitative trend of Λ is consistent with the numerically obtained result in figure 8.1, it is clear that the detailed functional shape of the dissipative term differs from the Gaussian approximation.

9.5.2. Twisted Gaussian Approximation

To extend the Gaussian approximation in a way that the conditional vorticity balance is fulfilled, we follow along the lines of Novikov's work [Nov93] and generalize the Gaussian approximation by adding an additional term according to

$$\begin{aligned}\left\langle \boldsymbol{\omega}(\boldsymbol{x}_0)\middle|\boldsymbol{\Omega}_1\right\rangle &= \left\langle \boldsymbol{\omega}(\boldsymbol{x}_0)\middle|\boldsymbol{\Omega}_1\right\rangle_G + \left\langle \boldsymbol{\omega}(\boldsymbol{x}_0)\middle|\boldsymbol{\Omega}_1\right\rangle_T \\ &= C(\boldsymbol{r})\boldsymbol{\Omega}_1 + c_T(r)\,(\hat{\boldsymbol{r}}\cdot\widehat{\boldsymbol{\Omega}}_1)\,(\widehat{\boldsymbol{\Omega}}_1\times\hat{\boldsymbol{r}}) \quad ,\end{aligned} \tag{9.45}$$

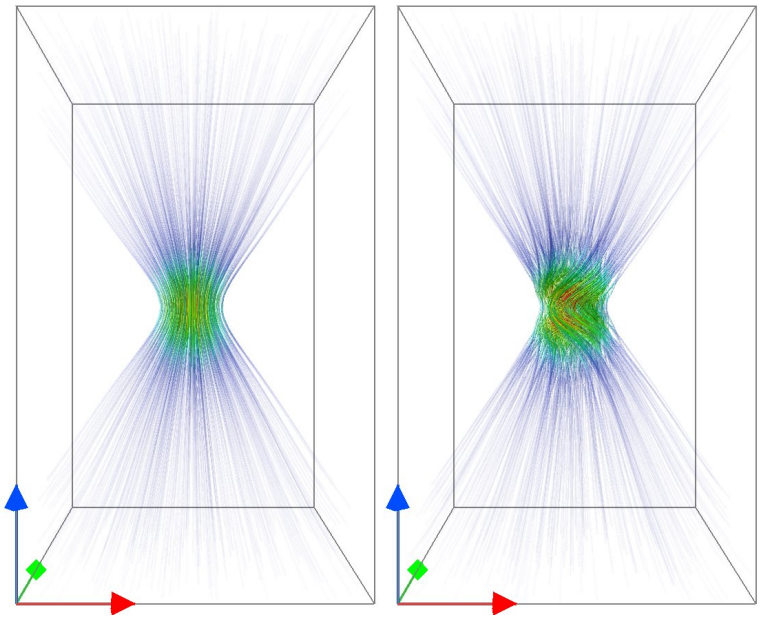

Figure 9.7.: Vorticity field in Gaussian (left) and Twisted Gaussian Approximation (right) for $\Omega_1 = 1$.

which corresponds to a model choice of

$$c(r, \Omega_1, \gamma) = c_T(r)\, \gamma \, \left(1 - \gamma^2\right)^{\frac{1}{2}} \quad . \tag{9.46}$$

Hereby we have introduced the up to now unspecified twist amplitude c_T. Note that this choice of a twist term is independent of the magnitude of vorticity, such that the rate-of-strain tensor calculated from this expression will not depend on the vorticity magnitude. It has already been checked by the general considerations above that a term introduced in such a way does not interfere with the solenoidality of the field and gives no contribution to the diffusive term. It is nevertheless instructive to calculate the terms for this particular choice of the twist term. The calculation is found in the appendix A.

To check for the contribution to the dissipative term, we calculate the Laplacian of the twist term yielding

$$\left\langle \Delta_{\boldsymbol{x}_0} \boldsymbol{\omega}(\boldsymbol{x}_0) \middle| \boldsymbol{\Omega}_1 \right\rangle_T = \Delta_{\boldsymbol{r}} \left[c_T(r) (\hat{\boldsymbol{r}} \cdot \widehat{\boldsymbol{\Omega}}_1)(\widehat{\boldsymbol{\Omega}}_1 \times \hat{\boldsymbol{r}}) \right] = \left(c_T'' + \frac{2c_T'}{r} - \frac{6c_T}{r^2} \right) (\hat{\boldsymbol{r}} \cdot \widehat{\boldsymbol{\Omega}}_1)(\widehat{\boldsymbol{\Omega}}_1 \times \hat{\boldsymbol{r}}) \quad , \tag{9.47}$$

which indeed gives no contribution to the diffusive term of the conditional enstrophy balance as the sum in brackets vanishes in the limit $r \to 0$ given both $c_T(0) = c_T'(0) = 0$. It additionally cannot give a contribution to Λ, because this term vanishes when projected onto the direction of the vorticity.

To calculate the contribution to the conditional vortex stretching term, we evaluate

$$\begin{aligned}\Sigma_T(\Omega_1) &= \left\langle \widehat{\boldsymbol{\omega}}_1 \mathrm{S}_1 \widehat{\boldsymbol{\omega}}_1 | \boldsymbol{\Omega}_1 \right\rangle \\ &= \frac{3}{4\pi} \int \mathrm{d}\boldsymbol{r}\, \frac{c_T(r)}{r^3} \left(\hat{\boldsymbol{r}} \cdot \widehat{\boldsymbol{\Omega}}_1\right)^2 \left(1 - \left(\hat{\boldsymbol{r}} \cdot \widehat{\boldsymbol{\Omega}}_1\right)^2\right) \\ &= \frac{3}{4\pi} \int \mathrm{d}r\, \mathrm{d}\varphi\, \mathrm{d}\vartheta\, \frac{c_T(r)}{r}\, \sin(\vartheta) \cos^2(\vartheta) \left(1 - \cos^2(\vartheta)\right) \\ &= \frac{3}{2} \int \mathrm{d}\vartheta\, \sin^3(\vartheta) \cos^2(\vartheta) \int \mathrm{d}r\, \frac{c_T(r)}{r} \\ &= \frac{2}{5} \int \mathrm{d}r\, \frac{c_T(r)}{r} \quad , \end{aligned} \tag{9.48}$$

where we have introduced spherical coordinates with the z-axis pointing into $\boldsymbol{\Omega}_1$-direction, such that $\gamma = \cos\vartheta$. The result shows that the conditional (normalized) enstrophy production is determined by an integral over the up to now unspecified twist amplitude c_T. The possible choices for c_T can be narrowed down by requiring the conditional balance

$$\Sigma_T(\Omega_1)\, \Omega_1 + \Lambda_G(\Omega_1) = 0 \quad . \tag{9.49}$$

This implies the relation

$$\int_0^\infty \mathrm{d}r\, \frac{c_T(r)}{r} = -\frac{5\nu}{2} \mathrm{TrC}''(\boldsymbol{0}) \quad , \tag{9.50}$$

an integral relation for the twist amplitude c_T. This relation obviously can be fulfilled in many ways. One consistent choice is

$$c_T(r) = \frac{5\nu}{2}\, r \left(\frac{1}{r} \mathrm{TrC}'(r)\right)' \quad , \tag{9.51}$$

which has also been investigated in [Nov93, MDN96]. By this the conditional local structure of the vorticity has been modeled in a way that the conditional balance (8.41) holds. In this way a closure of the kinetic equation (9.16) has been achieved. To put it differently, a careful analysis of the kinetic equation has led to a model for the local structure of turbulence. Unlike in the case of the Boltzmann closure, which allowed to determine the momentum PDF, this closure has determined the local structure of the vorticity field rather than the single-point PDF. We have seen in the preceding chapter that the determination of the single-point PDF eventually involves the conditional enstrophy dissipation tensor, which is related to the second moment of the conditional two-point PDF.

In figure 9.7 a visualization of the Gaussian approximation as well as the Twisted Gaussian Approximation (TGA) is shown. While the Gaussian approximation yields a non-screwed vorticity bundle, the Twisted Gaussian Approximation adds the twist already observed in the DNS results. A closer comparison with the visualization in figure 9.6 reveals a number of differences. First, the local structure extracted from

DNS appears to be more elongated. Second, and maybe more important, the twisting contribution appears to be more localized at the center of the field for the TGA. This can be made more quantitative with a direct comparison of the scalar functions a, b and c, which are presented in figure 9.8 for the TGA. The overall functional behavior of the scalars a and b observed in the DNS data is captured by the TGA. The comparison holds especially good for a, while stronger differences are present both in amplitude as well as in the functional dependence on γ for the scalar b. The most striking difference can be observed for the twisting contribution c. First of all, this function peaks for lower values of r for the TGA. Second, as the twist contribution has been modeled independent of the magnitude Ω_1, the functions collapse for different Ω_1. On a more general level one can criticize that, although the TGA fulfills the conditional balance (9.49), the functions Λ_G and Σ_T differ in the functional shape from the ones observed in DNS.

These shortcomings are likely to be fixed by construction of an improved approximation, which will remain a task for the future. For the present considerations the topological similarity of the model with the DNS results suffices to proceed further.

9.5.3. Generalization to Multi-Point Statistics

The advantage of taking Gaussian statistics as a starting point is that the generalization of the conditionally averaged vorticity field with respect to a single vorticity to a field conditionally averaged with respect to a number of fixed vorticities is straightforward. We calculate in appendix A that for a Gaussian random field the first conditional moment with respect to N fixed vorticities takes the form

$$\left\langle \boldsymbol{\omega}(\boldsymbol{x}_0) \middle| \boldsymbol{\Omega}_1, \ldots, \boldsymbol{\Omega}_N \right\rangle_G = \sum_{i,j=1}^{N} \mathcal{R}(\boldsymbol{x}_0, \boldsymbol{x}_i)\, \mathcal{R}^{-1}(\boldsymbol{x}_i, \boldsymbol{x}_j)\, \boldsymbol{\Omega}_j \quad . \tag{9.52}$$

For fixed i and j $\mathcal{R}(\boldsymbol{x}_i, \boldsymbol{x}_j)$ here denotes the 3×3 covariance tensor of the vorticities $\boldsymbol{\Omega}_i$ and $\boldsymbol{\Omega}_j$ located at position $\boldsymbol{x}_i$ and $\boldsymbol{x}_j$. This, of course, implies

$$\mathcal{R}(\boldsymbol{x}_1, \boldsymbol{x}_1) = \frac{\langle \boldsymbol{\omega}^2 \rangle}{3} \mathrm{E} \qquad \text{and} \qquad \mathcal{R}(\boldsymbol{x}_1, \boldsymbol{x}_2) = \frac{\langle \boldsymbol{\omega}^2 \rangle}{3} \mathrm{C}(\boldsymbol{x}_1, \boldsymbol{x}_2) \quad . \tag{9.53}$$

For the special case of two fixed vorticities, which will be of interest in the following, we simply have

$$\begin{aligned} \left\langle \boldsymbol{\omega}(\boldsymbol{x}_0) \middle| \boldsymbol{\Omega}_1, \boldsymbol{\Omega}_2 \right\rangle_G = {} & \mathcal{R}(\boldsymbol{x}_0, \boldsymbol{x}_1) \left[\mathcal{R}^{-1}(\boldsymbol{x}_1, \boldsymbol{x}_1)\, \boldsymbol{\Omega}_1 + \mathcal{R}^{-1}(\boldsymbol{x}_1, \boldsymbol{x}_2)\, \boldsymbol{\Omega}_2 \right] \\ & + \mathcal{R}(\boldsymbol{x}_0, \boldsymbol{x}_2) \left[\mathcal{R}^{-1}(\boldsymbol{x}_2, \boldsymbol{x}_1)\, \boldsymbol{\Omega}_1 + \mathcal{R}^{-1}(\boldsymbol{x}_2, \boldsymbol{x}_2)\, \boldsymbol{\Omega}_2 \right] \end{aligned} \tag{9.54}$$

with

$$\mathcal{R} = \frac{\langle \boldsymbol{\omega}^2 \rangle}{3} \begin{pmatrix} \mathrm{E} & \mathrm{C}(\boldsymbol{x}_1, \boldsymbol{x}_2) \\ \mathrm{C}(\boldsymbol{x}_2, \boldsymbol{x}_1) & \mathrm{E} \end{pmatrix} \quad , \tag{9.55}$$

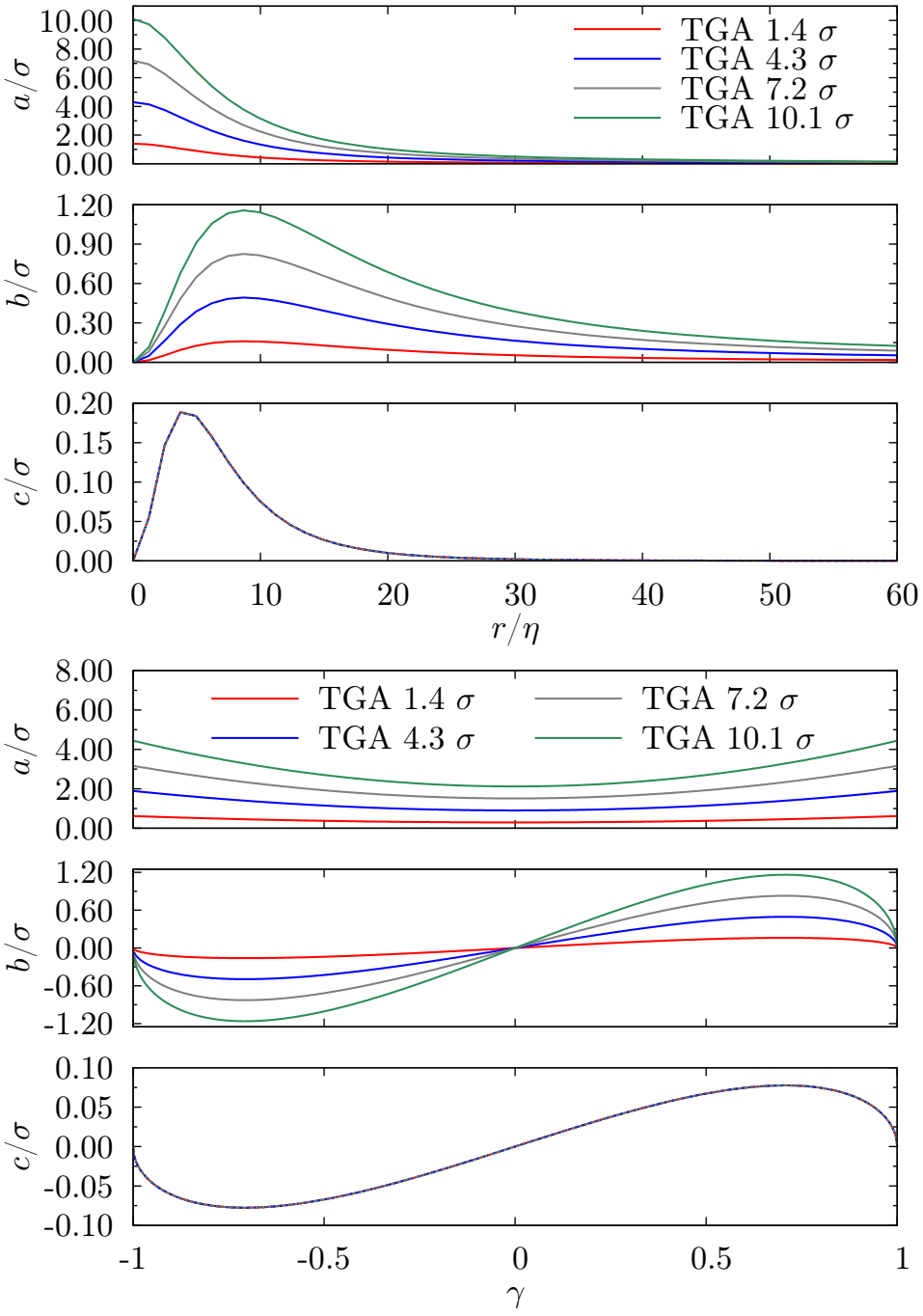

Figure 9.8.: Scalar functions a, b, c for the Twisted Gaussian Approximation (upper figure: fixed $\gamma = \frac{2}{3}$, lower figure: fixed $r = 9.9\,\eta$). Though the functions are qualitatively similar to the ones presented in figure 9.5, quantitative differences are visible.

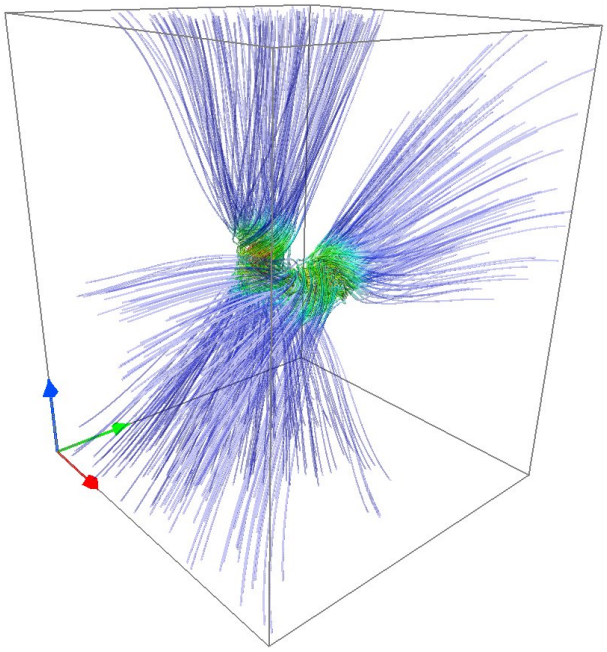

Figure 9.9.: Vorticity field for two fixed inclined vorticities in Twisted Gaussian Approximation for $\Omega_1 = 1$ and $\Omega_2 = 1$.

which explicitly can be inverted yielding

$$\mathcal{R}^{-1} = \frac{3}{\langle \boldsymbol{\omega}^2 \rangle} \left[\mathrm{E} - \mathrm{C}(\boldsymbol{x}_1, \boldsymbol{x}_2)^2 \right]^{-1} \begin{pmatrix} \mathrm{E} & -\mathrm{C}(\boldsymbol{x}_1, \boldsymbol{x}_2) \\ -\mathrm{C}(\boldsymbol{x}_2, \boldsymbol{x}_1) & \mathrm{E} \end{pmatrix} \quad , \tag{9.56}$$

where the prefactor is obtained according to (see appendix A)

$$\left[\mathrm{E} - \mathrm{C}^2 \right]^{-1}_{ij} = \frac{1}{1 - c_\perp^2} \delta_{ij} + \frac{c_\parallel^2 - c_\perp^2}{(1 - c_\parallel^2)(1 - c_\perp^2)} \frac{r_i r_j}{r^2} \quad . \tag{9.57}$$

The conditional vorticity field (9.54) has a number of interesting properties. First of all, if one of the vorticities is infinitely far away, the expression reduces to the conditional vorticity field with one fixed vorticity,

$$\begin{aligned} \lim_{|\boldsymbol{x}_0 - \boldsymbol{x}_2| \to \infty} \lim_{|\boldsymbol{x}_1 - \boldsymbol{x}_2| \to \infty} \left\langle \boldsymbol{\omega}_0 \middle| \boldsymbol{\Omega}_1, \boldsymbol{\Omega}_2 \right\rangle_G &= \left\langle \boldsymbol{\omega}_0 \middle| \boldsymbol{\Omega}_1 \right\rangle_G \\ \lim_{|\boldsymbol{x}_0 - \boldsymbol{x}_1| \to \infty} \lim_{|\boldsymbol{x}_1 - \boldsymbol{x}_2| \to \infty} \left\langle \boldsymbol{\omega}_0 \middle| \boldsymbol{\Omega}_1, \boldsymbol{\Omega}_2 \right\rangle_G &= \left\langle \boldsymbol{\omega}_0 \middle| \boldsymbol{\Omega}_2 \right\rangle_G \quad , \end{aligned} \tag{9.58}$$

which can be seen from the fact that the corresponding correlation functions tend to zero for infinitely large separations. This is just the *separation property* of the multi-point

PDFs used on the level of the conditional averages. For the limit $\boldsymbol{x}_1 \to \boldsymbol{x}_2$ the terms of equation (9.54) in brackets have to be considered. We obtain

$$\begin{aligned}\lim_{|\boldsymbol{x}_1-\boldsymbol{x}_2|\to 0} &\left[\mathcal{R}^{-1}(\boldsymbol{x}_1,\boldsymbol{x}_1)+\mathcal{R}^{-1}(\boldsymbol{x}_1,\boldsymbol{x}_2)\right]_{ij} \\ &= \frac{3}{\langle\boldsymbol{\omega}^2\rangle}\lim_{|\boldsymbol{x}_1-\boldsymbol{x}_2|\to 0}\left[\mathrm{E}-\mathrm{C}(\boldsymbol{x}_1,\boldsymbol{x}_2)^2\right]^{-1}_{ik}\left[\mathrm{E}-\mathrm{C}(\boldsymbol{x}_1,\boldsymbol{x}_2)\right]_{kj} \\ &= \frac{3}{\langle\boldsymbol{\omega}^2\rangle}\lim_{r\to 0}\left[\frac{1-c_\perp}{1-c_\perp^2}\,\delta_{ij}+\left(\frac{1}{1+c_\parallel}-\frac{1}{1+c_\perp}\right)\frac{r_i\,r_j}{r^2}\right] \\ &= \frac{1}{2}\frac{3}{\langle\boldsymbol{\omega}^2\rangle}\,\delta_{ij} \quad , \end{aligned} \tag{9.59}$$

where we have used l'Hospital's rule to perform the limit for the first term. Furthermore, we obtain $\boldsymbol{\Omega}_1 = \boldsymbol{\Omega}_2$ in this limit, such that we finally get

$$\lim_{|\boldsymbol{x}_1-\boldsymbol{x}_2|\to 0}\left\langle\boldsymbol{\omega}_0\middle|\boldsymbol{\Omega}_1,\,\boldsymbol{\Omega}_2\right\rangle_G = \left\langle\boldsymbol{\omega}_0\middle|\boldsymbol{\Omega}_1\right\rangle_G \quad , \tag{9.60}$$

which simply is the *coincidence property* for the conditional field. The third important property of this ansatz is the *reduction property*

$$\int \mathrm{d}\boldsymbol{\Omega}_2\left\langle\boldsymbol{\omega}_0\middle|\boldsymbol{\Omega}_1,\,\boldsymbol{\Omega}_2\right\rangle_G f_2(\boldsymbol{\Omega}_1,\boldsymbol{\Omega}_1;\boldsymbol{r}) = \left\langle\boldsymbol{\omega}_0\middle|\boldsymbol{\Omega}_1\right\rangle_G f_1(\boldsymbol{\Omega}_1) \quad , \tag{9.61}$$

which can be calculated explicitly for the multivariate Gaussian distribution. A detailed calculation shows that this result comes due to an intricate cancellation of terms. Hence, we cannot expect to maintain this property when additional terms are added to the Gaussian expression.

This flaw has to be kept in mind when introducing the twist term. However, the *separation* and *coincidence properties* can be fulfilled easily by an appropriate construction of the additional term. A particularly simple choice for the twist term is

$$\begin{aligned}&\left\langle\boldsymbol{\omega}_0\middle|\boldsymbol{\Omega}_1,\boldsymbol{\Omega}_2\right\rangle_T \\ &\quad= \frac{1-c_\perp(r_{12})}{1-c_\perp^2(r_{12})}\left[c_T(r_{01})\,(\hat{\boldsymbol{r}}_{01}\cdot\widehat{\boldsymbol{\Omega}}_1)\,(\widehat{\boldsymbol{\Omega}}_1\times\hat{\boldsymbol{r}}_{01})+c_T(r_{02})\,(\hat{\boldsymbol{r}}_{02}\cdot\widehat{\boldsymbol{\Omega}}_2)\,(\widehat{\boldsymbol{\Omega}}_2\times\hat{\boldsymbol{r}}_{02})\right] \\ &\quad=: \frac{1-c_\perp(r_{12})}{1-c_\perp^2(r_{12})}\left[\boldsymbol{T}(\boldsymbol{x}_0,\boldsymbol{x}_1,\boldsymbol{\Omega}_1)+\boldsymbol{T}(\boldsymbol{x}_0,\boldsymbol{x}_2,\boldsymbol{\Omega}_2)\right]\end{aligned} \tag{9.62}$$

with $\boldsymbol{r}_{01} = \boldsymbol{x}_1 - \boldsymbol{x}_0$, $\boldsymbol{r}_{02} = \boldsymbol{x}_2 - \boldsymbol{x}_0$ and $\boldsymbol{r}_{12} = \boldsymbol{x}_2 - \boldsymbol{x}_1$. It is readily checked that this choice fulfills the *separation property*, because

$$\lim_{|\boldsymbol{x}_0-\boldsymbol{x}_1|\to\infty} c_T(r_{01}) = 0 \tag{9.63a}$$

$$\lim_{|\boldsymbol{x}_0-\boldsymbol{x}_2|\to\infty} c_T(r_{02}) = 0 \quad . \tag{9.63b}$$

The *coincidence property* is fulfilled by the prefactor as a short calculation invoking l'Hospital's rule shows. By constructing a closure for the two-point statistics in this way, it is possible to study arbitrary configurations with two fixed vorticities. One such configuration of two nearby inclined vorticities is shown in figure 9.9 as an example. Apart from the twisted structure near the fixed vorticities one can observe a mutual influence of the localized vorticities. It is evident that an estimation from DNS data of such a setting is at the moment impossible due to statistical constraints, that is why a simplified modeling approach seems reasonable at this point. The analytical study of arbitrary configurations is, for example, necessary to evaluate the rate-of-strain tensor conditionally averaged with respect to two vorticities, which will be the topic of the following sections.

9.5.4. Two-Point Enstrophy Statistics in Twisted Gaussian Approximation

After this presentation of the two-point enstrophy statistics from our DNS data at the beginning of this chapter, we now want to study the two-point enstrophy statistics in the Twisted Gaussian Approximation. The strategy will be to first calculate the unclosed terms from the conditional vorticity field $\langle \boldsymbol{\omega}_0 | \boldsymbol{\Omega}_1, \boldsymbol{\Omega}_2 \rangle$ and then to project the result onto the Ω_1-Ω_2-plane. For conditional averages of arbitrary scalar functions $F(\boldsymbol{\omega}_1, \boldsymbol{\omega}_2)$ depending on the vorticity field in two distinct points this projection is achieved by

$$\langle F(\boldsymbol{\omega}_1, \boldsymbol{\omega}_2) | \Omega_1, \Omega_2 \rangle \, \tilde{f}_2(\Omega_1, \Omega_2) = \int \mathrm{d}\widehat{\boldsymbol{\Omega}}_1 \, \mathrm{d}\widehat{\boldsymbol{\Omega}}_2 \, \langle F(\boldsymbol{\omega}_1, \boldsymbol{\omega}_2) | \boldsymbol{\Omega}_1, \boldsymbol{\Omega}_2 \rangle \, f_2(\boldsymbol{\Omega}_1, \boldsymbol{\Omega}_2) \,, \quad (9.64)$$

i.e., by integrating the conditional average with respect to the vectors times the PDF over all possible directions of the two sample space vectors. We will calculate the resulting terms analytically whenever possible, however, especially the projection onto the plane has to be done numerically. To this end we take the analytically obtained expression for the conditional average with respect to the two sample space vorticities and evaluate it statistically by drawing the two vorticities from a joint normal PDF with prescribed correlation tensor. The result then is binned with respect to the magnitude of the vectors, which corresponds to a statistical evaluation of the above relation (9.64).

Before we proceed to the evaluation of the individual terms, let us recapitulate the results of the single-point enstrophy balance obtained in the Twisted Gaussian Approximation, for which the enstrophy balance is graphically represented in figure 9.1. It can be seen that the qualitative behavior compares well to the directly obtained result, however, the precise functional shape differs. While the enstrophy productions depends quadratically on the magnitude of vorticity for the Twisted Gaussian Approximation, differences occur for the results obtained from DNS as already discussed in chapter 8. The amplitudes of the functions obtained in Twisted Gaussian Approximation have been fixed such that the integral constraints of the functions are fulfilled, i.e., the conditional averages have to reduce to correct ordinary averages. It can be seen from the inset of the same figure that both the directly obtained and approximated conditional averages

will yield the same average upon integration. Consequently, we can expect qualitative rather than quantitative insights from the following calculations.

Dissipative Terms in TGA

To compute the dissipative terms, we consider

$$\left\langle \nu\boldsymbol{\omega}_1 \cdot \Delta_{\boldsymbol{x}_1}\boldsymbol{\omega}_1 \middle| \boldsymbol{\Omega}_1, \boldsymbol{\Omega}_2 \right\rangle = \nu\, \boldsymbol{\Omega}_1 \cdot \left[\lim_{|\boldsymbol{x}_0 - \boldsymbol{x}_1| \to 0} \Delta_{\boldsymbol{x}_0} \left\langle \boldsymbol{\omega}_0 \middle| \boldsymbol{\Omega}_1, \boldsymbol{\Omega}_2 \right\rangle \right] \quad . \tag{9.65}$$

For the Gaussian contribution to the dissipative terms we have to evaluate

$$\begin{aligned} \langle \boldsymbol{\omega}_1 \cdot \Delta_{\boldsymbol{x}_1}\boldsymbol{\omega}_1 | \boldsymbol{\Omega}_1,\, \boldsymbol{\Omega}_2 \rangle_G = \boldsymbol{\Omega}_1 \cdot & \left[\lim_{|\boldsymbol{x}_1 - \boldsymbol{x}_0| \to 0} \Delta_{\boldsymbol{x}_0} \mathcal{R}(\boldsymbol{x}_0, \boldsymbol{x}_1) \mathcal{R}^{-1}(\boldsymbol{x}_1, \boldsymbol{x}_1) \right] \boldsymbol{\Omega}_1 \\ + \boldsymbol{\Omega}_1 \cdot & \left[\lim_{|\boldsymbol{x}_1 - \boldsymbol{x}_0| \to 0} \Delta_{\boldsymbol{x}_0} \mathcal{R}(\boldsymbol{x}_0, \boldsymbol{x}_1) \mathcal{R}^{-1}(\boldsymbol{x}_1, \boldsymbol{x}_2) \right] \boldsymbol{\Omega}_2 \\ + \boldsymbol{\Omega}_1 \cdot & \left[\lim_{|\boldsymbol{x}_1 - \boldsymbol{x}_0| \to 0} \Delta_{\boldsymbol{x}_0} \mathcal{R}(\boldsymbol{x}_0, \boldsymbol{x}_2) \mathcal{R}^{-1}(\boldsymbol{x}_2, \boldsymbol{x}_1) \right] \boldsymbol{\Omega}_1 \\ + \boldsymbol{\Omega}_1 \cdot & \left[\lim_{|\boldsymbol{x}_1 - \boldsymbol{x}_0| \to 0} \Delta_{\boldsymbol{x}_0} \mathcal{R}(\boldsymbol{x}_0, \boldsymbol{x}_2) \mathcal{R}^{-1}(\boldsymbol{x}_2, \boldsymbol{x}_2) \right] \boldsymbol{\Omega}_2 \quad , \end{aligned} \tag{9.66}$$

which involves the computation of the Laplacian of $\mathcal{R}(\boldsymbol{x}_0, \boldsymbol{x}_1)$ and $\mathcal{R}(\boldsymbol{x}_1, \boldsymbol{x}_2)$ before taking the limit. We obtain

$$\begin{aligned} \lim_{|\boldsymbol{x}_1 - \boldsymbol{x}_0| \to 0} \Delta_{\boldsymbol{x}_0} \mathcal{R}(\boldsymbol{x}_0, \boldsymbol{x}_1) =& \frac{\langle \boldsymbol{\omega}^2 \rangle}{3} \left[\mathrm{TrC}''(\boldsymbol{0}) \right] \delta_{ij} \\ \lim_{|\boldsymbol{x}_1 - \boldsymbol{x}_0| \to 0} \Delta_{\boldsymbol{x}_0} \mathcal{R}(\boldsymbol{x}_0, \boldsymbol{x}_2) =& \frac{\langle \boldsymbol{\omega}^2 \rangle}{3} \left(\left[c_\perp{}'' + \frac{2}{r} c_\perp' + \frac{2}{r^2}(c_\parallel - c_\perp) \right] \delta_{ij} \right. \\ & \left. + \left[(c_\parallel - c_\perp)'' + \frac{2}{r}(c_\parallel - c_\perp)' - \frac{6}{r^2}(c_\parallel - c_\perp) \right] \frac{r_i r_j}{r^2} \right) \quad . \end{aligned} \tag{9.67}$$

Additionally the inverse matrices $\mathcal{R}^{-1}(\boldsymbol{x}_i, \boldsymbol{x}_j)$ have to be calculated, for which explicit expressions can be found in appendix A. Taking these terms together we obtain the

Gaussian part of the diffusive term according to

$$\begin{aligned}
&\big\langle \boldsymbol{\omega}_1 \cdot \Delta_{\boldsymbol{x}_1} \boldsymbol{\omega}_1 \big| \boldsymbol{\Omega}_1,\, \boldsymbol{\Omega}_2 \big\rangle_G = \\
&\frac{\mathrm{TrC}''(\mathbf{0})}{1-c_\perp^2}\,\Omega_1^2 + \frac{\big[\mathrm{TrC}''(\mathbf{0})\big](c_\parallel^2 - c_\perp^2)}{(1-c_\parallel^2)(1-c_\perp^2)}(\hat{\boldsymbol{r}}\cdot\boldsymbol{\Omega}_1)^2 \\
&- \frac{\big[\mathrm{TrC}''(\mathbf{0})\big]c_\perp}{1-c_\perp^2}\,(\boldsymbol{\Omega}_1\cdot\boldsymbol{\Omega}_2) - \frac{\big[\mathrm{TrC}''(\mathbf{0})\big](c_\parallel - g)(1+c_\parallel c_\perp)}{(1-c_\parallel^2)(1-c_\perp^2)}\,(\hat{\boldsymbol{r}}\cdot\boldsymbol{\Omega}_1)(\hat{\boldsymbol{r}}\cdot\boldsymbol{\Omega}_2) \\
&+ \left[c_\perp{}'' + \frac{2}{r}c_\perp' + \frac{2}{r^2}(c_\parallel - c_\perp)\right]\left[-\frac{c_\perp}{1-c_\perp^2}\Omega_1^2 - \frac{(c_\parallel - c_\perp)(1+c_\parallel c_\perp)}{(1-c_\parallel^2)(1-c_\perp^2)}(\hat{\boldsymbol{r}}\cdot\boldsymbol{\Omega}_1)^2\right. \\
&\quad \left. + \frac{1}{1-c_\perp^2}\,(\boldsymbol{\Omega}_1\cdot\boldsymbol{\Omega}_2) + \frac{c_\parallel^2 - c_\perp^2}{(1-c_\parallel^2)(1-c_\perp^2)}\,(\hat{\boldsymbol{r}}\cdot\boldsymbol{\Omega}_1)(\hat{\boldsymbol{r}}\cdot\boldsymbol{\Omega}_2)\right] \\
&+ \left[(c_\parallel - c_\perp)'' + \frac{2}{r}(c_\parallel - c_\perp)' - \frac{6}{r^2}(c_\parallel - c_\perp)\right]\left[\frac{1}{1-c_\parallel^2}(\hat{\boldsymbol{r}}\cdot\boldsymbol{\Omega}_1)(\hat{\boldsymbol{r}}\cdot\boldsymbol{\Omega}_2) - \frac{c_\parallel}{1-c_\parallel^2}(\hat{\boldsymbol{r}}\cdot\boldsymbol{\Omega}_1)^2\right].
\end{aligned} \tag{9.68}$$

While it is rather intricate to discuss this expression in detail, a number of simple observations can be made. As in the single-point case, all of the terms depend quadratically on the magnitudes of Ω_1 and Ω_2, however, also cross terms and direction cosines appear. It is also interesting to evaluate the limit of vanishing and infinite distances of $\boldsymbol{x}_1$ and $\boldsymbol{x}_2$, for which we obtain the Gaussian contribution of the single-point diffusive term,

$$\lim_{r\to 0} \big\langle \boldsymbol{\omega}_1 \cdot \Delta_{\boldsymbol{x}_1} \boldsymbol{\omega}_1 \big| \boldsymbol{\Omega}_1,\, \boldsymbol{\Omega}_2 \big\rangle_G = \mathrm{TrC}''(\mathbf{0})\,\Omega_1^2 \tag{9.69a}$$

$$\lim_{r\to \infty} \big\langle \boldsymbol{\omega}_1 \cdot \Delta_{\boldsymbol{x}_1} \boldsymbol{\omega}_1 \big| \boldsymbol{\Omega}_1,\, \boldsymbol{\Omega}_2 \big\rangle_G = \mathrm{TrC}''(\mathbf{0})\,\Omega_1^2 \quad . \tag{9.69b}$$

For the first result a regrouping of the terms and the application of l'Hospital's rule is needed. Of course, $\big\langle \boldsymbol{\omega}_2 \cdot \Delta_{\boldsymbol{x}_2} \boldsymbol{\omega}_2 \big| \boldsymbol{\Omega}_1,\, \boldsymbol{\Omega}_2 \big\rangle_G$ is calculated in exactly the same manner.

For the twist contribution to the dissipative terms we have to evaluate

$$\begin{aligned}
&\big\langle \boldsymbol{\omega}_1 \cdot \Delta_{\boldsymbol{x}_1} \boldsymbol{\omega}_1 \big| \boldsymbol{\Omega}_1, \boldsymbol{\Omega}_2 \big\rangle_T \\
&\quad = \frac{1-c_\perp(r_{12})}{1-c_\perp^2(r_{12})}\,\boldsymbol{\Omega}_1 \cdot \left[\lim_{|\boldsymbol{x}_1 - \boldsymbol{x}_0|\to 0} \Delta_{\boldsymbol{x}_0}\big[\boldsymbol{T}(\boldsymbol{x}_0, \boldsymbol{x}_1, \boldsymbol{\Omega}_1) + \boldsymbol{T}(\boldsymbol{x}_0, \boldsymbol{x}_2, \boldsymbol{\Omega}_2)\big]\right] \quad .
\end{aligned} \tag{9.70}$$

It has already been calculated in the single-point case in equation (9.47) that the first term gives no contribution after taking the limit. So only the second term is non-vanishing and we obtain

$$\big\langle \boldsymbol{\omega}_1 \cdot \Delta_{\boldsymbol{x}_1} \boldsymbol{\omega}_1 \big| \boldsymbol{\Omega}_1,\, \boldsymbol{\Omega}_2 \big\rangle_T = \left(\frac{1-c_\perp}{1-c_\perp^2}\right)\left(c_T'' + \frac{2c_T'}{r} - \frac{6c_T}{r^2}\right)(\hat{\boldsymbol{r}}\cdot\widehat{\boldsymbol{\Omega}}_2)\big[\boldsymbol{\Omega}_1 \cdot (\widehat{\boldsymbol{\Omega}}_2 \times \hat{\boldsymbol{r}})\big] \quad . \tag{9.71}$$

It is readily checked that this term vanishes in the two limiting cases. Additionally, when projected onto the Ω_1-Ω_2-plane, this term vanishes as well. This can be seen, since

while the joint Gaussian PDF is invariant with respect to a simultaneous change of sign of $\boldsymbol{\Omega}_1$ and $\boldsymbol{\Omega}_2$, the above expression is not, such that the expression vanishes upon projection. Hence only the Gaussian terms contribute to the dissipative terms of the two-point enstrophy statistics.

Enstrophy Production Terms in TGA

To compute the conditional enstrophy production, we have to evaluate

$$\left\langle \boldsymbol{\omega}_1 \mathrm{S}_1 \boldsymbol{\omega}_1 \middle| \boldsymbol{\Omega}_1, \boldsymbol{\Omega}_2 \right\rangle = \frac{3}{4\pi} \int \mathrm{d}\boldsymbol{x}_0 \, \frac{\boldsymbol{\Omega}_1 \cdot \hat{\boldsymbol{r}}_{01}}{r_{01}^3} \left[\hat{\boldsymbol{r}}_{01} \times \langle \boldsymbol{\omega}(\boldsymbol{x}_0) | \boldsymbol{\Omega}_1, \boldsymbol{\Omega}_2 \rangle \right] \cdot \boldsymbol{\Omega}_1 \quad . \tag{9.72}$$

Again we start with the Gaussian contribution, for which we have to evaluate

$$\begin{aligned} &\left\langle \boldsymbol{\omega}_1 \mathrm{S}_1 \boldsymbol{\omega}_1 \middle| \boldsymbol{\Omega}_1, \boldsymbol{\Omega}_2 \right\rangle_G \\ &= \frac{3}{4\pi} \int \mathrm{d}\boldsymbol{x}_0 \, \frac{\boldsymbol{\Omega}_1 \cdot \hat{\boldsymbol{r}}_{01}}{r_{01}^3} \, \boldsymbol{\Omega}_1 \cdot \Big[\hat{\boldsymbol{r}}_{01} \quad \times \quad \big(\mathcal{R}(\boldsymbol{x}_0, \boldsymbol{x}_1) \left[\mathcal{R}^{-1}(\boldsymbol{x}_1, \boldsymbol{x}_1) \, \boldsymbol{\Omega}_1 + \mathcal{R}^{-1}(\boldsymbol{x}_1, \boldsymbol{x}_2) \, \boldsymbol{\Omega}_2 \right] \\ &\qquad\qquad + \quad \mathcal{R}(\boldsymbol{x}_0, \boldsymbol{x}_2) \left[\mathcal{R}^{-1}(\boldsymbol{x}_2, \boldsymbol{x}_1) \, \boldsymbol{\Omega}_1 + \mathcal{R}^{-1}(\boldsymbol{x}_2, \boldsymbol{x}_2) \, \boldsymbol{\Omega}_2 \right] \big) \Big] \, . \end{aligned} \tag{9.73}$$

Without further calculation one can note that all of these terms vanish upon projection onto the Ω_1-Ω_2-plane, as the expression changes sign when $\boldsymbol{\Omega}_1$ and $\boldsymbol{\Omega}_2$ change sign simultaneously. Consequently, there is no Gaussian contribution to the enstrophy production terms in the plane. Still, the integrals can be evaluated analytically, which is demonstrated for the first one in the appendix A.

For the twist contribution to the conditional enstrophy production the integrals

$$\begin{aligned} &\left\langle \boldsymbol{\omega}_1 \mathrm{S}_1 \boldsymbol{\omega}_1 \middle| \boldsymbol{\Omega}_1, \boldsymbol{\Omega}_2 \right\rangle_T \\ &= \frac{3}{4\pi} \left(\frac{1 - c_\perp}{1 - c_\perp^2} \right) \int \mathrm{d}\boldsymbol{x}_0 \, \frac{\boldsymbol{\Omega}_1 \cdot \hat{\boldsymbol{r}}_{01}}{r_{01}^3} \, \boldsymbol{\Omega}_1 \cdot \Big[\hat{\boldsymbol{r}}_{01} \times \Big[\boldsymbol{T}(\boldsymbol{x}_0, \boldsymbol{x}_1, \boldsymbol{\Omega}_1) + \boldsymbol{T}(\boldsymbol{x}_0, \boldsymbol{x}_2, \boldsymbol{\Omega}_2) \Big] \Big] \end{aligned} \tag{9.74}$$

have to be evaluated. The integral related to the first twist term has already been evaluated for the single-point statistics and yields

$$\frac{3}{4\pi} \int \mathrm{d}\boldsymbol{x}_0 \, \frac{\boldsymbol{\Omega}_1 \cdot \hat{\boldsymbol{r}}_{01}}{r_{01}^3} \, \boldsymbol{\Omega}_1 \cdot \left[\hat{\boldsymbol{r}}_{01} \times \boldsymbol{T}(\boldsymbol{x}_0, \boldsymbol{x}_1, \boldsymbol{\Omega}_1) \right] = \frac{2}{5} \int \mathrm{d}r_{01} \, \frac{c_T(r_{01})}{r_{01}} \quad . \tag{9.75}$$

It turns out that the second integral unfortunately cannot be treated fully analytically. It takes the form

$$\begin{aligned} &\frac{3}{4\pi} \int \mathrm{d}\boldsymbol{x}_0 \, \frac{\boldsymbol{\Omega}_1 \cdot \hat{\boldsymbol{r}}_{01}}{r_{01}^3} \, \boldsymbol{\Omega}_1 \cdot \left[\hat{\boldsymbol{r}}_{01} \times \boldsymbol{T}(\boldsymbol{x}_0, \boldsymbol{x}_2, \boldsymbol{\Omega}_2) \right] \\ =&\frac{3}{4\pi} \Omega_1^2 \int \mathrm{d}\boldsymbol{x}_0 \, \frac{(\widehat{\boldsymbol{\Omega}}_1 \cdot \hat{\boldsymbol{r}}_{01}) \, (\widehat{\boldsymbol{\Omega}}_2 \cdot \hat{\boldsymbol{r}}_{02}) \, c_T(r_{02})}{r_{01}^3} \, \widehat{\boldsymbol{\Omega}}_1 \cdot \left[\hat{\boldsymbol{r}}_{01} \times (\widehat{\boldsymbol{\Omega}}_2 \cdot \hat{\boldsymbol{r}}_{02}) \right] \quad , \end{aligned} \tag{9.76}$$

from which it is clear that it depends quadratically on Ω_1. As the integrand depends both on $\boldsymbol{r}_{01}$ and $\boldsymbol{r}_{02}$, a further analytical treatment is not possible at this point. One can, however, note that in the limit of $\boldsymbol{x}_1 \to \boldsymbol{x}_2$ the above analytically tractable integral is recovered. To treat this integral numerically, it is expressed in terms of the fourth-order tensor

$$I^{\mathrm{S}}_{ijkl} = \frac{3}{4\pi} \int \mathrm{d}\boldsymbol{x}_0 \, \frac{h(r_{02})}{r_{01}^3} \, \hat{\boldsymbol{r}}_{01,i} \, \hat{\boldsymbol{r}}_{02,j} \, \hat{\boldsymbol{r}}_{01,k} \, \hat{\boldsymbol{r}}_{02,l} \quad . \tag{9.77}$$

This integral tensor has to be evaluated once for each choice of $\boldsymbol{r}$, such that this term can be treated numerically in an effective way. This leads to the desired result

$$\begin{aligned} &\frac{3}{4\pi} \int \mathrm{d}\boldsymbol{x}_0 \, \frac{\boldsymbol{\Omega}_1 \cdot \hat{\boldsymbol{r}}_{01}}{r_{01}^3} \, \boldsymbol{\Omega}_1 \cdot \left[\hat{\boldsymbol{r}}_{01} \times \boldsymbol{T}(\boldsymbol{x}_0, \boldsymbol{x}_2, \boldsymbol{\Omega}_2) \right] \\ =&\Omega_1^2 \left[\widehat{\Omega}_{1,i} \, \widehat{\Omega}_{2,j} \, (\widehat{\boldsymbol{\Omega}}_1 \cdot \widehat{\boldsymbol{\Omega}}_2) \, I^{\mathrm{S}}_{ijkk} - \widehat{\Omega}_{1,i} \, \widehat{\Omega}_{2,j} \, \widehat{\Omega}_{2,k} \, \widehat{\Omega}_{1,l} \; I^{\mathrm{S}}_{ijkl} \right] \quad . \end{aligned} \tag{9.78}$$

Longitudinal Velocity Increment in TGA

Finally, we investigate the conditional longitudinal velocity increment

$$\left\langle \boldsymbol{r}_{12} \cdot [\boldsymbol{u}(\boldsymbol{x}_2) - \boldsymbol{u}(\boldsymbol{x}_1)] \middle| \boldsymbol{\Omega}_1, \, \boldsymbol{\Omega}_2 \right\rangle = -\frac{1}{4\pi} \int \mathrm{d}\boldsymbol{x}_0 \, \boldsymbol{r}_{12} \cdot \left[\left[\frac{\boldsymbol{r}_{02}}{r_{02}^3} - \frac{\boldsymbol{r}_{01}}{r_{01}^3} \right] \times \langle \boldsymbol{\omega}(\boldsymbol{x}_0) | \boldsymbol{\Omega}_1, \, \boldsymbol{\Omega}_2 \rangle \right] . \tag{9.79}$$

For the Gaussian contributions the integrals

$$\begin{aligned} &\left\langle \boldsymbol{r}_{12} \cdot [\boldsymbol{u}(\boldsymbol{x}_2) - \boldsymbol{u}(\boldsymbol{x}_1)] \middle| \boldsymbol{\Omega}_1, \, \boldsymbol{\Omega}_2 \right\rangle_G \\ &\quad = -\frac{1}{4\pi} \int \mathrm{d}\boldsymbol{x}_0 \, \boldsymbol{r}_{12} \cdot \Bigg[\left[\frac{\boldsymbol{r}_{02}}{r_{02}^3} - \frac{\boldsymbol{r}_{01}}{r_{01}^3} \right] \times \Big(\mathcal{R}(\boldsymbol{x}_0, \boldsymbol{x}_1) \left[\mathcal{R}^{-1}(\boldsymbol{x}_1, \boldsymbol{x}_1) \, \boldsymbol{\Omega}_1 + \mathcal{R}^{-1}(\boldsymbol{x}_1, \boldsymbol{x}_2) \, \boldsymbol{\Omega}_2 \right] \\ &\qquad + \mathcal{R}(\boldsymbol{x}_0, \boldsymbol{x}_2) \left[\mathcal{R}^{-1}(\boldsymbol{x}_2, \boldsymbol{x}_1) \, \boldsymbol{\Omega}_1 + \mathcal{R}^{-1}(\boldsymbol{x}_2, \boldsymbol{x}_2) \, \boldsymbol{\Omega}_2 \right] \Big) \Bigg] \end{aligned} \tag{9.80}$$

have to be evaluated. However, with respect to the projection to the plane it is also already clear in this case that Gaussian terms will give no contribution as the integrand changes sign under a simultaneous change of sign of $\boldsymbol{\Omega}_1$ and $\boldsymbol{\Omega}_2$.

For the twisting contribution we have to evaluate

$$\begin{aligned} &\left\langle \boldsymbol{r}_{12} \cdot [\boldsymbol{u}(\boldsymbol{x}_2) - \boldsymbol{u}(\boldsymbol{x}_1)] \middle| \boldsymbol{\Omega}_1, \, \boldsymbol{\Omega}_2 \right\rangle_T \\ &\quad = -\frac{1}{4\pi} \left(\frac{1 - c_\perp}{1 - c_\perp^2} \right) \int \mathrm{d}\boldsymbol{x}_0 \, \boldsymbol{r}_{12} \cdot \left[\left[\frac{\boldsymbol{r}_{02}}{r_{02}^3} - \frac{\boldsymbol{r}_{01}}{r_{01}^3} \right] \times \left[\boldsymbol{T}(\boldsymbol{x}_0, \boldsymbol{x}_1, \boldsymbol{\Omega}_1) + \boldsymbol{T}(\boldsymbol{x}_0, \boldsymbol{x}_2, \boldsymbol{\Omega}_2) \right] \right] \quad , \end{aligned} \tag{9.81}$$

which, similar to the case of the rate-of-strain tensor, cannot be evaluated analytically. However, as in the case above it is possible to introduce two integral tensors

$$I^{\boldsymbol{u},1}_{ijk} = -\frac{1}{4\pi} \int \mathrm{d}\boldsymbol{x}_0 \, c_T(r_{01}) \, \hat{r}_{01,i} \, \hat{r}_{01,j} \, \left[\frac{\boldsymbol{r}_{02}}{r_{02}^3} - \frac{\boldsymbol{r}_{01}}{r_{01}^3} \right]_k \tag{9.82a}$$

$$I^{\boldsymbol{u},2}_{ijk} = -\frac{1}{4\pi} \int \mathrm{d}\boldsymbol{x}_0 \, c_T(r_{02}) \, \hat{r}_{02,i} \, \hat{r}_{02,j} \, \left[\frac{\boldsymbol{r}_{02}}{r_{02}^3} - \frac{\boldsymbol{r}_{01}}{r_{01}^3} \right]_k \quad , \tag{9.82b}$$

by which the whole expression may be written as

$$\begin{aligned}&\left\langle \boldsymbol{r}_{12}\cdot[\boldsymbol{u}(\boldsymbol{x}_2)-\boldsymbol{u}(\boldsymbol{x}_1)]\middle|\boldsymbol{\Omega}_1,\,\boldsymbol{\Omega}_2\right\rangle_T\\&\quad=\left(\frac{1-c_\perp}{1-c_\perp^2}\right)r_{12,l}\left[\widehat{\Omega}_{1,l}\,\widehat{\Omega}_{1,i}\,I^{\boldsymbol{u},1}_{ikk}-\widehat{\Omega}_{1,i}\,\widehat{\Omega}_{1,k}\,I^{\boldsymbol{u},1}_{ilk}+\widehat{\Omega}_{2,l}\,\widehat{\Omega}_{2,i}\,I^{\boldsymbol{u},2}_{ikk}-\widehat{\Omega}_{2,i}\,\widehat{\Omega}_{2,k}\,I^{\boldsymbol{u},2}_{ilk}\right].\end{aligned}\tag{9.83}$$

This expression then can be evaluated again numerically. It can already be seen at this stage that, as the expression does not depend on the magnitude of Ω_1 and Ω_2, the result will differ from our DNS results.

Comparison of TGA and DNS results

We start with a presentation of the terms related to the right-hand side of the kinetic equation (9.8), which are presented for various spatial distances in figure 9.10. At first sight a remarkable qualitative agreement with figures 9.2, 9.3 and 9.4 can be observed. The enstrophy production terms have an amplifying effect, whereas the diffusive terms tend to deplete the enstrophy. As observed in the DNS data, these two contributions cancel to a large extent such that only a small net vector field remains on small scales. This net vector field then vanishes for large spatial distances, where the pointwise conditional balance of enstrophy production and dissipation of the single-point statistics is recovered. That means, the local mechanisms of enstrophy production and dissipation are qualitatively captured by our simple ansatz (9.62). One shortcoming of the model in this context is that projection of the two-point enstrophy production term on the single-point enstrophy production fails, slightly underestimating the correct result. A deeper analytical analysis shows that the projection properties of the conditional averages are related to a subtle cancellation of terms, which is violated by an *ad hoc* introduction of the twist term. The reason for this is that this term is absent in the conditional averages of multivariate Gaussian PDFs. The dissipative terms, however, show the correct reduction properties, as they are calculated from the Gaussian contributions to the conditional vorticity field only.

A more severe shortcoming of the two-point Twisted Gaussian Approximation is that the resulting conditional longitudinal velocity increment is not captured correctly, therefore we refrain from a detailed presentation at this point. While it turns out that for small scales a comparable functional shape as observed in DNS is found, the conditional velocity increment shows a scale-dependent offset. As a result, the integral constraint (9.9) is not fulfilled, such that the simultaneous up- and downscale probability flux is not captured by the model. This is presumably related to the shortcoming regarding the reduction properties of the model ansatz (9.62) and to the fact that the twist contribution does not depend on the magnitude of the two vorticities.

The results seem promising with respect to the decent qualitative agreement of the terms related to enstrophy production and dissipation. It has been shown that the twisted structure of the conditional vorticity field yields reasonable results regarding

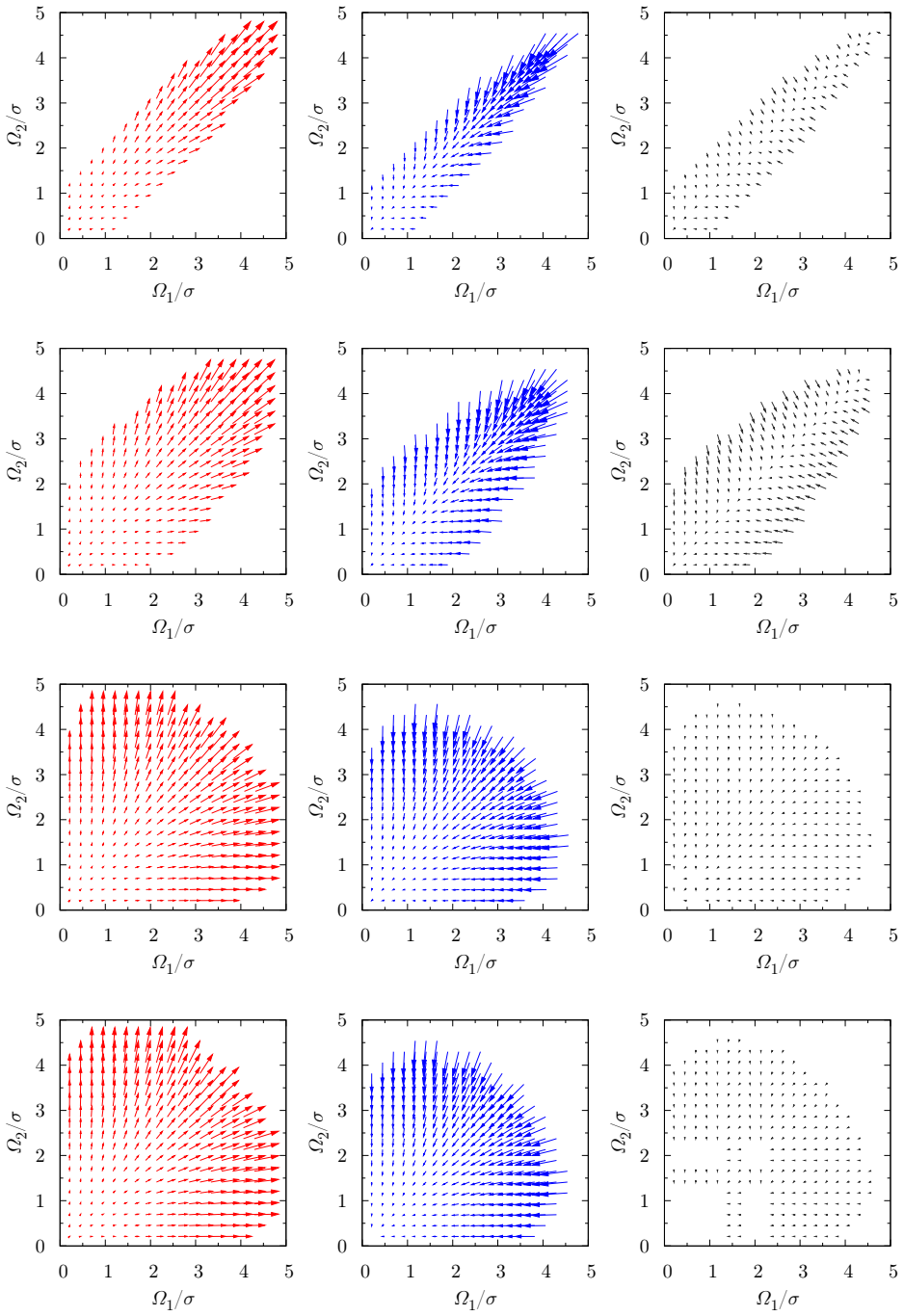

Figure 9.10.: Two-point enstrophy production and dissipation in Twisted Gaussian Approximation for $r \in \{1.2, 2.5, 19.8, 158.3\}\,\eta$.

the enstrophy production also on the two-point level and the Gaussian contribution is responsible for the dissipative contributions. The breakdown of the two-point TGA regarding the velocity increment shows that for an understanding of the probability flux in scale further research on the local conditional structure of turbulence is necessary. In this context an important next step would be to correct the reduction properties of the multi-point TGA.

9.6. Summary

The scope of the present chapter is two-fold. First of all, we have investigated the two-point enstrophy statistics within the framework of the LMN hierarchy both analytically and numerically. Compared to the single-point statistics considered so far, the two-point PDF equation contains a coupling of different spatial scales. An analysis of the equation showed that this probability flux in scale is related to a local imbalance of the conditional two-point enstrophy production and dissipation. Additionally, we have seen that due to an integral constraint a probability flux both up- and downscale is expected. The numerical evaluation of the unclosed terms then has indicated that the production and dissipation terms cancel to a large extent on all scales. However, for small distances the remaining effective vector field is non-vanishing leading to an interesting dynamical evolution in sample space. The investigation provides first insights into the spatial structure of the vorticity statistics, which up to now has only been treated sparsely in the literature. A next step obviously is to gain a deeper qualitative and quantitative understanding of these observations. A first step in this direction was made by introducing a simple ODE system for the characteristic equations, which captures the main topological features of the vector field found in DNS.

We then turned to an investigation of the closure problem in terms of multi-point statistics, which revealed that a closure of the kinetic equations discussed in this chapter involves the analysis of the conditional vorticity field with respect to multiple fixed vorticities. Following works by Novikov, we have investigated the conditional vorticity field both analytically and numerically, revealing that enstrophy production is related to the statistical twist of the conditional vorticity field. Then an extension to multiple points in space has been introduced, allowing for a semi-analytical treatment and a direct comparison to the two-point enstrophy statistics from DNS. The major outcome here is that, while the local dynamical effects of vortex stretching and diffusion of vorticity are qualitatively captured by the model, the probability flux in scale is not. Although oversimplifying assumptions have been made, the complexity of the analytical calculations indicates that an improvement of this simple model remains a challenging task for the future.

10. A Model for the Two-Point PDF of Turbulent Vorticity

10.1. Motivation

We have encountered the closure problem of turbulence in various ways throughout this thesis. It has been discussed in chapters 7 and 8 in terms of correlations between the statistical variable and dynamical influences related to the corresponding equation of motion. Knowledge of these unknown correlations has led to a closure of the kinetic equations determining the shape of the single-point PDF.

In chapter 9 we have then additionally treated the problem in terms of the local conditional structure of the vorticity field. There it became clear that the kinetic equations for the vorticity field can be closed in terms of the first moment of the conditional PDF. However, it has to be stressed that the particular type of kinetic equation considered does not fix the shape of the probability density function.

In the last chapter of this work we want to add yet another aspect to the discussion. To this end we first have to clarify the traditional notion of a closure. Regarding the hierarchy of PDF equations, closure in the traditional sense means to truncate the hierarchy on a given level, say N, by expressing (i.e. modeling) the $N+1$-point PDF in terms of the N-point PDF only. Probably the most simple ansatz for such a closure involves a factorization of the PDF assuming statistical independence of the $N+1$st point from the others. This assumption, however, does not lead to physically reasonable results in the case of strongly interacting systems like fully developed turbulence. A number of more sophisticated approaches have been proposed (see, e.g., [Lun72, TY04] for two different suggestions), the results show some more or less severe discrepancies when compared to experimental results.

It is thus just to ask whether a closure in the traditional sense is possible at all. On the contrary, one could ask, which information from the $N+1$-point PDF has to be incorporated into a model of the N-point PDF to yield a closure. This is exactly the issue discussed in this chapter at the example of the most simple PDF equation describing the single-point statistics of vorticity. Instead of modeling the two-point PDF only with single-point information, we try to incorporate as few information from the two-point PDF as possible in order to achieve a closure of the single-point PDF equation. Our closure shall especially allow to determine the shape of the single-point PDF, which makes clear that specification of the first conditional moment will not suffice. In this sense, the current approach aims at a *best bargain*: if we cannot get the closure for free, what is the minimum price to pay? Consequently, we do not achieve a true closure (in

the traditional sense), but the analysis will elucidate, which features of the two-point PDF play the important role when it comes to determine the single-point statistics.

Apart from the information necessary to close the next lower order of the PDF hierarchy, the multi-point PDFs have to fulfill a number of physical constraints, among which are the *reduction, coincidence* and *separation properties* already introduced in chapter 6. A perfect closure should, of course, fulfill all of these constraints. However, it turns out that for generally non-normal statistics it is hard to analytically specify a joint PDF. This brings up the question how an imperfect model can be improved, which will be treated in the context of a maximum entropy approach.

The remaining chapter is structured as follows. We first will reinvestigate the single-point PDF equation with respect to its coupling to the two-point PDF. This will lead to an analytical model, which then will be compared to DNS data and discussed in terms of its limitations. We will then turn to a generalization involving a maximum entropy formulation of the problem.

10.2. An Analytical Closure Approach

10.2.1. Formulation of the Model

We take the kinetic equation of the form (8.18) as the starting point of our investigations, however, neglecting the external forcing as in the preceding chapter. As has been exposed in chapter 8, this version of the kinetic equation involving the conditional enstrophy dissipation tensor eventually allows to calculate a stationary solution of the form (8.45). For a solution both the eigenvalues of the conditionally averaged rate-of-strain tensor as well as the conditional enstrophy dissipation tensor have to be known. We have seen in the preceding chapter that the scalar function determining the conditional enstrophy production can be calculated from the twisting contribution to the first conditional moment of the vorticity field, see equation (9.33). For the conditional dissipation tensor we consider the relation

$$\begin{aligned}\frac{\partial\omega_{1,i}}{\partial x_{1,k}}\frac{\partial\omega_{1,j}}{\partial x_{1,k}} &= \frac{1}{2}\left[\Delta_{\boldsymbol{x}_1}\,\omega_{1,i}\omega_{1,j} - \omega_{1,j}\,\Delta_{\boldsymbol{x}_1}\,\omega_{1,i} - \omega_{1,i}\,\Delta_{\boldsymbol{x}_1}\,\omega_{1,j}\right] \\ &= \frac{1}{2}\lim_{|\boldsymbol{x}_2-\boldsymbol{x}_1|\to 0}\left[\Delta_{\boldsymbol{x}_2}\,\omega_{2,i}\omega_{2,j} - \omega_{1,j}\,\Delta_{\boldsymbol{x}_2}\,\omega_{2,i} - \omega_{1,i}\,\Delta_{\boldsymbol{x}_2}\,\omega_{2,j}\right] \quad . \end{aligned} \tag{10.1}$$

Multiplying by ν and taking the conditional average results in an expression for the conditional enstrophy dissipation tensor,

$$\begin{aligned}&\left\langle \nu\frac{\partial\omega_{1,i}}{\partial x_{1,k}}\frac{\partial\omega_{1,j}}{\partial x_{1,k}}\middle|\boldsymbol{\Omega}_1\right\rangle \\ &\quad= \frac{1}{2}\nu\lim_{|\boldsymbol{x}_2-\boldsymbol{x}_1|\to 0}\left[\Delta_{\boldsymbol{x}_2}\left\langle\omega_{2,i}\omega_{2,j}\middle|\boldsymbol{\Omega}_1\right\rangle - \Omega_{1,j}\,\Delta_{\boldsymbol{x}_2}\left\langle\omega_{2,i}\middle|\boldsymbol{\Omega}_1\right\rangle - \Omega_{1,i}\,\Delta_{\boldsymbol{x}_2}\left\langle\omega_{2,j}\middle|\boldsymbol{\Omega}_1\right\rangle\right],\end{aligned} \tag{10.2}$$

which shows that this tensor can be calculated from the first and second moment of the conditional PDF $p(\boldsymbol{\Omega}_2|\boldsymbol{\Omega}_1)$. Consequently, specifying the first two conditional moments of the vorticity field suffices to calculate the terms determining the single-point velocity PDF according to the stationary solution (8.45). It has to be stressed, though, that these moments already contain a tremendous amount of information as has been pointed out in the context of the general functional structure of the first conditional moment in chapter 9. Following the analysis presented there, the second conditional moment may be built from δ_{ij} and all possible combinations of $\widehat{\boldsymbol{\Omega}}_1$, $\hat{\boldsymbol{\lambda}}$ and $\hat{\boldsymbol{\tau}}$ weighted by scalar prefactors depending on Ω_1, r and γ. Based on combinatorics only, we count ten possible scalar functions. As a side remark, one should note that the conditional second moment for Gaussian statistics is proportional to δ_{ij} only, demonstrating the simple functional structure of Gaussian statistics.

We now want to put these considerations into the context of the two-point PDF. The only assumption for our ansatz now is that we have a reasonable choice for the first two conditional moments of the vorticity field either by modeling or by knowledge from experiments or numerics. For the sake of brevity, these moments will be denoted as

$$\boldsymbol{\mu}^{(1)}(\boldsymbol{\Omega}_1, \boldsymbol{r}) := \langle \boldsymbol{\omega}_2 | \boldsymbol{\Omega}_1 \rangle \tag{10.3a}$$

$$\mu_{ij}^{(2)}(\boldsymbol{\Omega}_1, \boldsymbol{r}) := \langle \omega_{2,i}\, \omega_{2,j} | \boldsymbol{\Omega}_1 \rangle \quad . \tag{10.3b}$$

Let us from now on assume that the first two conditional moments are given as modeling input from, e.g., DNS data or analytical considerations. The first important thing to note is that parts of the desired constraints can be incorporated into the model by the limiting behavior of the conditional moments. For vanishing and infinite distances the moments behave like

$$\lim_{r\to 0} \boldsymbol{\mu}^{(1)}(\boldsymbol{\Omega}_1, \boldsymbol{r}) = \boldsymbol{\Omega}_1 \tag{10.4a}$$

$$\lim_{r\to 0} \mu_{ij}^{(2)}(\boldsymbol{\Omega}_1, \boldsymbol{r}) = 0 \tag{10.4b}$$

$$\lim_{r\to \infty} \boldsymbol{\mu}^{(1)}(\boldsymbol{\Omega}_1, \boldsymbol{r}) = \langle \boldsymbol{\omega}_2 \rangle = \mathbf{0} =: \boldsymbol{\mu}_\infty^{(1)} \tag{10.4c}$$

$$\lim_{r\to \infty} \mu_{ij}^{(2)}(\boldsymbol{\Omega}_1, \boldsymbol{r}) = \langle \omega_{2,i}\, \omega_{2,j} \rangle = \frac{\langle \boldsymbol{\omega}^2 \rangle}{3} \delta_{ij} =: \mu_{ij,\infty}^{(2)} \quad . \tag{10.4d}$$

The ansatz for our two-point model now consists of the product of two hitherto unspecified single-point PDFs f_1^{M}

$$f_2^{\mathrm{M}}(\boldsymbol{\Omega}_1, \boldsymbol{\Omega}_2; \boldsymbol{r}) = f_1^{\mathrm{M}}\big(\boldsymbol{\Omega}_2; \boldsymbol{\mu}^{(1)}, \mu_{ij}^{(2)}\big)\, f_1^{\mathrm{M}}\big(\boldsymbol{\Omega}_1; \boldsymbol{\mu}_\infty^{(1)}, \mu_{ij,\infty}^{(2)}\big) \quad , \tag{10.5}$$

of which the first one is shifted and rescaled according to the first two conditional moments. By this choice the first factor represents a model for the conditional PDF $p(\boldsymbol{\Omega}_2|\boldsymbol{\Omega}_1)$, whereas the second one just plays the role of the single-point PDF. By

construction, the first two conditional moments are readily obtained as

$$\left\langle \boldsymbol{\omega}_2 \middle| \boldsymbol{\Omega}_1, \boldsymbol{\Omega}_2 \right\rangle = \int \mathrm{d}\boldsymbol{\Omega}_2 \, \boldsymbol{\Omega}_2 \, f_1^{\mathrm{M}}\big(\boldsymbol{\Omega}_2; \boldsymbol{\mu}^{(1)}, \mu_{ij}^{(2)}\big) \tag{10.6a}$$

$$\left\langle \omega_{2,i}\omega_{2,j} \middle| \boldsymbol{\Omega}_1, \boldsymbol{\Omega}_2 \right\rangle = \int \mathrm{d}\boldsymbol{\Omega} \, \Omega_{2,i} \, \Omega_{2,j} \, f_1^{\mathrm{M}}\big(\boldsymbol{\Omega}_2; \boldsymbol{\mu}^{(1)}, \mu_{ij}^{(2)}\big) \quad . \tag{10.6b}$$

As it is further possible to calculate the conditional enstrophy production as well as the eigenvalues of the conditional dissipation tensor from the first two conditional moments, it is also possible to determine the shape of the single-point PDF with the help of equation (8.45). This lets us determine the up to now unspecified single-point PDF f_1^{M}. We thus have constructed a consistent model of the two-point PDF, which closes the single-point PDF equation and additionally allows to determine the single-point PDF in a correct manner.

To check for the *coincidence* and *separation property*, we recognize

$$\lim_{r\to 0} f_2^{\mathrm{M}}(\boldsymbol{\Omega}_1, \boldsymbol{\Omega}_2; \boldsymbol{r}) = \delta(\boldsymbol{\Omega}_2 - \boldsymbol{\Omega}_1) \, f_1^{\mathrm{M}}\big(\boldsymbol{\Omega}_2; \boldsymbol{\mu}_\infty^{(1)}, \mu_{ij,\infty}^{(2)}\big) \tag{10.7a}$$

$$\lim_{r\to \infty} f_2^{\mathrm{M}}(\boldsymbol{\Omega}_1, \boldsymbol{\Omega}_2; \boldsymbol{r}) = f_1^{\mathrm{M}}\big(\boldsymbol{\Omega}_1; \boldsymbol{\mu}_\infty^{(1)}, \mu_{ij,\infty}^{(2)}\big) \, f_1^{\mathrm{M}}\big(\boldsymbol{\Omega}_2; \boldsymbol{\mu}_\infty, \mu_{ij,\infty}^{(2)}\big) \quad . \tag{10.7b}$$

The *coincidence property* results from the fact that by the limiting behavior according to the relations (10.4) the conditional PDF shrinks toward zero variance, which under quite general assumptions can be represented by a delta distribution. The reduction property is fulfilled identically for the variable $\boldsymbol{\Omega}_2$,

$$\int \mathrm{d}\boldsymbol{\Omega}_2 \, f_1^{\mathrm{M}}\big(\boldsymbol{\Omega}_2; \boldsymbol{\mu}^{(1)}, \mu_{ij}^{(2)}\big) \, f_1^{\mathrm{M}}\big(\boldsymbol{\Omega}_1; \boldsymbol{\mu}_\infty^{(1)}, \mu_{ij,\infty}^{(2)}\big) = f_1^{\mathrm{M}}\big(\boldsymbol{\Omega}_1; \boldsymbol{\mu}_\infty^{(1)}, \mu_{ij,\infty}^{(2)}\big) \tag{10.8}$$

as this only requires normalization of the conditional PDF. However, the reduction property with respect to $\boldsymbol{\Omega}_1$ will only be fulfilled approximately to the extent the modeled conditional PDF will resemble the true one. Note that the ansatz works perfectly in the limit of vanishing and infinite separations, where it also obeys the correct *reduction property*. One should also note that the ansatz is fully consistent in the case of Gaussian two-point statistics, where the *reduction property* is fulfilled for arbitrary separations.

Another shortcoming of this ansatz concerns its asymmetry with respect to the exchange of $\boldsymbol{\Omega}_1$ and $\boldsymbol{\Omega}_2$ to be expected in the general case, which is clearly unphysical for homogeneous isotropic turbulence. Still, the simplicity of the ansatz together with the number of fulfilled properties seems promising and we now want to compare it to DNS results, before we discuss possible generalizations.

10.2.2. Comparison with DNS Data

As already discussed in the preceding chapter, a numerical evaluation and presentation of the full two-point PDF is impossible. For a comparison with the DNS data we therefore focus on the joint statistics of a component of the vorticity field at two distant spatial

points. The data is taken from the simulation `sim_512`. As the conceptual approach outlined above allows to fix the shape of the single-point PDF, we take knowledge of the first two conditional moments of the projected PDF as well as the single-point PDF itself for granted and evaluate equation (10.5) numerically. To this end we construct the conditional PDF $p^{\mathrm{M}}(\Omega_{2,x}|\Omega_{1,x}, r)$ from the single-point PDF $f_1(\Omega_{1,x})$ by a proper shifting and rescaling according to the first two conditional moments.

The resulting conditional PDFs are shown as a function of scale in figures 10.1 and 10.2 along with reference PDFs from DNS. For small as well as large spatial separations the agreement is best. The reason for this is that the model ansatz (10.5) by definition is exact in the two limiting cases. For intermediate separations a still moderate agreement is observable, the qualitative features of the PDF are captured. In view of the simplicity of the ansatz this result may be regarded as satisfactory.

To further quantify the performance of the model, the reduction property in the variable $\Omega_{2,x}$ is compared to the correct single-point PDF in figure 10.3. Although the reduction property in this direction does not hold by construction, the agreement still is very good for low to intermediate values of vorticity. Deviations are only visible in the tails of the PDF. The reason for this is that the imperfections of the model seem to cancel to a certain extent leading to a decent agreement with the true PDF. Maybe the most severe shortcoming from the model may be seen from figure 10.4, where the joint PDF is compared to the corresponding PDF from DNS. While the PDF from DNS is symmetric under the transformations $\Omega_{1,x} \leftrightarrow \Omega_{2,x}$ as well as $\Omega_{1,x} \leftrightarrow -\Omega_{2,x}$, the model PDF is not. The reason for this is the asymmetry of the ansatz (10.5). So the conclusion at this point is that the simple ansatz yields reasonable results regarding the modeling of the conditional PDF with shortcomings becoming especially apparent when the joint PDF is considered.

10.3. Improvement of Imperfect Models

10.3.1. Concept

If one now wishes to overcome the discussed shortcomings, the analytical possibilities are limited. One could, e.g., symmetrize the ansatz (10.5), but then would loose the correct reduction property also in the variable $\boldsymbol{\Omega}_1$.

One would rather like to take the imperfect model as a starting point and improve it, such that the yet missing constraints are fulfilled. Thus we end up with the quite general conceptual problem that we want to improve an imperfect model for a joint PDF with respect to a number of constraints. The improved model should be "as near as possible" to the already established one, at best obtained from the imperfect model by multiplication with a *correction factor*. A mathematical formulation of these desired properties naturally leads to the relative entropy or Kullback-Leibler divergence which

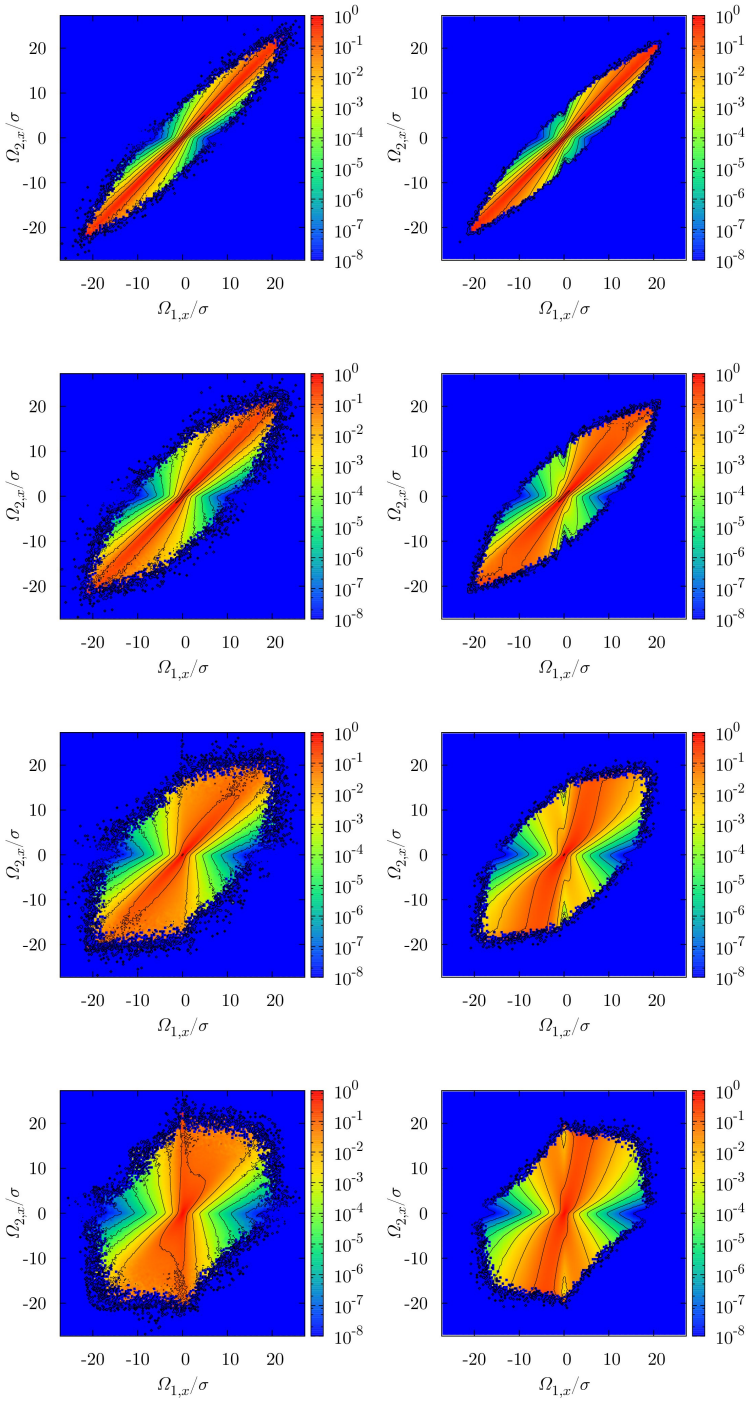

Figure 10.1.: Original (left) and model (right) conditional PDF for $r \in \{1.2, 2.5, 4.9, 9.9\}\eta$ (`sim_512`).

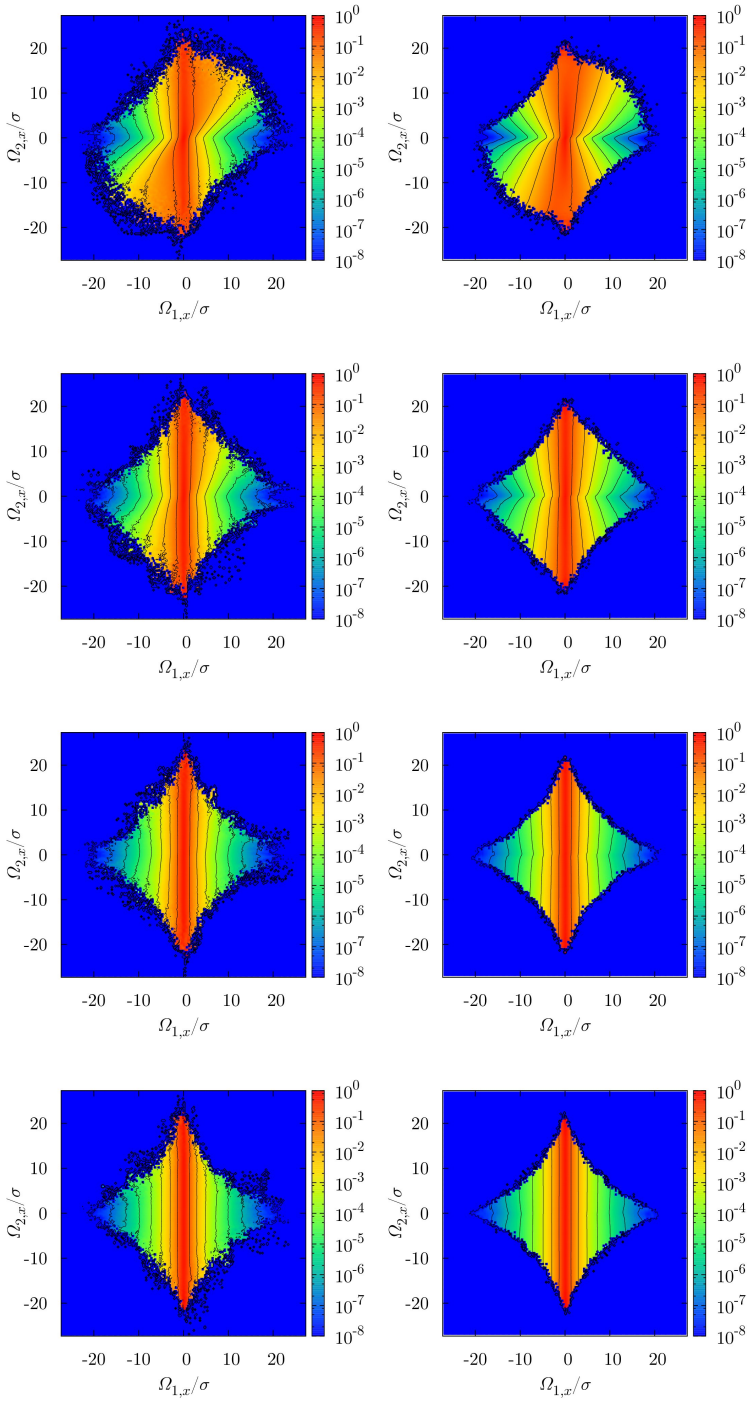

Figure 10.2.: Original (left) and model (right) conditional PDF for $r \in \{19.8, 39.6, 79.1, 158.3\}\eta$ (`sim_512`).

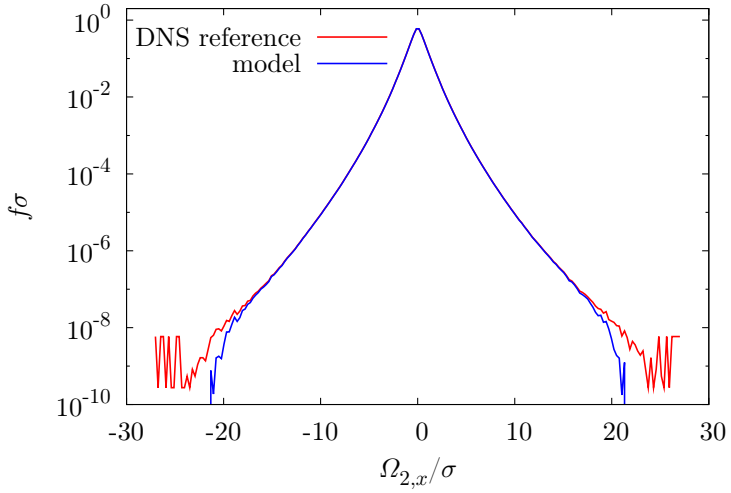

Figure 10.3.: Single-point PDF $f(\Omega_{2,x})$ for DNS data and the two-point model for $r = 2.5\eta$ (`sim_512`). Slight deviations occur in the tails of the PDF.

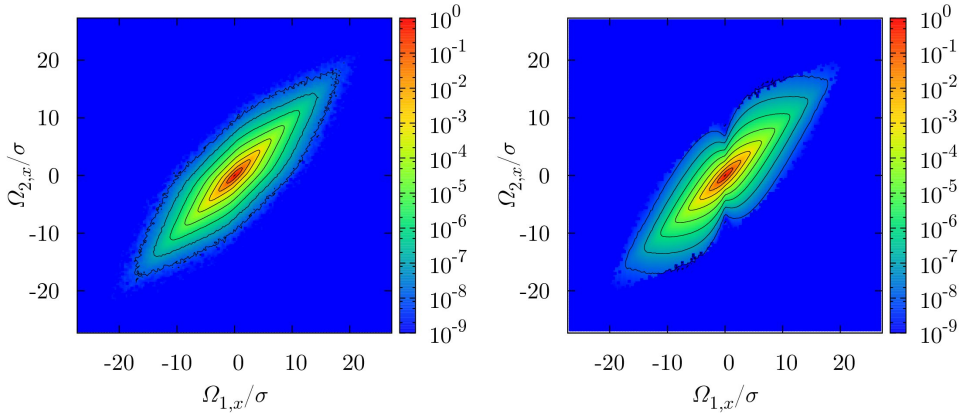

Figure 10.4.: Joint PDF for $r = 2.5\eta$ of DNS data (left) and the two-point model (right) (`sim_512`). The PDF estimated from DNS is symmetric in its arguments, which is not the case for the model PDF.

is defined as[1]

$$\mathcal{K}[f_2^{\mathrm{IM}}] = \int \mathrm{d}\boldsymbol{\Omega}_1\, \mathrm{d}\boldsymbol{\Omega}_2\, f_2^{\mathrm{IM}}(\boldsymbol{\Omega}_1, \boldsymbol{\Omega}_2) \ln \left[\frac{f_2^{\mathrm{IM}}(\boldsymbol{\Omega}_1, \boldsymbol{\Omega}_2)}{f_2^{\mathrm{M}}(\boldsymbol{\Omega}_1, \boldsymbol{\Omega}_2)} \right] \quad . \tag{10.9}$$

Here, f_2^{IM} defines the improved model. It is clear from the definition that the relative entropy shares some similarities with a distance measure [Hak06]. For instance, it is always positive or zero, of which the latter corresponds to the case that $f_2^{\mathrm{M}} = f_2^{\mathrm{IM}}$, i.e., that the imperfect and improved model already coincide. A difference to a true distance measure is that the relative entropy is not symmetric with respect to an exchange of f_2^{M} and f_2^{IM}. The relative entropy now shall be minimized in terms of a number of constraints, which are formulated in terms of the true PDF f_2. So the general situation is that we have a prior, imperfect model PDF f_2^{M}, that we want to improve to a PDF f_2^{IM}, which incorporates a number of features known from the true statistics described by f_2.

To proceed, we first have to list all desired properties in terms of functional constraints. We start with the constraints imposing the correct marginal distributions, i.e., incorporating the *reduction property*, as well as the first two conditional moments. These can be formulated as

$$\int \mathrm{d}\boldsymbol{\Omega}_2\, f_2^{\mathrm{IM}}(\boldsymbol{\Omega}_1, \boldsymbol{\Omega}_2; \boldsymbol{r}) - f_1(\boldsymbol{\Omega}_1) = 0 \tag{10.10a}$$

$$\int \mathrm{d}\boldsymbol{\Omega}_1\, f_2^{\mathrm{IM}}(\boldsymbol{\Omega}_1, \boldsymbol{\Omega}_2; \boldsymbol{r}) - f_1(\boldsymbol{\Omega}_2) = 0 \tag{10.10b}$$

$$\int \mathrm{d}\boldsymbol{\Omega}_2\, \Omega_{2,i}\, f_2^{\mathrm{IM}}(\boldsymbol{\Omega}_1, \boldsymbol{\Omega}_2; \boldsymbol{r}) - \mu_i^{(1)}(\boldsymbol{\Omega}_1; \boldsymbol{r}) f_1(\boldsymbol{\Omega}_1) = 0 \tag{10.10c}$$

$$\int \mathrm{d}\boldsymbol{\Omega}_1\, \Omega_{1,i}\, f_2^{\mathrm{IM}}(\boldsymbol{\Omega}_1, \boldsymbol{\Omega}_2; \boldsymbol{r}) - \mu_i^{(1)}(\boldsymbol{\Omega}_2; \boldsymbol{r}) f_1(\boldsymbol{\Omega}_2) = 0 \tag{10.10d}$$

$$\int \mathrm{d}\boldsymbol{\Omega}_2\, \Omega_{2,i}\Omega_{2,j}\, f_2^{\mathrm{IM}}(\boldsymbol{\Omega}_1, \boldsymbol{\Omega}_2; \boldsymbol{r}) - \mu_{ij}^{(2)}(\boldsymbol{\Omega}_1; \boldsymbol{r}) f_1(\boldsymbol{\Omega}_1) = 0 \tag{10.10e}$$

$$\int \mathrm{d}\boldsymbol{\Omega}_1\, \Omega_{1,i}\Omega_{1,j}\, f_2^{\mathrm{IM}}(\boldsymbol{\Omega}_1, \boldsymbol{\Omega}_2; \boldsymbol{r}) - \mu_{ij}^{(2)}(\boldsymbol{\Omega}_2; \boldsymbol{r}) f_1(\boldsymbol{\Omega}_2) = 0 \quad . \tag{10.10f}$$

Of course, the improved model should also be normalized,

$$\int \mathrm{d}\boldsymbol{\Omega}_1 \mathrm{d}\boldsymbol{\Omega}_2\, f_2^{\mathrm{IM}}(\boldsymbol{\Omega}_1, \boldsymbol{\Omega}_2; \boldsymbol{r}) - 1 = 0 \quad . \tag{10.11}$$

As we will discuss below, an additional class of constraints may be deduced from the fact that we want to represent homogeneous isotropic turbulence. For example, it turns out that the two-point vorticity PDF should be invariant with respect to an exchange of arguments according to

$$f_2^{\mathrm{IM}}(\boldsymbol{\Omega}_1, \boldsymbol{\Omega}_2; \boldsymbol{r}) - f_2^{\mathrm{IM}}(\boldsymbol{\Omega}_2, \boldsymbol{\Omega}_1; \boldsymbol{r}) = 0 \quad . \tag{10.12}$$

[1] The definitions of the entropy as well as the relative entropy usually include an additional sign. In this chapter we will, however, also loosely speak of the Kullback-Leibler divergence as a relative entropy.

Although there are more symmetry constraints, this one shall suffice for the moment to clarify the procedure. Finding the minimum Kullback-Leibler divergence with respect to these constraints naturally introduces the method of Lagrange multipliers. As all of the constraints, except for the normalization, are functions, the corresponding multipliers will be functions, too. Hence the task is to minimize the Kullback-Leibler distance with respect to these constraints, i.e., we have to minimize the relative entropy functional

$$
\begin{aligned}
&\mathcal{K}_c[f_2^{\mathrm{IM}}] = \\
&\int \mathrm{d}\boldsymbol{\Omega}_1\, \mathrm{d}\boldsymbol{\Omega}_2\, f_2^{\mathrm{IM}}(\boldsymbol{\Omega}_1, \boldsymbol{\Omega}_2) \ln\left[\frac{f_2^{\mathrm{IM}}(\boldsymbol{\Omega}_1, \boldsymbol{\Omega}_2)}{f_2^{\mathrm{M}}(\boldsymbol{\Omega}_1, \boldsymbol{\Omega}_2)}\right] \\
&+ \lambda^N \left[\int \mathrm{d}\boldsymbol{\Omega}_1 \mathrm{d}\boldsymbol{\Omega}_2\, f_2^{\mathrm{IM}}(\boldsymbol{\Omega}_1, \boldsymbol{\Omega}_2; \boldsymbol{r}) - 1\right] \\
&+ \int \mathrm{d}\boldsymbol{\Omega}_1\, \lambda^{1,0}(\boldsymbol{\Omega}_1)\left[\int \mathrm{d}\boldsymbol{\Omega}_2\, f_2^{\mathrm{IM}}(\boldsymbol{\Omega}_1, \boldsymbol{\Omega}_2; \boldsymbol{r}) - f_1(\boldsymbol{\Omega}_1)\right] \\
&+ \int \mathrm{d}\boldsymbol{\Omega}_2\, \lambda^{2,0}(\boldsymbol{\Omega}_2)\left[\int \mathrm{d}\boldsymbol{\Omega}_1\, f_2^{\mathrm{IM}}(\boldsymbol{\Omega}_1, \boldsymbol{\Omega}_2; \boldsymbol{r}) - f_1(\boldsymbol{\Omega}_2)\right] \\
&+ \int \mathrm{d}\boldsymbol{\Omega}_1\, \lambda_i^{1,1}(\boldsymbol{\Omega}_1)\left[\int \mathrm{d}\boldsymbol{\Omega}_2\, \Omega_{2,i}\, f_2^{\mathrm{IM}}(\boldsymbol{\Omega}_1, \boldsymbol{\Omega}_2; \boldsymbol{r}) - \mu_i(\boldsymbol{\Omega}_1; \boldsymbol{r}) f_1(\boldsymbol{\Omega}_1)\right] \\
&+ \int \mathrm{d}\boldsymbol{\Omega}_2\, \lambda_i^{2,1}(\boldsymbol{\Omega}_2)\left[\int \mathrm{d}\boldsymbol{\Omega}_1\, \Omega_{1,i}\, f_2^{\mathrm{IM}}(\boldsymbol{\Omega}_1, \boldsymbol{\Omega}_2; \boldsymbol{r}) - \mu_i(\boldsymbol{\Omega}_2; \boldsymbol{r}) f_1(\boldsymbol{\Omega}_2)\right] \\
&+ \int \mathrm{d}\boldsymbol{\Omega}_1\, \lambda_{i,j}^{1,2}(\boldsymbol{\Omega}_1)\left[\int \mathrm{d}\boldsymbol{\Omega}_2\, \Omega_{2,i}\Omega_{2,j}\, f_2^{\mathrm{IM}}(\boldsymbol{\Omega}_1, \boldsymbol{\Omega}_2; \boldsymbol{r}) - \mu_{ij}^{(2)}(\boldsymbol{\Omega}_2; \boldsymbol{r}) f_1(\boldsymbol{\Omega}_1)\right] \\
&+ \int \mathrm{d}\boldsymbol{\Omega}_2\, \lambda_{i,j}^{2,2}(\boldsymbol{\Omega}_2)\left[\int \mathrm{d}\boldsymbol{\Omega}_1\, \Omega_{1,i}\Omega_{1,j}\, f_2^{\mathrm{IM}}(\boldsymbol{\Omega}_1, \boldsymbol{\Omega}_2; \boldsymbol{r}) - \mu_{ij}^{(2)}(\boldsymbol{\Omega}_1; \boldsymbol{r}) f_1(\boldsymbol{\Omega}_2)\right] \\
&+ \int \mathrm{d}\boldsymbol{\Omega}_1\, \mathrm{d}\boldsymbol{\Omega}_2\, \lambda^s(\boldsymbol{\Omega}_1, \boldsymbol{\Omega}_2)\left[f_2^{\mathrm{IM}}(\boldsymbol{\Omega}_1, \boldsymbol{\Omega}_2; \boldsymbol{r}) - f_2^{\mathrm{IM}}(\boldsymbol{\Omega}_2, \boldsymbol{\Omega}_1; \boldsymbol{r})\right] \quad , \qquad (10.13)
\end{aligned}
$$

by which we also have introduced the functional Lagrange multipliers. To find an expression for the improved model, we calculate the functional derivative of the constrained relative entropy functional with respect to the improved model PDF and set it to zero,

$$
\frac{\delta \mathcal{K}_c[f_2^{\mathrm{IM}}](\boldsymbol{\Omega}_1, \boldsymbol{\Omega}_2)}{\delta f_2^{\mathrm{IM}}(\boldsymbol{\Omega}_1', \boldsymbol{\Omega}_2')} = 0 \quad , \qquad (10.14)
$$

which leads to the interesting result

$$
\begin{aligned}
f_2^{\mathrm{IM}}(\boldsymbol{\Omega}_1, \boldsymbol{\Omega}_2) = f_2^{\mathrm{M}}(\boldsymbol{\Omega}_1, \boldsymbol{\Omega}_2) \times \\
\exp\Big[& -\lambda^N - 1 - \lambda^{1,0}(\boldsymbol{\Omega}_1) - \lambda^{2,0}(\boldsymbol{\Omega}_2) \\
& - \Omega_{2,i}\, \lambda_i^{1,1}(\boldsymbol{\Omega}_1) - \Omega_{1,i}\, \lambda_i^{2,1}(\boldsymbol{\Omega}_2) \\
& - \Omega_{2,i}\Omega_{2,j}\, \lambda_{ij}^{1,2}(\boldsymbol{\Omega}_1) - \Omega_{1,i}\Omega_{1,j}\, \lambda_{i,j}^{2,2}(\boldsymbol{\Omega}_2) \\
& - \big[\lambda^s(\boldsymbol{\Omega}_1, \boldsymbol{\Omega}_2) - \lambda^s(\boldsymbol{\Omega}_2, \boldsymbol{\Omega}_1)\big] \Big] \quad . \qquad (10.15)
\end{aligned}
$$

This is exactly the formulation for an improved model outlined at the beginning of this section. The new, improved model is obtained from the old model by multiplication with a correction that ensures compliance with the imposed constraints. Having arrived at this central theoretical result, some further comments are in order.

First of all, it is *a priori* not clear if a minimum of this functional exists for a given situation. This surely depends on the particular choice of the model PDF to be improved as well as on the imposed constraints. Thus it is impossible for us to answer this question on a general level. However, if one, for example, considers a model PDF which assigns zero probability to a given combination of $\boldsymbol{\Omega}_1$ and $\boldsymbol{\Omega}_2$ in sample space, which is not consistent with the imposed constraints, it is clear that the correction factor cannot correct for this. This shows that an inappropriate model PDF as a starting point will yield no solution of the problem. The second interesting fact about these results concerns the particular choice of the model. Consider the case that we do not have an old model based on prior considerations. This corresponds to assume a uniform density for f_2^{M}. In this case the whole approach reduces from a maximum *relative* entropy approach to the standard maximum entropy approach (up to a sign) [Jay57a, Jay57b, Jay03]. As a result equation (10.15) then contains only the correction factor, which defines the PDF. This shows in particular that the possible functional classes of the resulting PDF depend heavily on the type of imposed constraints.[2]

The third, and maybe most important point in this context is that the method of Lagrange multipliers yields the general result (10.15), which expresses the improved model PDF in terms of the functional Lagrange multipliers. However, it does not give a constructive procedure to actually calculate them. In general it will be difficult, if not impossible, to obtain the Lagrange multipliers analytically. Thus we will outline an iterative way to numerically obtain the Lagrange multipliers below.

In some limiting cases, however, analytical solutions are at hand. Consider, for example, the case of infinite spatial separations, in which the two-point statistics factorizes. In this case our simple model ansatz suggests the correct results

$$
\lim_{r\to\infty} f_2^{\mathrm{M}}(\boldsymbol{\Omega}_1, \boldsymbol{\Omega}_2; \boldsymbol{r}) = f_1(\boldsymbol{\Omega}_1)\, f_1(\boldsymbol{\Omega}_2) \qquad (10.16)
$$

[2] Compare this to the ordinary moment maximum entropy problem for a univariate PDF, where the result always is an exponential of a polynomial.

and therefore already fulfills all the imposed functional constraints. As a consequence all the Lagrange multipliers are zero yielding a unit correction factor. In this case the improved model already coincides with the simple model. This can also be stated in the opposite case of vanishing spatial separation, in which the simple model ansatz yields

$$\lim_{r\to 0} f_2^{\mathrm{M}}(\boldsymbol{\Omega}_1, \boldsymbol{\Omega}_2; \boldsymbol{r}) = \delta(\boldsymbol{\Omega}_2 - \boldsymbol{\Omega}_1)\, f_1(\boldsymbol{\Omega}_2) \quad . \tag{10.17}$$

A general feature of this whole approach is that, when the original model already fulfills a number of constraints, these will not lead to further corrections.

We close the section with a more general, but non-trivial example, where we assume a uniformly distributed prior model, that means we are considering the standard maximum entropy approach. If we impose the two marginal PDFs as the only constraints, it can be seen directly from (10.15) that the two corresponding Lagrange multipliers read

$$\lambda^{1,0}(\boldsymbol{\Omega}_1) = \ln f_1(\boldsymbol{\Omega}_1) \tag{10.18a}$$

$$\lambda^{2,0}(\boldsymbol{\Omega}_2) = \ln f_1(\boldsymbol{\Omega}_2) \quad , \tag{10.18b}$$

which leads to

$$f_2^{\mathrm{IM}} = f_1(\boldsymbol{\Omega}_1)\, f_1(\boldsymbol{\Omega}_2) \quad , \tag{10.19}$$

i.e., the maximum entropy approach here leads to statistical independence of $\boldsymbol{\Omega}_1$ and $\boldsymbol{\Omega}_2$, something very reasonable.

10.3.2. More on Symmetry Constraints

In the above discussion we have already included a symmetry constraint which should be fulfilled by an improved model. This naturally brings up the question what type of symmetries are expected for a joint PDF and how to find them. As highlighted a number of times throughout this thesis, these symmetry constraints originate from the fact that statistical observables of fully developed, stationary, homogeneous isotropic turbulence are invariant with respect to transformations from the symmetry group O(3), i.e.,

$$f_2(\boldsymbol{\Omega}_1, \boldsymbol{\Omega}_2; \boldsymbol{r}) = f_2(\mathrm{R}\boldsymbol{\Omega}_1, \mathrm{R}\boldsymbol{\Omega}_2; \mathrm{R}\boldsymbol{r}) \quad \forall\, \mathrm{R} \in \mathrm{O}(3) \quad . \tag{10.20}$$

Now choosing a special transformation from this group corresponding to, e.g., an exchange of certain components of the arguments, reveals a particular symmetry expected from the PDF. For example, any transformation turning $\boldsymbol{r} = \boldsymbol{x}_2 - \boldsymbol{x}_1$ to $-\boldsymbol{r} = \boldsymbol{x}_1 - \boldsymbol{x}_2$ is equivalent to an exchange of coordinates $\boldsymbol{x}_1$ and $\boldsymbol{x}_2$.

These considerations are especially of interest, when projections of the full two-point PDF are considered as in the numerical data presented in this chapter. Without loss of generality, we take in the following $\boldsymbol{r} = r\boldsymbol{e}_x$. Consider, for example, the PDF $f_2(\Omega_{1x}, \Omega_{2x}; r)$ subject to a rotation $\mathrm{R}_y(\pi)$ around the y-axis with an angle of π. This yields

$$f_2(\Omega_{1x}, \Omega_{2x}; \boldsymbol{r}) = f_2(-\Omega_{1x}, -\Omega_{2x}; -\boldsymbol{r}) = f_2(-\Omega_{2x}, -\Omega_{1x}; \boldsymbol{r}) \quad , \tag{10.21}$$

transformation	transformed $\boldsymbol{\Omega}$	transformed $\boldsymbol{v}$	sign of $\boldsymbol{r}$
$\mathrm{R}_x(\pi)$	$(\Omega_x, -\Omega_y, -\Omega_z)$	$(v_x, -v_y, -v_z)$	+
$\mathrm{R}_x(\frac{\pi}{2})$	$(\Omega_x, -\Omega_z, \Omega_y)$	$(v_x, -v_z, v_y)$	+
$\mathrm{R}_x(-\frac{\pi}{2})$	$(\Omega_x, \Omega_z, -\Omega_y)$	$(v_x, v_z, -v_y)$	+
$\mathrm{R}_y(\pi)$	$(-\Omega_x, \Omega_y, -\Omega_z)$	$(-v_x, v_y, -v_z)$	-
$\mathrm{R}_z(\pi)$	$(-\Omega_x, -\Omega_y, \Omega_z)$	$(-v_x, -v_y, v_z)$	-
reflection in $\mathbf{0}$	$(\Omega_x, \Omega_y, \Omega_z)$	$(-v_x, -v_y, -v_z)$	-

Table 10.1.: Transformation properties of vorticity and velocity under rotation and inversion.

where the first equality comes from isotropy and the second from the above exchange argument. This symmetry can immediately be checked with numerical or experimental data and may serve as a test for the fulfillment of isotropy.

To find further symmetries, we now consider transformations that map coordinate axes on coordinate axes. A number of examples are listed in tabular 10.1. By projecting onto the components of interest, the expected symmetries can be obtained. These considerations also directly show that longitudinal and transversal components display different transformation properties. Additionally, the inversion symmetry yields an interesting result when vorticity and velocity are compared. Due to the pseudo-vector character of the vorticity the transformation property differs from the velocity under reflection. This implies

$$f(\Omega_{1x}, \Omega_{2x}; \boldsymbol{r}) = f(\Omega_{2x}, \Omega_{1x}; \boldsymbol{r}) \quad , \tag{10.22}$$

a symmetry not present for the corresponding velocity PDF.

10.3.3. Outline of an Iterative Method: A Steepest Descent Algorithm

To obtain the Lagrange multipliers iteratively, the problem may be regarded as an optimization problem, for which a large number of algorithms exist. We here outline a steepest descent algorithm, which turns out to be particularly simple. In principle Newton methods outperform steepest descent approaches with respect to stability and rate of convergence, however, these methods involve matrix inversions. As we are dealing with a functional problem here, where the discretized PDFs are sampled on $\mathcal{O}(100)$ grid points, this quickly leads to numerically demanding problems depending on the number and type of constraints imposed. That is why a steepest descent algorithm, where only a gradient has to be evaluated, is chosen here.

We start with the definition

$$\mathcal{Z}[\boldsymbol{\lambda}] = \int \mathrm{d}\boldsymbol{\Omega}_1 \, \mathrm{d}\boldsymbol{\Omega}_2 \, f_2^{\mathrm{IM}}(\boldsymbol{\Omega}_1, \boldsymbol{\Omega}_2; \boldsymbol{r}) \quad , \tag{10.23}$$

which in some sense resembles the partition function known from statistical mechanics. To perform a descent, we have to define a potential, which is introduced as

$$\begin{aligned}\mathcal{F}[\boldsymbol{\lambda}] = &- \mathcal{Z}[\boldsymbol{\lambda}] - \lambda_N - \int \mathrm{d}\boldsymbol{\Omega}_1\, \lambda^{1,0}(\boldsymbol{\Omega}_1)\, f_1(\boldsymbol{\Omega}_1) - \int \mathrm{d}\boldsymbol{\Omega}_2\, \lambda^{2,0}(\boldsymbol{\Omega}_2)\, f_1(\boldsymbol{\Omega}_2) \\ &- \int \mathrm{d}\boldsymbol{\Omega}_1\, \lambda_i^{1,1}(\boldsymbol{\Omega}_1)\, \mu_i^{(1)}(\boldsymbol{\Omega}_1)\, f_1(\boldsymbol{\Omega}_1) - \int \mathrm{d}\boldsymbol{\Omega}_2\, \lambda_i^{2,1}(\boldsymbol{\Omega}_2)\, \mu_i^{(1)}(\boldsymbol{\Omega}_2)\, f_1(\boldsymbol{\Omega}_2) \\ &- \int \mathrm{d}\boldsymbol{\Omega}_1\, \lambda_{ij}^{1,2}(\boldsymbol{\Omega}_1)\, \mu_{ij}^{(2)}(\boldsymbol{\Omega}_1; \boldsymbol{r})\, f_1(\boldsymbol{\Omega}_1) \\ &- \int \mathrm{d}\boldsymbol{\Omega}_2\, \lambda_{ij}^{2,2}(\boldsymbol{\Omega}_2)\, \mu_{ij}^{(2)}(\boldsymbol{\Omega}_2)\, f_1(\boldsymbol{\Omega}_2) \quad , \end{aligned} \tag{10.24}$$

where $[\boldsymbol{\lambda}]$ indicates the functional dependence on the set of Lagrange multipliers. The important property of this functional now is that calculating the functional gradient of this potential readily gives the constraints. We obtain, for example,

$$\frac{\delta \mathcal{F}[\boldsymbol{\lambda}](\boldsymbol{\Omega}_1')}{\delta \lambda^{1,0}(\boldsymbol{\Omega}_1)} = \int \mathrm{d}\boldsymbol{\Omega}_2\, f_2^{\mathrm{IM}}(\boldsymbol{\Omega}_1, \boldsymbol{\Omega}_2) - f_1(\boldsymbol{\Omega}_1) \quad , \tag{10.25}$$

for which we have made use of equation (10.15). As a consequence when

$$\nabla_{\boldsymbol{\lambda}} \mathcal{F}[\boldsymbol{\lambda}] = \mathbf{0} \quad , \tag{10.26}$$

we have reached a local extremum of this potential corresponding to the fulfillment of all imposed constraints.

The numerical implementation then is straightforward. Starting with f_2^{M} as an initial guess, we calculate the gradient, which is the difference between the evaluated constraints based on the current estimate for the $\boldsymbol{\lambda}$ (which are chosen to be zero initially) and the reference constraints. We then update the Lagrange multipliers according to

$$\boldsymbol{\lambda}^{i+1} = \boldsymbol{\lambda}^i - \alpha \nabla_{\boldsymbol{\lambda}} \mathcal{F}[\boldsymbol{\lambda}^i] \quad , \tag{10.27}$$

approaching (10.26) iteratively. The parameter α has to be chosen in an appropriate manner, such that convergence of the algorithm is as fast as possible and still stable.

A number of open questions remain. As already indicated above, it is by no means clear if the introduced potential actually possesses an extremum. Furthermore, the optimization problem has to be convex in order to ensure convergence to a unique minimal configuration. This, however, can be ensured by calculating the second variations of $\mathcal{F}$ and showing that this functional Hessian is positively (semi-)definite. This is actually possible for the present problem, however, the lengthy calculations exceed the scope of this presentation.

10.3.4. Comparison with DNS Data

For the comparison with numerical data some more comments on the numerical implementation of the algorithm are in order. As in the first part of this chapter, we apply

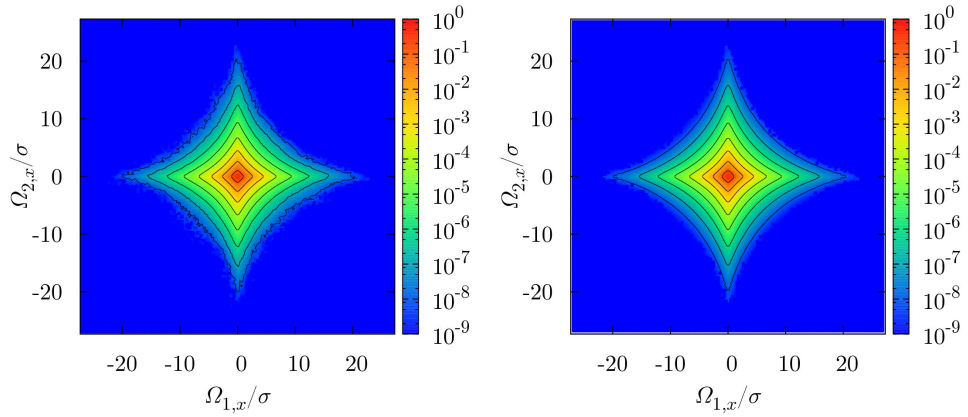

Figure 10.5.: Left: joint PDF from DNS in the statistically independent regime for $r = 316.6\eta$. Right: maximum entropy solution with the single-point PDF as given constraints obtained from the steepest descent algorithm with $\alpha = 0.1$ and $\beta = 0.5$.

the method to a projection of the full two-point PDF to the plane. For the examples presented here, we again take the PDF of the two longitudinal components of vorticity $f_2(\Omega_{1,x}, \Omega_{2,x}; \boldsymbol{r})$ with $\boldsymbol{r} = r\boldsymbol{e}_x$.

Furthermore, the algorithm is only applied in regions of sample space, in which data points have been measured. This is achieved by masking bins without any entries. In a sense, this incorporates additional information not included in the constraints so far, which might be problematic on a conceptual basis. However, when dealing with real data, additional assumptions like this have to be made in order to set up a well-defined numerical procedure.

A second modification of the algorithm is introduced with respect to the rate of convergence. For the present example the convergence to the non-Gaussian tails is of special interest. While choosing a constant α leads to a fast convergence in the core of the PDF, convergence in the tails is worse. That is why for the constraints related to the *reduction property* and the first two conditional averages a modification increasing convergence in the tails is introduced by a proper weighting with the marginal distribution. For the constraints depending on $\Omega_{1,x}$ we choose

$$\alpha \mapsto \alpha \, f_1(\Omega_{1,x})^{-\beta} \quad . \tag{10.28}$$

For $\beta = 0$ this ansatz reduces to an ordinary optimization ansatz, whereas a $\beta > 0$ leads to a faster convergence in the tails. We found in numerous tests that this modification results in a significantly increased rate of convergence. It has further been checked in a number of cases that these modifications do not change the outcome of the optimization procedure. Furthermore, it has turned out to be useful to treat the symmetry constraints by calculating the logarithmic differences between the estimated and actual PDF leading to an improved convergence.

The optimization procedure is stopped if the norm of functional gradient becomes small for a given consecutive number of iterations. This is checked by

$$\ln |\mathcal{F}[\boldsymbol{\lambda}^i]|^2 \leq \epsilon_{\text{threshold}} \tag{10.29}$$

for a given threshold. Note that this is equivalent to computing the logarithm of the norm of the error between imposed and actually fulfilled constraints. As the symmetry constraints appear to converge more rapidly, only the constraints concerning the marginal distributions and the conditional moments are taken into account for this criterion.

In total we see that the numerical implementation involves a number of modifications and arbitrary choices of thresholds, which may be subject to future improvements. In this sense the following results shall be understood as a proof of principle rather than a final answer to the problem.

To benchmark the numerical implementation, we take the particularly simple case of an ordinary maximum entropy setting with given marginal distributions already introduced above. According to the exact results discussed there, the algorithm is expected to converge to the factorized joint PDF $f_1(\Omega_{1,x})f_1(\Omega_{2,x})$ starting from a uniform initial distribution f_2^{M}. The numerical result for this case is shown in figure 10.5 together with the true two-point PDF. The agreement is perfect demonstrating the conceptual validity of the numerical approach.

As a second example we take the analytical model for $r = 2.5\eta$ as shown in figures 10.1 and 10.4 as an initial condition for the numerical optimization. As constraints we choose the marginal PDFs, the first two conditional moments as well as the symmetry constraints (10.21) and (10.22). The outcome is presented in figure 10.6. By comparison with the conditional and joint PDFs from the DNS also shown in 10.1 and 10.4, it can be concluded that the improved model actually yields a better result than the analytical model. Especially the symmetries present for the data from DNS are captured by the improved model. However, as the initial analytical model displays characteristic "kinks" on the $\Omega_{1,x} = 0$ line, these kinks are symmetrized by the algorithm and persist until the algorithm has converged.

10.4. Summary

In this chapter we have treated the closure problem in terms of a modeling of the two-point vorticity PDF. We first have shown that the stationary solution of the vorticity PDF can be calculated from the kinetic equation if the first two moments of the conditional PDF are specified. The obvious conclusion is that a model for the two-point PDF should contain these moments in order to allow for a closure of the single-point equation. We then have introduced an analytically tractable model for the two-point PDF, incorporating these conditional averages and fulfilling a number of constraints like, e.g., the *separation property*. The model has been compared to numerical data by considering a lower-dimensional projection. The results have been found to be in particularly good agreement in the limiting cases of small and large separations, where

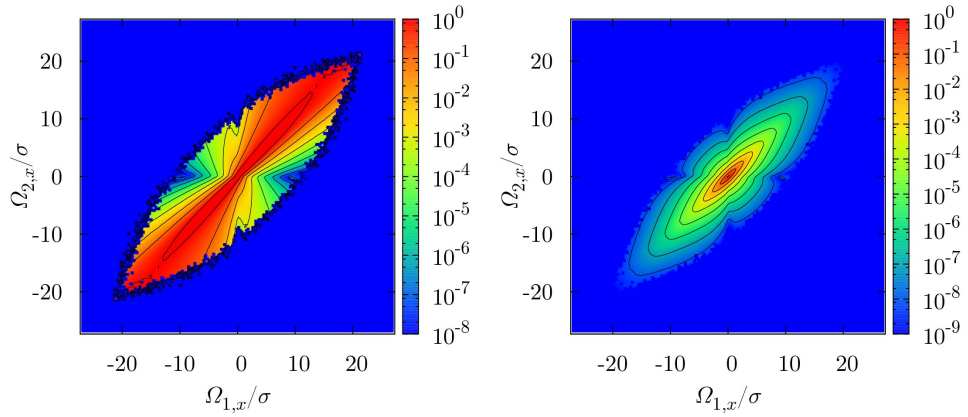

Figure 10.6.: Conditional (left) PDF and joint PDF (right) of the improved model with the initial condition of the analytical model shown in figures 10.1 and 10.4 for $r = 2.5\eta$. All constraints, including the symmetry constraint, were subject to optimization with $\alpha = 0.01$ and $\beta = 0.1$.

we have discussed that the present ansatz is exact. For intermediate separations the results prove to be acceptable, where the most obvious discrepancies originate from the fact that the model PDF does not account for a number of symmetries observable in the statistics of turbulent flows.

To correct for these shortcomings, we were naturally led to a maximum relative entropy approach, where the simple model ansatz has been taken as a starting point for further improvements. Apart from discussing the theoretical framework for such an approach, a numerical algorithm was outlined and implemented. The results have been shown to yield reasonable results in simple benchmark cases. However, as some theoretical points as well as a number of technical issues have not been fully clarified by the time of the finishing of this thesis, further research has to be spent on this approach. In this respect it is of particular interest to improve the convergence rates of the algorithm. A different numerical implementation using a Monte-Carlo method could perform better.

Although not all issues have been resolved, the results of the presented chapter are interesting on a conceptual basis. For instance, it might prove to be very useful to treat the closure problem of turbulence on the level of PDFs with the help of maximum entropy methods. As indicated in this chapter, the choice of the imposed constraints is particularly important. Based on the outcome of the presented optimization procedure, a provocative working hypothesis for future research on this topic could be: What if the two-point statistics of turbulence is fully characterized by the fact that a closure of the single-point equation is achieved while fulfilling the constraints generally to be imposed on multi-point PDFs, like, e.g., the *reduction* property?

11. Summary and Conclusions

The central aim of the current thesis is to add some new insights to the statistical description of fully developed turbulence in terms of probability density functions. To this end we have combined the statistical equations of the Lundgren-Monin-Novikov hierarchy with direct numerical simulations of fully developed homogeneous isotropic turbulence. Estimating the unclosed terms from the simulation data especially has allowed to establish a connection between the basic dynamical features and the statistical properties of turbulence.

The purpose of the first part of the thesis has been to introduce the reader both into the fundamental physical questions of statistical fluid mechanics as well as into the algorithmic details of the simulation code developed and used within this PhD project. Beyond a detailed description of the algorithm and its implementation, performance benchmarks were presented, documenting a good scaling performance of the code.

The second part of the thesis started with a presentation and characterization of a number of standard statistical evaluations of the simulation data. The purpose here has been to highlight the intermittent statistical properties typical for turbulence as well as to benchmark the simulation results. The first aim was supported by a comparison to random fields, which allowed to highlight the typical features of turbulence. The second aim was supplemented with a comparison to experimentally obtained results to work out the strengths and shortcomings of direct numerical simulations. It has turned out here that, due to the amount of generated data, DNS is especially appropriate to study high-order statistics of turbulence related to the extreme events observable. Additionally, new kinematic results relating the covariance tensors of velocity, vorticity and the velocity gradients have been obtained and checked numerically.

Seeking for analytically tractable cases, the second chapter of this part has dealt with properties of the multi-dimensional Burgers equations. Although not directly applicable to the case of viscous incompressible Navier-Stokes turbulence, still some useful insights have been gained from studying the self-amplification mechanisms of the velocity gradients with respect to small-scale dynamics of fully developed turbulence. The main results of this chapter are the derivation of exact solutions for the evolution of the velocity gradient tensor along Lagrangian trajectories as well as a systematic characterization of the dynamics of the velocity gradient tensor invariants. The structure of the arising equations revealed the systematic coupling of the invariants and their relation to the formation of finite-time singularities typical for the Burgers equation. The presented results also apply to non-potential initial conditions, in which the Hopf-Cole transformation is not applicable, adding insights to this sparsely studied case. The hope here is that the analytically obtained results might also be applicable to highly

compressible Navier-Stokes turbulence, which could be a future direction of research.

After starting the third, central part of the thesis with an introduction into the Lundgren-Monin-Novikov hierarchy and discussing its relation to the BBGKY hierarchy known from statistical mechanics, a chapter on the single-point statistics of the velocity field followed. In this chapter the application of statistical symmetries has been explained in detail and eventually has led to the homogeneous and stationary solutions of the PDF equations as a new, central result. It turned out that the single-point statistics may be quantified in terms of the conditional pressure gradient and forcing statistics as well as the eigenvalues of the conditional kinetic energy dissipation tensor. Another central theoretical aspect concerned the application of the method of characteristics to decaying turbulence. The theoretical part was completed by a discussion of an analytical closure approximation leading to Gaussian statistics. Data from DNS then has been used to estimate the unclosed terms. Here, among others, non-vanishing pressure gradient contributions to the single-point statistics as well as correlations between the conditional dissipation tensor and the velocity were found as main results. Both facts up to now have been neglected in the literature on PDF equations. However, the current thesis shows that the sub-Gaussian shape of the velocity PDF can been related to these observations. The investigation of an ensemble of decaying velocity fields revealed the presence of a self-similar regime, in which the unclosed terms turned out to be particularly simple. It turned out that the method of characteristics is particularly useful to study and interpret such non-stationary situations. An investigation of Lagragian or Eulerian intermittency of the velocity increments with this method would be a possible direction of future research.

Basically the same considerations then have been applied to the vorticity field, for which also homogeneous and stationary solutions have been derived. Here the corresponding stationary PDF has been expressed in terms of the conditional vortex stretching, the forcing as well as the eigenvalues of the conditional enstrophy dissipation tensor. Already the theoretical section has indicated the possibility that the external forcing is of minor importance for the vorticity statistics. Furthermore, an analytical closure approach has been shown to lead to slowly decaying, strongly non-Gaussian tails. The corresponding DNS results revealed pronounced statistical correlations between the rate-of-strain tensor as well as the conditional enstrophy dissipation tensor. These more pronounced correlations (compared to the velocity statistics) have been related to the more localized nature of the vorticity field and eventually were shown to cause the highly non-Gaussian shape of the PDFs. The DNS results also have confirmed the prior results by Novikov and have confirmed the conditional balance of vortex stretching and vorticity diffusion, in which the external forcing is negligible, at an unprecedented numerical and statistical quality. As a consequence, the external forcing mechanism does not influence the shape of the single-point vorticity PDF. This result may be seen as a nice example that the small-scale statistics of turbulence can become independent from the large-scale driving. The chapter was completed with a discussion of the influence of coherent vortex structures on the statistics of turbulence from two different aspects. It has been shown for an ensemble of Burgers vortices that the resulting statistics generically is non-Gaussian.

Numerical simulations starting from Gaussian initial conditions, on the other hand, have demonstrated that the emergence of coherent structures goes along with unbalanced vortex stretching until a statistically stationary situation with non-Gaussian vorticity statistics is obtained. The direct comparison of the results on the single-point velocity and vorticity statistics has shown that the vorticity is particularly well-suited quantity to connect the dynamics and the statistics of fully developed turbulence.

The following two chapters have dealt with different aspects of the two-point vorticity statistics of turbulence, which up to now has only been treated sparsely in the literature. We first have studied the two-point enstrophy statistics, which has allowed to characterize the spatial structure of the vorticity field as well as the interaction of different spatial scales. The evaluation of DNS data explicitly revealed a simultaneous up- and downscale probability flux going along with an imbalance of enstrophy production and diffusion. The method of characteristics was used to discuss the shape deformation across the scales in terms of these dynamical influences, and a simple analytical model resembling the main characteristics of the vector field has been introduced. In the second half of the chapter the connection between the conditional averages arising in the kinetic description and the two-point vorticity statistics has been discussed. Extending works by Novikov, we have introduced the semi-analytically tractable Twisted Gaussian Approximation, which has been shown to qualitatively capture the enstrophy production and dissipative effects both on the single-point and two-point level. The understanding of the probability fluxes in scale related to the conditional longitudinal velocity increment, however, remains a challenging task for future research with the aim of explaining the direct cascade in terms of the vorticity statistics. The final chapter has dealt with the question how a consistent model for the two-point PDF of the vorticity can be established. As a main result we have introduced a model for the two-point PDF incorporating the first two conditional moments of the two-point statistics. With an appropriate choice of the first two conditional moments it has been shown that this ansatz provides a closure of the single-point PDF equation allowing to determine the shape of the single-point PDF. Furthermore, it has been shown that this simple analytical ansatz fulfills the majority of desired constraints imposed on the two-point PDF. In the second part of this chapter we have embedded this simple model into the context of maximum relative entropy methods to correct for the shortcomings of the analytical model. It has been shown that an improved model is obtained from the initial one by multiplication with a correction factor involving functional Lagrange multipliers. We finally have outlined an iterative method to obtain the Lagrange multipliers and presented first results of a numerical implementation in the form of a steepest descent approach. This new systematic approach to construct consistent models for joint PDFs is not restricted to turbulence theory only and may be as well applied within the theory of stochastic processes.

To conclude, we have demonstrated in this thesis how combined theoretical and numerical efforts may be used to yield new insights into the statistical nature of turbulence. The close joint analytical and numerical investigation of the PDF equations may be regarded as a main novelty of this thesis. First identifying the statistical

quantities that govern the evolution and shape of probability density functions from the Lundgren-Monin-Novikov hierarchy, the subsequent numerical evaluation of these terms has yielded a detailed explanation of the connection between average dynamical influences and the resulting statistics. Beyond giving this characterization, this thesis provides an identification of necessary properties for systematic closures. The hope is that these results can be used for a qualitatively and quantitatively improved understanding of the closure problem of turbulence and for the formulation of simple models that capture the central aspects of the statistics.

While we have been able to treat the single-point statistics of velocity and vorticity on a comprehensive level, already the investigation of the two-point statistics has made clear that compromises regarding the dimensionality of the considered statistical quantities have to be made. As a consequence it is clear that future advancements of the theory most likely have to go along with the development of new conceptual ideas reducing the complexity of the statistical equations to be treated.

On a more general level the results of the current thesis show that, when seeking for an understanding of the statistics of fully developed turbulence, one can distinguish different types of deviations from Gaussianity, namely regarding the shape and inner structure of statistics. While the first type may be modeled by a proper mapping of Gaussian random fields, the latter type necessitates the challenging task of developing an understanding of the statistics of non-Gaussian random fields.

A. Mathematical Details

A.1. Some Properties of the Delta Distribution

The derivation of the PDF equations relies on some properties of the delta distribution. We want to mention the most important ones.

The delta distribution may be introduced by

$$\int_{-\infty}^{\infty} \mathrm{d}x\, \delta(x-a) f(x) = f(a) \quad . \tag{A.1}$$

It is clear from this definition that

$$\delta(x-a) = \delta(a-x) \quad . \tag{A.2}$$

It further can be concluded that

$$f(x)\delta(x-a) = f(a)\delta(x-a) \quad , \tag{A.3}$$

which is sometimes called the "sifting property" of the delta distribution. This relation is especially important in the context of the derivation of PDF equations as it allows to interchange realizations with the corresponding sample space variable. Another important point refers to derivation of the delta distribution. It is evident that

$$\frac{\partial}{\partial a}\delta(x-a) = -\frac{\partial}{\partial x}\delta(x-a) = -\frac{\partial\, \delta(x-a)}{\partial (x-a)} \quad . \tag{A.4}$$

A generalization to vector notation is straightforward.

A.2. Multivariate Gaussian Distributions

A.2.1. PDF and Characteristic Function

We consider the statistics of the vorticities $\boldsymbol{\Omega}_0, \ldots \boldsymbol{\Omega}_N$ at the spatial points $\boldsymbol{x}_0, \ldots, \boldsymbol{x}_N$. In the case of Gaussian statistics the joint PDF takes the form

$$f_{N+1}(\boldsymbol{\Omega}_0, \ldots, \boldsymbol{\Omega}_N) = (2\pi)^{-\frac{3N}{2}} \det(\mathcal{R})^{-\frac{1}{2}} \quad \exp\left[-\frac{1}{2}\sum_{i,j=0}^{N} \boldsymbol{\Omega}_i \mathcal{R}^{-1}(\boldsymbol{x}_i, \boldsymbol{x}_j)\boldsymbol{\Omega}_j\right] \quad . \tag{A.5}$$

The corresponding characteristic function can be obtained by Fourier transform and simply reads

$$\phi_{N+1}(\boldsymbol{\alpha}_0,\ldots,\boldsymbol{\alpha}_N) = \exp\left[-\frac{1}{2}\sum_{i,j=0}^{N}\boldsymbol{\alpha}_i\mathcal{R}(\boldsymbol{x}_i,\boldsymbol{x}_j)\boldsymbol{\alpha}_j\right] \quad . \tag{A.6}$$

Some remarks on the notation are in order. For fixed i and j $\mathcal{R}(\boldsymbol{x}_i,\boldsymbol{x}_j)$ represents the 3×3 covariance tensor of the vorticities $\boldsymbol{\Omega}_i$ and $\boldsymbol{\Omega}_j$ located at position $\boldsymbol{x}_i$ and $\boldsymbol{x}_j$. Hence $\mathcal{R}$ is a matrix with covariance tensors as entries.

A.2.2. Conditional Averages

The evaluation of conditional averages is analytically possible for Gaussian statistics. For example, the first conditional moment is calculated according to

$$\begin{aligned}
&\langle\boldsymbol{\omega}(\boldsymbol{x}_0)|\boldsymbol{\Omega}_1,\ldots,\boldsymbol{\Omega}_N\rangle f_N(\boldsymbol{\Omega}_1,\ldots\boldsymbol{\Omega}_N)\\
&= \int \mathrm{d}\boldsymbol{\Omega}_0\,\boldsymbol{\Omega}_0\, f_{N+1}\\
&= \int \mathrm{d}\boldsymbol{\Omega}_0\,\boldsymbol{\Omega}_0 \int \mathrm{d}\{\boldsymbol{\alpha}_i\}\,\exp\left[\mathrm{i}\sum_{i=0}^{N}\boldsymbol{\alpha}_i\cdot\boldsymbol{\Omega}_i\right]\phi_{N+1}\\
&= \frac{1}{\mathrm{i}}\int \mathrm{d}\boldsymbol{\Omega}_0 \int \mathrm{d}\{\boldsymbol{\alpha}_i\}\,\nabla_{\boldsymbol{\alpha}_0}\exp\left[\mathrm{i}\sum_{i=0}^{N}\boldsymbol{\alpha}_i\cdot\boldsymbol{\Omega}_i\right]\phi_{N+1}\\
&= -\frac{1}{\mathrm{i}}\int \mathrm{d}\boldsymbol{\Omega}_0 \int \mathrm{d}\{\boldsymbol{\alpha}_i\}\,\exp\left[\mathrm{i}\sum_{i=0}^{N}\boldsymbol{\alpha}_i\cdot\boldsymbol{\Omega}_i\right]\nabla_{\boldsymbol{\alpha}_0}\phi_{N+1}\\
&= \frac{1}{\mathrm{i}}\int \mathrm{d}\boldsymbol{\Omega}_0 \int \mathrm{d}\{\boldsymbol{\alpha}_i\}\,\exp\left[\mathrm{i}\sum_{i=0}^{N}\boldsymbol{\alpha}_i\cdot\boldsymbol{\Omega}_i\right]\left(\sum_{j=0}^{N}\mathcal{R}(\boldsymbol{x}_0,\boldsymbol{x}_j)\boldsymbol{\alpha}_j\right)\phi_{N+1}\\
&= -\int \mathrm{d}\boldsymbol{\Omega}_0\left(\sum_{j=0}^{N}\mathcal{R}(\boldsymbol{x}_0,\boldsymbol{x}_j)\nabla_{\boldsymbol{\Omega}_j}\right)f_{N+1}\\
&= \sum_{i,j=1}^{N}\mathcal{R}(\boldsymbol{x}_0,\boldsymbol{x}_i)\,\mathcal{R}^{-1}(\boldsymbol{x}_i,\boldsymbol{x}_j)\,\boldsymbol{\Omega}_j\, f_N \quad .
\end{aligned} \tag{A.7}$$

Next we check the limiting properties of this expression

$$\begin{aligned}
\lim_{|\boldsymbol{x}_0-\boldsymbol{x}_k|\to 0}\langle\boldsymbol{\omega}(\boldsymbol{x}_0)|\boldsymbol{\Omega}_1,\ldots,\boldsymbol{\Omega}_N\rangle &= \sum_{i,j=1}^{N}\mathcal{R}(\boldsymbol{x}_k,\boldsymbol{x}_i)\,\mathcal{R}^{-1}(\boldsymbol{x}_i,\boldsymbol{x}_j)\,\boldsymbol{\Omega}_j\\
&= \sum_{i,j=1}^{N}\delta_{kj}\,\boldsymbol{\Omega}_j = \boldsymbol{\Omega}_k \quad .
\end{aligned} \tag{A.8}$$

To get an explicit expression for the conditional averages, one has to invert $\mathcal{R}$. When only two points are considered, the situation is especially simple. Then we have

$$\mathcal{R} = \frac{\langle \boldsymbol{\omega}^2 \rangle}{3} \begin{pmatrix} \mathrm{E} & \mathrm{C}(\boldsymbol{x}_1, \boldsymbol{x}_2) \\ \mathrm{C}(\boldsymbol{x}_2, \boldsymbol{x}_1) & \mathrm{E} \end{pmatrix} \quad . \tag{A.9}$$

We now introduce the short-hand notation $\mathcal{R}(\boldsymbol{x}_1, \boldsymbol{x}_1) = R(\boldsymbol{0}) = \frac{\langle \boldsymbol{\omega}^2 \rangle}{3}\mathrm{E}$ and $\mathcal{R}(\boldsymbol{x}_1, \boldsymbol{x}_2) = \frac{\langle \boldsymbol{\omega}^2 \rangle}{3}\mathrm{C}(\boldsymbol{x}_1, \boldsymbol{x}_2)$, defining how different entries of this matrix are accessed. The inverse of $\mathcal{R}$ explicitly reads

$$\mathcal{R}^{-1} = \frac{3}{\langle \boldsymbol{\omega}^2 \rangle} \left[\mathrm{E} - \mathrm{C}(\boldsymbol{x}_1, \boldsymbol{x}_2)^2\right]^{-1} \begin{pmatrix} \mathrm{E} & -\mathrm{C}(\boldsymbol{x}_1, \boldsymbol{x}_2) \\ -\mathrm{C}(\boldsymbol{x}_2, \boldsymbol{x}_1) & \mathrm{E} \end{pmatrix} \quad . \tag{A.10}$$

$\mathrm{C}(\boldsymbol{x}_1, \boldsymbol{x}_2) = \mathrm{C}(\boldsymbol{x}_2 - \boldsymbol{x}_1) = \mathrm{C}(\boldsymbol{r})$ represents the ordinary correlation matrix

$$C_{ij}(\boldsymbol{r}) = c_\perp(r)\, \delta_{ij} + (c_\parallel - c_\perp)(r)\, \frac{r_i r_j}{r^2} \quad , \tag{A.11}$$

i.e., $c_\parallel$ and $c_\perp$ represent the longitudinal and transversal correlation functions, respectively. From this we get

$$(\delta_{ij} - C_{ik}C_{kj}) = (1 - c_\perp^2)\delta_{ij} + (c_\perp^2 - c_\parallel^2)\frac{r_i r_j}{r^2} \quad , \tag{A.12}$$

which explicitly is inverted to

$$(\delta_{ij} - C_{ik}C_{kj})^{-1} = \frac{1}{1 - c_\perp^2}\, \delta_{ij} + \frac{c_\parallel^2 - c_\perp^2}{(1 - c_\parallel^2)(1 - c_\perp^2)}\frac{r_i r_j}{r^2} \quad , \tag{A.13}$$

such that we have obtained an explicit expression of $\mathcal{R}^{-1}(\boldsymbol{x}_1, \boldsymbol{x}_2)$ in terms of $c_\parallel$ and $c_\perp$. This allows to explicitly compute the inverse matrices

$$\mathcal{R}_{ij}^{-1}(\boldsymbol{x}_1, \boldsymbol{x}_1) = \mathcal{R}_{ij}^{-1}(\boldsymbol{x}_2, \boldsymbol{x}_2) = \frac{3}{\langle \boldsymbol{\omega}^2 \rangle}\left(\frac{1}{1 - c_\perp^2}\, \delta_{ij} + \frac{c_\parallel^2 - c_\perp^2}{(1 - c_\parallel^2)(1 - c_\perp^2)}\frac{r_i r_j}{r^2}\right) \tag{A.14a}$$

$$\mathcal{R}_{ij}^{-1}(\boldsymbol{x}_1, \boldsymbol{x}_2) = \mathcal{R}_{ij}^{-1}(\boldsymbol{x}_2, \boldsymbol{x}_1) = \frac{3}{\langle \boldsymbol{\omega}^2 \rangle}\left(-\frac{c_\perp}{1 - c_\perp^2}\, \delta_{ij} - \frac{(c_\parallel - c_\perp)(1 + c_\parallel c_\perp)}{(1 - c_\parallel^2)(1 - c_\perp^2)}\frac{r_i r_j}{r^2}\right) \quad . \tag{A.14b}$$

A.3. More Details on the Twisted Gaussian Approximation

A.3.1. Gaussian Contribution to the Single-Point Enstrophy Statistics

The conditional rate-of-strain tensor in the Gaussian approximation has the general structure

$$\begin{aligned}\big\langle S_{1,ij}\big|\boldsymbol{\Omega}_1\big\rangle_G &= \frac{3}{8\pi}\int \mathrm{d}\boldsymbol{r}\,\epsilon_{ikl}\,\frac{r_k r_j}{r^5}\,C_{lm}(\boldsymbol{r})\Omega_{1,m} + (i\leftrightarrow j)\\ &= \frac{3}{8\pi}\int \mathrm{d}\boldsymbol{r}\,\epsilon_{ikl}\,\frac{r_k r_j}{r^5}\,\Big(c_\perp(r)\,\delta_{lm} - (c_\parallel - c_\perp)(r)\,\frac{r_l r_m}{r^2}\Big)\,\Omega_{1,m} + (i\leftrightarrow j)\\ &= \frac{3}{8\pi}\int \mathrm{d}\boldsymbol{r}\,c_\perp(r)\,\epsilon_{ikl}\,\frac{r_k r_j}{r^5}\,\Omega_{1,l} + (i\leftrightarrow j)\\ &= \frac{3}{8\pi}\int \mathrm{d}\boldsymbol{r}\,\frac{c_\perp(r)}{r^3}\,\big(\hat{\boldsymbol{r}}\times\boldsymbol{\Omega}_1\big)_i\,\hat{r}_j + (i\leftrightarrow j)\quad . \end{aligned} \tag{A.15}$$

Multiplying this expression from both sides with $\boldsymbol{\Omega}_1$ yields the conditional enstrophy production, which vanishes:

$$\big\langle \boldsymbol{\omega}_1 \mathrm{S}_1 \boldsymbol{\omega}_1\big|\boldsymbol{\Omega}_1\big\rangle_G = \frac{3}{4\pi}\int \mathrm{d}\boldsymbol{r}\,\frac{c_\perp(r)}{r^3}\,\underbrace{\boldsymbol{\Omega}_1\cdot\big(\hat{\boldsymbol{r}}\times\boldsymbol{\Omega}_1\big)}_{=0}\,(\hat{\boldsymbol{r}}\cdot\boldsymbol{\Omega}_1) \tag{A.16}$$

A.3.2. Solenoidality of the Twisted Gaussian Approximation

For the contribution to the divergence of the conditional vorticity field we obtain

$$\begin{aligned}\big\langle \nabla_{\boldsymbol{x}_0}\cdot\boldsymbol{\omega}(\boldsymbol{x}_0)\big|\boldsymbol{\Omega}_1\big\rangle_T &= \frac{\partial}{\partial r_i}\,c_T(r)\,\hat{r}_p\widehat{\Omega}_{1,p}\,\epsilon_{ikl}\widehat{\Omega}_{1,k}\hat{r}_l\\ &= c_T'\,\hat{r}_i\,\hat{r}_p\widehat{\Omega}_{1,p}\,\epsilon_{ikl}\widehat{\Omega}_{1,k}\hat{r}_l\\ &\quad + c_T\left(\frac{\delta_{ip}}{r} - \frac{r_i r_p}{r^2}\right)\widehat{\Omega}_{1,p}\,\epsilon_{ikl}\widehat{\Omega}_{1,k}\hat{r}_l\\ &\quad + c_T\,\hat{r}_p\widehat{\Omega}_{1,p}\,\epsilon_{ikl}\widehat{\Omega}_{1,k}\left(\frac{\delta_{il}}{r} - \frac{r_i r_l}{r^2}\right)\\ &= 0\quad , \end{aligned} \tag{A.17}$$

showing that each term vanishes independently.

A.3.3. Gaussian Contribution to the Two-Point Enstrophy Statistics

As discussed in chapter 9 the Gaussian contribution to the two-point enstrophy production takes the form

$$\begin{aligned}\langle \boldsymbol{\omega}_1 \mathrm{S}_1 \boldsymbol{\omega}_1 | \boldsymbol{\Omega}_1, \boldsymbol{\Omega}_2 \rangle_G \\ = \frac{3}{4\pi} \int \mathrm{d}\boldsymbol{x}_0 \, \frac{\boldsymbol{\Omega}_1 \cdot \hat{\boldsymbol{r}}_{01}}{r_{01}^3} \, \boldsymbol{\Omega}_1 \cdot \big[\hat{\boldsymbol{r}}_{01} \quad \times \quad \big(\mathcal{R}(\boldsymbol{x}_0, \boldsymbol{x}_1) \left[\mathcal{R}^{-1}(\boldsymbol{x}_1, \boldsymbol{x}_1) \, \boldsymbol{\Omega}_1 + \mathcal{R}^{-1}(\boldsymbol{x}_1, \boldsymbol{x}_2) \, \boldsymbol{\Omega}_2 \right] \\ + \quad \mathcal{R}(\boldsymbol{x}_0, \boldsymbol{x}_2) \left[\mathcal{R}^{-1}(\boldsymbol{x}_2, \boldsymbol{x}_1) \, \boldsymbol{\Omega}_1 + \mathcal{R}^{-1}(\boldsymbol{x}_2, \boldsymbol{x}_2) \, \boldsymbol{\Omega}_2 \right] \big) \big] \, .\end{aligned} \tag{A.18}$$

As an example, we want to evaluate the first integral explicitly, that means, we have to evaluate

$$\frac{3}{4\pi} \int \mathrm{d}\boldsymbol{x}_0 \, \frac{\boldsymbol{\Omega}_1 \cdot \hat{\boldsymbol{r}}_{01}}{r_{01}^3} \left[\hat{\boldsymbol{r}}_{01} \times \mathcal{R}(\boldsymbol{x}_0, \boldsymbol{x}_1) \mathcal{R}^{-1}(\boldsymbol{x}_1, \boldsymbol{x}_1) \boldsymbol{\Omega}_1 \right] \cdot \boldsymbol{\Omega}_1 \quad . \tag{A.19}$$

Here the integrand takes the form

$$\left[\hat{\boldsymbol{r}}_{01} \times \mathrm{A}(\boldsymbol{x}_0, \boldsymbol{x}_1, \boldsymbol{x}_2) \boldsymbol{\Omega}_1 \right] \cdot \boldsymbol{\Omega}_1 \tag{A.20}$$

with

$$\begin{aligned} A_{ij}(\boldsymbol{x}_0, \boldsymbol{x}_1, \boldsymbol{x}_2) = a(\boldsymbol{x}_0, \boldsymbol{x}_1, \boldsymbol{x}_2) \, \delta_{ij} + b(\boldsymbol{x}_0, \boldsymbol{x}_1, \boldsymbol{x}_2) \, \hat{r}_{01,i} \, \hat{r}_{01,j} \\ + c(\boldsymbol{x}_0, \boldsymbol{x}_1, \boldsymbol{x}_2) \, \hat{r}_{12,i} \, \hat{r}_{12,j} + d(\boldsymbol{x}_0, \boldsymbol{x}_1, \boldsymbol{x}_2) \, (\hat{\boldsymbol{r}}_{12} \cdot \hat{\boldsymbol{r}}_{01}) \, \hat{r}_{01,i} \, \hat{r}_{12,j} \quad , \end{aligned} \tag{A.21}$$

where the scalar functions a, b, c and d depend on the longitudinal and transversal correlation functions at the different spatial points. It can be seen easily that the integrals related to a, b and d vanish because of the structure of the integrand. The scalar function c is evaluated yielding

$$c(\boldsymbol{x}_0, \boldsymbol{x}_1, \boldsymbol{x}_2) = \frac{c_\parallel^2(r_{12}) - c_\perp^2(r_{12})}{(1 - c_\parallel^2(r_{12}))(1 - c_\perp^2(r_{12}))} \, c_\perp(r_{01}) \quad . \tag{A.22}$$

Hence the integral takes the form

$$\begin{aligned} &\frac{c_\parallel^2(r_{12}) - c_\perp^2(r_{12})}{(1 - c_\parallel^2(r_{12}))(1 - c_\perp^2(r_{12}))} \, (\boldsymbol{\Omega}_1 \cdot \hat{\boldsymbol{r}}_{12}) \, \Omega_{1,i} \, (\boldsymbol{\Omega}_1 \times \hat{\boldsymbol{r}}_{12})_j \, \frac{3}{4\pi} \int \mathrm{d}\boldsymbol{x}_0 \, \frac{c_\perp(r_{01})}{r_{01}^3} \, \hat{r}_{01,i} \hat{r}_{01,j} \\ &= \frac{c_\parallel^2(r_{12}) - c_\perp^2(r_{12})}{(1 - c_\parallel^2(r_{12}))(1 - c_\perp^2(r_{12}))} \, (\boldsymbol{\Omega}_1 \cdot \hat{\boldsymbol{r}}_{12}) \, \Omega_{1,i} \, (\boldsymbol{\Omega}_1 \times \hat{\boldsymbol{r}}_{12})_j \, 3\delta_{ij} \int \mathrm{d}r_{01} \, \frac{c_\perp(r_{01})}{r_{01}} \\ &= 0 \quad , \end{aligned} \tag{A.23}$$

showing that this term already vanishes before projection. The remaining Gaussian terms can be treated similarly, which we will not demonstrate here. They will in general, however, not vanish identically.

List of Figures

Bibliography

[Bat53] G.K. Batchelor. *The theory of homogeneous turbulence.* Cambridge University Press, Cambridge, England, 1953.

[BK07] Jeremie Bec and Konstantin Khanin. Burgers turbulence. *Physics Reports*, 447(1-2):1–66, 2007.

[Bog66] N.N. Bogolyubova. *Foundations of kinetic theory. N.N. Bogolyubov's method.* Nauka, 1966.

[Boy01] J. P. Boyd. *Chebyshev and Fourier Spectral Methods: Second Revised Edition.* Dover Publications, 2 revised edition, 2001.

[Bur39] J.M. Burgers. On the application of statistical mechanics to the theory of of turbulent fluid motion. *Proc. Roy. Neth. Acad. Sci.*, 32:414,643,818, 1939.

[Bur48] J.M. Burgers. Advances in applied mechanics. Academic, New York, 1948.

[Bur74] J.M. Burgers. *The Nonlinear Diffusion Equation.* Reidel, 1974.

[Can92] Brian J. Cantwell. Exact solution of a restricted Euler equation for the velocity gradient tensor. *Physics of Fluids A*, 4(4):782–793, 1992.

[Cha51] S. Chandrasekhar. The invariant theory of isotropic turbulence in magnetohydrodynamics. *Proceedings of the Royal Society of London. Series A, Mathematical and Physical Sciences*, 204(1079):435–449, 1951.

[CHQZ87] C. Canuto, M.Y. Hussaini, A. Quarteroni, and T. A. Zang. *Spectral Methods in Fluid Dynamics.* Springer-Verlag, Berlin, 1987.

[CM06] L. Chevillard and C. Meneveau. Lagrangian dynamics and statistical geometric structure of turbulence. *Physical Review Letters*, 97(17):174501, 2006.

[CMBT08] L. Chevillard, C. Meneveau, L. Biferale, and F. Toschi. Modeling the pressure Hessian and viscous Laplacian in turbulence: Comparisons with direct numerical simulation and implications on velocity gradient dynamics. *Physics of Fluids*, 20(10):101504, 2008.

[CMNR07] John Clyne, Pablo Mininni, Alan Norton, and Mark Rast. Interactive desktop analysis of high resolution simulations: application to turbulent plume dynamics and current sheet formation. *New J. Phys*, 9(301), 2007.

[Col51] J. Cole. On the quasi-linear parabolic equation occuring in hydrodynamics. *Q. Appl. Math*, 9:225–236, 1951.

[CPC90] M. S. Chong, A. E. Perry, and B. J. Cantwell. A general classification of three-dimensional flow fields. *Physics of Fluids A*, 2(5):765–777, 1990.

[CPS99] Michael Chertkov, Alain Pumir, and Boris I. Shraiman. Lagrangian tetrad dynamics and the phenomenology of turbulence. *Physics of Fluids*, 11(8):2394–2410, 1999.

[CR05] John Clyne and Mark Rast. A prototype discovery environment for analyzing and visualizing terascale turbulent fluid flow simulations. In *Proceedings of Visualization and Data Analysis 2005*, 2005.

[Dai09] Anton Daitche. *Statische und geometrische Eigenschaften turbulenter Strömungen*. Diplomarbeit, Westfälische Wilhelms-Universität Münster, 2009.

[Dav04] P. A. Davidson. *Turbulence - An Introduction for Scientists and Engineers*. Oxford University Press, Oxford, England, 2004.

[FFO10] G. Falkovich, I. Fouxon, and Y. Oz. New relations for correlation functions in Navier-Stokes turbulence. *Journal of Fluid Mechanics*, 644(-1):465–472, 2010.

[fft] `www.fftw.org`.

[FJ05] Matteo Frigo and Steven G. Johnson. The design and implementation of FFTW3. *Proceedings of the IEEE*, 93(2):216–231, 2005. Special issue on "Program Generation, Optimization, and Platform Adaptation".

[FL97] G. Falkovich and V. Lebedev. Single-point velocity distribution in turbulence. *Phys. Rev. Lett.*, 79(21):4159–4161, 1997.

[FP97] R. Friedrich and J. Peinke. Description of a Turbulent Cascade by a Fokker-Planck Equation. *Physical Review Letters*, 78(5):863–866, 1997.

[Fri95] U. Frisch. *Turbulence - The Legacy of A.N. Kolmogorov*. Cambridge University Press, Cambridge, England, 1995.

[Gea71] C. William Gear. *Numerical initial value problems in ordinary differential equations*. Prentice-Hall, 1971.

[GFN02] Toshiyuki Gotoh, Daigen Fukayama, and Tohru Nakano. Velocity field statistics in homogeneous steady turbulence obtained using a high-resolution direct numerical simulation. *Physics of Fluids*, 14(3):1065–1081, 2002.

[Hak78] H. Haken. *Synergetics: An Introduction. Nonequilibrium Phase Transitions and Self-Organization in Physics, Chemistry and Biology (Springer Series in Synergetics)*. Springer, 1978.

[Hak06] H. Haken. *Information and self-organization: a macroscopic approach to complex systems.* Springer, 2006.

[HK97] N. Hatakeyama and T. Kambe. Statistical laws of random strained vortices in turbulence. *Physical Review Letters*, 79(7), 1997.

[HL07] T. Y. Hou and R. Li. Computing nearly singular solutions using pseudo-spectral methods. *J. Comp. Phys*, 226:379 – 397, 2007.

[Hom06] H. Homann. *Lagrangian Statistics of Turbulent Flows in Fluids and Plasmas.* Doktorarbeit, Ruhr-Universität Bochum, 2006.

[Hop50] E. Hopf. The partial differential equation $u_t + uu_x = \mu u_{xx}$. *Comm. Pure Appl. Math*, 3:201–230, 1950.

[Hop52] E. Hopf. *J. Rat. Mech. Anal.*, 1:87, 1952.

[Hos07] Iwao Hosokawa. One- and two-point velocity distribution functions and velocity autocorrelation functions for various reynolds numbers in decaying homogeneous isotropic turbulence. *Fluid Dynamics Research*, 39(1-3):49 – 67, 2007.

[Hos08] Iwao Hosokawa. One-point velocity statistics in decaying homogeneous isotropic turbulence. *Physical Review E*, 78(6):066312, 2008.

[Jay57a] E. T. Jaynes. Information Theory and Statistical Mechanics. *Phys. Rev.*, 106(4):620–630, 1957.

[Jay57b] E. T. Jaynes. Information Theory and Statistical Mechanics. II. *Phys. Rev.*, 108(2):171–190, 1957.

[Jay03] E. T. Jaynes. *Probability Theory: The Logic of Science.* Cambridge University Press, 2003.

[Jim98] Javier Jimenez. Turbulent velocity fluctuations need not be Gaussian. *Journal of Fluid Mechanics*, 376(-1):139–147, 1998.

[JW98] J. Jimenez and A. A. Wray. On the characteristics of vortex filaments in isotropic turbulence. *Journal of Fluid Mechanics*, 373, 1998.

[JWSR93] J. Jimenez, A. A. Wray, P. G. Saffman, and R. S. Rogallo. The structure of intense vorticity in isotropic turbulence. *Journal of Fluid Mechanics*, 255, 1993.

[Kol41a] Andrey Nikolaevich Kolmogorov. Dissipation of energy in the locally isotropic turbulence. *Doklady Akademii Nauk SSSR*, 32(1):16–18, 1941.

[Kol41b] Andrey Nikolaevich Kolmogorov. The local structure of turbulence in incompressible viscous fluid for very large Reynolds numbers. *Doklady Akademii Nauk SSSR*, 30(4):299–303, 1941.

[Kol62] A. N. Kolmogorov. A refinement of previous hypotheses concerning the local structure of turbulence in a viscous incompressible fluid at high Reynolds number. *Journal of Fluid Mechanics*, 13(01):82–85, 1962.

[Kol91a] A. N. Kolmogorov. Dissipation of Energy in the Locally Isotropic Turbulence. *Proceedings of the Royal Society: Mathematical and Physical Sciences (1990–1995)*, 434(1890):15–17, 1991.

[Kol91b] A. N. Kolmogorov. The Local Structure of Turbulence in Incompressible Viscous Fluid for Very Large Reynolds Numbers. *Proceedings of the Royal Society: Mathematical and Physical Sciences (1990–1995)*, 434(1890):9–13, 1991.

[LP83] E.M. Lifschitz and L.P. Pitajewski. *Lehrbuch der Theoretischen Physik Bd. X: Physikalische Kinetik*. Akademie-Verlag Berlin, 1983.

[Lüc01] Stephan Lück. *Skalenaufgelöste Experimente und statistische Analysen von turbulenten Nachlaufströmungen*. Doktorarbeit, Carl von Ossietzky Universität Oldenburg, 2001.

[Lun67] T.S. Lundgren. Distribution functions in the statistical theory of turbulence. *Physics of Fluids*, 10(5):969–975, 1967.

[Lun72] T.S. Lundgren. A closure hypothesis for the hierarchy of equations for turbulent probability distribution functions. In M. Rosenblatt and C. Van Atta, editors, *Statistical Models and Turbulence*, volume 12 of *Lecture Notes in Physics*, pages 70–100. Springer Berlin / Heidelberg, 1972.

[Lun82] T. S. Lundgren. Strained spiral vortex model for turbulent fine structure. *Physics of Fluids*, 25(12), 1982.

[Lun93] T. S. Lundgren. A small-scale turbulence model. *Physics of Fluids A: Fluid Dynamics*, 5(6), 1993.

[Lun08] T.S. Lundgren. private communication. 61st APS DFD Meeting, San Antonio, 2008.

[MDN96] R. C. Y. Mui, D. G. Dommermuth, and E. A. Novikov. Conditionally averaged vorticity field and turbulence modeling. *Phys. Rev. E*, 53(3):2355–2359, 1996.

[MDV98] Jesús Martín, César Dopazo, and Luis Valiño. Dynamics of velocity gradient invariants in turbulence: Restricted Euler and linear diffusion models. *Physics of Fluids*, 10(8):2012–2025, 1998.

[MHK03] Hideaki Mouri, Akihiro Hori, and Yoshihide Kawashima. Vortex tubes in velocity fields of laboratory isotropic turbulence: Dependence on the Reynolds number. *Physical Review E*, 67(1):016305, 2003.

[MHK04] H. Mouri, A. Hori, and Y. Kawashima. Vortex tubes in turbulence velocity fields at Reynolds numbers Re[sub lambda] = 300–1300. *Physical Review E*, 70(6):066305, 2004.

[Mon67] A.S. Monin. Equations of turbulent motion. *Prikl. Mat. Mekh.*, 31(6):1057, 1967.

[MY71] A. S. Monin and A. M. Yaglom. *Statistical fluid mechanics; Mechanics of turbulence.* 1971.

[MY75] A. S. Monin and A. M. Yaglom. *Statistical fluid mechanics: Mechanics of turbulence. Volume 2 /revised and enlarged edition/.* 1975.

[ND94] E. A. Novikov and D.G. Dommermuth. Conditionally averaged dynamics of turbulence. *Mod. Phys. Lett. B*, 8(23):1395, 1994.

[Nov68] E. A. Novikov. Kinetic equations for a vortex field. *Soviet Physics-Doklady*, 12(11):1006–1008, 1968.

[Nov93] E. A. Novikov. A new approach to the problem of turbulence, based on the conditionally averaged Navier-Stokes equations. *Fluid Dynamics Research*, 12(2):107 – 126, 1993.

[NWL+97] A. Noullez, G. Wallace, W. Lempert, R. B. Miles, and U. Frisch. Transverse velocity increments in turbulent flow using the relief technique. *Journal of Fluid Mechanics*, 339(-1):287–307, 1997.

[OP72] Steven A. Orszag and G. S. Patterson. Numerical simulation of three-dimensional homogeneous isotropic turbulence. *Phys. Rev. Lett.*, 28(2):76–79, 1972.

[Ors71] Steven A. Orszag. On the elimination of aliasing in finite-difference schemes by filtering high-wavenumber components. *Journal of the Atmospheric Sciences*, 28:1074, 1971.

[PC93] S. B. Pope and Emily S. C. Ching. Stationary probability density functions: An exact result. *Physics of Fluids A: Fluid Dynamics*, 5(7):1529–1531, 1993.

[PO71] G. S. Patterson Jr. and Steven A. Orszag. Spectral calculation of isotropic turbulence: Efficient removal of aliasing interaction. *Physics of Fluids*, 14:2538–2541, 1971.

[Pop00] S. B. Pope. *Turbulent Flows.* Cambridge University Press, Cambridge, England, 2000.

[Ren02] Christoph Renner. *Markowanalysen stochastisch fluktuierender Zeitserien.* Doktorarbeit, Carl von Ossietzky Universität Oldenburg, 2002.

[Ris96] Hannes Risken. *The Fokker-Planck Equation: Methods of Solutions and Applications.* Springer Series in Synergetics. Springer, 2nd ed. 1989. 3rd printing edition, 1996.

[Rob40] H.P. Robertson. The invariant theory of isotropic turbulence. *Proc. Camb. Phil. Soc.*, 36:209, 1940.

[Rog77] R. S. Rogallo. An ILLIAC program for the numerical simulation of homogeneous, incompressible turbulence. Technical Report TM-73203, NASA, 1977.

[Rog81] R. S. Rogallo. Numerical experiments in homogeneous turbulence. Technical Report TM-81315, NASA, 1981.

[RPF01] Ch. Renner, J. Peinke, and R. Friedrich. Experimental indications for markov properties of small-scale turbulence. *Journal of Fluid Mechanics*, 433(-1):383–409, 2001.

[Saf92] P.G. Saffman. *Vortex Dynamics.* Cambridge University Press, Cambridge, England, 1992.

[Sig81] Eric D. Siggia. Numerical study of small-scale intermittency in three-dimensional turbulence. *Journal of Fluid Mechanics*, 107(-1):375–406, 1981.

[SJO90] Z.-S. She, E. Jackson, and S. A. Orszag. Intermittent vortex structures in homogeneous isotropic turbulence. *nature*, 344:226 – 228, 1990.

[SO88] C. Shu and S. Osher. Efficient implementation of essentially non-oscillatory shock-capturing schemes. *J. Comp. Phys.*, 77(12):379 – 397, 1988.

[TL83] H. Tennekes and J. L. Lumley. *A First Course in Turbulence.* MIT Press, Cambridge, MA, 1983.

[Tow51] A. A. Townsend. On the Fine-Scale Structure of Turbulence. *Proceedings of the Royal Society of London. Series A, Mathematical and Physical Sciences*, 208(1095), 1951.

[Tsi09] A. Tsinober. *An Informal Conceptual Introduction to Turbulence.* Springer, 2009.

[TY04] Tomomasa Tatsumi and Takahiro Yoshimura. Inertial similarity of velocity distributions in homogeneous isotropic turbulence. *Fluid Dynamics Research*, 35(2):123–158, 2004.

[TYF07] Cameron Tropea, Alexander L. Yarin, and John F. Foss. *Handbook of Experimental Fluid Mechanics*. Springer, 2007.

[UL69] L.R. Ulinich and B. Ya. Lyubimov. The statistical theory of turbulence of an incompressible fluid at large Reynolds number. *Soviet Physics JETP*, 28(3):494–500, 1969.

[Vie82] P. Vieillefosse. Local interaction between vorticity and shear in a perfect incompressible fluid. *Journal de Physique*, 43(6):837–842, 1982.

[Vie84] P. Vieillefosse. Internal motion of a small element of fluid in an inviscid flow. *Physica A: Statistical and Theoretical Physics*, 125(1):150 – 162, 1984.

[VM91] A. Vincent and M. Meneguzzi. The spatial structure and statistical properties of homogeneous turbulence. *Journal of Fluid Mechanics*, 225(-1):1–20, 1991.

[WDF10a] Michael Wilczek, Anton Daitche, and Rudolf Friedrich. On the Velocity Distribution in Homogeneous Isotropic Turbulence: Correlations and Deviations from Gaussianity. *Journal of Fluid Mechanics, submitted*, 2010.

[WDF10b] Michael Wilczek, Anton Daitche, and Rudolf Friedrich. Theory for the single-point velocity statistics of fully developed turbulence. *European Physics Letters, submitted*, 2010.

[WF09a] Michael Wilczek and Rudolf Friedrich. Dynamical origins for non-Gaussian vorticity distributions in turbulent flows. *Physical Review E*, 80(1):016316, 2009.

[WF09b] Michael Wilczek and Rudolf Friedrich. A Langevin equation for the turbulent vorticity. In Joachim Peinke, Martin Oberlack, and Alessandro Talamelli, editors, *Progress in Turbulence III*, volume 131 of *Springer Proceedings in Physics*, pages 255–258. Springer Berlin Heidelberg, 2009.

[WJF08] M. Wilczek, F. Jenko, and R. Friedrich. Lagrangian particle statistics in turbulent flows from a simple vortex model. *Phys. Rev. E*, 77(5):056301, 2008.

[YIU+02] Mitsuo Yokokawa, Ken'ichi Itakura, Atsuya Uno, Takashi Ishihara, and Yukio Kaneda. 16.4-Tflops direct numerical simulation of turbulence by a Fourier spectral method on the Earth Simulator. In *Supercomputing '02: Proceedings of the 2002 ACM/IEEE conference on Supercomputing*, pages 1–17, Los Alamitos, CA, USA, 2002. IEEE Computer Society Press.

Danksagungen

> Das Publikum war heute wieder wundervoll,
> und traurig klingt der Schlussakkord in Moll.
> Wir sagen Dankeschön und auf Wiedersehen,
> schauen Sie mal wieder rein,
> denn etwas Schau muss sein ...
>
> *(Bugs Bunny und Duffy Duck)*

Mehr als drei Jahre Arbeit liegen nun hinter mir. Blendet man mal die kleinen Widrigkeiten des Alltages aus, so war diese Zeit vor allem geprägt von forscherischer Freiheit und vielen schönen Erlebnissen. Zeit also, Danke zu sagen.

Zunächst möchte ich Herrn Prof. Dr. Rudolf Friedrich für die Betreuung dieser Arbeit danken. Ich habe während der letzten Jahre in den zahlreichen, manchmal auch kontroversen fachlichen Diskussionen nicht nur viel gelernt, sondern auch viel Freude gehabt.

Herrn Prof. Dr. Frank Jenko möchte ich für die Mitbetreuung dieser Arbeit danken. Es war für mich stets wertvoll, einen Ansprechpartner zu haben, der den Fortgang der Arbeit aus etwas Distanz mitverfolgt. In diesem Zusammenhang auch ein herzlicher Dank an Klaus Reuter und Florian Merz, die mir besonders am Anfang der Arbeit bei vielen technischen Problemen weitergeholfen haben.

Auch bei Holger Homann und Prof. Dr. Rainer Grauer möchte ich mich für die Beantwortung vieler Fragen zur Numerik bedanken. Dem Rechenzenrum Garching sowie dem Leibniz Rechenzentrum München möchte ich für die Bereitstellung der Rechenzeit danken, was die numerischen Grundlage dieser Arbeit erst ermöglicht hat. Besonderer Dank geht dabei auch an die stets hilfsbereiten Mitarbeiter der Rechenzentren.

Der Gruppe um Prof. Dr. Joachim Peinke und im Besonderen Robert Stresing möchte ich für die Bereitstellung der experimentellen Daten danken.

Von unschätzbarem Wert waren für mich die Diskussionen mit den Turbulenzlern der Arbeitsgruppe, darunter Oliver Kamps, Anton Daitche, Michel Voßkuhle und Johannes Lülff. Der stets offene Austausch war für mich nicht nur äußerst hilfreich, sondern hat auch maßgeblich zu meiner Freude an der Arbeit beigetragen. Neben den in Stunden nicht mehr zu zählenden Diskussionen über Turbulenz im Speziellen und Gott und die Welt im Allgemeinen möchte ich Oliver Kamps für die zahlreichen, teils abenteuerlichen Reisen von Bad Kissingen bis San Francisco danken, die die letzten Jahre zweifelsohne versüßt haben. Vielen Dank auch an Anton Daitche, die vielen gemeinsamen Diskussionen und die gemeinsame Entwicklung des Simulationscodes haben mir nicht nur viel Freude

bereitet, sondern waren auch äußerst hilfreich.

Vielen Dank auch an Cornelia Petrović und Johannes Lülff für die stets entspannte Arbeitsatmosphäre in unserem gemütlichen Büro.

Allen Korrekturlesern, dazu gehören Anton Daitche, Christoph Honisch, Oliver Kamps, Michael Köpf, Johannes Lülff und Katharina Wilczek, möchte ich ganz herzlich danken. Ihr habt maßgeblich zum (zum jetzigen Zeitpunkt mutmaßlichen) Gelingen dieser Arbeit beigetragen!

Danke an dieser Stelle auch an meine Familie für die stete Unterstützung. Ihr seid prima! Für Rat, Tat, und vielerlei Hinsicht in einem Boot sitzen möchte ich auch meiner Frau Katharina danken, denn ich weiß: Ein Leben ohne Mops ist möglich, aber sinnlos.